Volatile organic compounds by-products generation in photocatalytic oxidation reactor: Experimental and modelling

Mojtaba Malayeri

A Thesis

In the Department

of

Building, Civil and Environmental Engineering

Presented in Partial Fulfillment of the Requirements

For the Degree of

Doctor of Philosophy (Building Engineering) at

Concordia University

Montreal, Quebec, Canada

August 2021

CONCORDIA UNIVERSITY
SCHOOL OF GRADUATE STUDIES

This is to certify that the thesis prepared

By: Mojtaba Malayeri

Entitled: Volatile organic compounds by-products generation in photocatalytic oxidation

          reactor: Experimental and modelling

and submitted in partial fulfillment of the requirements for the degree of

Doctor Of Philosophy (Building Engineering)

complies with the regulations of the University and meets the accepted standards with respect to originality and quality.

Signed by the final examining committee:

_____	Chair
Dr. Kudret Demirli	
_____	External Examiner
Dr. Jianshun (Jensen) S. Zhang	
_____	External to Program
Dr. Alex De Visscher	
_____	Examiner
Dr. Zhi Chen	
_____	Examiner
Dr. Catherine Mulligan	
_____	Thesis Supervisor (s)
Dr. Fariborz Haghighat	
_____	
Dr. Chang Seo Lee	

Approved by

_____

    Dr. Michelle Nokken, Graduate Program Director

August 30, 2021

_____

  Dr. Mourad Debbabi, Dean

  Gina Cody School of Engineering & Computer Science

Abstract

Volatile organic compounds by-products generation in photocatalytic oxidation reactor: Experimental and modelling

Mojtaba Malayeri, Ph.D.
Concordia University, 2021

The presence of volatile organic compounds (VOCs) in indoor air is inevitable. Their adverse effect on human health has encouraged researchers to develop various technologies for air pollution remediation. Photocatalytic oxidation (PCO) has been regarded as a promising and emerging technique for air purification and extensively investigated in the last two decades to characterize and improve the effectiveness and performance of this technology. In addition, the development of appropriate models can enhance the understanding of reactor performance and the evaluation of intrinsic kinetic parameters that enable the scale-up or re-design of more efficient large-scale photocatalytic reactors.

This research works on mathematical modeling of gas phase photocatalytic reactors and analyses different key factors that can enhance pollutants decomposition. At the first step, a one-dimensional time-dependent mathematical model for continuous flow UV-PCO reactor has been developed. In this model, transfer of pollutants by advection and dispersion in bulk phase incorporates with the reaction rate based on the extended Langmuir Hinshelwood model in the catalyst phase. CFD modeling was also used to determine the flow distribution in the reactor at various airflow rates. Moreover, the light intensity distribution on the photocatalyst surface was simulated using the linear source spherical emission model. A dimensionless form of the model was then proposed to generalize the result for any scale. The proposed model was validated first by comparing with predictions of other models (inter-model comparison) and then by experimental data from two different scales (pilot and bench) of UV-PCO reactors. Furthermore, a sensitivity analysis using dimensionless parameters was conducted to find the controlling step in the PCO process. To validate the model, acetone, MEK, and toluene were tested in the UV-PCO reactor

with a commercial PCO filter (TiO$_2$ coated on silica fiber felts) at various operating conditions, such as concentration, relative humidity, irradiance and air velocity.

The main issue for applying PCO technology in the indoor environment is the generation of hazardous by-products. The effect of by-products formation was usually ignored in former modeling studies. The next effort was to improve the model and build a comprehensive one to consider by-products generation in the UV-PCO reactor. To achieve this goal, a possible reaction pathway for degradation of each challenge compound was proposed based on identified by-products in analytical methods (GC-MS and HPLC). Different possible reaction rate scenarios were evaluated to find the best expression fitted to experimental data at the steady-state condition. The obtained reaction coefficients were then used to validate the model under various operating conditions. Finally, the Health Risk Index was used to investigate the implications of generated by-products on human health under varying operating conditions. The results indicated that the proposed model has a great potential to simulate the behavior of UV-PCO reactor in a real application.

ACKNOWLEDGMENT

Table of Contents

List of Figures

List of Tables

List of symbols

<u>English symbols</u>

A	Cross-section area, (m^2)
a_s	Geometric surface area per unit volume, (m^2/m^3)
C_A	Concentration of compound A in gas phase, (ppm)
C_{As}	Concentration of compound A in catalyst phase, (ppm)
C_{in}	Inlet concentration, (ppm)
C_{out}	Outlet concentration, (ppm)
C_w	Water vapor concentration, (ppm)
C_{byp}	By-product concentration, (ppm)
$C_{i\text{-}C\text{-}VOC}$	Concentration of compound i formed by MEK degradation, (ppb)
$C_{i,feed}$	Feed concentration of compound i, (ppb)
$C_{i,exit}$	Exit concentration of Compound i, (ppb)
D	Reactor diameter, (m)
d	Fiber diameter, (μm)
D_{ax}	Axial dispersion coefficient, (m^2/s)
D_m	Molecular diffusion coefficient, (m^2/s)
I	Light intensity, (W/m^2)
I_{ave}	Average light intensity, (W/m^2)
I_w	Light intensity at lamp wall, (W/m^2)
k	Reaction rate constant, $(ppm\ s^{-1}\ W^{-1}\ m^2)$
k_{app}	Apparent reaction rate constant, $(1/s)$
$k_{m,ext}$	External mass transfer coefficient, (m/s)
k_{LH}	Reaction rate constant, $(ppm\ s^{-1}\ W^{-1}\ m^2)$
$k_H{}'$	Reaction rate constant, $(s^{-1}\ W^{-1}\ m^2)$
K_A	Adsorption equilibrium constant of compound A in a single site, (ppm^{-1})
K_w	Water adsorption equilibrium constant in a single site, (ppm^{-1})
K_{byp}	By-product adsorption equilibrium constant in a single site, (ppm^{-1})
$K_{A.1}$	Adsorption constant of compound A on two types of site (site 1), (ppm^{-1})

$K_{A.2}$	Adsorption constant of compound A on two types of site (site 2), (ppm^{-1})
$K_{w.1}$	H_2O adsorption constant on two types of site (site 1), (ppm^{-1})
$K_{w.2}$	H_2O adsorption constant on two types of site (site 2), (ppm^{-1})
$K_{byp.1}$	By-product adsorption constant on two types of site (site 1), (ppm^{-1})
$K_{byp.2}$	By-product adsorption constant on two types of site (site 2), (ppm^{-1})
L	Reactor length, (m)
L_f	Thickness of PCO filter, (m)
L_{fb}	Length of fiber, (m)
L_p	Length of the lamp, (m)
m_{cat}	Mass of removal media(g)
P	Pressure, (atm)
p_{ws}	Pressure of saturated water vapor, (atm)
Q	Feed flow rate, (L/min)
q_e	adsorption capacity (mg/g)
q_m	maximal adsorption capacity (mg/g)
R_j	Distance between the lamp axis and the point of interest, (m)
r_A	Reaction rate, $(ppm\ s^{-1})$
r_l	Radius of the lamp, (m)
REL	Recommended exposure limit (ppm)
RH	Relative humidity (water vapor content), (%)
R^2	Determination coefficient
$S^2{}_R$	Sum of squared residuals between experimental and calculated outlet concentration (ppm^{-2})
t	Time (s)
t_d	Time delay (s)
$\bar{t}_m$	Mean residence time, (s)
T	Temperature, (°C)
u	Superficial velocity, (m/s)
u_b	Interstitial velocity (m/s), $u_b = u/\varepsilon$

y	Distance in reactor lateral coordinate, (m)
y_{lamp}	Distance of the lamp axis from the origin in lateral coordinate, (m)
Z	Distance in vertical coordinate, (m)

Greek letters

α	Parameter defined in Eq.(6.2), $\alpha = K_A C_{A,0}$
β	Parameter defined in Eq.(6.2), $\beta = K_w C_{w,0}$
γ	Parameter defined in Eq.(6.2), $\gamma = K_{byp} C_{byp,s}$
ε	Bed porosity
μ	Attenuation coefficient, (μm^{-1})
φ	Overall effective TiO$_2$ layer thickness, (μm)
φ_{max}	Maximum overall effective TiO$_2$ layer thickness, (μm)
σ	Variance of the residence time
σ_θ	Dimensionless variance
δ	Time interval, (s)
δ_f	TiO$_2$ layer thickness of single fiber, (μm)
ϑ	Air kinematic viscosity, (m^2/s)
ν_t	Turbulent kinematic viscosity, (m^2/s)
τ	Hydraulic residence time, (s)
ρ_{air}	Air density, (kg/m^3)
η_{min}	Mineralization efficiency
μ	Attenuation coefficient, μm^{-1}

Dimensionless parameters

$\bar{C}$	Dimensionless concentration, $\bar{C} = C/C_0$
$\bar{C}_s$	Dimensionless concentration in catalyst phase, $\bar{C}_s = C_s/C_0$
$\bar{C}_{by}$	Dimensionless concentration of by-products, $\bar{C}_{by} = C_{by}/C_{by,s}$

$\bar{C}_{sw}$	Dimensionless concentration of water in catalyst phase, $\bar{C}_{sw} = C_{sw}/C_{w,0}$
E	Residence time distribution function
HRI	Health Risk Index, $HRI = \sum \frac{C_i}{REL_i}$
$\bar{I}$	Dimensionless light absorption rate, $\bar{I} = I/I_{ave}$
Da	Damköhler number, $Da = k\, I\, L_f\, /u_b C_{i,0}$
Pe_L	Peclet number for the duct, $Pe_L = uL/D_{ax}$
Pe	Peclet number for PCO filter, $Pe = u_b L_f/D_{ax}$
Re_f	Reynolds number in fibrous media, $Re = u_b d/\varepsilon\vartheta$
Re_D	Reynolds number of reactor, $Re = u_b D/\varepsilon\vartheta$
Sc	Schmidt number, $Sc = \vartheta/D_m$
Sh	Sherwood number, $Sh = k_m D/D_m$
St	Stanton number, $St = k_m a_s L_f/u_b$
$\bar{t}$	dimensionless time, $\bar{t} = u_b d/L_f$
X	Removal efficiency
$\bar{x}$	dimensionless filter thickness, $\bar{x} = x/L_f$
Φ	Dimensionless overall effective TiO$_2$ layer thickness, $\Phi = \varphi/\varphi_{max}$

1. Introduction

1.1. Background

Indoor air quality (IAQ) has become a growing concern in developed countries, as most people spend more than 90% of their time indoors, namely in the home, office, car, or shopping center [1, 2]. Moreover, the rates of respiratory illnesses such as asthma, infection, and allergies are growing especially in children. These increases are believed to be related to the changes in the air quality of indoor environments, as the levels of pollutants in indoor air are generally higher than that of outdoor air [3, 4]. Therefore, there is an increasing concern for the removal of these pollutants even at relatively low concentrations found in indoor environments, since long-term exposure to indoor air pollutants causes sick building syndrome, and even cancer in extreme cases [2, 5].

Sources of indoor air pollutants can be outdoor air, furniture, construction materials, occupants and their activities. In terms of chemical pollutants, nitrogen oxides, ozone, radon, volatile organic compounds (VOCs) can be produced. VOCs are the major sources of gaseous pollutants in the building environment [2]. VOCs can originate from various sources such as construction materials, cooking, combustion by-products, office equipment, etc. [6]. Aromatics, aldehydes, halocarbons, alcohols, and esters are the main groups of VOCs identified in the indoor air[7].

Generally, there are three main methods to improve indoor air quality: source control, ventilation and air purification. Source control would be the best solution that can remove/reduce the source of emissions. However, occupants themselves (occupant activities, tobacco smoking, photocopying, cleaning and other activities) are the source of pollutions in most indoor environments such as classrooms and workplaces [8]. Ventilation also is the most common approach to reduce the pollutants concentrations inside the buildings. Nevertheless, it may transmit unwanted pollutants from outdoor to indoor environments. Another limitation of this method is that increasing the ventilation rate requires higher energy to minimize pollution levels. Air cleaning is another possible technique that eliminates chemical pollutants from the air. In addition, it is believed that a combination of air cleaning and ventilation method is the effective approach to reach a healthy indoor air quality and low energy consumption [9, 10].

Adsorption, a traditional air cleaning technology, has high efficiency for removing VOCs in the air [11]. Since VOCs are separated from the air stream by adsorbing on the adsorbent filter, this method requires regular adsorbent replacement. Among various adsorbents, activated carbon is the most common because of its high surface area and storage capacity [12]. Although the adsorption

method is economically favorable, it transfers pollutants from gas phase to adsorbed phase instead of decomposing them.

Another promising technology in this respect is photocatalytic oxidation (PCO) for the destruction of VOCs. The most important characteristic of this method is the operation at ambient pressure and temperature without a significant energy supply. Furthermore, the PCO method, in an ideal condition, can decompose hydrocarbons and create carbon dioxide and water at the end [13]. Despite the known advantages of PCO, the generation of hazardous by-products (i.e., O_3, CO, and organic by-products), which can be even more harmful than the target VOCs, can be significant in this process [14]. Moreover, low efficiency and slow reaction rate are other shortcomings, which highlight the necessity of more studies to enhance the capability of this method for indoor environment application [15, 16].

For the materials scientist, the main research interest centers on the synthesis of more efficient materials and the investigation of degradation mechanisms, whereas for the engineers, most research has been concerned with the development of appropriate models to enhance the understanding of photocatalytic reactor performance [17]. Besides, one of the major challenges in studying the potential of UV-PCO reactors for commercial applications is to find a reliable tool to assist the design, scale-up, and optimization. An appropriate mathematical model of the photocatalytic reactor can be a powerful tool to consider all phenomena involved in the PCO process [6].

1.2. Research objective

Based on the aforementioned facts, this research is aiming to develop a reliable and validated mathematical model for UV-PCO reactor, which can facilitate the extensive application for indoor air remediation. As many factors influence the performance of PCO, it is essential to study the impact of affecting parameters on the simulation result and removal efficiency.

Most existing models of the UV-PCO reactor have been developed without consideration of by-products formation. However, in reality, due to a very small residence time, VOCs partially oxidized, and some by-products appear in the outlet stream. The main goal of this research is to find an adequate mathematical model to predict by-product generation in a continuous UV-PCO reactor. To do this, the first step is finding a validated model for degradation of VOCs, and the second step is to improve that model to take both removal of challenge compound and formation of by-products into account. The following steps are the specific tasks of this research:

- CFD modeling was used to determine the flow distribution in the reactor.
- Evaluation of mass transfer parameters, including dispersion and interphase-mass transfer coefficients to develop a reliable model.
- Finding the best reaction rate model to describe the experimental data.
- Developing a validated mathematical model for degradation of challenge compound in UV-PCO reactor.
- Presenting a dimensionless model to generalize the result for any scale (scale-up) and then parametric simulations analysis based on non-dimensional parameters.
- Proposing reaction pathways for degradation of challenge compounds based on identified by-products by analytical methods.
- Proposing a by-product predictive model based on reaction pathways and, accordingly, reaction rate expressions.
- Validation of by-product predictive model at different operating conditions.

1.3. Thesis outline

Chapter 1. Introduction – This chapter presents a brief background, problem statements, and main objectives of this research.

Chapter 2. Literature review – This chapter presents the fundamentals of PCO technology and overviews by-products of some common indoor VOCs. Then, this chapter provides different reaction rate models, mass transfer equations used for the UV-PCO system. Finally, it presents a brief literature review on the effect of operating parameters, including flow rate, catalyst surface area, and porosity, and catalyst thickness, on degradation efficiency.

Chapter 3. Methodology – This chapter explains the principal of model development for PCO, including mass balance, radiation model, and reaction rate expression. Then, it describes the solving method, experimental procedures for adsorption and PCO tests, analytical methods, and air sampling procedures.

Chapter 4. Modeling of PCO reactor in the presence of mass transfer limitation and axial dispersion – This chapter focuses on CFD simulation to describe the flow distribution in the reactor and validate it with the RTD tracer experiment. In the next section, it evaluates the mass transfer parameters, including axial dispersion coefficient and mass transfer coefficient, in the presence of mass transfer limitation in the PCO system.

Chapter 5. Kinetic modeling of the photocatalytic degradation for removal of MEK– This chapter focuses on kinetic modeling of MEK in PCO using different Langmuir Hinshelwood base reaction rate models. In this chapter, the curve fitting was conducted by dispersion model and ideal plug flow model to find the best fitting result. A radiation field model was also developed and validated at different intensity levels. The mass transfer effect on the PCO reaction was also evaluated in this chapter.

Chapter 6. Modeling of MEK in PCO: Systematic Model Development and Validation – This chapter is dedicated to comprehensive validation of the developed model in both small and pilot-scale reactors. An inter-model comparison between the proposed model and two other models available in literature has been conducted. This chapter also presents the sensitivity analysis using dimensionless parameters to find the controlling step in PCO and generalize the model for application on any scale.

Chapter 7. Reaction pathway and predictive model for generated by-products in the PCO reactor – The first section of this chapter focuses on kinetic modeling and reaction mechanism of acetone and MEK to predict the generation of by-products in the PCO system. The next section of this chapter is dedicated to that of toluene with a greater number of by-products. The validation of the by-product predictive model is tested at various operating conditions.

Chapter 8. Conclusions and recommendations – This chapter presents the summary and findings of this thesis and provides recommendations for future research on the present study.

1.4. Current thesis type

This dissertation is a manuscript-based thesis in which the contents of chapters 2 to 7 are part of the published journal papers in the area of environmental chemical engineering as:

- Chapter 2:
  Malayeri, M., F. Haghighat, and C.-S. Lee, Modeling of volatile organic compounds degradation by photocatalytic oxidation reactor in indoor air: A review. *Building and Environment*, 2019.
- Chapter 3 & 4:

Malayeri, M., C.-S. Lee, F. Haghighat, and L. Klimes, Modeling of gas-phase heterogeneous photocatalytic oxidation reactor in the presence of mass transfer limitation and axial dispersion. *Chemical Engineering Journal*, 2020. 386: p. 124013.

- Chapter 3 & 5:

  Malayeri, M., F. Haghighat, and C.-S. Lee, Kinetic modeling of the photocatalytic degradation of methyl ethyl ketone in air for a continuous-flow reactor. *Chemical Engineering Journal*, 2021. 404: p. 126602.

- Chapter 3 & 6:

  Malayeri, M., C.-S. Lee, and F. Haghighat, Modeling of Photocatalytic Oxidation Reactor for Methyl Ethyl Ketone Removal from Indoor Environment: Systematic Model Development and Validation. *Chemical Engineering Journal*, 2020: p. 128265.

- Chapter 3 & 7:

  - Malayeri, M., C.-S. Lee, J. Niu, J. Zhu, and F. Haghighat, Kinetic and reaction mechanism of generated by-products in a photocatalytic oxidation reactor: Model development and validation. *Journal of Hazardous Materials*, 2021: p. 126411.

  - Malayeri, M., C.-S. Lee, J. Niu, J. Zhu, et al., Kinetic modeling and reaction mechanism of toluene and by-products in photocatalytic oxidation reactor. *Chemical Engineering Journal*, 2021: p. 131536.

2. Literature Review

2.1. Fundamentals of PCO

PCO, as a new generation of air cleaning technology, has a great potential to eliminate gaseous pollutants even at low concentrations [18-20] and applicable for different kinds of pollutants [21, 22]. Basically, PCO is performed using photocatalyst, ultraviolet (UV) light and oxygen to decompose chemical pollutants [23]. Among different types of photocatalysts, TiO_2 has attracted significant attention owing to its high stability, low cost, simple preparation, the excellent capability to destruct various compounds [24, 25].

The main step of PCO is the creation of electron/hole pairs via absorption of photons from UV light on the surface of the photocatalyst [22, 23]. In this step, when photon energy is equal to or greater than photocatalyst's band gap, photocatalyst reaction is started, in which highly reactive hydroxyl radicals ($OH^\bullet$) in the presence of H_2O molecules are generated. Moreover, oxygen reacts with electron and produce hydroxyl radical after a series of reactions [21, 26, 27]. These reactive species can oxidize adsorbed VOCs and degrade them to lower molecular weight products. Under optimal circumstances (total mineralization), CO_2 and H_2O would be final products from the PCO reaction of hydrocarbon compounds [20, 28, 29]. The prime photocatalytic reaction mechanism using TiO_2 activated by UV light can be described as follows [22]:
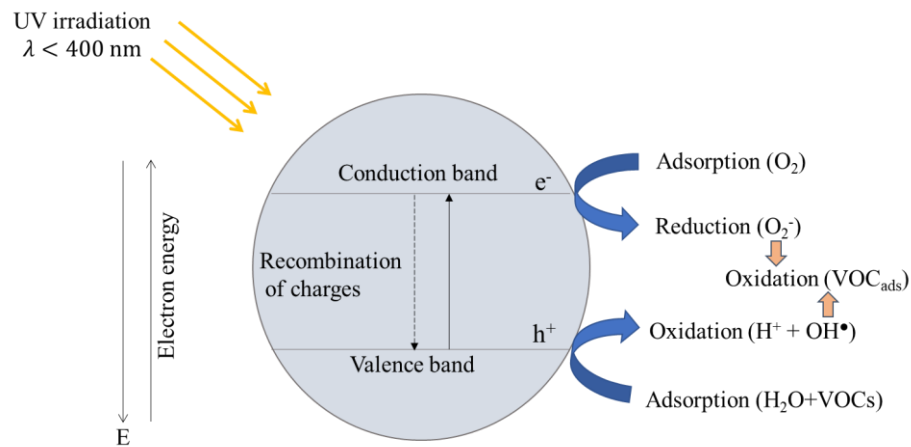
Fig. 2.1: Reaction mechanisms of PCO on photocatalyst

$$TiO_2 + hv \rightarrow TiO_2\ (h^+ + e^-) \qquad (2.1)$$

$$OH^- + h^+ \rightarrow OH^\bullet \qquad (2.2)$$

$$O_{2\,ads} + e^- \rightarrow O_{2\,ads}^- \qquad (2.3)$$

$$H_2O \rightarrow OH^- + H^+ \qquad (2.4)$$

$$O_{2\,ads}^- + H^+ \rightarrow HOO^\bullet \qquad (2.5)$$

$$HOO^\bullet + e^- \rightarrow HOO^- \qquad (2.6)$$

$$HOO^- + H^+ \rightarrow H_2O_2 \qquad (2.7)$$

$$VOC + OH^\bullet + O_2^- \rightarrow H_2O + CO_2 + by\text{-}products \qquad (2.8)$$
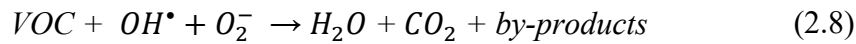
The unfavorable phenomenon during the photocatalytic reaction is the recombination of hole and electron, which happens on the surface or in bulk very fast. This process reduces the performance of PCO due to the reduction of oxidized species on the surface of the photocatalyst. Thus, it is necessary to develop a photocatalysts with high efficiency, in which the recombination process is slow and charge carriers have a high conductivity [20, 30, 31].

2.1.1. PCO process

Understanding the photocatalysis fundamentals is vital for interpreting experimental results, modeling of PCO reactor, and analyzing the affecting parameters on performance [20]. Generally, as Fig. 2.2 shows, the PCO process can be divided into seven main steps: (1) transfer of species by air flow (advection), (2) mass transfer from the bulk fluid to the external surface of catalyst (external mass transfer), (3) motion of reactants from the exterior surface into the interior pore of catalyst through diffusion (internal mass transfer), (4) adsorption of the reactant on the interior surface, (5) PCO reaction in the presence of photons, (6) desorption of products from the surface, and (7) motion of species from the interior of pores to bulk fluid by internal and external mass transfer [21, 27, 32].
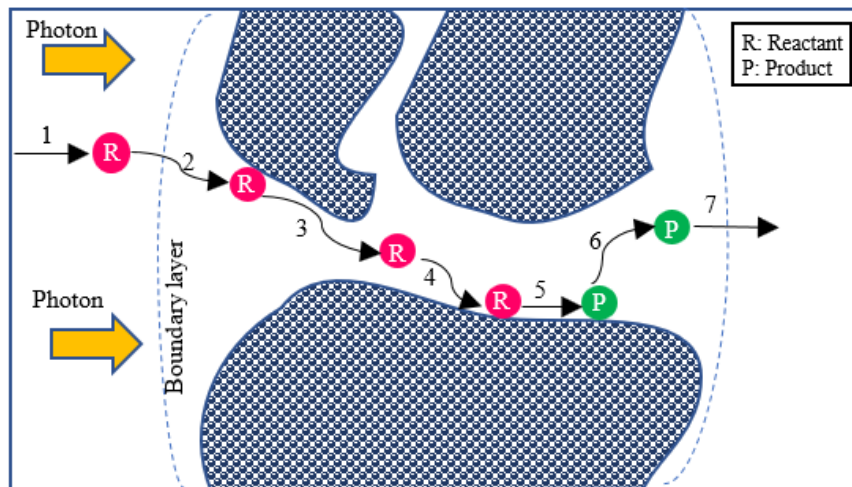
Fig. 2.2: Individual steps of catalytic fluid-solid reaction on a porous catalyst

As can be seen in Fig. 2.2, adsorption, surface reaction, and desorption are consecutive steps. On the other hand, as the photochemical reaction takes place on the catalyst surface, the mass transfer rate (external or internal mass transfer) is in a steady-state and, in terms of timescale, equivalent to the reaction rate. It is worthwhile to mention that most of the reaction occurs in step 2 (external surface reaction), where more hydroxyl radicals are available owing to direct radiation of light and higher photon energy. Generation of these highly reactive radicals, to a large extent, rely on number of active sites, dispersion of Titania particles, and distribution of light within the catalyst bed. In this regard, altering the catalyst density or thickness can have a major impact on radiation distribution throughout the reaction volume and, hence, the activation of catalyst particles. Besides, adsorption on the surface of the catalyst has an important role in the reaction rate and decomposition of VOCs. To be more specific, adsorption of challenge compounds is influenced by humidity level, physicochemical properties of challenge compounds, the adsorption capacity of catalyst [22, 33, 34].

Internal and external mass transfers from bulk to surface of the catalyst depend on temperature and velocity of the air, molecule collision, and size of the pores. Depending on the situation (reaction rate-limited or mass transfer-limited), any of these steps can control the total removal rate of the PCO reactor. In this regard, when mass transfer steps (i.e., steps 1, 2, 6, and 7 in Fig. 2.2) occur too fast, mass transfer resistance from bulk to catalyst surface and from surface to pore site can be neglected, and it can be implied that concentration around the catalyst is the same as that of the bulk one. Under this circumstance, mass transfer steps do not influence the rate of reaction. On the other hand, if mass transfer from bulk to catalyst surface takes place slowly, the resistance of external mass transfer is high, and it controls the overall reaction rate. To overcome

the external mass transfer limit, varying design parameters (e.g., flow conditions and catalyst characteristics) can help to reduce this resistance [20, 32, 34-37].

2.1.2. PCO Reaction By-products

Due to the short residence time of reactants in PCO reactor, in reality, VOC degradation can continue up to a certain level (partial oxidation), and many by-products/intermediates exist both in the gas phase and on photocatalyst. Formation of the undesired by-products is the main concern in the application of the PCO technology in buildings as some of these by-products are more toxic than their parent compounds [22]. The concentration of each by-product is usually in the range of ppb. Detecting very low concentrations of these compounds is a big challenge. Table 2.1 presents the by-products of some contaminants in the PCO reactor.

Table 2.1: By-products of some VOCs in PCO reactions

Compound	Intermediates/by-products	Analysis methods	Ref.
Acetaldehyde	Formaldehyde, acetic acid	GC-FID, FTIR	[38]
	Acetic acid, formic acid, formaldehyde	FTIR	[39]
Acetone	Acetaldehyde, methyl and isopropyl alcohol, MEK, ethyl acetate, acetic acid, mesityl oxide, diacetone alcohol	GC/MS, GC-FID	[40]
	Acetaldehyde, formaldehyde, acetic acid, formic acid	FTIR	[41]
	Formic acid, acetic acid, formaldehyde, bicarbonate	FTIR	[42]
Benzene	2-propenoic acid, 2-methyl-1-propanol	GC	[43]
	1,5-hexadien-3-yne, 2,4-hexadiyne, 1,3-hexadien-5-yne, formic acid	GC/MS, FTIR	[44]
	Hydroquinone,4-benzoquinone, phenol, formic, acetic acids	GC/MS, HPLC	[45]
Ethanol	Acetaldehyde, formaldehyde, acetic acid, formic acid	GC-FID, FTIR	[38]
	Acetaldehyde, formaldehyde	HPLC	[46]
n-Butanol	Butanal, propanal, ethanal, crotonaldehyde	GC/MS, GC/FID	[47]
MEK	Acetone, ethanol, acetaldehyde, acetic acid, methanol, formaldehyde, formic acid	GC/MS, GC-FID	[48]
Toluene	benzyl alcohol, benzaldehyde, benzoic acid, p-toluquinone, cresol	GC/MS, GC/FID	[49]
	Benzoic acid, benzyl alcohol, and benzaldehyde, formic acid, acetic acid	GC/MS, HPLC	[45]
	Benzaldehyde, benzene, formaldehyde, MEK, cresol, phenol, benzyl alcohol	GC/MS, HPLC	[50]
	Benzyl alcohol, benzoic acid, benzaldehyde, hydroquinone, cresol	FTIR	[41]
	Acetone, acetic acid, butyraldehyde, benzene, pentanal, benzaldehyde, benzoic acid	PTR-MS, GC/MS	[51]

	Formaldehyde, acetaldehyde and methanol, propylene, acetone, acetic acid, benzene	PTR-MS	[52]
1-propanol	Propionaldehyde, acetaldehyde	GC/MS	[53]

The generation of intermediate highly depends on reaction mechanisms of different contaminants in the PCO process. In addition, the form and quantity of by-products have a close relationship with the operational conditions, the PCO reactor configurations, and the characteristics of the catalysts [16, 54]. Some intermediates/by-products adsorb on the catalyst surface and block the reactive sites, which can inhibit the photocatalytic degradation of the target compound. Therefore, with increasing the illumination time, conversion of VOC reduces due to the deactivation of the catalysts [55].

2.2. Modeling of PCO

Designing an efficient photocatalytic reactor requires knowledge of the kinetic reaction mechanism, mass transfer of VOCs and radiation transfer. The lower operating costs are of great importance for utilizing a PCO reactor in a real application, which can be achieved by optimizing light radiation and by providing efficient mass transfer of reactants. Therefore, the scale-up and finding the efficient operation of the PCO reactor are demanding tasks, which may hamper commercial development [56, 57]. Mathematical modeling of the PCO process can be an effective tool for design, scale-up, and optimization studies, as it opens up an opportunity to comprehend the optimal performance of the reactor and its limitation [56]. In addition, developing a mathematical model is crucial to investigate the influence of parameters on each step of PCO (Fig. 2.2). To reach this purpose, a combination of an appropriate reaction kinetic with an elemental mass balance is required to be considered. Such an equation can predict the removal rate of pollutants as a function of operating parameters, reactor geometry, and physical property of photocatalyst [6, 21, 58]. In the PCO process, there are interactions among pollutants, catalyst, and irradiation, which make modeling of photocatalytic reactor a complex task. For instance, the concentration of catalyst (amount of titania per unit volume) has a direct impact on radiation distribution and, consequently, on the activity of catalyst [59-63].

2.2.1. Reaction kinetic models

Reaction kinetic gives information about the mechanisms that the reactants are converted to products and is used to determine the performance of the photoreactor for VOC degradation. Theoretically, the kinetics of reaction can be described as decreasing rate of reactants or raising

rate of products. The degradation rate of challenge compounds in the PCO reactor depends on operating conditions such as concentration of VOCs, temperature, irradiation, humidity, and catalyst loading such that [21, 23, 64]:

$$-r = k\,(f\,[C]) \qquad\qquad (2.9)$$

$$k = f\,(T, I, W_{cat}) \qquad\qquad (2.10)$$

where $f\,[C]$ is a function of VOC concentration and relative humidity. Moreover, $f\,(T, I, W_{cat})$ reperesnts dependency of kinetic constant on temprature, irradiation and catalyst loading, respectively. Concentration is one of the key factors in reaction rate. Generally, the reaction rate increases with reactant concentration due to the increment in the frequency of collision. The relationship between reaction rate and reactant concentrations is described mathematically by rate law (shown in the next section). Temperature is also regarded as a major factor that influences the rate of a chemical reaction. Raising temperature provides enough activation energy for more effective molecular collisions. In terms of humidity, it is believed that complete degradation to carbon dioxide is unachievable without the presence of water vapor. On the other hand, introducing excessive humidity leads to reduction in catalyst active sites and, consequently, a decrease in reaction rate. As for catalyst loading, it has a major impact on catalyst activity and degradation rate. Depending on saturation value, support material and coating method, the amount of semiconductor on the substrate is dissimilar in different studies, which affects catalyst activity and, consequently, the reaction rate. Since photons activate semiconductors to create charge carriers for the degradation of VOCs, light intensity has a prime impact on the reaction rate and removal efficiency of the PCO reactor.

2.2.1.1. Pollutant and water vapor concentrations

As photocatalyst reaction rate relies on surface coverage of pollutants on catalyst particle, kinetic modeling of PCO reactor is associated closely with adsorption model [26]. In this respect, the relationship between concentration of VOCs and reaction rate can be described through various adsorption isotherm including Langmuir, Freundlich, and Brunauer–Emmett–Teller (BET) [65-69]. Among them, Langmuir isotherm is widely used in the literature. This isotherm is based on the hypothesis that there is monolayer adsorption on a uniform catalyst site. It also assumes that each site holds only one adsorbate molecule and there is no interaction between adsorbate molecules [65, 66, 69].

In general, the kinetic model of PCO is commonly described as unimolecular (first-order) or bimolecular (second-order) reaction rates. As the mechanism of photocatalytic decomposition contains numerous reaction steps and pathways as well as many different reaction intermediates, developing a reliable reaction rate model that is applicable for various pollutants and conditions is a complex task. Practically, kinetic experiments are employed to investigate the dependency of degradation rate and influencing parameters (i.g. concentration, irradiation, water content and temperature). Unimolecular removal of VOCs based on Langmuir adsorption model can be described as following equation (also known as Langmuir-Hinshelwood) [70-72]:

$$-r = k \frac{K\,C_s}{1+KC_s} \qquad (2.11)$$

where k and K are global kinetic coefficient and adsorption constant respectively. C_s is the sorbed-phase concentration of challenge compounds. In the absence of mass transfer limitation, the concentration at the catalyst surface is equivalent to that in the bulk flow. Curve fitting routine (least-square method) is applied in order to measure kinetic data.

Eq.(2.11) is applicable under the assumption that there is no competition between the target compound and other compounds (including intermediate and by-product). By considering the effect of other compounds, the concentration of adsorbed target compound reduces and can be indicated by modified Langmuir relation [21, 73-76]:

$$-r = k \frac{K\,C_s}{1+\sum_{i=1}^{n} K_i C_{s,i}} \qquad (2.12)$$

where n stands for the number of compounds existing in the air. One of the main compounds that compete with other reagents for adsorption on the surface of the catalyst is water vapor. Including the effect of water molecules for adsorption in Eq.(2.12), the removal rate of compound p can be stated as [77-82]:

$$-r_p = k \frac{K_p C_p}{1+K_p C_p + K_w C_w} \qquad (2.13)$$

where K_w is the Langmuir adsorption constant of water vapor and C_w is the gas-phase concentration of the water vapor. Eq.(2.13) is applicable under the assumption that reaction products do not have any effect on the degradation rate and the reaction kinetics is mainly dominated by competitive interaction between water (C_w) and inlet concentration of challenge compound (C_p) [78].

By considering the second-order (bimolecular) Langmuir adsorption model, there are three different scenarios: (1) adsorption of target gas and water on the same type of sites with competitive adsorption, (2) adsorption of target gas and water on different types of sites with competitive adsorption, and (3) adsorption of target gas and water on different types of sites without competitive adsorption. Bimolecular reaction rate equations for each above-mentioned case are presented in Table 2.2 [83-85].

Table 2.2: Three different types of bimolecular reaction in Langmuir model

Reaction rate equation		Principles	Ref.
$-r_p = k \dfrac{K_p C_p}{1+K_p C_p} \dfrac{K_w C_w}{1+K_w C_w}$	(2.14)	Adsorption on different types of sites, without competitive adsorption	[83-86]
$-r_p = k \dfrac{K_p C_p K_w C_w}{(1+K_p C_p + K_w C_w)^2}$	(2.15)	Adsorption on the same type of sites, with competitive adsorption	[43, 83-86]
$-r_p = k \dfrac{K_1 C_p}{1+K_1 C_p + K_2 C_w} \dfrac{K_4 C_w}{1+K_3 C_p + K_4 C_w}$	(2.16)	adsorption on different types of sites, with competitive adsorption	[83-85, 87-90]

In practice, Eqs. (2.14) to (2.16) are applicable when the relative humidity of air is low enough and hydroxyl radicals concentration on catalyst surface is the rate-limiting element. In this case, mass transfer of water molecule from bulk to catalyst particle becomes rate-limiting step of PCO process. It is also worthwhile to be noted that the kinetic model varies with operating conditions or reactor designs. Fig. 2.3 presents some common types of PCO reactor. For instance, the results of the kinetic model for formaldehyde in a flat plate reactor [91] using Eq.(2.16) were different from that in the monolith reactor [92] or were not the same as flat plate reactor results with a different operating condition [83]. To be more specific, at same operating condition, monolith reactor provides better mass transfer of VOCs than flat plate reactor. In a monolith reactor, more VOC molecules are in contact with catalyst active sites, so more reactions can happen for the same adsorbed photons [26]. Additionally, reaction rate highly depends on operating conditions and kinetic parameters may change with operating parameters (such as flow rate, relative humidity, light intensity).
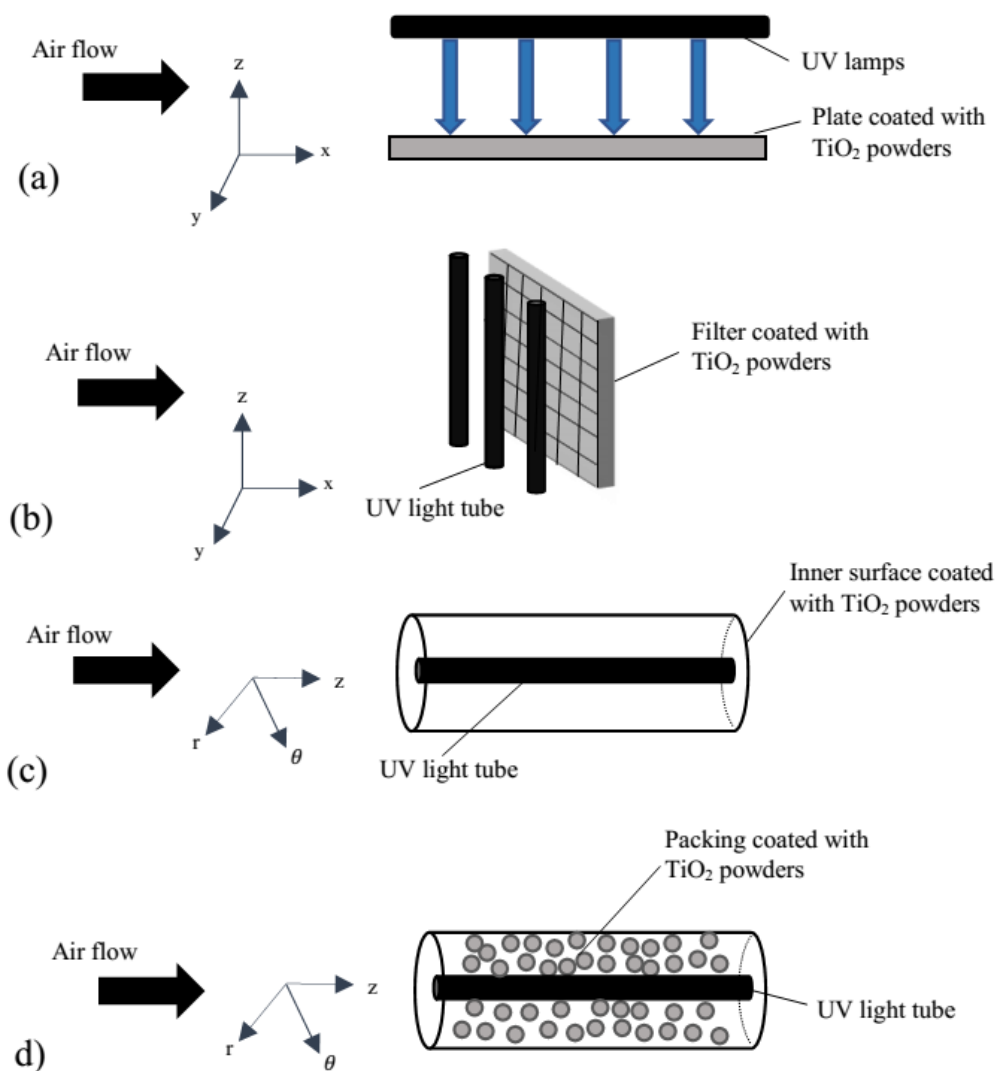
Fig. 2.3: Schematics of typical PCO reactors a) flat plate reactor b) monolith reactor c) annular reactor d) packed bed reactor

In some earlier research works, Langmuir kinetic model could not be well-fitted with experimental data and a new kinetic model has presented with some modifications in Langmuir model. Demeestere et al. [93] presented a new kinetic model for TCE (Trichloroethylene) after reaching inadequate fitting for the first order Langmuir equation, in which reactions of electron-holes and the effect of recombination are explicitly regarded. Muñoz et al. [94] implemented the same approach for toluene through the second-order reaction rate, in which toluene, water, and other compounds are considered to have a competition for adsorption on the same site. In general, a higher initial concentration of pollutants leads to reaction rate increment until it reaches its plateau but ends up having lower removal efficiency [95, 96]. In contrast, a lower concentration

of VOCs raises removal efficiency and degradation of pollutants to carbon dioxide [97]. Increasing inlet concentration enhances the number of adsorbed molecules on the catalyst surface and, then, the reaction rate. However, it declines the removal efficiency of the PCO reactor due to the reduction in number of active sites. Moreover, as the initial concentration rises, the mass of by-products and intermediates occupying catalyst active sites increase, which causes more gas molecules to leave the reactor without reaction [84].

Many authors enquired into the influence of inlet pollutant concentration on decomposition rate. Mo et al. [98] investigated the effect of toluene concentration on various catalysts in a flat plate type of PCO reactor. They showed that with raising concentration from 0.5 to 4.5 ppm, removal efficiency reduces up to 40%. Likely, Cao et al. [99] revealed that conversion of butene drops with increasing inlet concentration from 1 to 9 ppm; however, the oxidation rate grows with butene concentration. They also indicated that the changing magnitude of oxidation rate at low concentrations of butene is higher than at high concentrations. Lopes et al. [100] investigated the impact of PCE concentration on degradation efficiency, which showed that the efficiency declines about 1.8 times as feed concentration raises 4.25 fold. This occurs because more PCE molecules pass through the catalytic bed without being decomposed, either by the hydroxyl or chloride radicals. Therefore, it can be concluded from the observation of each research that low inlet concentration results in higher degradation performance of PCO reactor.

2.2.1.2. Light source and intensity

The light source provides the energy required to initiate the photocatalytic process. Theoretically, TiO_2 photocatalysts are activated at a wavelength of less than 380 nm [51, 101]. Fluorescent black-light lamps (300-400 nm) and germicidal lamps (UVC, 254 nm) are the most commonly used light sources in PCO of air pollutants. The energy of these spectrums is equivalent to or higher than the 3.2eV band-gap energy of TiO_2 [102, 103].

Increasing light intensity leads to more excitation and electron-hole pairs creation, accordingly, an increase in hydroxyl radical generation and, then, in VOC degradation rate. The influence of light intensity on reaction rate can be divided into two regimes: first-order regime at low light intensity, where chemical reaction dominates recombination of electron-hole pairs, and a half order regime at high light intensity, where recombination speed is more than chemical reaction. Therefore, the correlation between reaction rate and light intensity can be summarized as follows [21, 22, 91, 104]:

$$r \propto I^n \begin{cases} n=0.5 & I > \text{one sun} \\ n=1 & I \leq \text{one sun} \end{cases} \qquad (2.17)$$

where r is the reaction rate and I is the light intensity. One sun is equivalent to about 10-20 W/m^2 for wavelengths below 350 and 400 nm, respectively [21, 105].

In addition, some researchers proposed a zero order (n=0) regime to describe the relationship between reaction rate and light intensity, where the overall rate is limited by mass transfer. In this situation, the degradation rate becomes independent of light intensity, and the conversion reaches a constant value. This happens when light intensity is very high and the concentration of pollutants is quite low (ppb range). In such cases, they indicated that raising light intensity does not have any effect on the reaction rate as reactions take place under mass transfer control [40, 106]. In general, the relationship between reaction rate and the exponent of light intensity can be classified as three different regimes, depending on the amount of intensity (Fig. 2.4).
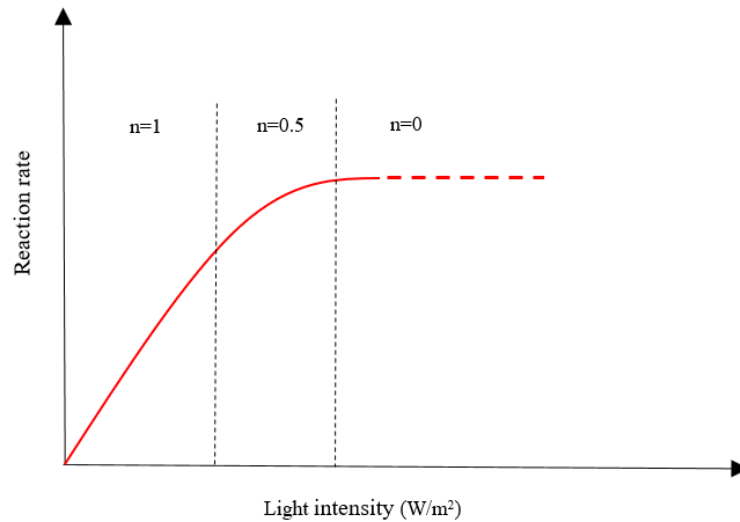
Fig. 2.4: Reaction rate versus light intensity for different regimes

For the purpose of the optimal design of PCO reactor, radiation field has also been simulated using different methods, such as geometrical method using differential view factors ([81, 92, 107]), Monte Carlo simulation ([108-110]), and Beer-Lambert law ([111-113]). The last one, owing to its simplicity, was used frequently in literature to describe the distribution of light inside the catalyst. When the catalyst particles are in very close proximity to each other (a non-scattering medium), the influence of absorption is much more than scattering and Beer-Lambert law (eq (2.18)) can be readily applied for light intensity [113].

$$I = I_0 e^{-\mu x} \qquad (2.18)$$

where I_0 is the intensity of incident (W/m²), μ is the attenuation coefficient for UV in the catalyst (m⁻¹) and x is catalyst thickness. According to this equation, the intensity of light decreases exponentially with depth in the material.

2.2.1.3. Temperature

Temperature is one of the most significant factors in gas-solid photocatalytic reactions. Temperature influences the activity of photocatalyst and consequently affects not only kinetic reaction but also adsorption of gas compounds on the catalyst. However, oxidation reactions are not sensitive to minor alterations in temperature [114-117]. The dependency of temperature to rate constant, k, can be expressed using Arrhenius equation [83, 115]:

$$k \propto f\left(exp\left(\frac{-E_a}{RT}\right)\right) \qquad (2.19)$$

where E_a is apparent activation energy (kcal mol⁻¹) which is usually greater than zero. R and T stand for gas constant (1.987×10^{-3} kcal mol⁻¹K⁻¹) and titania temperature in Kelvin, respectively. Increasing temperature has a positive effect on the removal rate of VOCs, owing to the increment in collision frequency. Nevertheless, adsorption is an exothermic process; enhancing temperature reduces the coverage of photocatalyst by VOCs, and consequently, decreases adsorption capacity [118-120]. The relationship between adsorption equilibrium coefficient, K, and temperature, T, can be stated similarly to Arrhenius equation [78, 121, 122]:

$$K \propto f\left(exp\left(\frac{Q}{RT}\right)\right) \qquad (2.20)$$

where Q represents the heat generation of adsorption.

In general, it can be noted that in low temperature, adsorption is the dominant process and in high temperature, kinetic reaction plays a dominant role. Since the overall reaction rate considers the combined adsorption and kinetic reaction processes, a maximal reaction rate can be reached at an optimal temperature [120, 123, 124]. Depending on the rate-controlling process, raising temperature can enhance reaction rate or drop it. For instance, when adsorption is the rate-limiting process, raising temperature decreases the reaction rate. On the other hand, increasing temperature enhances reaction rate when kinetic reaction becomes a controlling process. This may result in dissimilar results by researchers when they perform experiments with different chemical pollutions [105, 123, 124].

2.2.1.4. Catalyst loading

Though photocatalytic reaction takes place on the surface, catalyst loading (catalyst concentration) has a significant effect on the reaction rate. Increasing catalyst loading in a PCO reactor enhances the concentration of the active site. This improvement leads to a higher reaction rate and, consequently, greater degradation efficiency [63, 125, 126]. Numerous researchers reported that the decomposition rate firstly raises with increasing catalyst loading, but it drops after a specific limit. This decline in reaction rate is attributed to poor light penetration, increase in light scattering effect, and particle accumulation created by the high catalyst concentration. In this case, the optimal value of catalyst loading should be found to reach the maximum level of VOC conversion [127, 128].

Einaga et al. [101] studied the dependency of benzene conversion on the loading of TiO_2 catalyst in the PCO reactor. They observed that with increasing catalyst loading from 0 to 0.24g, benzene conversion grows sharply from 0 to 100%. Alternatively, some researchers pointed out a decreasing tendency of catalyst activity as an excessive amount of TiO_2 particle is loaded on the support surface. For instance, Takeda et al. [125] noticed that for TiO_2 loading less than about 50 wt%, the mineralization rate of propionaldehyde is plainly proportional to TiO_2 particle content, and its adsorbed amount does not have any great effect. However, after about 50% loading, with elevating TiO_2 concentration, the photodecomposition rate drops. They highlighted that before the critical point, the illuminated photons were effectively utilized in photoexcitation of the loaded TiO_2, but beyond this value, a fraction of loaded catalyst is not utilized in photoexcitation and leads to the decrease in degradation rate. Romero et al. [128] demonstrated that increment in catalyst (Aldrich titanium dioxide) concentration from 0.05×10^{-3} to 0.5×10^{-3} $g.cm^{-3}$ results in increased scattering and absorption effects as well as smaller intensities. They also compared the result of this catalyst with Degussa P25 titanium dioxide at catalyst concentration of 0.3×10^{-3} $g.cm^{-3}$ and found that the latter equivalent to duplicating the mass particle concentration of Aldrich titanium dioxide. Likewise, Alonso-Tellez et al. [129] compared two different catalysts, UV100 and P25, to find the effect of enhancing catalyst loading on the degradation of MEK. Raising TiO_2 particle content elevated MEK removal efficiency for both catalysts until optimum value and beyond this to reach a plateau level. The optimal amount of loading for UV100 and P25 were about 1.25mg cm^{-2} with 40% decomposition and 0.75 mg cm^{-2} with 19% conversion, respectively. They concluded that the received irradiance and light transmission through UV100 photocatalyst is

higher than the other one at similar catalyst loading. The deeper light penetration inside the UV100 results in activation of more TiO₂ particles and, accordingly, a higher level of degradation.

2.3. Mass transfer model

The performance of PCO reactor can be divided into two main parts: (1) VOC transport from bulk to catalyst surface (2) removal of them by the photocatalytic reaction. Referring to last section (reaction kinetic model), most researchers presumed that the PCO process being limited by the kinetic reaction and mass transport is often ignored in photocatalysis studies, especially by chemistry groups. The reason is that they try to concentrate more on catalyst activity and its efficiency, even though knowing mass transfer phenomenon has a vital role in interpreting experimental results and scaling up of PCO reactor [130, 131]. Therefore, to obtain a complete model and apply the photocatalytic reactor on a larger scale, a kinetic reaction model coupled with a mass transfer model provides a more comprehensive and accurate model [40, 106].

2.3.1. Internal and external mass transfer

The mass transfer phenomenon can be categorized as internal and external mass transfer. The internal mass transfer in porous media includes diffusion of molecules from the external surface of the catalyst particle to the inside of the pore. As the internal mass transfer resistance of TiO₂ is assumed to be negligible (a very small thickness of TiO₂ layer), this type of mass transfer is usually neglected in most numerical modeling studies. The presence of rate-limiting step by internal mass transfer can be determined using dimensionless Weisz–Prater criterion (C_{WP}). This criterion is defined as the actual reaction rate per diffusion rate. When the value of C_{WP} is greater than one, internal diffusion limits the reaction [132-134]. The external mass transfer involves the motion of molecules from bulk to catalyst surface via diffusion and convection. This kind of mass transfer controls the PCO process when the driving force is large enough, and the transport of molecules from high concentration (bulk) to low concentration (catalyst surface) is slower than reaction [40, 132].

The diffusion step incorporates the diffusivity of challenge gas in the film layer. The convection step associates with fluid velocity, fluid characteristics, and geometry of the reactor. However, the mass transfer coefficient expresses both diffusion and convection concepts and their influencing parameters in a single number [135, 136]. The rate of external mass transfer (N) on catalyst surface can be stated as below[40]:

$$N = k_m(C_b - C_s) \qquad (2.21)$$

where k_m is external mass transfer coefficient, C_b and C_s are bulk and surface concentration. Consequently, mass balance over film layer can be rewritten as follow [137]:

$$\frac{dC_b}{dt} = k_m\, a_s\, (C_b - C_s) \qquad (2.22)$$

where a_s represents the ratio between the surface area of film and reactor volume. Mass transfer coefficient (k_m) can be calculated using Sherwood number (Sh), Reynolds number (Re), and Schmidt number (Sc) as follow:

$$Sh = x\, Re^y\, Sc^{1/3} \qquad (2.23)$$

where the value of x and y, depending on flow characteristic and type of reactor, can be vary. Vezzoli et al. [137] used this correlation to calculate mass transfer constant in a flat plate PCO reactor with laminar flow, in which values of 0.664 and 0.5 were considered as x and y coefficients. In another study by Yang et al. [138] for a tubular PCO reactor, these parameters changed into 1.17 and 0.58, respectively, due to different experimental conditions and flow property.

In the case of external mass transfer limitation, changes in concentration during the time by considering reaction rate can be expressed as below:

$$\frac{dC_s}{dt} = k_m\, a_s\, (C_b - C_s) - r_p \qquad (2.24)$$

Where r_p is *the* reaction rate presented in section 3.1. Chen et al. [132] and Vezzoli et al. [137] studied the effect of mass transfer in a flat plate reactor with a porous media. They found that internal mass transfer resistance can be neglected according to the magnitude of Thiele modulus and external mass transfer controls the overall rate of reaction. Dijkstra et al. [139] observed that the system is limited by mass transfer since the removal rate rises with increasing Reynolds number. In terms of mass transfer, they also realized external mass transfer limitation happens in the PCO reactor.

2.3.2. Material balance

The overall mass balance in each control volume for the PCO reactor can be applied in both gas and solid phase. According to Fig. 2.2, conservation of mass for species involves diffusion, advection phenomenon and photochemical reaction. The mass balance equation in bulk phase for species i can be indicated as [140]:

$$\frac{\partial C_i}{\partial t} = -\nabla \cdot (VC_i) - \nabla \cdot J_i + R_i \qquad (2.25)$$

where, C_i is the molar concentration of species i, J and V are the diffusion flux and velocity vector, respectively, and R_i represents the rate of production or depletion of species i by the photocatalytic reaction. In this equation, the left-hand side appears for the accumulation of species, and the first term on the right-hand side represents the mass transfer of species through advection. To simplify Eq.(2.25), Fick's law is often used for gas diffusion, which represents that the rate of diffusion is proportional to the concentration gradient. Some researchers applied a 2D model and assumed diffusion term in the axial direction and/or advection in perpendicular to flow direction are neglected [141, 142]. In order to do more simplification on the model, plug flow and laminar flow for velocity profile are frequently used.

Assadi et al. [143] proposed one dimensional mathematical model for scaling up of different continuous flow reactors (cylindrical reactor, planar reactor and pilot unit) to remove Isovaleraldehyde (Isoval) in gas phase. In this model, they considered mass transfer phenomena combined with the kinetic model as well as the chemical pathways of reaction. Model validation indicated an average error of less than 10%, which shows a great agreement between model and experiment. Adjimi et al. [144] modeled a continuous stirred-tank reactor, under simulated UV intensity, for degradation of ethanol over TiO_2/SiO_2 in the gas phase by coupling the convection-diffusion equations for mass transfer and the light intensity model for UV penetration. They also investigated two types of flows (counter and co-current) and found out that differences in concentration and diffusive flow patterns can cause a discrepancy in the activity of photocatalyst. Lopes et al. [100] presented a complete mathematical model in a continuous-flow tubular photoreactor, under simulated solar irradiation, for degradation of Perchloroethylene (PCE). To develop the model, they tested six different kinetic rate equations, suggesting that Perchloroethylene and water molecules should be taken into account in relation to the different active sites of the surface. This model considered the effects of operating parameters, namely PCE concentration, feed flow rate, and water vapor content, on process performance. Zhong et al. [35] developed a time-dependent model for an in-duct PCO air cleaner under conditions related to actual application. This model integrates the kinetic reaction model, mass balance, and light scattering model, including the effect of reactor geometry, parameters of mass transfer and kinetic, and properties of catalyst and light source. Tomasic et al. [145] compared three different mathematical models, one-dimensional (1D) model and two-dimensional (2D) models based on ideal flow and laminar flow conditions, in the annular photocatalytic reactor for removing toluene

21

from the air. They highlighted that the overall rate of this reactor is controlled mainly by the interphase mass transfer and concluded that 2D model based on the laminar flow is the most appropriate model for a comprehensive description of annular photocatalytic air purification system.

In terms of advection, laminar flow and ideal plug flow are most commonly implemented assumptions in PCO reactor. In plug flow, the velocity profile is assumed constant (uniform flow) in each direction along the reactor, and there is no boundary layer near the wall, whereas laminar flow takes the effect of boundary layer into account and velocity profile has a parabolic shape after fully developed region. One important shortcoming of most modeling studies is related to the effects of intermediates and by-products in the reaction term. Effects of these products are assumed to be negligible in kinetic rate, while they can impact the adsorption of main compounds and activity of the catalyst.

Some authors, for example, Hossain et al. [92] and Jarandehei et al. [146], presented a comprehensive three-dimensional advection-diffusion-reaction model to investigate elimination of VOCs in monolith and flat plate PCO reactor, respectively, under steady-state condition, which the result was impressively fitted with experimental data. In addition, Wang et al. [88, 147] developed a three-dimensional and unsteady-state mathematical model, which reached a good agreement with experiments. However, these models considered only the mass balance of pollutants in gas phase and assumed reaction occurs in a control volume adjacent to the catalyst surface.

Applying advection and diffusion in gas phase and reaction rate model in the solid phase, as well as boundary layer transfer, can provide detailed modeling of all involving steps in PCO process (Fig. 2.2). To date, most studies considered the mass balance of species in either gas or solid phase and only a few models presented mass balance in both phases [81, 145]. In this context, some authors (for example, Zhang et al. [148], Boulinguiez et al. [149], Biard et al. [150] and Tomašić et al. [145]) introduced a simple 1D mass conservation equation, in which mass transfer happens through gas boundary layer near catalyst surface and pore diffusion has been assumed negligible due to very thin catalyst layer. Considering the aforementioned facts, they implemented the following mass balance in the gas phase (Eq.(2.26)) and solid-phase (Eq.(2.27)):

$$u\frac{dC}{dx} = k_m a_s (C - C_s) \qquad\qquad (2.26)$$

$$k_m a_s (C - C_s) = r = f[C_s] \qquad\qquad (2.27)$$

The more realistic mass transfer model can be achieved when the concentration gradient by diffusion (Fick's law) along the PCO reactor is taken into consideration. This model provides a better approximation than the previous one, where a quick drop of concentration at gas boundary layer is unrealistic [145]. Similarly, Marečić et al. [151] and Tomašić et al. [145] developed a two-dimensional and unsteady-state mathematical model for both gas and solid phase with considering molecular diffusion in the gas phase. A more comprehensive model was presented by Zhong et al. [81] and Assadi et al.[143] for PCO reactor by considering advection, diffusion, and boundary layer transfer of molecule in the gas phase as well as reaction in the solid phase.

2.4. Parameters affecting PCO performance

As decomposition of challenge gas in photocatalytic oxidation reactor depends on airflow condition, type of pollutant for adsorption process and properties of photocatalyst, determining the influence of each parameter can provide great insight into removal performance of VOC. Accordingly, this section briefly reviews the effect of flow rate, catalyst surface area, porosity, and catalyst thickness.

2.4.1. Airflow rate

The airflow rate plays an important role in the degradation rate of VOCs in PCO reactor. The general idea about the influence of air flow rate is that it has a dual adverse effect on PCO reaction. Increasing flow rate reduces residence time in the photoreactor, which, accordingly, causes decrease in removal efficiency. On the other hand, as the flow rate increases, the rate of mass transfer between gas and photocatalyst surface grows, which leads to enhancement of reaction rate [152, 153]. In case of higher residence time, VOC molecules have a more chance to be adsorbed on the catalyst surface. In consequence, the number of compounds that react with hydroxyl radicals or superoxide anions increases; hence, removal efficiency enhances [97]. Therefore, in the mass balance equation, the mass transfer coefficient (k_m) is influenced by changing airflow rate in the PCO reactor. As airflow rate (or velocity) increases boundary layer thickness (or film thickness), δ decreases according to relation $k_m = D/\delta$, and consequently, k_m increases. As long as mass transfer controls the overall rate, increasing the airflow rate can improve the reactor efficiency. By contrast, degradation efficiency is declined by increasing flow rate when the PCO process is not limited by mass transfer.

Bouazza et al. [154] reported that removal of benzene over P25 decreases sharply up to 72% when flow rate rises from 7.5 to 60 ml/min, which represents the negative effect of lower residence time dominates the positive effect of higher mass transfer. Yang et al. [155] observed that the reaction rate enhanced when the airflow rate increased from 0.3 to 0.6 m/s and decreased when the flow velocity changed from 0.6 to 0.94 m/s. They concluded that mass transfer and surface reaction are two vital factors controlling the overall reaction rate of PCO. When mass transfer controls the overall reaction rate, the conversion enhances with the increase of flow velocity. Conversely, when surface reaction controls the overall reaction rate, the removal efficiency decreases with the increase of velocity because of a shorter resident time [155].

2.4.2. Catalyst surface area and porosity

The surface area and porosity can have a major impact on photocatalyst activity and accordingly on degradation efficiency. As for the surface area, pollutant adsorption capacity and the ability of hydroxyl radical generation enhance at the higher surface area. In this case, more VOC molecules can transfer to the catalyst surface and react, which promotes decomposition of challenge compound to final products [129]. The impact of surface area (a_s) in mass balance equation of PCO appears in interphase mass transfer term ($k_g a_s(C\text{-}C_s)$) and adsorption constant (K) in reaction rate (defined by L-H model). Increment in surface area enhances both mass transfer and reaction rates, which, consequently, increases removal efficiency of the reactor. Maira et al. [156] showed that the activity of the TiO_2 is strongly affected by crystal size. In view of this, the smaller TiO_2 crystals provide a higher surface area for the adsorption of pollutants, which results in higher conversion. Alonso-Tellez et al. [155] compared the performance of UV100 and P25 in PCO reactor. They found that UV100, owing to its larger surface area, has a higher ability to store large amount of pollutants and means that UV100 can provide higher removal efficiency for the same VOC content.

Porosity plays an essential role in photocatalytic activity. High porosity implicates higher surface contact for reactants and enhances the degradation rate. Moreover, the porous structure facilitates the harvesting of light because of the enlarged surface area [157, 158]. As for the modeling perspective, porosity can affect both mass transfer and reaction rate terms. With raising porosity (ε), effective diffusion coefficient ($D_e = D.\varepsilon/\tau$) in diffusion terms increases, resulting in higher mass transfer of VOCs. Moreover, in terms of reaction rate, rate constant (k) (due to better light penetration in catalyst bed) is enhanced by increasing porosity. Arconada et al. [157] evaluated the effect of porosity in photocatalytic activity. They showed that porous TiO_2 film could

improve TCE conversion by around 20% higher than that of dens film. Alonso-Tellez et al. [155] also reported that UV100, owing to the smaller size of the porous network, has better photocatalytic activity than P25. They pointed out that this large fraction of microporosity can lead to an artificial increase in the residence time of the pollutant within the UV100 particles. In consequence, reactants and intermediates can escape from P25 much easier than from UV100, resulting in a lower degradation yield.

2.4.3. Catalyst thickness

Another key factor that impacts the final product conversion and photocatalyst efficiency is the thickness of photocatalyst film. Basically, varying catalyst thickness influences both the available surface of the catalyst and the percentage of absorbed light. Increasing catalyst thickness enhances external mass transfer on account of increment in diffusional length of reacting molecules from bulk to the catalyst surface. As the film thickness increases, at some point, light can be totally absorbed by photocatalyst layers and, therefore, the reaction rate can be reached at maximum. Besides, with a further increase in catalyst length, the reaction rate would not change, and the diffusional length of the charge carrier to the solid-gas interface remains constant, which restricts the reactivity of the catalysts near the surface of the support material [132, 159, 160]. In terms of modeling, the impact of catalyst thickness is on mass transfer rate and reaction rate. In terms of mass transfer, with increasing thickness, internal diffusion ($\nabla \cdot J_{i,p}$) gets more significant role in degradation of VOCs and, hence, may cause internal mass transfer limitation. Beer-Lambert equation (Eq.(2.18)) shows that increment in thickness increases rate constant ($k = k_0(I)^n$) due to improvement in light absorption (I) .

Chen et al. [132] proposed an optimal catalyst layer thickness (5 μm) at which the degradation rate is at maximum. They found that while the film layer is thin, the light absorption will not be strong enough and therefore, the activity of photocatalyst layer cannot be at its highest possible level. When the catalyst thickness increases, more electrons and holes will be created and then, reaction rate can reach to its maximum value. However, further increase in catalyst length results in recombination of charge carrier at relatively far from solid-gas interface, which cause to lower reaction rate. Vezzoli et.al [59] pointed out that using a very thin film layer of catalyst in the PCO reactor can reduce diffusion limitation. Meanwhile, the decrease of light absorption declines the reactor efficiency, which represents wasting resources and money. They noticed that the final conversion of phenol grows with the increase of average film thickness up to about 4-5 μm and

reaches to a plateau after that. Up to this thickness, diffusion of pollutants inside the film layer have minimal effect on reaction rate and growth in reaction rate nearly follows light absorption.

3. Methodology

3.1. Model development

3.1.1. Mass balance

A one-dimensional heterogeneous mathematical model of UV-PCO reactor was developed by considering the following physical phenomena: 1) advection and dispersion of molecule in bulk as well as mass transfer across the boundary layer in the gas phase; and 2) adsorption and PCO reaction in the solid phase (Fig. 3.1). The following assumptions are made in the model development:

i) Axially dispersed plug flow along the bed,

ii) Constant bed porosity,

iii) Negligible temperature gradient in the PCO filter,

iv) Negligible light reflection or scattering by photocatalyst,

v) Uniform coating of TiO_2 particles on the support material,

vi) PCO reaction on the TiO_2 surface, and

vii) Negligible internal diffusion,

(a)

PCO filter   UV lamp

27

(b)

(c)
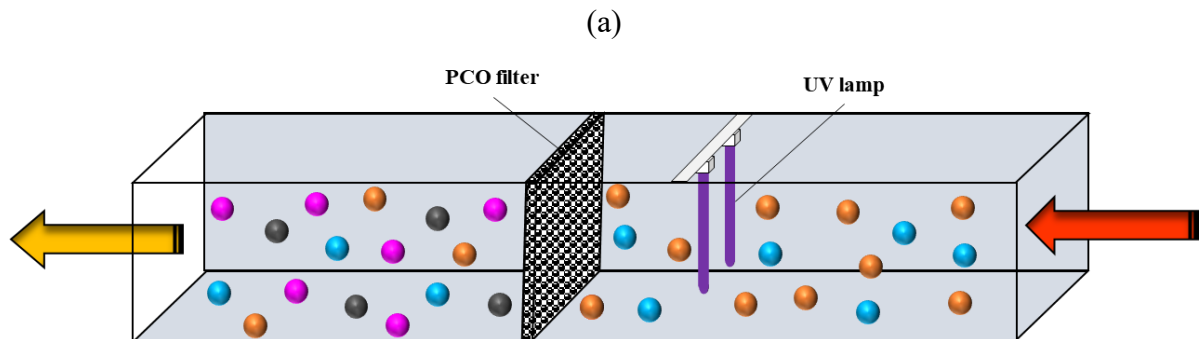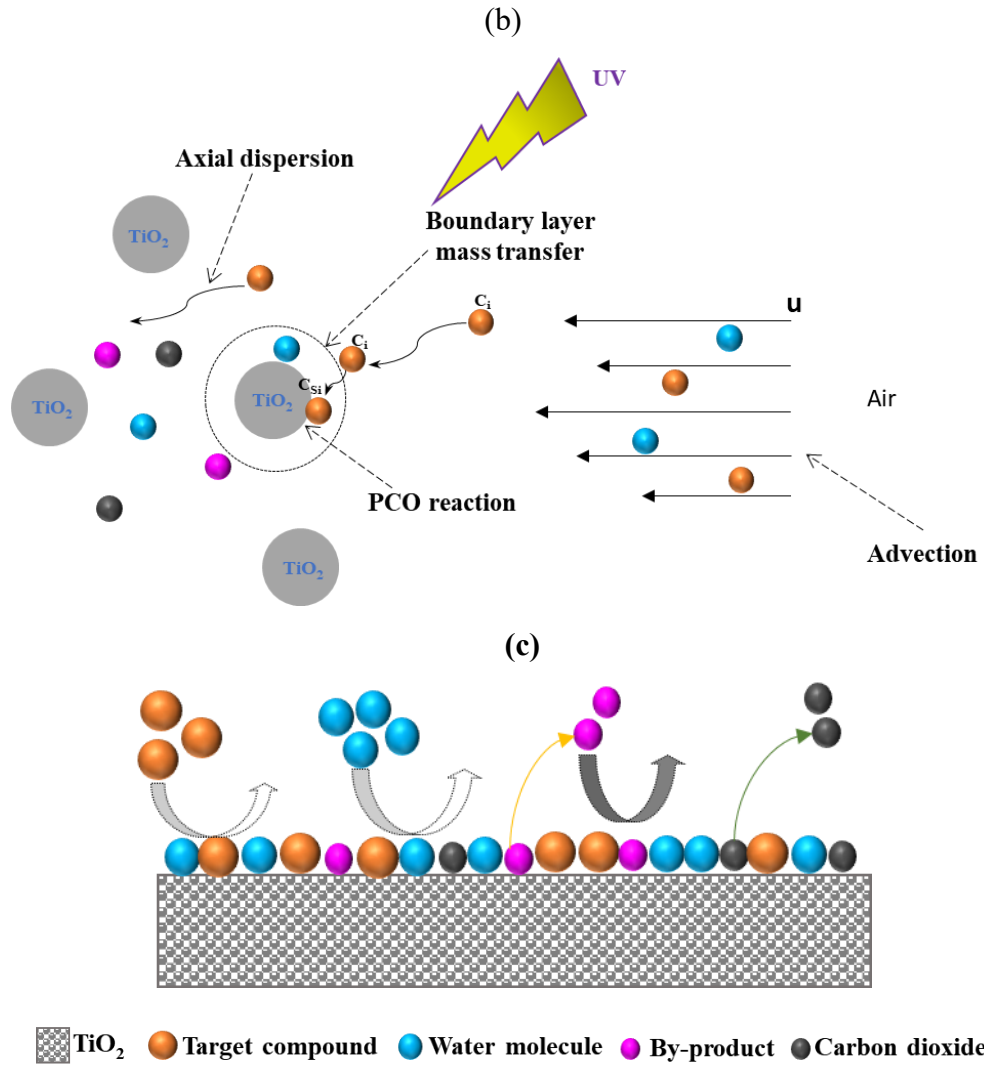
Fig. 3.1: Schematic diagram of (a) UV-PCO system (b) mass transfer in the PCO filter (c) adsorption-desorption and reaction of molecules on TiO_2.

Accordingly, VOCs mass balance in gas-solid phase can be expressed as:

- Gas phase:

$$\frac{\partial C_i}{\partial t} = D_{ax}\frac{\partial^2 C_i}{\partial x^2} - u_b\frac{\partial C_i}{\partial x} - \frac{(1-\varepsilon)}{\varepsilon}k_m a_s(C_i - C_{si}) \qquad (3.1)$$

- Solid phase:

$$\frac{dC_{si}}{dt} = k_m a_s(C_i - C_{si}) - r_i \qquad (3.2)$$

Initial conditions:

$$C_i = C_{si} = 0 \quad \text{at t=0} \qquad (3.3)$$

where ε, u_b, D_{ax}, k_m, a_s and r are defined as the bed porosity, interstitial air velocity, axial dispersion coefficient, inter-phase mass transfer coefficient, geometric surface area per unit volume of PCO filter, the reaction rate for challenge compound and by-products, respectively. C, and C_s stand for concentration in the gas and solid phases.

The Danckwerts' boundary conditions for the closed-closed system are applied [161]. In this system (Fig.3.2-a), plug flow (no dispersion) to the immediate left of the entrance line (x=0⁻) (closed) and to the immediate right of the exit (x = L_f^+) (closed) is counted. However, dispersion and reaction occur between x=0⁺ and x = L_f^-. At the reactor exit, concentration is continuous (no concentration gradient) (Fig.3.2-b). Hence, a Robin-type boundary condition at the inflow boundary and a Neumann-type one at the outflow were defined [162]. Boundary conditions are expressed as follows:
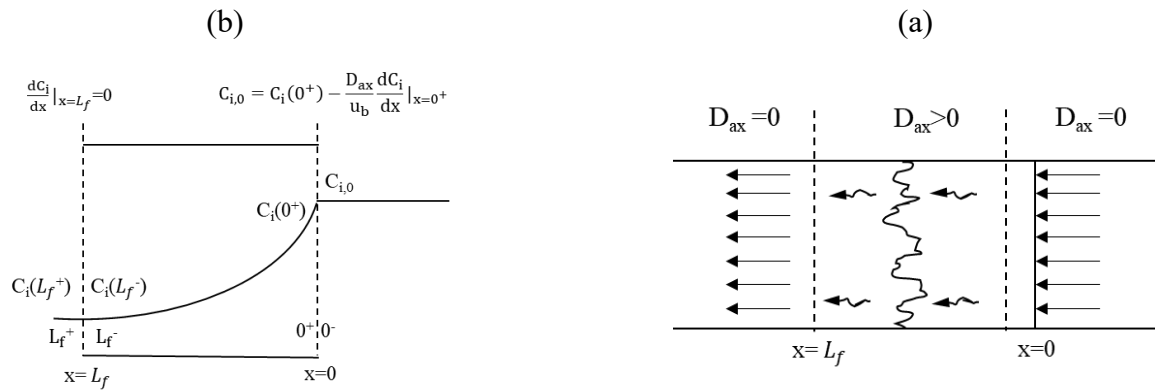
Fig.3.2: a) Closed-closed vessel b) Schematic of Danckwerts boundary conditions at entrance and exit

$$u_b C_{i,0} = u_b C_i - D_{ax} \frac{dC_i}{dx} \qquad \text{at x=0} \qquad (3.4)$$

$$\frac{dC_i}{dx} = 0 \qquad \text{at x=}L_f \qquad (3.5)$$

3.1.2. Radiation model

The radiation model is based on the linear source spherical emission model (LSSE) [6]. The model regards the UV lamp as a line source, with each point on this line emitting radiation in every direction isotropically. The incident radiation intensity at any position (y, z) on the PCO filter surface was modeled with the following assumptions [6, 163]: 1) isothermal conditions; 2) negligible absorption, scattering, or radiation emission by the gaseous media between UV lamps and filter; and 3) negligible lamp radius compared to the lamp-to-filter distance.
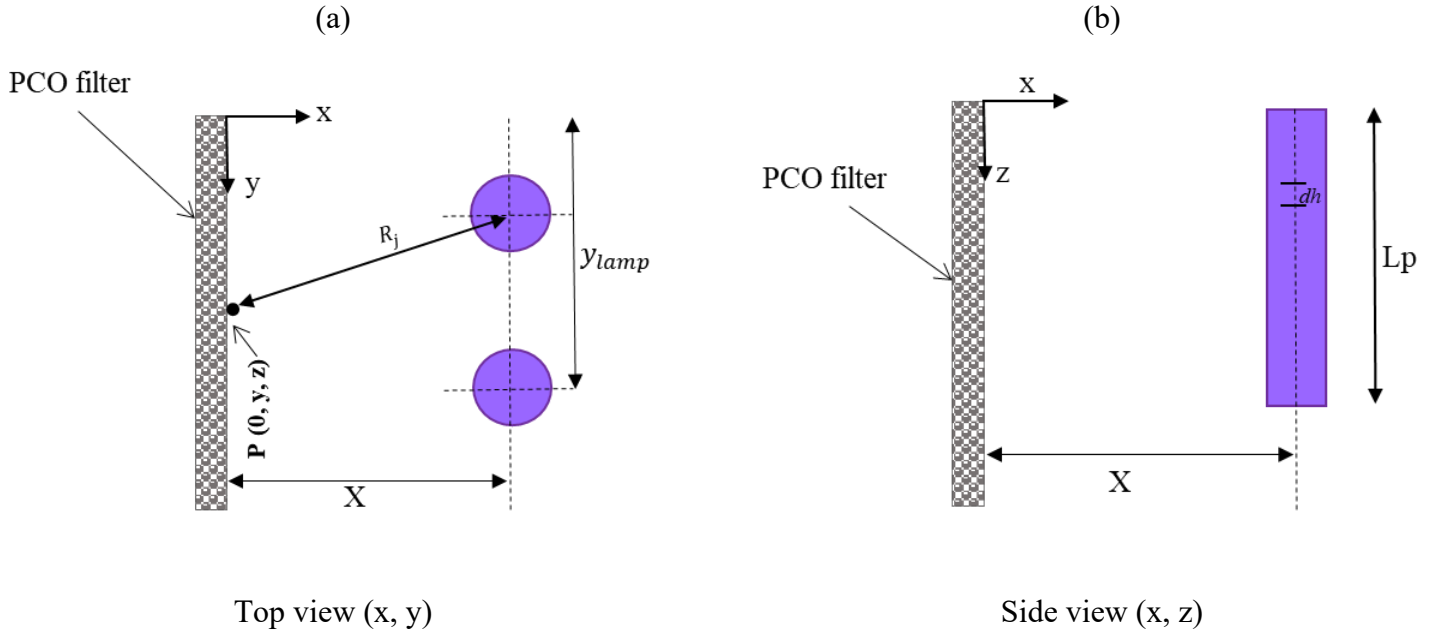
Fig. 3.3. Schematic of PCO reactor representing LSSE model coordinates

Considering I_L as the light intensity emitted per unit length of the lamp, radiation intensity at point $\boldsymbol{P}$ (see Fig. 3.3) for a specular source is obtained by [163]:

$$dI = \frac{I_L\,dh}{4\pi(R_j^{\,2} + (z-h)^2)} \tag{3.6}$$

$$I(y,z)|_{x=0} = \int_0^{L_p} \frac{I_L\,dh}{4\pi(R_j^{\,2}+(z-h)^2)} = \frac{I_L}{4\pi}\int_0^{L_p}\frac{dh}{(R_j^{\,2}+(z-h)^2)} = \frac{I_L}{4\pi R_j}\left(\tan^{-1}\left(\frac{z}{R_j}\right) - \tan^{-1}(\frac{z-L_p}{R_j})\right) \tag{3.7}$$

where z is the vertical coordinate, y is the lateral reactor coordinate, L_p is the lamp length, and R is the distance between lamp axis and the point of interest on filter surface (Fig. 3.3). When there are multiple lamps (N lamps) laterally parallel to the PCO filter, the distance between the axis of lamp j and a point (P) on the photocatalytic surface can be estimated by:

$$R_j = [X^2 + \left(y_{lamp,j} - y\right)^2]^{0.5} \tag{3.8}$$

where $y_{lamp,j}$ is the distance of the lamp axis from the origin (Fig. 3.3). The radiation intensity on the surface of the photocatalyst equals the sum of contributions from each lamp. By measuring radiation intensity at the lamp wall (I_w), the incident light intensity on the catalyst surface is defined as follows [163]:

$$I(y,z)|_{x=0} = \sum_{N\ lamps} \left(\frac{r_l I_{w,j}}{4R_j} \left(\tan^{-1}\left(\frac{Z}{[X^2 + (y_{lamp,j} - y)^2]^{0.5}}\right) - \tan^{-1}\frac{Z - L_p}{[X^2 + (y_{lamp,j} - y)^2]^{0.5}}\right) \right)_j \tag{3.9}$$

where r_l is the radius of the lamp. It should be noted that Eq.(3.9) is valid only for monochromatic irradiation.

The UV light irradiance inside Titania film can be estimated according to the Beer-Lambert law [164] (Eq. (3.10)).

$$I = I_{ave}\exp(-\mu\varphi) \tag{3.10}$$

$$\varphi = L_f(1 - \varepsilon)\frac{\delta_f}{d} \tag{3.11}$$

where I is the UV light incident intensity, μ is the attenuation coefficient, and φ is the overall effective TiO$_2$ layer thickness. I_{ave} is considered the average UV light intensity at the catalyst surface, calculated by:

$$I_{ave} = \frac{\iint I(y,z)dA}{A} \tag{3.12}$$

3.1.3. PCO rate expressions

Several models have been proposed to study the kinetics of photocatalytic oxidation of a contaminant, and they are mainly based on Langmuir Hinshelwood (L-H) expressions [15, 165-167]. The L-H model quantitatively describes the PCO gas-solid reaction rate based on the hypothesis that monolayer adsorption occurs on a uniform catalyst site [165]. At the steady-state condition, the L-H degradation rate of compound A in PCO (r_A) can be expressed by (model **M-1**) [70, 71, 168]:

$$r_A = k_{LH}\frac{K_A C_A}{1 + K_A C_A} \tag{3.13}$$

where k_{LH} is the reaction rate coefficient, K_A is the adsorption equilibrium constant, and C_A is the compound A adsorbate concentration. When adsorbate concentration is low, $K_A C_A$ becomes <<1 and the reaction rate can be simplified by a linear expression (model **M-2**) [27, 35]:

$$r_A = k'_H. C_A \tag{3.14}$$

where k'_H is the apparent reaction rate coefficient ($k'_H = k_{LH} K_A$). In addition, Eq. (3.13) can be modified to consider the inhibiting effect of water molecules and by-products (competitive

adsorption with water molecules and byproducts) in the reaction rate. In such a scenario, the water vapor and by-products compete with the pollutant for adsorption sites on the photocatalyst, hence decreasing the pollutant removal rate [52, 123]. In this case, the L-H rate expression of challenge compound in PCO is determined by (model *M-3*):

$$r_A = k_{LH} \frac{K_A C_A}{1 + K_A C_A + K_w C_w + \sum_i K_{byp,i} C_{byp,i}} \qquad (3.15)$$

where K_w and K_{byp} represent the water adsorption equilibrium constant and adsorption coefficient of by-product on a single site, respectively. Models *M-1*, *M-2*, and *M-3* are generally called unimolecular L-H models as they describe the reaction rate only based on challenge compound and catalyst surface interaction [64].

However, bimolecular L-H models consider interactions between both target compounds and water vapor molecules (dual adsorption of both species on the photocatalyst surface sites) [165]. In these models, water molecules have dual effects on the PCO rate; they produce hydroxyl radicals to attack VOCs and adsorbs competitively with pollutants. If dual adsorption happens on the same type of site, the model is defined as competitive adsorption of target gas (compound *A*) with water vapor molecules and by-products on the same type of sites [90, 165]. In this case, the PCO reaction rate is calculated considering the bimolecular competitive single site L-H model (model *M-4*), [90]:

$$r_A = k_{LH} \frac{K_A K_w C_A C_w}{\left(1 + K_A C_A + K_w C_w + \sum_i K_{byp,i} C_{byp,i}\right)^2} \qquad (3.16)$$

where all variables are the same as in Eq. (3.16).

On the other hand, there are also two other bimolecular L-H models for cases when dual adsorption occurs on two different types of surface sites, with or without the competition of challenge compounds with water molecules and by-products. They are called non-competitive two types of sites bimolecular L-H (model *M-5*) and competitive two types of sites bimolecular L-H (model *M-6*) models, respectively. In this regard, models *M-5* (Eq. (3.17)) and *M-6* (Eq. (3.18)) are defined as follows [87, 165, 169, 170]:

$$r_A = k_{LH} \left(\frac{K_A C_A}{1 + K_A C_A + \sum_i K_{byp,i} C_{byp,i}} \right) \left(\frac{K_w C_w}{1 + K_w C_w + \sum_i K_{byp,i} C_{byp,i}} \right) \qquad (3.17)$$

$$r_A = k_{LH}\left(\frac{K_{A,1}C_A}{1 + K_{A,1}C_A + K_{w,1}C_w + \sum_i K_{byp,1i}C_{byp,i}}\right)\left(\frac{K_{w,2}C_w}{1 + K_{A,2}C_A + K_{w,2}C_w + \sum_i K_{byp,2i}C_{byp,i}}\right) \qquad (3.18)$$

where $K_{A,1}$, $K_{A,2}$, $K_{w,1}$, $K_{w,2}$, $K_{byp,1}$ and $K_{byp,2}$ are the target compounds, water vapor molecules and by-products adsorption equilibrium constants on the two types of sites (1 and 2), respectively.

The PCO reaction rate coefficient (k_{LH}) in models *M-1* to *M-6* is a function of light intensity, electron-hole generation and recombination. Hence, this coefficient can be modified as [83]:

$$k_{LH} = \left(\frac{k_\emptyset I}{k_{recom}}\right)^{0.5} k_{h^+} * k_A \qquad (3.19)$$

where $k_\emptyset$ and k_{recom} are the photon generation and recombination rate coefficients, respectively. This expression is on the basis of the constant concentration of holes h^+ at steady-state and the same concentration as electrons (e^-) [171]. Moreover, it was assumed that the recombination rate coefficient of the separated electron and hole is much faster than the holes generation coefficient (k_{h^+}) [171, 172]. Eq.(3.19) can be simplified by combining $k_\emptyset$, k_{recom}, and k_{h^+} to form Eq.(3.20), which make the estimated parameters of reaction rate model more reliable (less unknown parameters leading to narrower confidence interval in the curve fitting).

$$k_{LH} = k.I^{0.5} \qquad (3.20)$$

To estimate kinetic parameters of models *M-3* to *M-6* through nonlinear curve fitting, overparameterization may occur due to a greater number of parameters. In this regard, adsorption coefficients of the challenging compound and water vapor were obtained independently in the dark condition (in the absence of UV light). In the PCO reactor, the primary competition for adsorption on photocatalyst happens between target compound and water owing to the higher amount of these compounds in the air compared with by-products. Langmuir adsorption isotherm by considering competitive adsorption of challenging compound and water vapor on a single adsorption site can be defined as [173]:

$$q_e = q_m \frac{K_A C_A}{1 + K_A C_A + K_w C_w} \qquad (3.21)$$

where q_e and q_m are the adsorption capacity of adsorbents (mg_{voc}/g_{cat}) and the maximal adsorption capacity (mg_{voc}/g_{cat}), respectively. The adsorption capacity can be expressed as the total mass of the adsorbed VOC till adsorption equilibrium time per mass of PCO filter [68]:

$$q_e = \frac{\int_0^{t_{eq}} Q\big(C_{up}{}^{(t)} - C_{down}{}^{(t)}\big)dt}{m_{cat}} \qquad (3.22)$$

where t_{eq} is the elapsed time of adsorption test (min), Q is the airflow rate (L/min), $C_{up}{}^{(t)}$ and $C_{down}{}^{(t)}$ are the upstream and downstream target compound concentration, and m_{cat} is the mass of removal media (g). It should be highlighted that the obtained adsorption coefficients from Eq. (3.21) are applied in Models *M-3* and *M-4*, as they consider single site competition adsorption of compounds. To calculate the adsorption parameters of models *M-5* and *M-6*, independently, through two sites adsorption isotherm under dark condition, overparameterization problem is occurred again due to a large number of unknown parameters[174] with the limited amount of available data. Therefore, kinetic parameters of models *M-5* and *M-6* were estimated directly from PCO reaction tests and then compared with the results of other models (*M-1* to *M-4*).

The water concentration in the air (C_w) was calculated from the pressure of saturated water vapor p_{ws} using the Antonine equation [175]:

$$\ln p_{ws} = 23.196 - \frac{3816.44}{T - 46.13} \qquad (3.23)$$

where T (°K) is the air temperature. Then, C_w can be defined as [175]:

$$C_w = \frac{0.62198 * RH * \rho_{air}}{p_{atm}/p_{ws} - RH} \qquad (3.24)$$

where p_{atm} and RH are the standard atmospheric pressure and relative humidity, respectively.

3.2. Model implementation

The developed model was solved numerically by the finite difference in MATLAB R2018a. For the estimation of the kinetic parameters, two built-in MATLAB® subroutines were used: *bvp5c* for numerical integration of differential equations and *lsqcurvefit* for minimizing the objective function, which was the difference between the numerical solution and experimental result. The mass transfer model combined with the reaction rate equation was solved using *bvp5c*, a finite difference code that implements an implicit Runge-Kutta formula with fifth-order accuracy (four-point Lobatto IIIA formula). The *bvp5c* function is an effective BVP (Boundary Value Problems) solver that controls both the scaled residual and true error [176]. Moreover, the non-linear least-square based on the Levenberg–Marquardt algorithm [177] was employed for curve fitting, which minimized the error between experimental data and predicted one. This algorithm works based on the combination of gradient descent and Gauss-Newton methods. To solve the

34

problem numerically, the catalyst bed is decomposed into n=500 elemental cells connected in series (see Fig. 3.4). Gas-phase concentration (C_i) and solid phase concentration (C_{si}) are assumed uniform within the same cell and differ from one cell to another. Simulations were performed with an absolute and relative tolerance of 1×10^{-5}.

Moreover, the governing equations of transient state were solved by the ODE15S function via the method of line (MOL). This function is an implicit method that solves the equation at each time by backward differentiation formulas with 5th order Taylor expansion (Gear's method). Gear's auto-adaptive algorithm selects step size automatically and changes orders from one to five (e.g., $k = 1 - 5$). Based on MOL, the Partial Differential Equation (PDE) and Ordinary Differential Equation (ODE) resulting from the mass balance in gas and solid phases were converted into a system of ODEs, in which the second-order central scheme was utilized in the spatial domain discretization. Then, the ODE system was solved by using ODE15S function.

Fig.3.5 illustrates the numerical simulation flowchart. Input parameters are either computed from the existing empirical equations or measured using experimental results. The adsorption isotherm and kinetic reaction expression are obtained through curve fitting of experimental data, and the mass transfer parameters are computed from empirical correlations. Other parameters are measured directly before the experiment. Then, they are applied in the overall mass balance equations for gas and solid phases. Ultimately, ODE15s integrates the differential equations system to calculate the downstream concentration during the UV-PCO reaction.
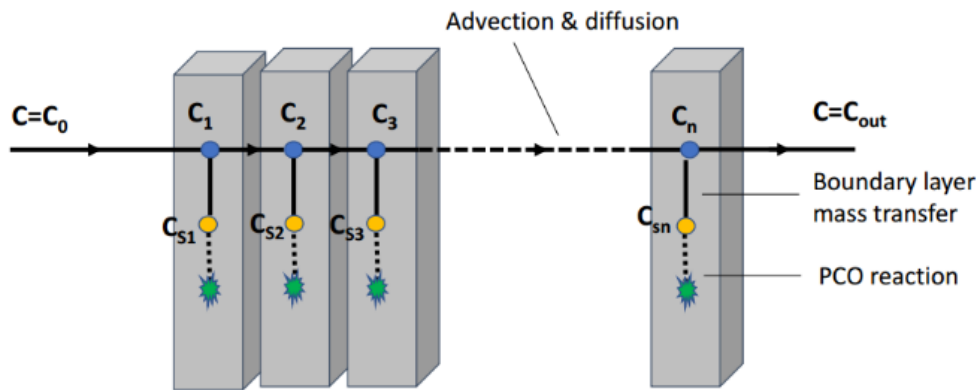
Fig. 3.4. Spatial discretization of the catalyst bed.
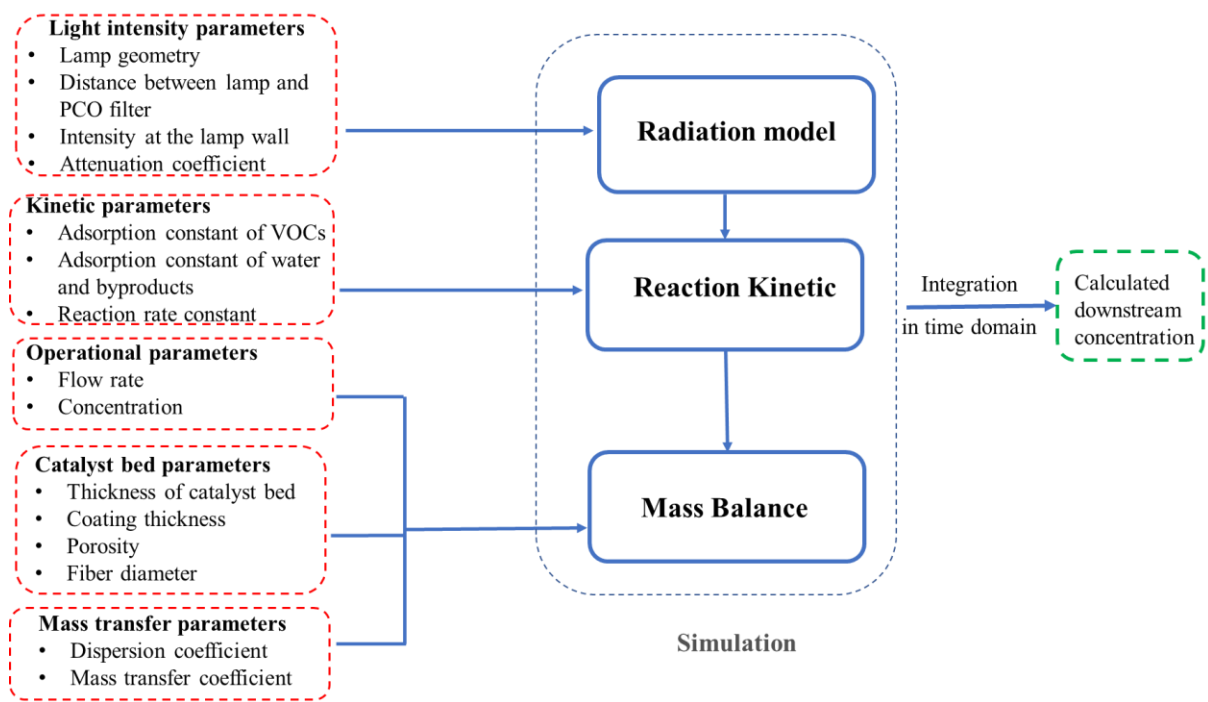
Fig.3.5: Structure of the simulation program.

3.3. Experimental investigation

3.3.1. Material and characterization

A commercially available PCO filter (Saint-Gobain Quartz made up of TiO_2 coated on amorphous silica fiber felts (SFF)) was used in this study. The Scanning Electron Microscopy (SEM) system (Hitachi Tungsten Filament S-3400N Variable Pressure SEM) was used to analyze the media surface. In the SEM test, a small piece of TiO_2/SFF was coated with gold nanoparticles (for better resolution), placed on the sample holder, and scanned. SEM images of TiO_2 coated on silica fiber felts at different magnifications were displayed in Fig. 3.6. BET surface area and pore parameters of the PCO filter were investigated by N_2 adsorption measurement (Quantachrome, Autosorb-1). Some of the main properties of the photocatalysts are listed in Table 3.1. Methyl ethyl ketone, acetone, and toluene (99.9%) (Fisher Scientific Inc., Canada) were chosen as a challenging compound. Acetonitrile (HPLC grade) was used for HPLC analysis.
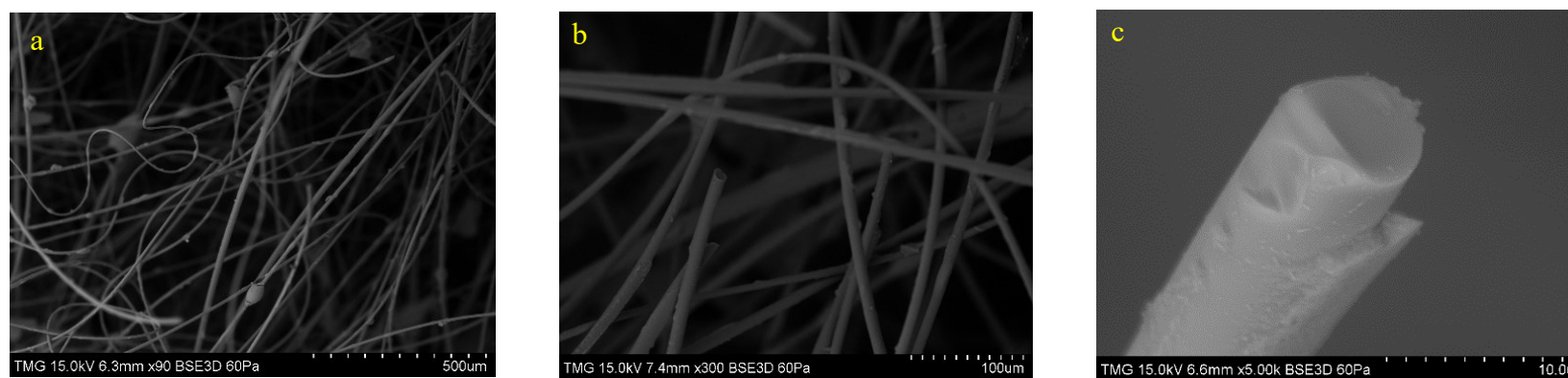
Fig. 3.6. SEM images of the TiO_2/SFF filter at different magnifications.

Table 3.1:Technical data for TiO_2/SFF filter obtained from BET and SEM analysis

Parameter	PCO filter
Fiber diameter (d)	10 μm
Specific surface area (BET)	150.8 m^2/g
Bed porosity (ε)	0.96
TiO_2 layer thickness of a fiber (δ_f)	1 μm
Filter thickness (L_f)	10-12 mm
Filter weight (m_{cat})	1.4 ± 0.05 g

3.3.2. Experimental set-up and procedure

The schematic of the experimental set-up employed to study the PCO performance is displayed in Fig. 3.7. The photocatalytic reactor is made up of an aluminum duct with 10 cm × 10 cm inner cross-section area and 1.3 m in length to deliver a uniform airflow on the PCO media. Compressed air with 0% relative humidity and temperature of about 20 ℃ was used as the carrier gas. The airflow rate was adjusted by a mass flow controller (OMEGA, FMA5542A) and measured accurately using a calibrated flow meter (DryCal DC-Lite). The inlet air was humidified by passing a portion of it through a bubbling system filled with distilled water. A sensor (DATAQ Instruments, Model ELUSB-2) was placed in the reactor to monitor the temperature and humidity. The light intensity was provided by the UV lamps (Philips, TUV PL-S 5 W/4P), and it was measured using a Germicidal Radiometer IL77. The light intensity on each lamp's wall was 650 W/m^2 and its intensity varied from 7 to 104 W/m^2 on the PCO filter. Challenge compounds were automatically injected into the airflow by a syringe pump (KD Scientific, Model KDS-210).
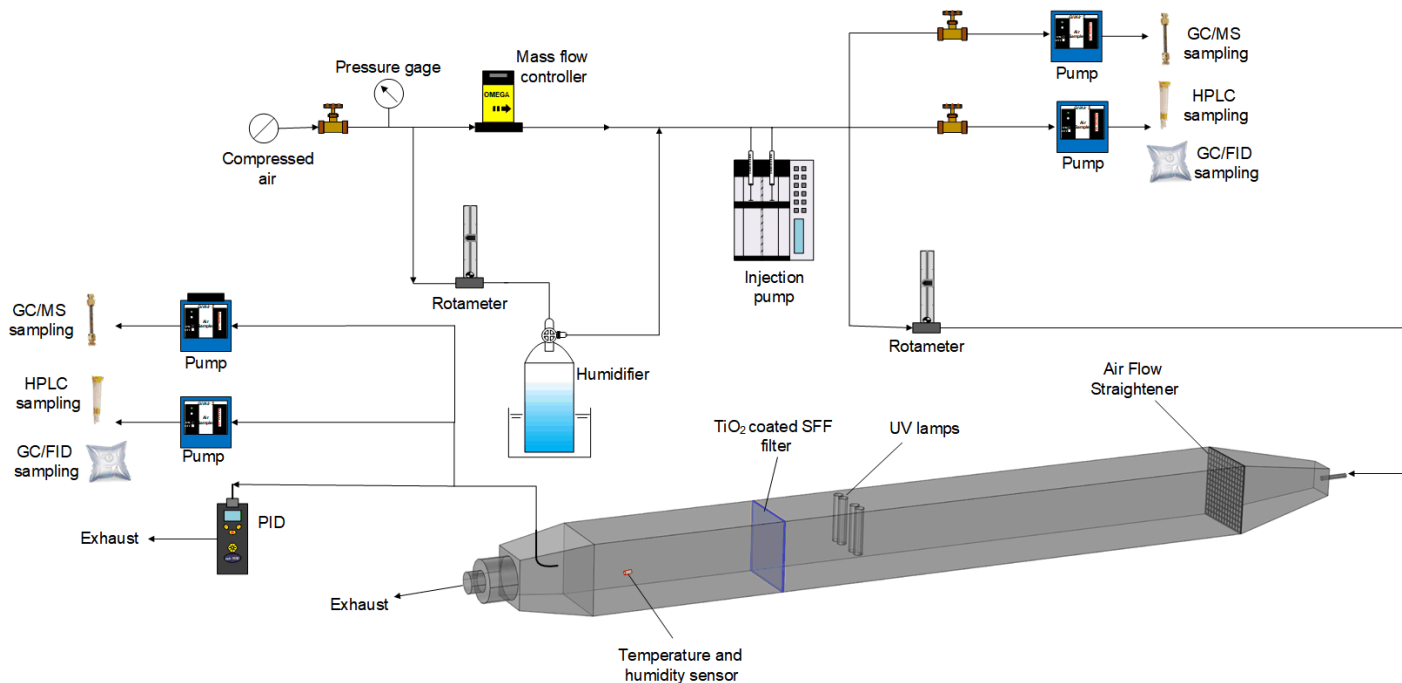
Fig. 3.7. Schematic diagram of the experimental set-up for PCO experiments.

3.3.3. Adsorption experiment

The adsorption test was performed at airflow rate of 30 L/min under dark condition with a layer of TiO_2/SFF filter. The challenge compound was injected at four different concentrations (250, 500, 800, 1000 ppb) and at relative humidity ranging from 15% to 50%. The challenge compound was introduced into the airflow and concentration at the outlet was recorded with the time using a PID detector (ppb3000 RAE with measurement range of 1 ppb to 10,000 ppm). The adsorbed amount of mass by the PCO media was computed according to the time scale from the beginning of injection till the saturation time.

3.3.4. PCO reaction test

3.3.4.1. Steady-state PCO experiment

The PCO reaction for the kinetic study was carried out at the steady-state condition using a layer of PCO filter. The test was done at two steps—preliminary dark adsorption step (lamp turned off) and then photocatalytic reaction step by turning on the lamp. After injection of challenge compound (concentration range of 50 to 1000 ppb) into the air stream, the downstream concentration of the reactor was monitored by PID until the PCO filter was saturated

(concentration was the same as upstream). Then, the UV lamp was turned on to start the PCO reaction step and it was continued till reaching the steady-state condition.

3.3.4.2. Time-dependent PCO experiment

A time-dependent experiment was carried out to validate the developed model in transient condition. The experiment was conducted with a layer of TiO_2/SFF filter and two UV lamps on each side of the filter. Before starting the PCO reaction, the UV lamps were turned on, then the challenge compound at specific concentration was automatically injected into the inlet air stream at flow rate of 20 L/min and relative humidity of 50±1%. The downstream concentration was monitored during the test till it reaches the steady-state condition.

3.3.5. Air sampling and analysis method

3.3.5.1. HPLC analysis.

Aldehydes and ketones were collected on the high-purity silica adsorbent coated with 2, 4-dinitrophenylhydrazine (2, 4-DNPH) cartridge (SUPLECO LpDNPH S10L, Sigma Aldrich) and analyzed by HPLC method. The sampling pump flow rate was 1 L/min, and the sampling duration was 20 min for the steady-state test. In the case of time-dependent experiment, the sampling flow rate was 2 L/min for the duration of 3 min. The absorbed compound was extracted with acetonitrile based on US EPA TO-11a [178] and analyzed by PerkinElmer Flexar HPLC with LC-18 column (SUPELCOSIL^{TM} LC-18, 25 cm × 4.6mm, 5 µm) and a UV–Vis detector. The mobile phase in HPLC was 72% acetonitrile and 28% of deionized water with a total flow rate of 0.017 mL/s. The minimum detection limit of HPLC based on calibration curve was around 15 ng/DNPH cartridge.

3.3.5.2. TD-GC/MS analysis

VOCs were collected in AirToxic tubes (SUPELCO). The AirToxic adsorbent tube is made up of stainless steel filled with Carbotrap B followed by Carbosieve adsorbent for capturing C3-C12 VOCs. GC tubes were conditioned for 30 min at 320 with helium (as carrier gas) before sampling. Samples were collected at flow rate of around 15 mL/min and a sampling duration of 10 min. The adsorbed VOCs in tubes were released into GC/MS ((Agilent 88 90 GC coupled with Agilent 5977B GC/MSD system) using coupled Gerstel thermal desorption unit (Gerstel TD3.5$^+$) and Gerstel Cooled Injection System (CIS4). The primary desorption (Gerstel TD3.5$^+$) was conducted in splitless mode with initial temperature of 30 °C (no hold) and raised to 230 at a rate of 240 °C/min (hold 10 min) while CIS was held at -30 °C. The secondary desorption (Gerstel CIS4) was operated in split mode (ratio: 15:1). The temperature in CIS was rapidly increased to 250 °C at a

rate of 10 ºC/sec (hold 10 min). Analytes were separated in the GC at a flow rate of 1 ml/min using an Agilent DB624 column (60 m, 0.250mm I.D., and 1.4 μm film thickness) with the following GC oven temperature program: Initial temperature: 40 ºC, hold time: 5 min, ramp rate of 10ºC/min, final temperature: 250 ºC, hold time: 10 min. MS was operated in electron impact (EI) ionization mode with a scan a range of m/z 30 to m/z 300. Ionization source and quadruple temperatures were set at 230 ºC and 150 ºC, respectively. Helium was used as carrier gas for the TD-GC/MS analysis. Peak areas based on total ion current (TIC) were used for quantification. The detection limit for measuring the sample was between 1-5 ng/tube depending on the challenge compounds and the lowest calibration levels.

3.3.5.3. GC-FID analysis

Additionally, the grab sampling of upstream and downstream, simultaneously, were also taken using 1liter Supel-Inert foil gas sampling bags. The air was then injected manually into the gas chromatograph (GC-7890B, Agilent Technologies) equipped with a flame ionization detector (FID)- methanizer in order to analyze carbon dioxide (CO_2). The GC/FID system contained a J&W GC packed column in UltiMetal tubing (length 6 ft (1.83 M), 1/8 in. OD, 2 mm ID, Hayesep Q packing, mesh size 80/100). Helium was used as carrier gas (31.8 psi). The oven temperature was kept at 60 ℃ with 8 min holding time. The FID temperature was 250 ℃ and the flow rate of Air, H_2, and N_2 (makeup flow) were 500, 48, 2 mL/min, respectively. The range of quantification by FID-methanizer was around 0.4 ppm-0.2%.

4. Modeling of PCO reactor in the presence of mass transfer limitation and axial dispersion

Mass transfer plays a critical role in the efficiency of photocatalytic oxidation (PCO) technology for air purification applications. Photocatalytic reactors are often different from ideal reactors like batch, perfect mixed, and plug flow reactors. Although substantial research work has been published on the modeling of the PCO reactor for air purification, most of the existing models were verified based on small scales under ideal conditions [35, 81]. In the small-scale reactors, the plug flow model and laminar velocity profile (with negligible dispersion) could describe flow behavior and mass transfer in the reactor. However, an appropriate description of the hydrodynamics is necessary to consider fluid mixing, mass transfer from the gas phase to solid phase and reaction at the catalyst surface for proper evaluation of reaction rate. This is increasingly more important when simulating large-scale reactors, in which dispersion, bypass, recirculation, and dead zone may happen and the effect of fluid elements containing different velocities cannot be ignored [6, 26]. Therefore, the performance of existing PCO models validated for small scale could be questionable and may not be scaled up to simulate the full-scale reactors correctly [35]. Moreover, most of the correlations for the mass transfer coefficient were obtained for non-photocatalyst media with larger characteristic length. Nevertheless, in fiberglass-based PCO filter, the characteristic length is very small (due to the micro-size of fiber), and consequently, the Reynolds number is quite low. This can cause a considerable deviation when a mass transfer correlation validated for non-fiber is used for fiber one. This work presents a modeling study on the photocatalytic oxidation of methyl ethyl ketone (MEK) by SFF modified with titanium dioxide as a photocatalyst when the kinetic reaction rate does not control the system (very fast reaction). First, a three-dimensional CFD modeling has been conducted to simulate the behavior of flow in the photochemical reactor. An accurate CFD model can provide greater insight into the evaluation of the velocity profile on the PCO filter. Since airflow in the continuous system deviates from ideal flow, a residence time distribution (RTD) analysis with tracer gas is then performed to find a quantitative characterization of the carrier fluid hydrodynamics and its divergence from ideal conditions. The experimental data were compared to the CFD simulation results. Moreover, an axial dispersion plug flow model was proposed to represent the residence time distribution of the challenge compounds in the reactor. Finally, this paper focuses on the modeling of the PCO reactor

under mass transfer-controlled regime. A mass transfer correlation (Sherwood formula) for the SFF filter in the UV-PCO reactor was proposed and compared with the results of other existing ones in the literature.

4.1. Methodology

4.1.1. Modeling with COMSOL Multiphysics

Modeling in COMSOL Multiphysics (from COMSOL Inc.) was performed in two stages; first, a steady-state turbulent flow study within the reactor, and second, a tracer study (RTD analysis) with a solution of mass balance including the flow distribution from the first stage but considering unsteady conditions (transient simulation).

The simulation of airflow in the PCO reactor was conducted using the CFD module of COMSOL, which is a commercial finite-element-method-based modeling tool. Even though the fluid flow through the main part of the reactor is laminar, the value of Reynolds number at the entrance region was high in the bench-scale system using compressed air, representing a turbulent regime. Due to this complexity, the use of an appropriate model allowing for consideration of turbulence effects is crucial. Various turbulent models are available in COMSOL, such as k-ε and k-ω. The k-ε model is the most widely-used engineering turbulence model [179]. This model is quite robust, economical, and reasonably accurate in a wide range of flow conditions. However, it is suitable rather for external flows, is accurate only in the fully turbulent regime and some difficulties can occur in complex 3-D cases. Moreover, the k-ε model tends to over predict turbulence generation in regions where the flow is highly accelerated or decelerated [180]. On the other hand, the k-ω model is often more suitable in cases where the k-ε model is not accurate, such as with internal flows in non-circular ducts. Moreover, the k-ω model possesses high accuracy and applicability when used in regions with the laminar flow for which the turbulent kinetic energy becomes zero [181]. Due to these reasons, the k-ω turbulence model was applied in this study to simulate the fluid flow in the PCO reactor. The reasons for using the turbulent model can be expressed as follows:

1) The straight inlet pipe with a diameter of 6 mm was considered in the model to simulate turbulent effects inside a flexible hose. The flow in the inlet pipe was turbulent due to a small diameter of the hose and high air velocity through it.

2) The wire mesh located near the inlet of the reactor for the airflow homogenization caused a local reduction of the cross-section of the reactor. Such reduction necessitates an increased air velocity, resulting in a locally increased Reynolds number corresponding to the turbulent flow. Moreover, the fluid flow pattern in the vicinity and behind the wire mesh was, in general, expected to be more complex and rather turbulent.

The fluid flow was solved in COMSOL Multiphysics 5.1 as an incompressible flow with the k-ω model, which was the two-equation turbulence model adopting the Wilcox revised model [182] with realizability constraints and the Reynolds-averaged Navier–Stokes (RANS) approach. The internal geometry of the reactor was created in COMSOL as a geometry node. Then, due to its symmetry, the geometry was divided longitudinally in half to save computational resources. The lateral face (longitudinal cut) was set to a symmetry boundary condition. The boundary conditions of the internal walls of the reactor were treated with a built-in procedure employing wall functions. A uniform velocity profile u_0 at the inlet and zero gauge pressure (meaning the atmospheric pressure) at the outlet were specified.

The mesh used in the simulations consisted of mainly tetrahedral and swept elements. The influence of the mesh density to simulation results was investigated by means of eight various mesh configurations. It was necessary to create a sufficiently dense mesh near the entrance of the reactor and the wire mesh where large velocity gradients and vortexes can exist. The finest considered mesh contained about 8.1 million of elements, while the coarsest one consisted of 0.31 million mesh elements. The mesh independence and the suitable mesh configuration was evaluated and identified, respectively, by refining the mesh until the velocity profile was affected less than 1% by a further refinement. The mesh with 2.36 million elements with an average element quality of 0.71 was determined as suitable in this respect (more details can be found in the supporting information file in [183]). The mesh generation process was made by considering the maximum element size, minimum element size, element growth rate, and curvature factor 5.7, 1.1, 1.13, and 0.5, respectively. At the entrance section (including the expansion in the geometry of the duct and the wire mesh), at the middle part of the reactor (where the lamps are placed), and at the outlet, the tetrahedral type of mesh elements was used. In other sections of the reactor, where the geometry of the duct has a simple geometry, the swept mesh (prism mesh elements) was adopted.

In the next stage, a tracer study (RTD analysis) was performed by means of the solution of mass balance in the time domain. As the tracer was present in a diluted form, a COMSOL built-in model for transport of diluted species from Chemical Reaction Engineering Module was applied. This

model allows for the solution of diffusion and convection and for modeling the component concentration in the fluid. In the advection-diffusion mode, the turbulent kinematic viscosity v_t was used as the turbulent diffusivity in the mass balance equation [184]. The tracer concentration over time at the inlet of the reactor (the input signal) was defined as follows [184, 185]:

$$C_{in} = C_{0,inj} \exp\left(-(t - t_d)^2\right) \qquad (4.1)$$

where t_d stands for the time delay during the injection (in the present paper, $t_d = 4\ s$ was applied).

The simulation was conducted with an insulation boundary condition (no-flux) and also advective flux specified as boundary conditions at the internal walls and the outlet, respectively. For the outlet concentration, it was assumed that mass transfer was only caused due to convection in the free-flowing fluid. A summary of the boundary conditions is presented in Table 4.1.

Table 4.1: Boundary conditions for the CFD model

	inlet	outlet	channel wall
Momentum balance	u_0	p_0	Wall function
Component mass balance	C_{in}	Convective flux	No flux

4.1.2. Residence time distribution experiment

To characterize the flow in the PCO reactor, the Residence Time Distribution (RTD) was determined by the injection of carbon dioxide (CO_2) and methyl ethyl ketone (MEK) tracers into the process fluid (air). The CO_2 tracer gas was used to evaluate the effect of SFF filter on RTD since it is an inert passive gas that is adsorbed little on the photocatalyst. The RTD experiment with MEK (as a target compound for the PCO reaction) for flow rates, ranging from 10 L/min to 40 L/min, was also performed to determine the axial dispersion coefficient. In order to verify the applicability of the result, RTD test was also conducted at flow rates of 50 L/min and 60 L/min.

An input signal of 1 mL of CO_2 was loaded instantly into the inflow stream, using a syringe at time t=0 s (flow rate of 10 L/min). CO_2 outlet concentrations were measured as a function of time using a CO_2 analyzer (Fluke 975 AirMeter with measurement range of 0 to 5000 ppm) (Fig. **4.1**). In the case of MEK tracer signal (input signal of 1 uL), its outlet concentrations were measured in time for various flow rates by a PID detector (ppb3000 RAE). The exit age distribution function, E(t) is defined as follows [186]:

$$E(t) = \frac{C(t)}{\int_0^\infty C(t)dt} = \frac{\text{Tracer concentration in the outlet at time t}}{\text{Total area under tracer concentration curve versus time}} = \frac{C(t_i)}{\sum_0^\infty C(t_i)\delta(t_i)} \qquad (4.2)$$
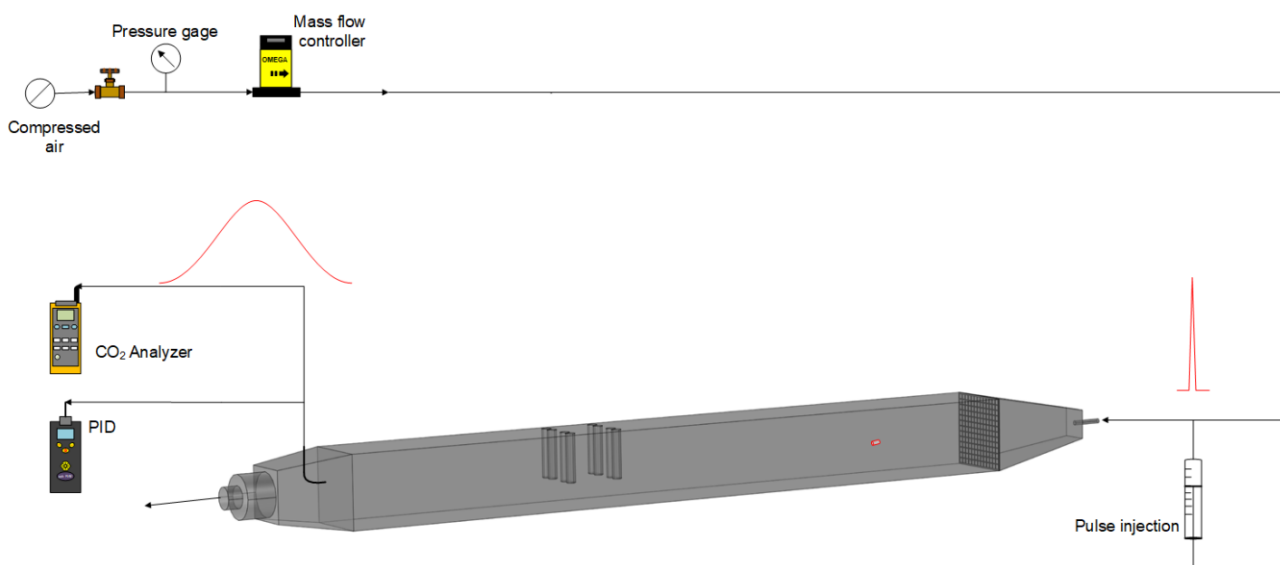
Fig. 4.1. Schematic of the experimental set-up for RTD experiments.

It should be noted that for CO_2 testing, the RTD experiment was performed in presence of PCO filter, due to the non-adsorptive characteristic of CO_2 on the media while MEK testing was carried out without the filter (as shown in Fig. **4.1**).

4.1.3. Mass-transfer limited PCO experiment

Experimental conditions for the mass transfer-controlled regime in the PCO reactor include the use of high light intensity and an extremely active photocatalyst. Moreover, the short residence time is necessary to limit the conversion. This can be accomplished by means of high flow rates. The PCO filter with thicknesses of 3 mm and 5 mm, and the MEK concentration of 150 ppb were utilized. A low challenge concentration was chosen to achieve a high conversion of the oxidation reaction at a lower level of light intensity. In order to investigate the mass transfer rate effect on the performance, it is more favorable to operate at high conversions since the efficiency reduction with flow rate increment can be observed clearer than at low conversions. To ensure that the photocatalyst was operating in the mass transfer limited regime, experiments at various light intensities (26, 52, 78, and 104 mW/cm^2) were carried out to determine the independency of the MEK removal efficiency on the light intensity. Further, the experiments in the second series were performed for a constant intensity (78 mW/cm^2) with the variation of the gas flow rate in the range of 10 to 40 L/min.

4.2. Result and discussion

4.2.1. CFD Simulations

In the steady-state analysis, the CFD model provided the velocity distribution throughout the flow domain. Numerical results demonstrate that the velocity distribution through the reactor, particularly, at the entrance, after and behind the wire mesh, and also in the reaction section is non-uniform (see Fig. **4.2**). The simulations were performed for various airflow rates, the range of 10-40 L/min, to investigate fluid dynamics in the photocatalytic reactor. Fig. **4.3** shows the distribution and contours of the velocity magnitude at the filter cross-section for various flow rates. It is clear from the figure that the lamp has a major impact on the flow distribution on the filter. However, the velocity at the lower part of the filter is more uniform as there is no effect of the lamp in that region. With increasing the flow rate, the relative velocity distribution (regardless of its magnitude) is almost the same, and the flow tends to pass below the lamp. In the contour plots (Fig. **4.3**), it can be pointed out that the magnitudes of velocity on the filter media corresponding to the lamp location are nearly identical for all the considered flow rates, and the main variation can be observed in the area below the lamp.

The CFD simulation results indicated that the expansion and reduction in the geometry as well as the presence of lamps at the middle part, cause a significant flow mixing in the channel, resulting in the non-uniform flow in the PCO reactor. Although the streamlines behind the wire mesh become more uniform, they deviate when the flow is close to the lamps and also behind the lamps, where the PCO filter is placed, leading to the non-uniform flow in the PCO filter.
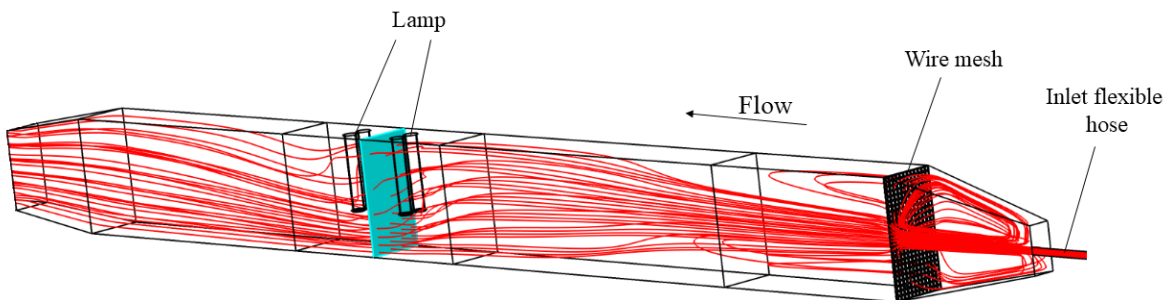
Fig. 4.2. CFD modeling of the fluid field in the reactor channel at Q=10 L/min (red lines show the streamlines).
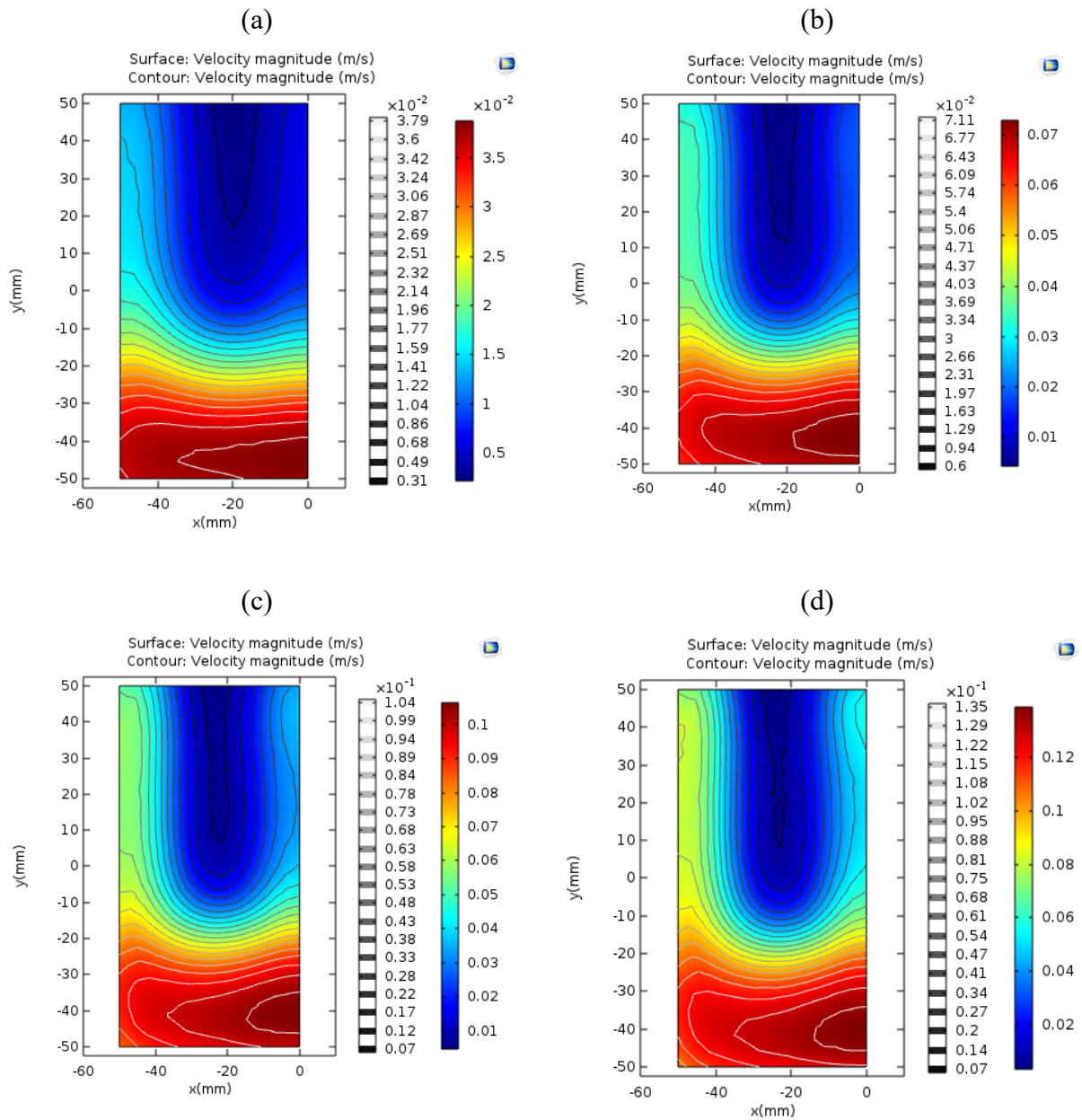
Fig. 4.3. Contours and distribution of the velocity magnitude at the PCO filter cross-section for various flow rates; (a) Q=10 L/min, (b) Q=20 L/min, (c) Q=30 L/min, (d) Q=40 L/min

In the next step, results from the simulation of the tracer gas were compared with experimental data. For this purpose, distribution functions E(t) were plotted versus time using the CO_2 outlet concentration by applying Eq. (4.2). The RTD experiment was also performed, and the concentration of CO_2 tracer was measured with the flow rate of 10 L/min lasting 224 seconds both in the presence and in the absence of the photocatalyst media (see Fig. **4.4**-a). It can be observed from this figure that the results of the residence time distribution in the PCO reactor for the experiment, including the filter, are very similar to those gained in the experiment without the

filter. This can be justified and attributed to the fact that the SFF filter is highly porous ($\varepsilon = 0.96$), and the non-adsorbing gas (CO_2) can easily pass through it. Further, the results obtained from the numerical simulation are in good agreement with the experimental one. This indicates that this simulation approach can be used to predict the flow behavior, even in complex geometries, and with high accuracy. The simulations were also performed for the assumption of ideal plug flow and laminar flow to investigate deviations with respect to the actual flow. Fig. **4.4**-b confirms that the dispersion in the PCO reactor is not negligible, as the RTD curve for the actual flow is fairly different from those of ideal flows. In the case of plug flow, molecules have the same residence time and move with the same velocity and concentration. However, in the laminar flow, molecules in the centerline of the reactor channel move faster than those near the wall (as the velocity profile of laminar flow is parabolic), which leads to a higher dispersion than in the case of plug flow. Fig. **4.4**-c displays that with increasing flow rate up to 40 L/min, dispersion increases. However, there is a considerable deviation from ideal plug flow and laminar flow. It should be mentioned that the results in Fig. **4.4** determined in a way that the area under the E(t) curve of RTD is unity. The analytical model displayed in this figure will further be explained in section 4.2.2.

(a)

(b)

(c)
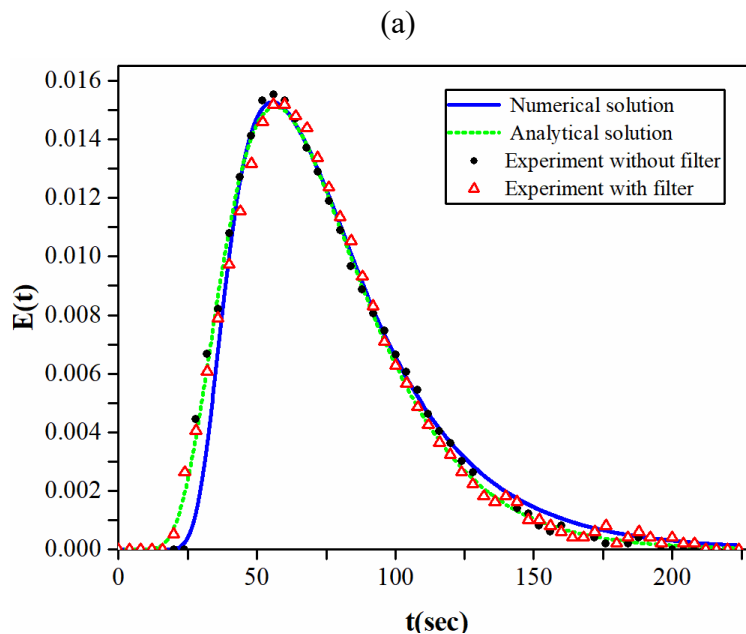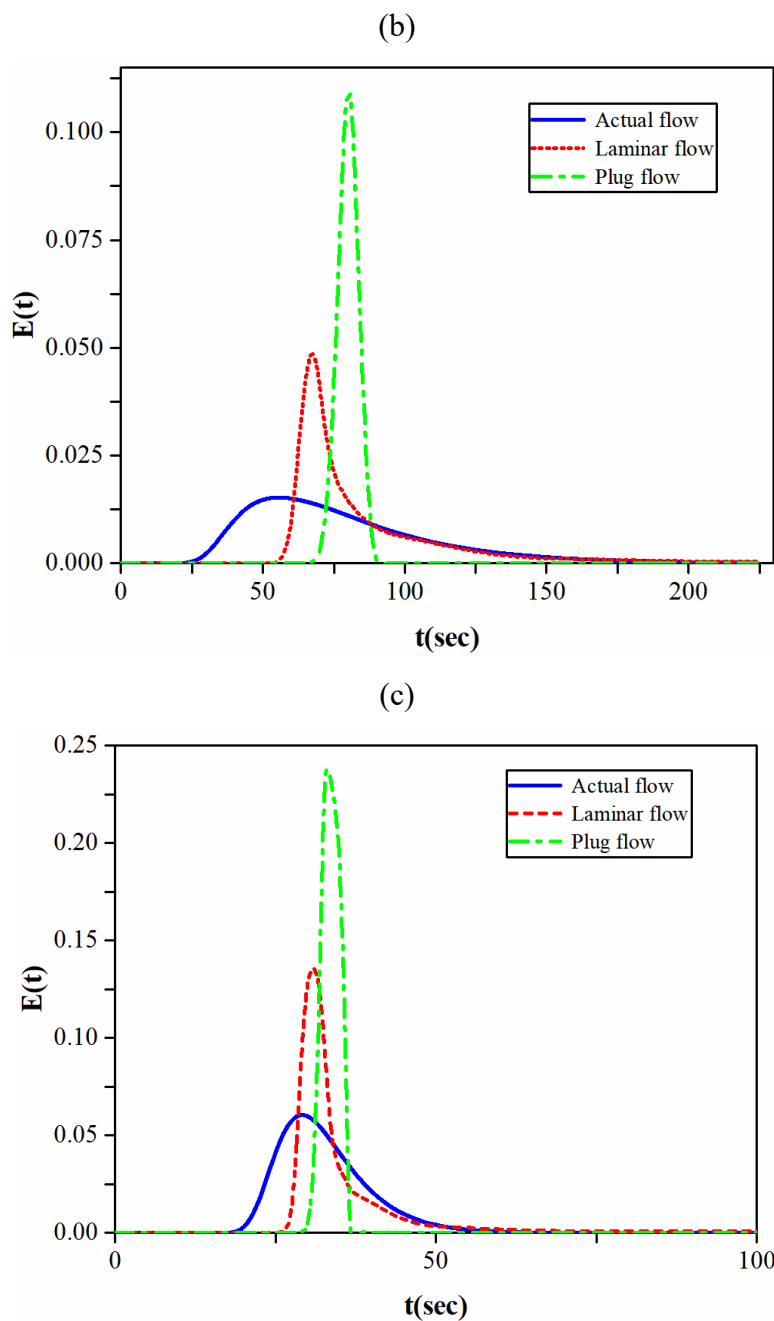
Fig. 4.4. Residence time distribution E(t) of CO_2 in the PCO reactor; (a) the comparison between simulation and experimental results in the presence/absence of catalyst (b) the deviation of the actual flow from the ideal plug flow and the laminar flow at Q=10 L/min (c) the deviation of the actual flow from the ideal plug flow and the laminar flow at Q=40 L/min determined by a simulation.

4.2.2. Analytical analysis of RTD

Users of photocatalysts generally do not have access nor knowledge of CFD tools. Thus, one of the aims of this research is to develop a simple and straightforward methodology for the evaluation of flow characteristics in the presence of dispersion using the RTD curve. To

characterize the non-ideal flow within reactors, several models have been developed, namely, continuous stirred tank reactors in series and dispersion models [162, 186].

Since RTD data are generally known for a number of discrete time intervals, the mean residence time $(\bar{t}_m)$ and the variance of the residence time (σ^2) can be evaluated as [186]:

$$\bar{t}_m = \int_0^\infty tE(t)dt = \frac{\sum_0^\infty t_i C(t_i)\Delta t_i}{\sum_0^\infty C(t_i)\Delta t_i} \tag{4.3}$$

$$\sigma^2 = \frac{\int_0^\infty (t - \bar{t}_m)^2 C(t)dt}{\int_0^\infty C(t)dt} = \frac{\sum_0^\infty (t_i - \bar{t}_m)^2 C(t_i)\Delta t_i}{\sum_0^\infty C(t_i)\Delta t_i} \tag{4.4}$$

The axial dispersed plug flow model, or simply the dispersion model has been applied to simulate the non-ideal behavior of the gas in the PCO reactor. Considering the fact that the axial dispersion is mainly due to velocity gradients whereas the lateral dispersion is owing to the molecular diffusion only [186], the differential equation representing this dispersion can be expressed as:

$$\frac{\partial C}{\partial t} = D_{ax}\frac{\partial^2 C}{\partial x^2} - u\frac{\partial C}{\partial x} \tag{4.5}$$

where D_{ax} is the axial dispersion coefficient, which characterizes the degree of dispersion. It should be noticed that the concentration gradient in lateral directions was assumed to be negligible. By considering an opened-opened vessel, the analytical solution of the model can be described as follows [186]:

$$E(t) = \frac{u}{\sqrt{4\pi D_{ax}t}}\exp\left[-\frac{(L - ut)^2}{4D_{ax}t}\right] \tag{4.6}$$

$$\sigma_\theta^2 = \frac{\sigma^2}{\bar{t}_m} = \frac{2}{Pe} + \frac{8}{Pe^2} \qquad \text{with } Pe = \frac{uL}{D_{ax}} \tag{4.7}$$

where L, u, and Pe represent the characteristic length, the superficial velocity, and the Peclet number, respectively. By applying the proposed method for the CO_2 tracer, the result is demonstrated in Fig. **4.4**. It can be observed that the analytical solution perfectly matches the experimental result. This method was then used to evaluate the RTD analysis of MEK at various flow rates. Fig. **4.5**-a presents the residence time distribution behavior of the PCO reactor and simulation results gained with the use of the axial dispersion model at flow rates of 10, 20, 30, 40, 50, 60 L/min. It was found that, with an increase in the airflow rate, the peak value of the tracer increases as well. Moreover, the higher the flow rate, the shorter the time after which the peak was observed. Thus, the dispersion increases with enhancing the flow rate, which is in accordance with

the earlier studies [187-189]. As Peclet number indicates the extent of axial dispersion, it was plotted versus velocity in Fig. **4.5**-b. Under our experimental conditions, the Pe value is lower than 100, which is the acceptable minimum limit for plug-flow [186]. These low values of Pe imply that the PCO reactor cannot be considered as an ideal plug-flow reactor owing to that substantial axial dispersion. On the other hand, it is easy to see that the axial dispersion coefficient (D_{ax}) continuously increases as superficial velocity increases (see Fig. **4.5**-b). As the value of Re.Sc in the present study is between 200 to 700, the axial dispersion coefficient, according to the Aris-Taylor correlation [190, 191], can be represented by a quadratic function of the superficial velocity ($D_{ax} = \alpha u^2$) [186]. However, the correlation proposed by Aris-Taylor is only valid for cylindrical channels. In this research, the best fit is given by:

$$D_{ax} = 2.207\ u^2 \qquad\qquad (4.8)$$

(a)

51
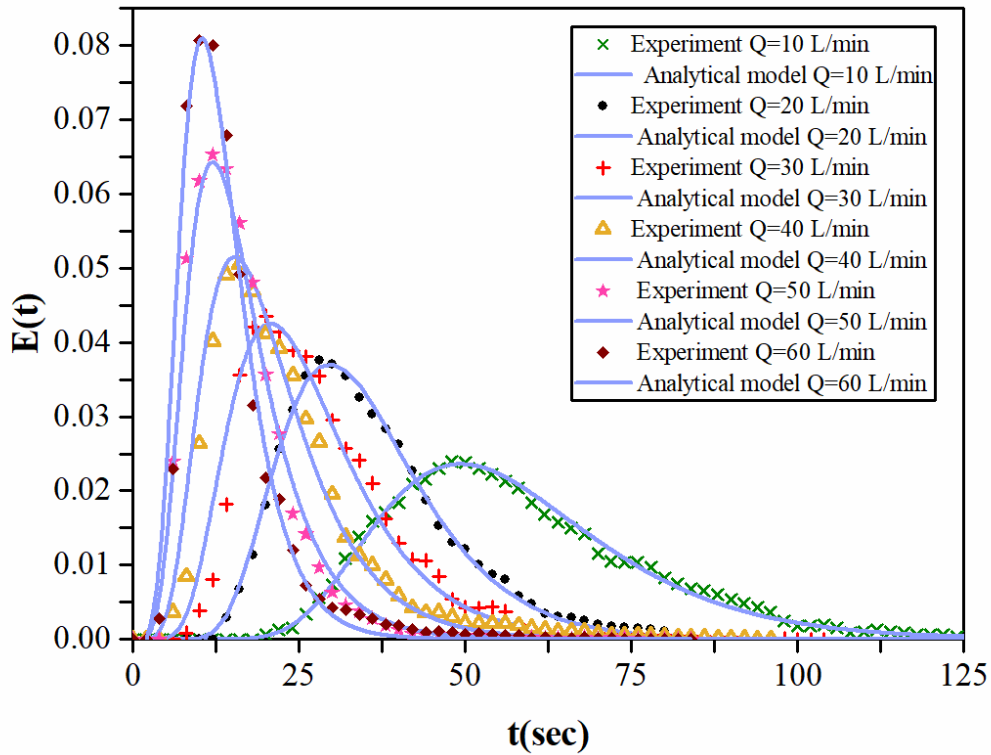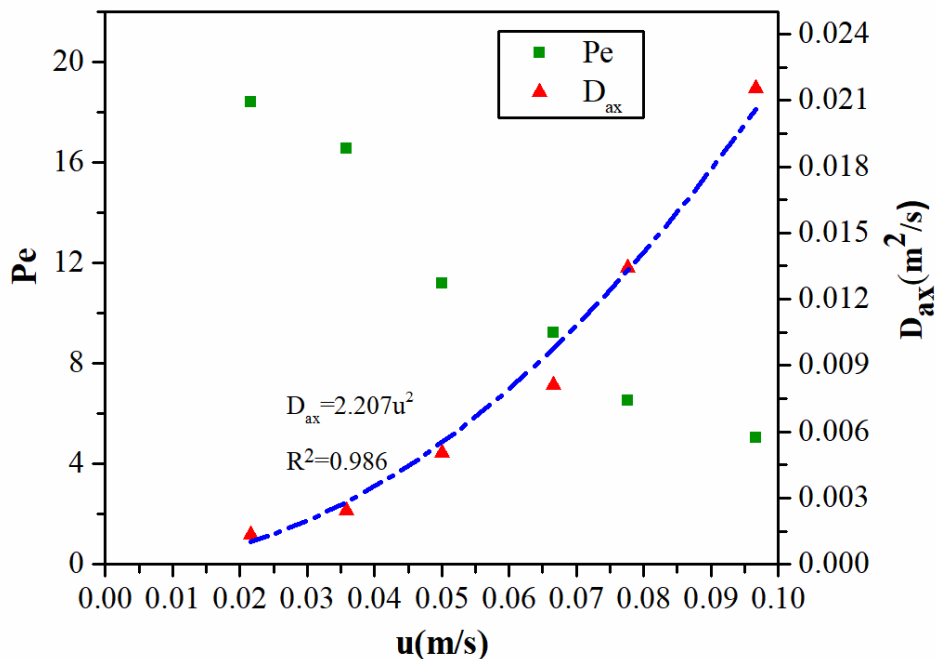
Fig. 4.5. (a) the residence time distribution E(t) of MEK at various flow rates, (b) the dependence of the Peclet number and axial dispersion values on the superficial velocity

4.2.3. PCO reaction under mass transfer limitation

Fig. **4.6** demonstrates the removal efficiency of MEK versus light intensity and flow rate for two different PCO filter thicknesses. As it is mentioned in the methodology section of this chapter, the reaction requires to be conducted at shorter filter thickness and high lamp radiation to ensure that the system operates at the mass transfer-controlled regime. This way, it was assured that the lights with high intensities could completely penetrate the media, resulting in an extremely active photocatalyst. Therefore, to determine the optimum value, the photocatalysis reaction experiment was performed at various light intensities (Fig. **4.6**-a). This figure shows that the optimum point for both filters was at a light intensity of 78 mW/cm^2. It should be noted that all experiments were performed at a low concentration of MEK (150 ppb) to reach high conversion under the mass transfer-limited condition. In Fig. **4.6**, at lower light intensity, the filter with a thickness of 3 mm has higher removal efficiency, whereas, at high light intensity, it has lower efficiency compared to the filter with 5 mm thickness. This can be attributed to the possibility of electron-hole recombination in the thick photocatalyst [36]. However, with elevating the light intensity, the

number of activated particles in the filter with 5 mm thickness increases, which leads to outperform the other one.

Fig. **4.6**-b demonstrates the dependence of the experimentally measured MEK conversions upon flow rate. The experimental light intensity was taken equal to 78 mW/cm^2 when the apparent reaction rate is completely controlled by mass transfer limitations. As expected, for all samples, the observed removal efficiency decreases as the flow rate increases (due to the corresponding reduction of the residence time).

(a)

(b)
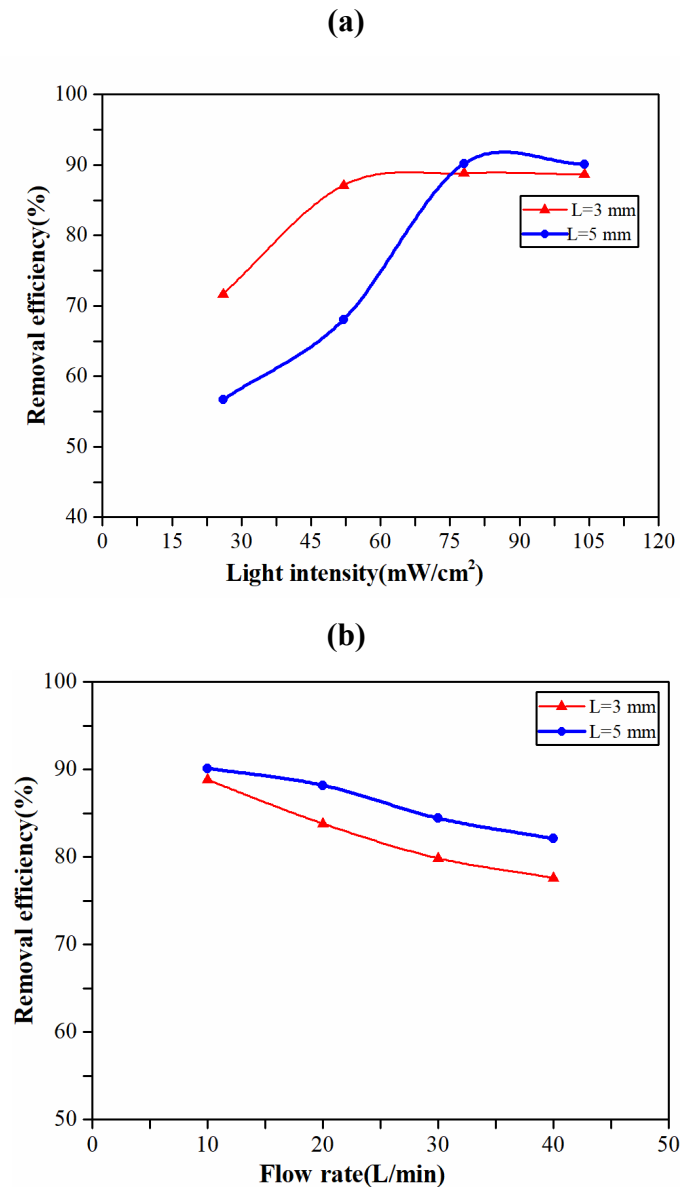
Fig. 4.6. MEK PCO efficiency as a function of (a) light intensity (flow rate=10 L/min) (b) flow rate (intensity=78 mW/cm^2)

The mass balance through the PCO filter considering axially dispersed plug flow and steady-state condition and assuming a pseudo-first-order reaction is given by:

$$D_{ax}\frac{d^2C}{dx^2} - u_b\frac{dC}{dx} - \frac{(1-\varepsilon)}{\varepsilon}k_m a_s(C - C_s) = 0 \qquad (4.9)$$

$$r = k_m a_s(C - C_s) = k_{app}C_s \qquad (4.10)$$

where k_m , a_s , ε, C_s , r and k_{app} are the external mass transfer coefficient, the geometric surface area per unit volume, the bed porosity, VOC concentration at the catalyst phase, the photocatalysis reaction rate, and the apparent photodegradation rate constant, respectively. In the case of a high reagent consumption in comparison with the mass-transfer process, a significant concentration gradient happens in the boundary layer. It means the surface reaction is extremely rapid, and the mass transfer rate to the surface dictates the overall rate of reaction. Accordingly, the concentration C_s becomes much lower than the bulk-gas concentration (i.e., $C_s \ll C$) [192]. Eq. (4.9) and Eq. (4.10) are readily combined to give:

$$D_{ax}\frac{d^2C}{dx^2} - u_b\frac{dC}{dx} - \frac{(1-\varepsilon)}{\varepsilon}k_{ov}C = 0 \qquad (4.11)$$

where the overall rate constant (k_{ov}) is stated as:

$$\frac{1}{k_{ov}} = \frac{1}{k_{mt}} + \frac{1}{k_{app}} \qquad (4.12)$$

Since mass transfer is the rate-controlling process ($k_{app} \gg k_{mt}$), then $k_{ov} \approx k_{mt}$. To solve the Eq. (4.11), Danckwert's boundary conditions were applied as:

$$u_b C_{in} = u_b C - D_{ax}\frac{dC}{dx} \qquad (4.13)$$

$$\frac{dC}{dx} = 0 \qquad (4.14)$$

The analytical solution of Eq. (4.11) in term of removal efficiency can be written as [186]:

$$X = 1 - \frac{C_{out}}{C_{in}} = 1 - \frac{4q\ exp(\frac{u_b L_f}{2D_{ax}})}{(1 + q)^2 \exp\left(\frac{qu_b L_f}{2D_{ax}}\right) - (1 - q)^2\exp\left(-\frac{qu_b L_f}{2D_{ax}}\right)} \qquad (4.15)$$

The parameter q is expressed as:

$$q = \sqrt{1 + \frac{4k_{m,ext}a_s\tau D_{ax}(1-\varepsilon)}{u_b L_f \varepsilon}} \qquad (4.16)$$

where τ, and L_f are the hydraulic residence time of reactor (s) and thickness of SFF filter, respectively. The geometric surface area a_s (m²/m³) was calculated on the basis of fiber diameter and coating thickness (shown in Fig. **4.7**) through Eq.(4.17).
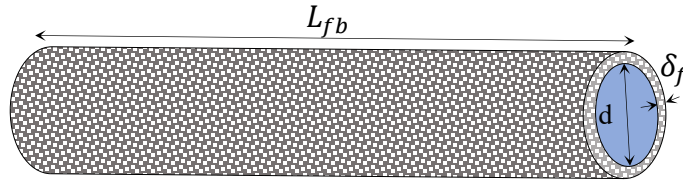
Fig. 4.7. Schematic of a silica fiber coated with TiO₂

$$a_s = \frac{2\pi \left(\frac{d}{2} + \delta_f\right) L_{fb}}{\pi \left(\left(\frac{d}{2} + \delta_f\right)^2 - \left(\frac{d}{2}\right)^2\right) L_{fb}} = \frac{d + 2\delta_f}{d\delta_f + \delta_f^2} \qquad (4.17)$$

where d, δ_f and L_{fb} represent fiber diameter, the TiO₂ layer thickness, and the fiber length, respectively. For the SFF filter used in this study, a value of 109×10^3 (m²/m³) was calculated based on SEM analysis.

The relevant variables were then expressed in dimensionless form by calculating the Sherwood (Sh), Schmidt (Sc), and Reynolds (Re) numbers, as defined in the Nomenclature section. For the range of experimental conditions, Sc was calculated to be 1.04. Using this value of Sc, Sh is calculated based on the mass transfer coefficients obtained for two different catalyst thicknesses and plotted against Re, as shown in Fig. **4.8**. This figure displays that Sh number for airflow rate ranging from 10 L/min to 40 L/min using thickness of L=3 mm is very close to L=5 mm. This indicates that mas transfer is independent of the catalyst bed thicknesses due to the same geometry and characteristic of the fibrous catalyst. Following correlation was obtained using least squares regression:

$$Sh = 0.0056 Re^{0.4663} Sc^{\frac{1}{3}} \qquad (4.18)$$

where Re is defined based on fiber diameter and interstitial velocity. Due to very small fiber diameters, Re becomes lower than unity in the SFF filter. Correspondingly, the observed dimensionless mass transfer coefficients are very low.
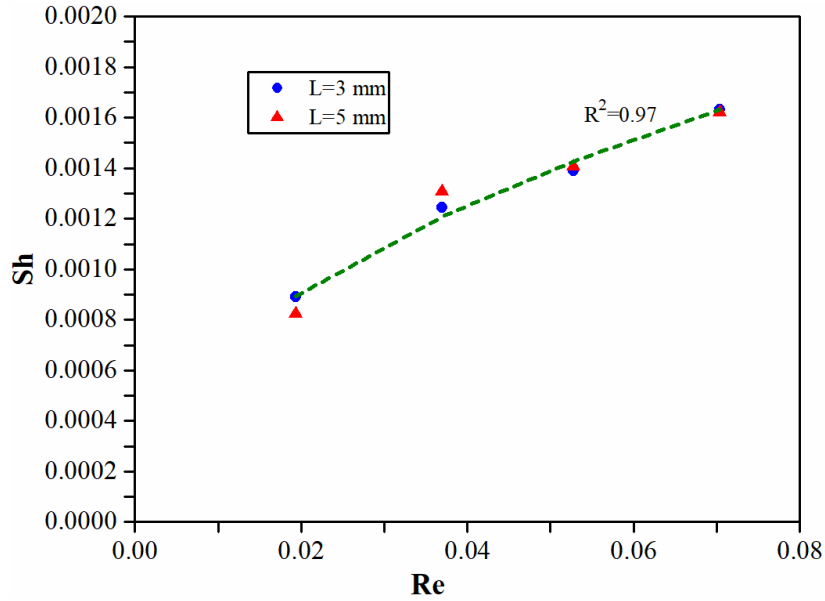
Fig. 4.8. Dependence of the Sh number upon the Re number in SFF filter with varying thickness and velocity (Sc=1.04).

Contrary to earlier works on fiber-based structured materials, which focused more on the activity of the catalyst, limited numbers of articles covering mass transfer are available [193]. To date, just a few correlations between Sherwood and Reynolds numbers for a fibrous catalyst in the gas phase with a low Reynolds number are available. Table 4.2 demonstrates some literature correlations for mass transfer in fiber-based catalyst supports (except Ref. [194]; for monolith structure) validated for the relatively low range of Reynolds number. Groppi et al. [195] studied the gas/solid mass transfer in a metallic fiber filter. Their results showed significantly low values for Sh number. Satterfield [196] and Ahlstrom-Silversand [197] studied the mass transfer characteristics of wire-mesh catalysts with high porosity and then proposed correlations for the mass transfer coefficient in the absent of axial dispersion. The correlation proposed by Votruba [194] for the monolithic structure was commonly used in PCO studies [35, 71, 198]. Zhong [35] used Votruba's correlation to evaluate the mass transfer coefficient of fiberglass filter by considering fiber diameter as the characteristic length. However, this correlation was obtained based on mass transfer through the vaporization of liquid from the surface of monolithic structure. Furthermore, in Votruba's correlation, the hole diameter of monolith was defined as characteristic length.

Fig. **4.9** compares the correlation developed in the present study with those given in the literature for 0.01<Re<10 at a constant Sc=1.04. At low values of Re, prediction by Groppi is closer to the present study. However, the deviation increases when it is compared with other ones. By increasing the value of Re, the calculated Sh number of all other correlations deviated considerably from that of the present study. One of the possible explanations for higher deviation is the effect of axial dispersion on mass transfer, which was neglected for studies related to wire mesh and honeycomb type of catalyst (i.e., Refs. [194, 196, 197]). Although Groppi accounted the axial dispersion effect for developing the mass transfer equation, the correlation demonstrates a weaker dependence on Re than that of present work. Groppi's correlation was validated for lower porosity and higher fiber diameter, which over-predicts the mass transfer for the condition related to the present study. Correlations related to wire mesh (i.e., Satterfield and Ahlstrom-Silversand) are validated for high Re number where turbulences may occur. Votruba obtained the relationship by considering the hydraulic diameter of the monolith as the characteristic length, which may cause such a significant deviation [194].

The above observations highlight the necessity for the verification and assessment of the applicability of mass transfer correlations for actual conditions prior to their use for performance estimation.

Table 4.2: Experimental parameters and correlations used in different research works.

Application	Study	Media type	ε	d (μm)	Re	Pe	Correlation
Photocatalytic reaction	Present work	Fiberglass	0.96	10	0.02-0.07	8-17	$Sh = 0.0059Re^{0.4663}Sc^{\frac{1}{3}}$
Catalytic reaction	Groppi [195]	Metal fiber	0.86	25	0.25-1	>10	$Sh = 0.089Re^{0.72}Sc^{\frac{1}{3}}$
	Satterfield [196]	Wire mesh	0.71-0.91	68.5-84	1-100	very high	$Sh = 0.47Re^{0.283}Sc^{\frac{1}{3}}$
	Ahlstrom-Silversand [197]	Wire mesh	> 0.7	300-1650	0.8-140	very high	$Sh = 0.78Re^{0.45}Sc^{\frac{1}{3}}$
Liquid vaporization	Votruba [194]	Honeycomb	0.32-0.38	1-10× 10^3	3-480	very high	$Sh = 0.705\left(Re\frac{d}{L_f}\right)^{0.43}Sc^{0.56}$
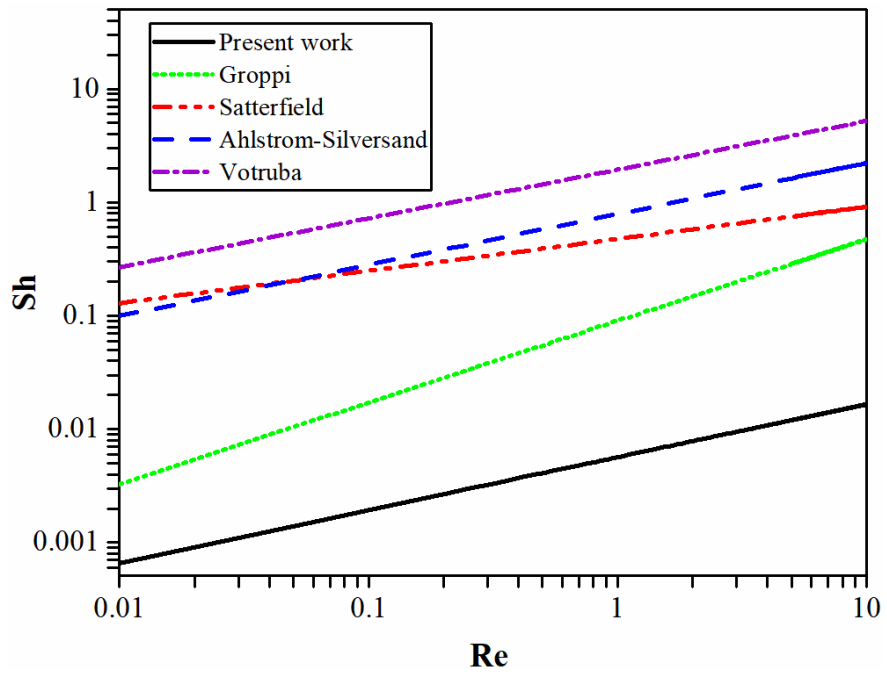
Fig. 4.9. Effect of Re on Sh as predicted by various correlations at Sc=1.04

5. Kinetic modeling of the photocatalytic degradation for removal of MEK

Kinetic analysis is a powerful tool to assess the catalytic properties of material and reaction rate in the PCO process. The prominent factors affecting catalytic performance or kinetic parameters of photoreaction are the adsorption capacity and oxidation capability of the photocatalysts [199, 200]. Most reported kinetic parameters in the literature strongly depend on the experimental conditions and cannot be easily extrapolated to other conditions. For a continuous flow reactor, it was usually assumed that reactors operate under ideal plug flow; hence, reaction rates are determined by ignoring dispersion/diffusion. This model is based on the assumption that the velocity profile is uniform and, accordingly, dispersion is negligible ($D_{ax}/uL \approx 0$). However, the result of the previous chapter demonstrated that significant dispersion occurs in the PCO reactor ($D_{ax}/uL > 0.01$), and flow in the reactor deviated from the ideal plug flow [183]. Additionally, the main limitation of previous kinetic studies on the PCO reactor is that they were validated at very low velocities, in which high/complete mineralization efficiency to CO_2 and H_2O was achieved with little generation of by-products. Nevertheless, at higher velocities (due to the short residence time), complete mineralization cannot be achieved (partial oxidation) and amount of by-products is not negligible. In such case, by-products can compete with challenge compounds for adsorption on the active sites of the photocatalyst. This chapter compares the result of kinetic modeling using both ideal plug flow and axially dispersed flow in the PCO reactor. Six kinetic rate equations on the basis of Langmuir-Hinshelwood (L-H) expression were examined to find the best model that fits the experimental data. The L-H model was extended to consider the competition effect of by-products in the reaction rate. Moreover, the light intensity distribution on the photocatalyst surface was simulated using the linear source spherical emission model (LSSE) and validated with the experimental data.

5.1. Methodology

5.1.1. Dispersion model

As kinetic modeling of VOCs in this research was performed under steady-state condition, the developed model in chapter 3 is simplified as follows:

Gas phase:

$$D_{ax}\frac{d^2 C_A}{dx^2} - u_b \frac{dC_A}{dx} - \frac{(1-\varepsilon)}{\varepsilon} k_m a_s (C_A - C_{As}) = 0 \qquad (5.1)$$

Catalyst phase:

$$k_m a_s (C_A - C_{As}) = - \, r_A \qquad (5.2)$$

Boundary conditions:

$$u_b C_{A,in} = u_b C_A - D_{ax} \frac{dC_A}{dx} \qquad \text{at } x = 0 \qquad (5.3)$$

$$\frac{dC_A}{dx} = 0 \qquad \text{at } x = L_f \qquad (5.4)$$

5.1.2. Ideal plug-flow model.

To compare dispersion model results with the ideal plug-flow, the dispersion term was neglected and Eq. (5.1)-(5.4) were simplified as follows:

Gas phase:

$$u_b \frac{dC_A}{dx} - \frac{(1-\varepsilon)}{\varepsilon} k_m a_s (C_A - C_{As}) = 0 \qquad (5.5)$$

Catalyst phase:

$$k_m a_s (C_A - C_{As}) = -r_A \qquad (5.6)$$

boundary conditions:

$$C_A = C_{As} = C_{A,in} \qquad \text{at } x = 0 \qquad (5.7)$$

Assuming that the bulk concentration of component **A** (C_{Ab}) changes linearly in the PCO filter, a reasonable estimate is [201]:

$$C_{Ab} = \frac{C_{A,in} + C_{A,out}}{2} \qquad (5.8)$$

Eq. (5.8) can be stated $\Delta C_A = C_{Ab} - C_{As}$ and solved using Eq. (5.6):

$$\Delta C_A = \frac{-r_A}{k_{m,ext} a_s} \qquad (5.9)$$

The mass transfer effect is significant if the following criterion occurs [202]:

$$\frac{\Delta C_A}{C_{Ab}} \geq 0.1 \qquad (5.10)$$

5.1.3. Experimental procedure

The PCO reaction test of MEK was conducted using the reactor set-up displayed in Fig. 3.7. A layer of TiO$_2$/SFF was installed in front of the UV lamp and MEK was injected automatically into

humid air by a syringe pump. Table 5.1 also shows the experimental conditions at which the PCO test was performed. In addition, an adsorption test was conducted in the PCO reactor with a layer of TiO$_2$/SFF filter under dark condition. The detail of the adsorption test condition is provided in section 3.3.3.

Table 5.1: Experimental conditions employed in gas-phase PCO of MEK carried out in a continuous-flow photoreactor (T=20 °C; P=1 atm)

# of Experiment	Q_{Feed}	$C_{MEK,feed}$	RH_{Feed}	I
	[L/min]	[ppb]	[%]	[W/m^2]
1	30	100	33	7
2	30	250	33	7
3	30	375	33	7
4	30	500	33	7
5	30	600	33	7
6	30	800	33	7
7	30	900	33	7
8	30	1000	33	7
9	30	250	50	7
10	30	500	50	7
11	30	800	50	7
12	30	1000	50	7
13	30	500	17	7
14	30	500	67	7
15	30	500	33	14
16	30	500	33	23.5
17	20	1000	33	7
18	10	1000	33	7

5.2. Results and discussion

5.2.1. UV radiation intensity

Fig. 5.1 illustrates the radiation intensity distribution on the photocatalyst surface for three different lamp arrangements and positions as predicted by the LSSE model. The irradiance distribution using one lamp (presented in Fig. 5.1-a) indicates intensity at the side of the filter, where the lamp was mounted, was higher than other positions. However, when two lamps were

used, the light intensity distribution on the filter surface became more uniform (see Fig. 5.1-b), due to the symmetrical lamp placement in the duct. Decreasing the distance between the lamps and the filter (at x=15 cm) increases light intensity magnitude but reduces the light uniformity (see Fig. 5.1-c). To validate the results, after measuring lamp walls intensity (I_w for each lamp was 650 w/m^2), irradiation intensity on the catalyst surface was measured at 5 points for each case and compared with the LSSE model predictions. A good agreement was observed between the model prediction and experimental results (R^2 ≥0.94).

To simulate photon absorption rate in TiO$_2$ film, the attenuation coefficient was obtained. In this regard, the light intensity was measured at the front and back of the media for different thicknesses. Fig. 5.2 presents the dimensionless light absorption rate ($\bar{I} = I_{ave,b}/I_{ave,f}$) versus overall effective TiO$_2$ layer thickness. The average light intensity at the front was $I_{ave,f}$=7 W/m^2 and average light intensity at the back of the media was measured for filter thicknesses of 0.2, 0.45, 0.8, and 1.2 cm. The attenuation coefficient was calculated and presented in Table 5.2.

Table 5.2: Attenuation coefficient in the Beer-Lambert model.

Parameter	Unit	Value	95% CI	R^2
μ	μm^{-1}	0.1053	0.0082	0.98

(a)

(b)

(c)
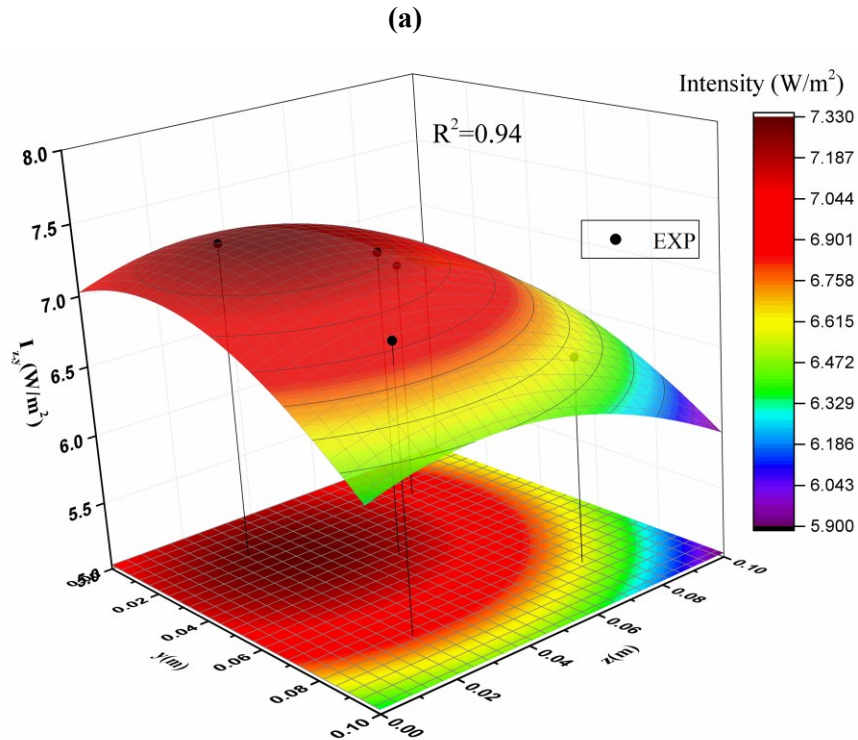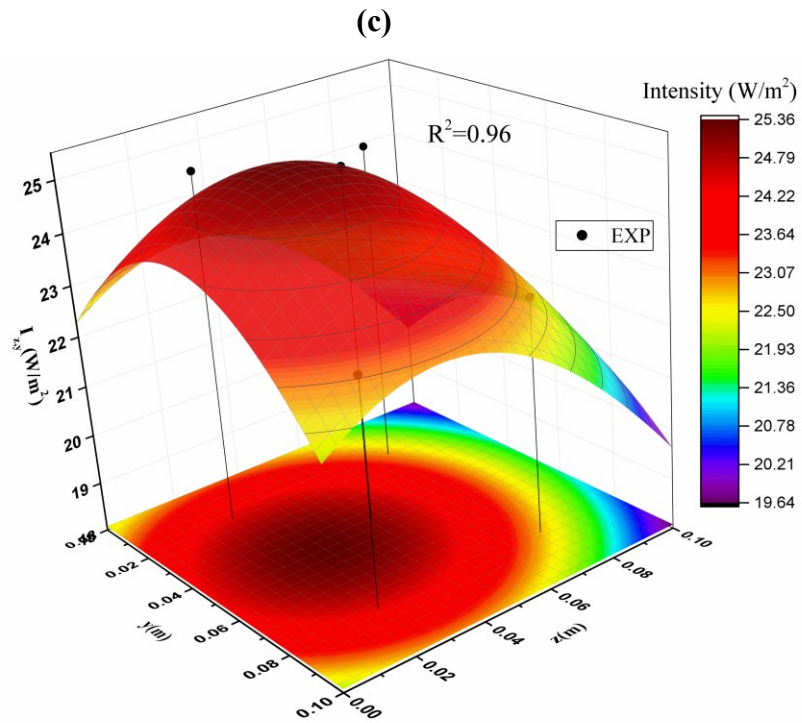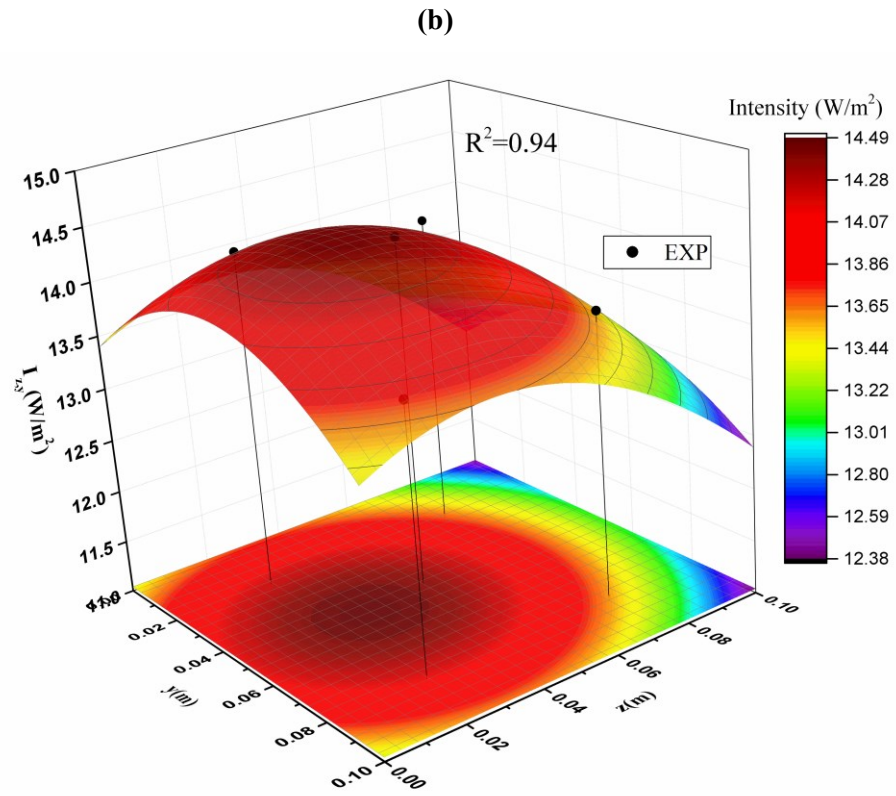
Fig. 5.1. Distribution of radiation intensity on the surface of the PCO filter for (a) one lamp at x=20 cm, (b) two lamps at x=20 cm and (c) two lamps at x=15 cm.
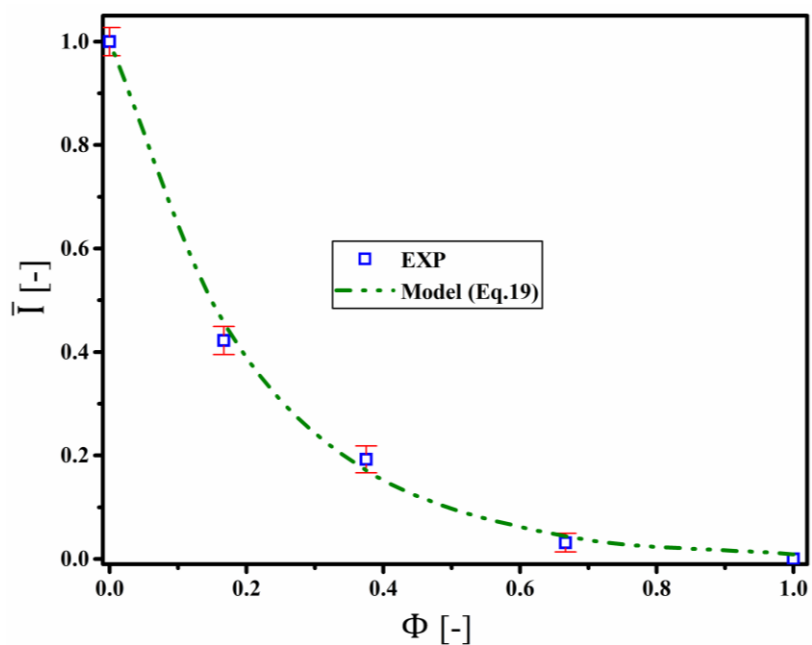
Fig. 5.2. Dimensionless light intensity versus overall effective photocatalytic TiO$_2$ layer thickness.

5.2.2. By-products of MEK in the PCO

The MEK degradation mechanism and corresponding formation of its intermediates/by-products have been studied [48, 203-205]. Results show that aldehydes and ketones are the primary intermediates/by-products of MEK. Vincent et al.[204] and Raillard et al. [48] detected acetaldehyde (by GC/MS) as the main by-product of MEK decomposition under UV light illumination. However, the latter authors observed the presence of formaldehyde, acetone, acetic acid at very low concentrations. Zhong et al.[97] and Mamaghani et al.[203] analyzed MEK by-products in the UV-PCO reactor quantitatively and found formaldehyde, acetaldehyde, and acetone were the major detected compounds. In this study, identification and quantification of MEK photocatalytic reaction by-products were measured by HPLC. The result is presented in Table 5.3 for the experimental conditions of run 8 (described in Table 5.1). The identified compounds in the reactor exit were (for Run 8): unreacted MEK (816.3 ppb), formaldehyde (70.5 ppb), acetaldehyde (74.6 ppb), acetone (5.8 ppb), and traces of propionaldehyde. Aldehydes (formaldehyde and acetaldehyde) are the main by-products of the PCO reaction, which is in line with previous studies [97, 203].

Considering that $C_{i,C-MEK}$ is representative of carbon atom concentration of compound i formed by MEK decomposition (including unreacted MEK and its by-products), it can be expressed as below [85]:

$$C_{i,C-MEK} = C_i * n(C) \qquad\qquad (5.11)$$
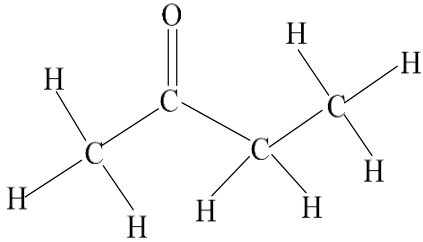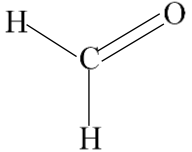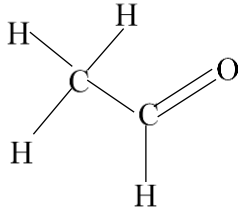
where C_i (ppb), and $n(C)$ represent the gas phase concentration and the number of carbon atoms of each component i molecule, respectively. Therefore, the mineralization efficiency can be evaluated [85]:
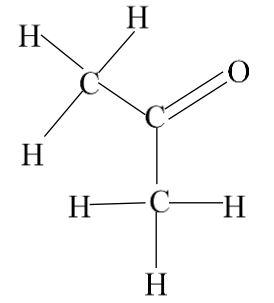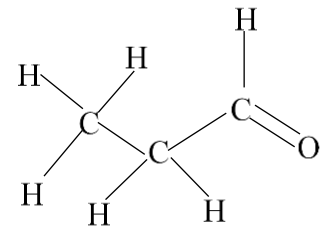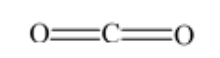
$$\eta_{min}(\%) = \frac{(C_{C-CO_2})_{exit}}{(C_{C-MEK})_{feed}} \qquad\qquad (5.12)$$

The carbon atom concentration of each identified by-product arising from MEK photooxidation and also unreacted MEK are calculated using Eq. (5.11) and shown in Table 5.3. Then, the result showed that for 18.4% conversion of feed, 4.7% of MEK mineralized into CO_2 (see Table 5.3). It was also found from carbon mass balance that 99.14% of carbon detected by analytical methods (HPLC and GC-FID), and only 0.86% of carbon concentration is related to undetected by-products. The total atoms concentration of all by-products formed by MEK photodegradation was around 6.4%. This indicates that by-products effect on adsorption of MEK should be considered in order to describe the PCO reaction rate appropriately.

Table 5.3:Product analysis by HPLC for the photocatalytic reaction of MEK; experimental conditions described in Table 5.1(run 8)

Compound (i)	Molecular		CAS no.	C_i [ppb]	$C_{i,C}$ [ppb]	$C_{i,C}/ C_{C\text{-MEK,feed}}$ [%]
	Formula	Structure				
MEK[a]	C_4H_8O		78-93-3	816.3	3265.2	88.03[a]
Formaldehyde	CH_2O		50-00-0	70.5	70.5	1.9
Acetaldehyde	C_2H_4O		75-07-0	74.6	149.2	4.03

Acetone	C_3H_6O		67-64-1	5.8	17.4	0.47
Propionaldehyde	C_3H_6O		123-38-6	trace	-	-
Carbone dioxide	CO_2	$O=C=O$	124-38-9	175	175	4.7

[a] Carbon atom concentration of MEK in feed stream ($C_{MEK,feed}$ = 927 ppb) was $C_{C-MEK,feed}$ = 3709.2 ppb

5.2.3. Kinetic data and model fitting

MEK degradation through PCO was simulated for six kinetic rate expressions (see Eqs. (3.13)-(3.18)) using the ideal plug flow model and the dispersion model (see Eqs. (5.1)-(5.7)). It should be noted that the LSSE and Beer-Lambert model were also used to simulate the radiation intensity applied in the rate expressions (models *M-1* to *M-6*). Additionally, within this work, reaction parameters were estimated under kinetics-controlled regimes (free of mass transfer limitations). In order to consider the competition effect of by-products in models *M-3* to *M-6*, an assumption was made to find the adsorption coefficients of by-products with higher confidence. According to the identified concentration of by-products (given in Table 5.3), the major generated by-products were aldehydes (formaldehyde and acetaldehyde), and the mass of others was negligible. In this regard, both formaldehyde and acetaldehyde have been lumped into a single pseudo species to reduce the number of kinetic parameters. Therefore, the term $K_{byp}C_{byp}$ in the denominator of models *M-3* to *M-6* was defined as:

$$K_{byp}C_{byp} = K_{Ald}C_{Ald} = K_{F-Ald}C_{F-Ald} + K_{A-Ald}C_{A-Ald} \qquad (5.13)$$

where *Ald*, *F-Ald*, and *A-Ald* stand for the Aldehyde, Formaldehyde, and Acetaldehyde, respectively.

The equilibrium adsorption of MEK (0.25-1 ppm) under different relative humidities for the PCO filter is presented in Fig. 5.3. As can be seen, the adsorption capacity drops as the relative humidity increases. This indicates that despite water solubility and polarity of MEK, relative humidity can have a considerable inhibitive effect [206]. Similarly, the adsorption reduction effect of formaldehyde by increasing relative humidity was reported by Kibanova et al.[207]. The adsorption parameters of the Langmuir model (Eq.(3.21)) are determined and given in Table 5.4. The maximum adsorption capacity (q_m) was computed at different levels of humidity separately and correlated by a linear equation. However, the adsorption coefficients of MEK and water were obtained independently to be applied in the L-H reaction rate model. Some authors [208-210] reported that the adsorption coefficient obtained from the dark condition is different from the equivalent coefficient determined in the photocatalytic reaction process. But it should be noticed that the rate expression used in their studies was applied only for the degradation of single compound, and it was assumed that the intermediate/by-products do not influence the reaction rate. If the adsorption coefficient truly reflects the adsorption affinity between adsorbate and the surface, this coefficient determined in PCO should be the same as measured in the dark adsorption [208, 211]. Thus, the estimated adsorption parameters from dark adsorption (single site adsorption) were applied in the models **M-3** and **M-4** to find other unknown parameters.

Table 5.5 reports the kinetic and adsorption equilibrium parameters resulting from models fitting to the experimental data by considering the ideal plug flow model and dispersion model. From Table 5.5, it can be concluded that both plug and dispersion models provided a high fitting accuracy ($R^2>0.99$) to the reaction data. However, the dispersion model gives less residual error (S^2_R). In terms of kinetic rate expression, all rate models applied in modeling can qualitatively express experimental results of MEK degradation through the PCO filter (see curve fitting results in Fig. 5.4). Models *M-5* and *M-6*, because of the greater number of parameters and limited

experimental data, result in a large value of confidence intervals. However, these two models were used to compare with other models at different operating conditions.

The results of curve fitting were then used to validate experimental data at different operating conditions. Fig. 5.5 demonstrates the prediction of both models (plug and dispersion) at various concentrations (at RH=50%). According to this figure, the rate expressions *M-3*, *M-4*, and *M-6* show a better prediction than others, particularly at high concentrations. This can be attributed to the competitive adsorption of MEK with water and by-products on active sites of the photocatalyst. Due to the hydrophilic characteristic of TiO_2[68], all of these polar compounds take part in competitive adsorption on each site. On the other hand, *M-5* has less accuracy, especially in the plug flow model, since it considers the adsorption of MEK and water separately in two different adsorption sites without any competition. *M-1* and *M-2* also have less accuracy at higher concentrations as the competition of other molecules was neglected. In terms of RH, Fig. 5.6 displayed that *M-3* and *M-6* provided the best prediction for variation in relative humidity, and *M-4* deviated from the experimental result, particularly at low RH. This might attribute to the dominant effect of by-products at lower RH, and its hindering effect cannot be predicted properly by *M-4*.

It was also observed that all rate expressions failed to fit the change in air velocity (Fig. 5.7-a) and light intensity (Fig. 5.8-a) when the ideal plug flow model was used. The reason can be the presence of large dispersion in the PCO reactor, which is neglected in a plug flow model. In previous study [183], residence time distribution (RTD) analysis with a tracer gas indicated that the flow regime in the photoreactor cannot be considered as ideal plug flow and that a significant axial dispersion is available. Therefore, ignoring the dispersion term in the ideal plug flow model (Eq. (5.5)) causes such a major discrepancy between simulation results and experimental ones in Fig. 5.7-a and Fig. 5.8-a.

Results show that the dispersion model using rate expressions *M-3* and *M-6* could provide an acceptable fit to describe the variation in velocity (see Fig. 5.7-b) and light intensity (see Fig. 5.8-b). Kinetic modeling suggests that MEK and water vapor molecules must be considered in the rate expression. Due to the significant impact of the water molecule on the MEK degradation rate, models *M-1* and *M-2* cannot properly describe the experimental data. Considering the inhibiting effect of water and by-products on MEK adsorption, *M-3* could provide the best fitting results among unimolecular rate expressions. Furthermore, among different bimolecular L-H models (*M-4* to *M-6*), the most appropriate fit was achieved by assuming MEK, H_2O, and by-products adsorbed competitively on the different types of active sites (*M-6*). From a purely statistical standpoint (see Table 5.5), the *M-3* model produces the best fit for the existing experimental data according to the highest R^2 and lowest S^2_R values. Moreover, for the sake of simplicity, model *M-3* has the least number of required parameters, which leads to narrower confidence interval and plausible value of estimated parameters.

The kinetic study of PCO degradation of MEK was reported by Arconada et al.[212] and Raillard et al.[213] using *M-1* rate expression considering the ideal plug flow reactor. However, the kinetic parameters obtained were for a very high concentration (hundreds of ppm), which resulted in lower values of these parameters in comparison with the present study (concentration

of less than 1 ppm). That could be due to the possibility of multi-layer adsorption formation at very high concentrations, which may affect the value of kinetic parameters. Another possible explanation is that the nature and characteristics of the photocatalyst used in those studies are different from the one used in this study. Apart from that, the kinetic parameters in this research were obtained at a different air velocity than those from [212, 213]. As Fig. 5.7-a shows, the ideal plug flow model failed to predict the PCO performance at various velocities, which may cause the discrepancy between calculated kinetic parameters derived from the literature and the present study.

The kinetic study result in the present study indicates that the ideal plug flow model cannot properly describe PCO reactor behavior since significant deviations were observed, particularly, when light intensity and air velocity were changed. This implies that the axial dispersion cannot be ignored in the PCO reactor, which is in agreement with [183]. In that work, it was found that significant deviation from the plug flow reactor occurred because of low Peclet number (less than 100) or high value of axial dispersion. Therefore, the validated dispersion model combined with the rate expression *M-3* is the most appropriate model to be applied in building mechanical ventilation air purification systems.
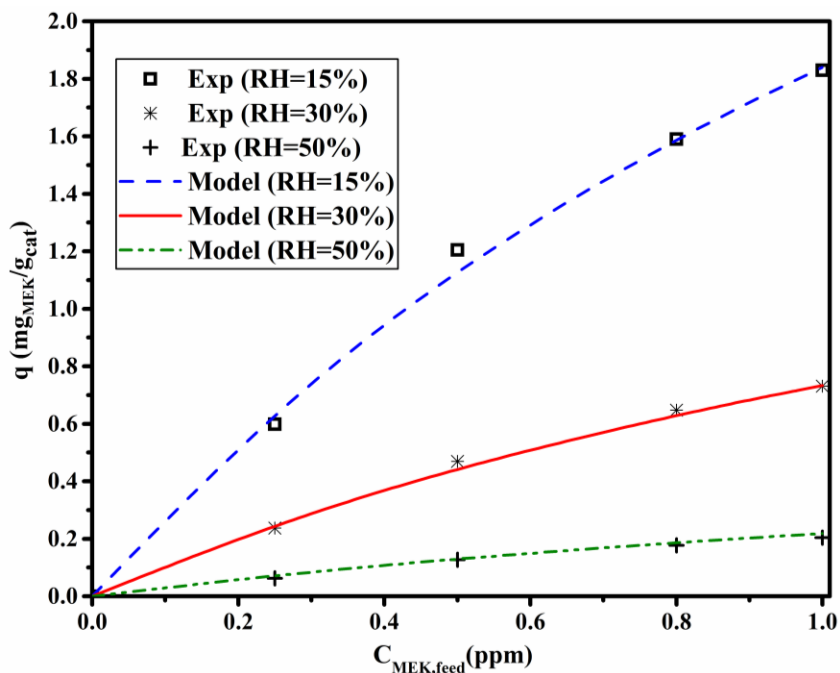
Fig. 5.3. Adsorption of MEK under various relative humilities for TiO$_2$/SFF filter

Table 5.4: Langmuir parameters for adsorption of MEK on TiO$_2$/SFF filter.

Parameter	Value	95% CI
q_m (mg$_{MEK}$/g$_{cat}$)	-0.0003C$_w$ [ppm]+4.0215	-
K_{MEK} (ppm^{-1})	7.5	0.067
K_W (ppm^{-1})	8.6×10^{-6}	2.08×10^{-7}
R^2	0.98	

Table 5.5: Kinetic and adsorption equilibrium parameters obtained from the application of rate expressions M-1 to M-6 in the plug flow model and the dispersion model (for run 1 to 8).

Model	Par.	Units	Plug flow model				Dispersion model			
			Values	95% CI	R^2	$S^2_R \times 10^2$ (ppm^{-2})	Values	95% CI	R^2	$S^2_R \times 10^2$ (ppm^{-2})
M-1	k	ppm s^{-1} mW^{-1} m^2	5.37	0.25	0.997	0.18	7.86× 10^3	0.40× 10^3	0.997	0.12
	K_{MEK}	ppm^{-1}	1.52	0.14			2.01	0.19		
M-2	k'	s^{-1} W^{-1} m^2	3.95	0.63	0.992	0.55	6.27×10^3	0.25×10^3	0.993	0.47
M-3	k	ppm s^{-1} W^{-1} m^2	8.33	0.95	0.998	0.14	14.28×10^3	0.2×10^3	0.998	0.10
	K_{MEK}	ppm^{-1}	7.5	-			7.5	-		
	K_w	ppm^{-1}	8.6×10^{-4}	-			8.6×10^{-4}	-		
	K_{byp}	ppm^{-1}	13.8	1.2			14	1.5		
M-4	k	ppm s^{-1} W^{-1} m^2	13.13	1.38	0.997	0.19	21.7×10^3	0.23×10^3	0.997	0.12
	K_{MEK}	ppm^{-1}	7.5	-			7.5	-		
	K_w	ppm^{-1}	8.6×10^{-4}	-			8.6×10^{-4}	-		
	K_{byp}	ppm^{-1}	3.13×10^{-3}	4.97×10^{-4}			2.33×10^{-3}	4.81×10^{-4}		
M-5	k	ppm s^{-1} W^{-1} m^2	169.4	113.34	0.997	0.19	9.06×10^3	3.4×10^3	0.997	0.12
	K_{MEK}	ppm^{-1}	0.98	3			1.95	4.2		
	K_w	ppm^{-1}	6.85	13.8			75.9	11.9		

	$K_{byp,1}$	ppm^{-1}	270	1700			2	7		
	$K_{byp,2}$	ppm^{-1}	980	110			99	360		
M-6	k	ppm s^{-1} W^{-1} m^2	43.73	773	0.998	0.17	9.24×10^3	101×10^3	0.998	0.11
	$K_{MEK,1}$	ppm^{-1}	0.99	11			9.3	95		
	$K_{w,1}$	ppm^{-1}	0.046	10			0.037	6.6		
	$K_{MEK,2}$	ppm^{-1}	3.15	784			3.15	63.3		
	$K_{w,2}$	ppm^{-1}	0.046	13.3			0.063	9.17		
	$K_{byp,1}$	ppm^{-1}	970	2170			920	1440		
	$K_{byp,2}$	ppm^{-1}	980	2800			1032	1890		
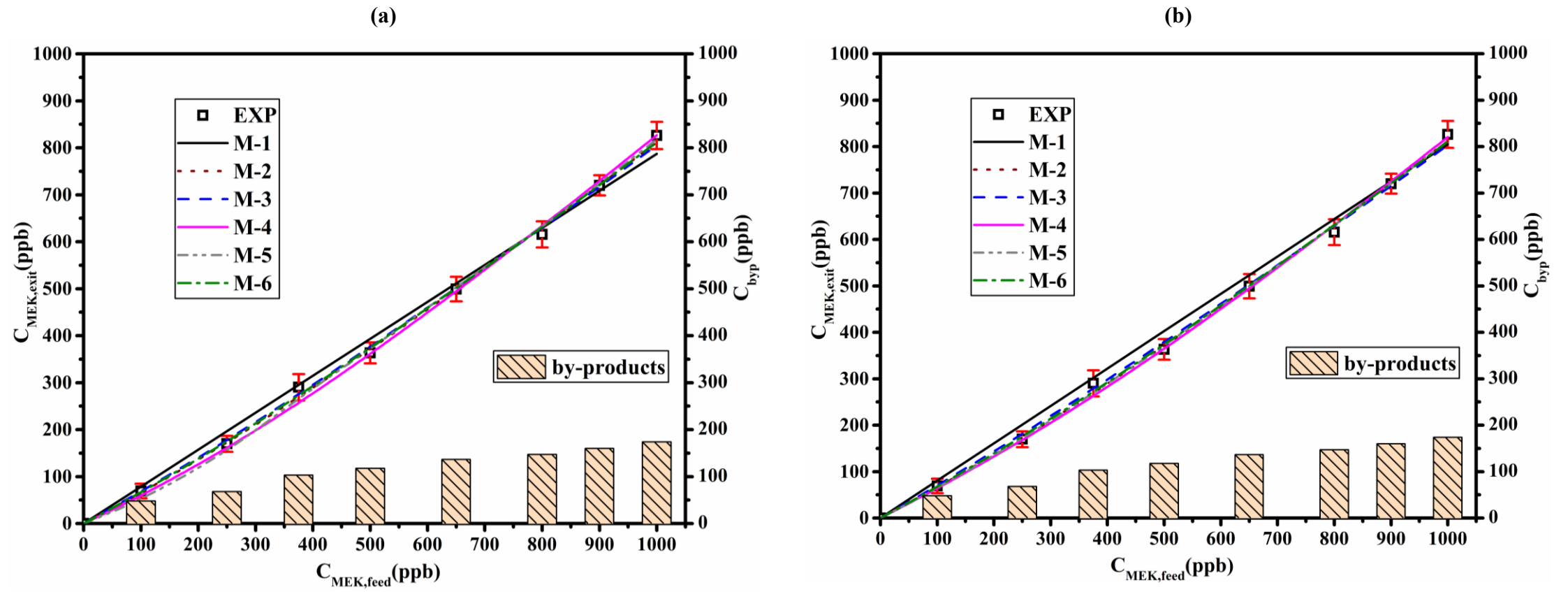
Fig. 5.4. Results of curve fitting for different kinetic rate expressions (models M-1 to M-6) using (a) Plug-flow model; (b) dispersion model; u=0.05 m/s; RH_{Feed}=33%; I_{ave}=7 W/m^2 (Run 1-8).
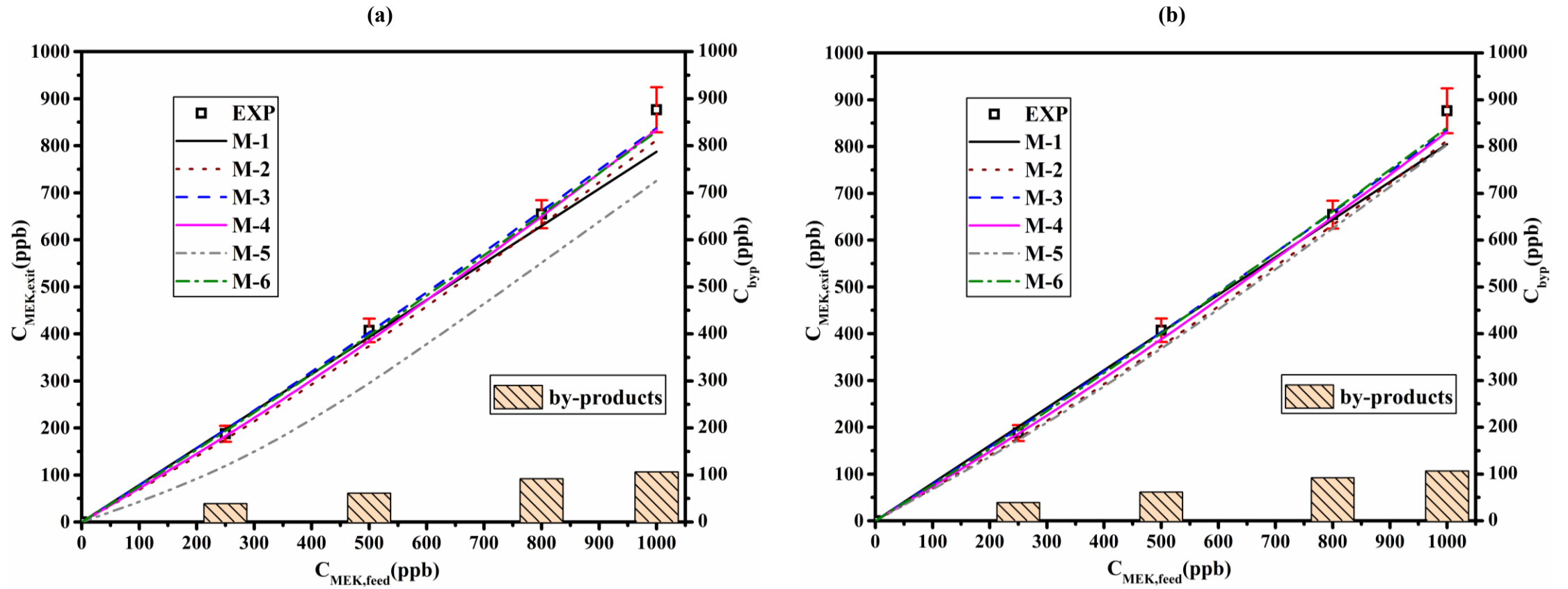
Fig. 5.5. Effect of MEK inlet concentration [$C_{MEK,feed}$] on the PCO degradation ($C_{MEK,exit}$ at steady state conditions) with different kinetic rate expressions (models M-1 to M-6) using (a) Plug-flow model; (b) dispersion model; u=0.05 m/s; RH_{Feed}=50%; I_{ave}=7 W/m^2 (Run 9-12).
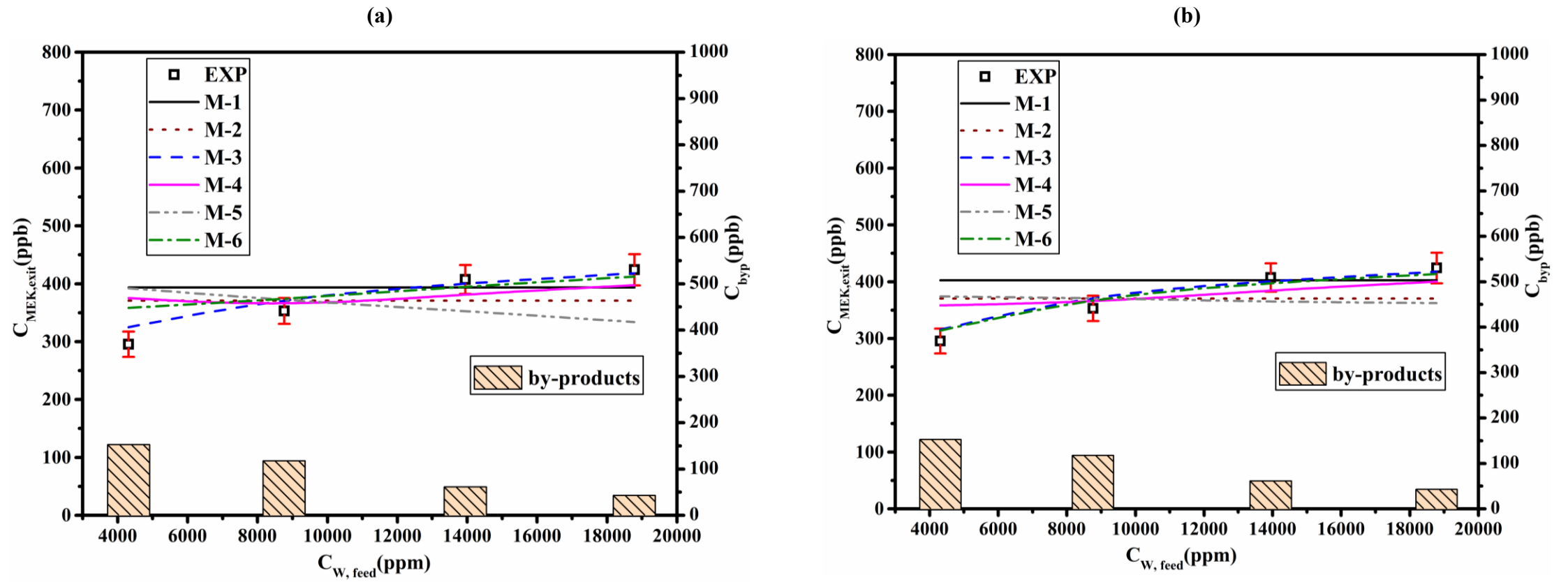
Fig. 5.6. Effect of relative humidity [RH_{Feed}] on PCO degradation of MEK ($C_{MEK,exit}$ at steady state conditions) with different kinetic rate expressions (models M-1 to M-6) using (a) Plug-flow model; (b) dispersion model; $C_{MEK,feed}$=500 ppb; u=0.05 m/s; I_{ave}=7 W/m² (Run 4, 10, 13-14).
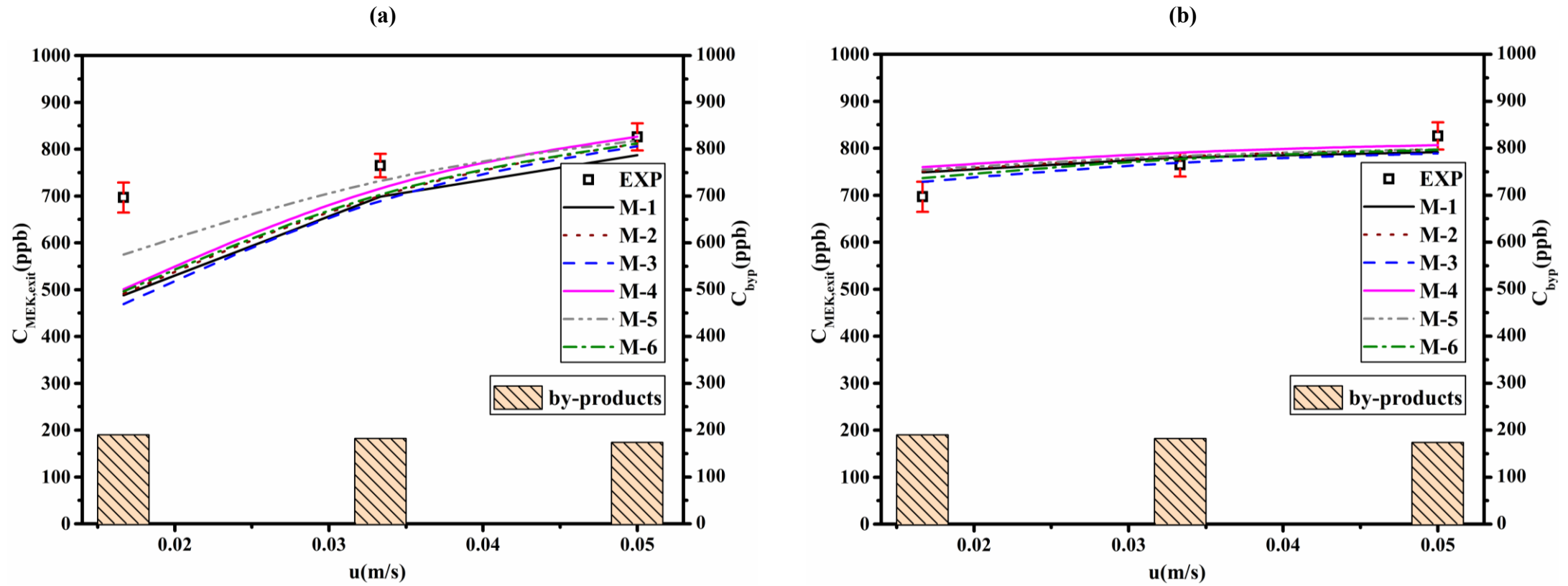
Fig. 5.7. Effect of velocity [u] on PCO degradation of MEK ($C_{MEK,exit}$ at steady state conditions) with different kinetic rate expressions (models M-1 to M-6) using (a) Plug-flow model; (b) dispersion model; $C_{MEK,feed}$=1000 ppb; RH_{Feed}=33%; I_{ave}=7 W/m^2 (Run 8, 17-18).
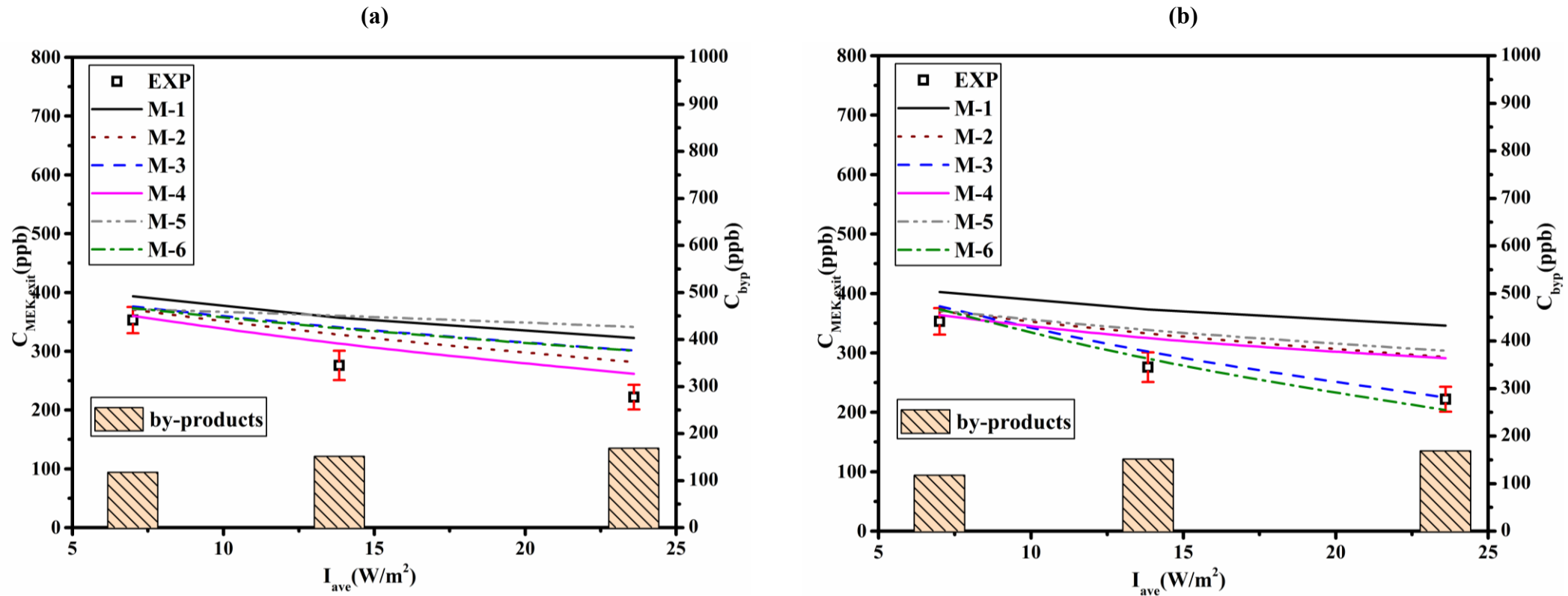
Fig. 5.8. Effect of Light intensity [I] on PCO degradation of MEK ($C_{MEK,exit}$ at steady state conditions) with different kinetic rate expressions (models M-1 to M-6) using (a) Plug-flow model; (b) dispersion model; $C_{MEK,feed}$=500 ppb; RH_{Feed}=33%; u=0.05 m/s (Run 4, 15-16).

5.2.4. Evaluation of mass transfer effects

Fig. 5.9-a demonstrates the effect of air velocity on the mass transfer coefficient in the PCO reactor using Eq. (4.18) (a value of 109×10^3 m^2/m^3 making use of Eq.(4.17) for the geometric surface area is applied according to parameters reported in Table 3.1). This figure indicates that higher velocity increases the mass transfer coefficient, leading to the increment in the mass transfer rate. The relationship between the air velocity and $\Delta C_A/C_{Ab}$, (Eq. (5.8) to Eq.(5.10)), for various removal efficiencies using rate expression *M-3* for plug flow model and dispersion model are presented in Fig. 5.9-b and Fig. 5.9-c, respectively. Since mass transfer plays a more significant role at a lower concentration, the inlet concentration of 250 ppb was chosen for simulation. Both figures show that the concentration gradient criteria increases when removal efficiency increases at a fixed air velocity. Consequently, the mass transfer effect becomes more important. However, increasing air velocity at a constant conversion decreases this criterion (due to higher external mass transfer coefficient). It is observed from the simulation that for all cases, $\Delta C_A/C_{Ab}$ <0.1. This demonstrates that the mass transfer limitation effect in the process is not important and that the rate-limiting step is the PCO reaction. Hence, the mass transfer resistance can be ignored, and the surface concentration is considered equivalent to the gaseous concentration.

(a)

(b)
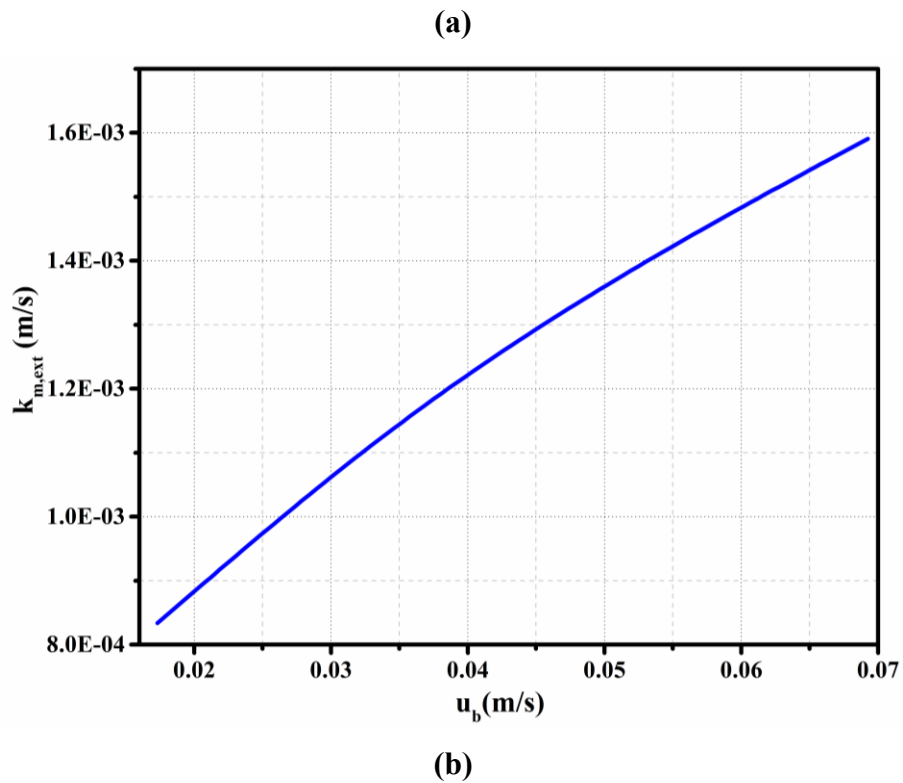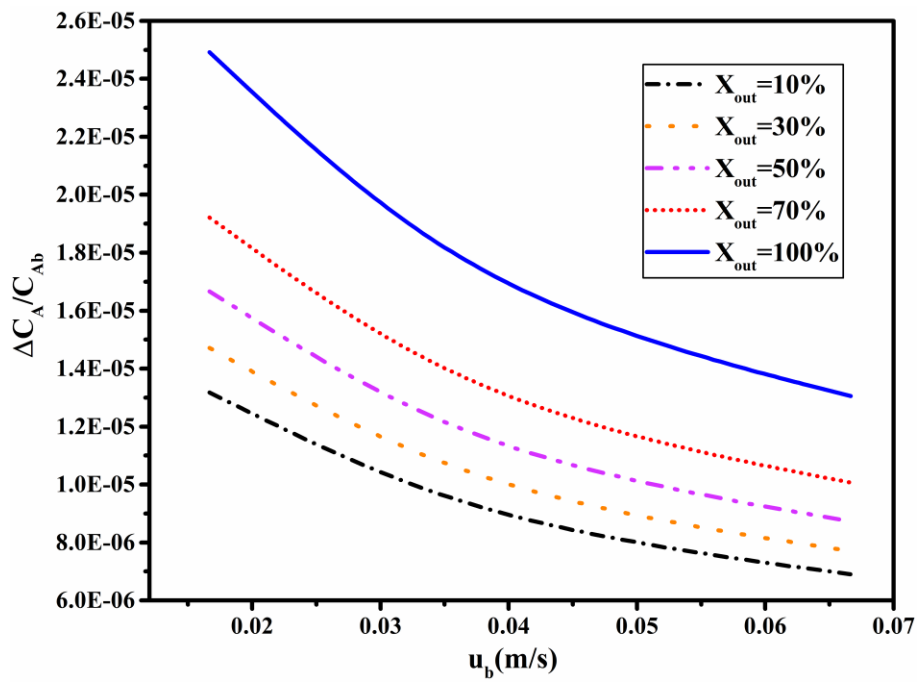
(c)
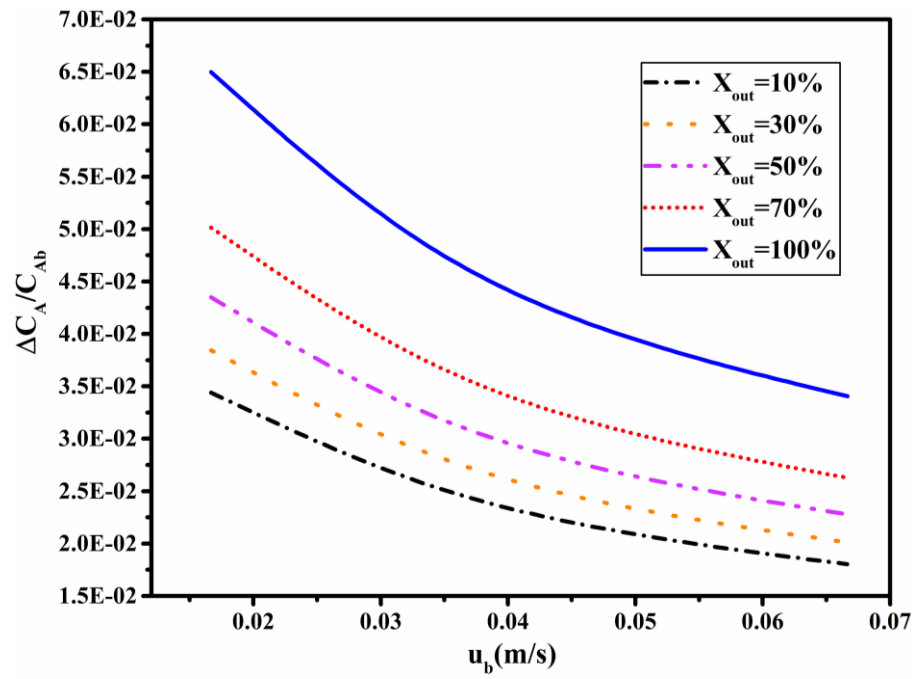
Fig. 5.9. Influence of air velocity on (a) mass transfer coefficient; and (b) concentration gradient criteria in the plug flow model; (c) concentration gradient criteria in the dispersion model; $C_{A,in}$=250 ppb, RH=17%.

6. Modeling of MEK in PCO: Systematic Model Development and Validation

One of the major challenges in studying the potential of UV-PCO reactors for commercial applications is finding a reliable tool to assist in designing, scaling up, and optimization. Most of the developed models in the literature were validated in a small-scale UV-PCO reactor and cannot be applied in an actual application (larger scale). Since the PCO performance depends on many factors (operating conditions, experimental set-up, and kinetic parameters), the scaling-up of this reactor is challenging. Limited work has been conducted to identify the critical parameters influencing PCO performance. For mass transfer limited process, affecting parameters such as inter-phase mass transfer, velocity, and dispersion/diffusion can be critical. For the reaction rate limited process, critical parameters can be the catalyst surface area, inlet concentration, relative humidity, and light intensity. Therefore, there is a strong need for a detailed model to consider all these physical and chemical phenomena. This chapter presents a comprehensive validation process at three different levels; inter-model comparison; validation with experimental data, which were collected in small-scale, as well as large-scale set-ups. in the inter-model comparison, the prediction made by the model was compared with that of two other existing models. Finally, this chapter presents a dimensionless form of the proposed model and investigates the impact of non-dimensional parameters on reactor efficiency in order to find the controlling steps in the process.

6.1. Methodology

6.1.1. Mathematical model

The developed model in chapter 3, including **M-3** L-H reaction rate model, the LSSE model for irradiance distribution on the photocatalyst surface and the Beer-lambert model for incident light absorption within the filter, were used for inter-model comparison and model validation in both bench and pilot scales. This model was then used for dimensionless model analysis in the PCO (section 6.1.2).

6.1.2. Dimensionless model

The developed model (Eq.(3.1) and Eq.(3.2)) was non-dimensionalized to generalize the theoretical and experimental investigation results and facilitate the UV-PCO reactor scale-up. This was done using the following expressions:

$$\bar{C}_i = \frac{C_i}{C_{i,0}} \quad , \quad \bar{C}_{si} = \frac{C_{si}}{C_{i,0}} \quad , \quad \bar{C}_{sw} = \frac{C_{sw}}{C_{w,0}} \quad , \quad \bar{C}_{by,i} = \frac{C_{by,i}}{C_{byp,s}} \quad , \quad \bar{t} = \frac{u_b t}{L_f} \quad , \quad \bar{x} = \frac{x}{L_f} \quad , \quad Pe = \frac{u_b L_f}{D_{ax}} \quad , \quad St = \frac{k_m a_s L_f}{u_b}$$

$$Da = \frac{k.I^{0.5}.L_f}{u_b C_{i,0}} \quad , \quad \alpha = K_i C_{i,0} \quad , \quad \beta = K_w C_{w,0} \quad , \quad \gamma_i = K_{byp,i} C_{byp,s}$$

This leads to the following dimensionless expressions:

$$\frac{\partial \bar{C}_i}{\partial \bar{t}} = \frac{1}{Pe} \frac{\partial^2 \bar{C}_i}{\partial \bar{x}^2} - \frac{\partial \bar{C}_i}{\partial \bar{x}} - \frac{1-\varepsilon}{\varepsilon} St (\bar{C}_i - \bar{C}_{si}) \qquad (6.1)$$

$$\frac{\partial \bar{C}_{si}}{\partial \bar{t}} = St (\bar{C}_i - \bar{C}_{si}) - Da \frac{\alpha \bar{C}_{si}}{1 + \alpha \bar{C}_{si} + \beta \bar{C}_{sw} + \sum_i \gamma_i C_{byp,i}} \qquad (6.2)$$

with the initial and boundary conditions of:

$$\bar{C}_i = \bar{C}_{si} = 0 \qquad\qquad at\ \bar{t} = 0 \qquad\qquad (6.3)$$

$$\bar{C}_i - \frac{1}{Pe}\frac{\partial \bar{C}_i}{\partial \bar{x}} = 1 \qquad\qquad at\ \bar{x} = 0 \qquad\qquad (6.4)$$

$$\frac{\partial \bar{C}_i}{\partial \bar{x}} = 0 \qquad\qquad at\ \bar{x} = 1 \qquad\qquad (6.5)$$

6.1.3. Experimental investigation

6.1.3.1. Experimental set-up

Two different UV-PCO reactors scales (bench and pilot) have been studied in this chapter. The detail of bench-scale reactor was explained in chapter 3. The pilot-scale reactor (Fig.6.1) was made of four 3.6 m parallel aluminum ducts with 0.31m×0.31m inner cross-sectional area. Each duct had an adjustable fan to control the airflow rate. The UV-PCO reactor has two 0.31m×0.31m PCO filters, including two UV lamps (Ster-L-Ray, Atlantic Ultraviolet Inc.). Because the experimental set-up is an open duct system, laboratory air was used as a carrier gas, and three humidifiers (using deionized water) were placed near the entrance of the set-up to provide the required level of relative humidity. The inlet air was monitored for humidity and temperature by a sensor (HMT 100, Vaisala). The airflow rate over the photocatalyst media in this set-up was between 0.034 to 0.082 m^3/s. UV lamps provided an average of 50 W/m^2 light intensity (lamp walls intensity (I_w) was 270 W/m^2).
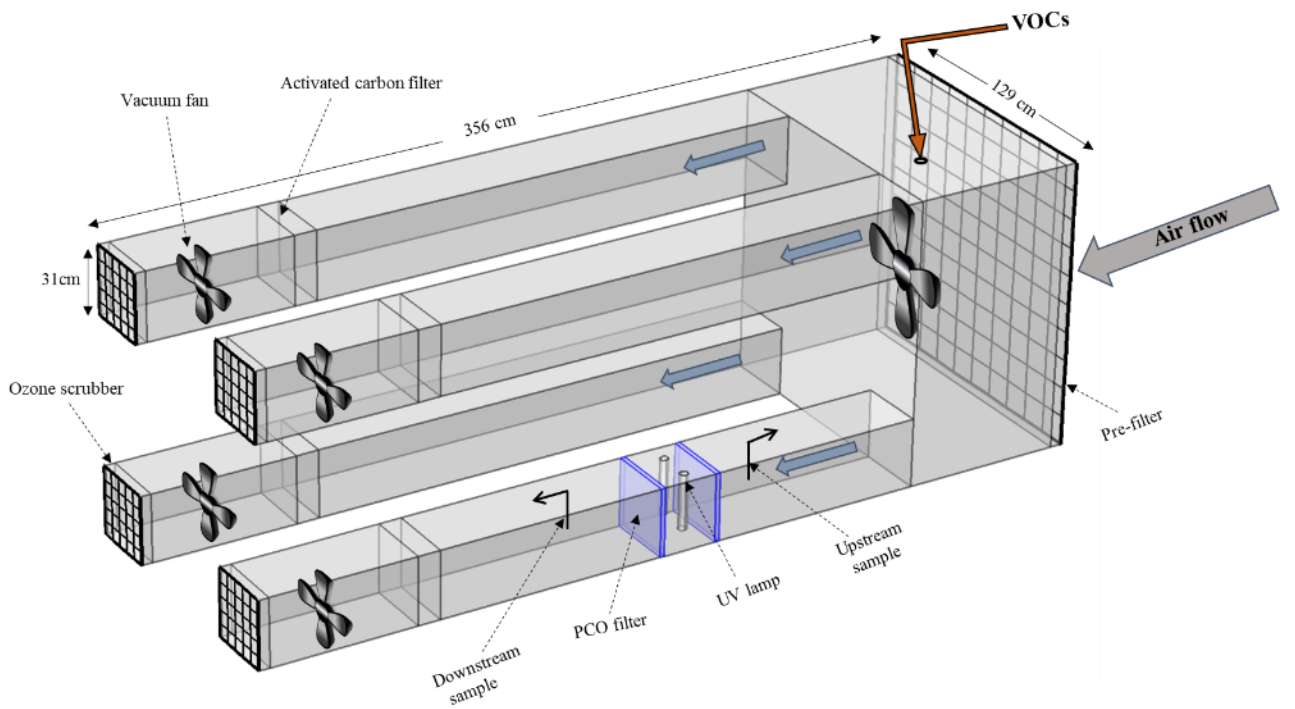
Fig.6.1: Schematic diagram of the pilot-scale reactor.

6.1.3.2. PCO reaction test

Two kinds of PCO tests were conducted; time-dependent and steady-state. The time-dependent PCO test was performed in the bench-scale reactor to compare the prediction of the proposed model with the predictions made by two existing models (inter-model comparison). The steady-state reaction test was used to validate the proposed model for both bench-scale and pilot-scale reactors under various operating conditions.

6.1.3.3. Time-dependent PCO experiment

A time-dependent experiment was performed in the bench-scale reactor with a PCO filter (TiO$_2$/SFF) using two low-pressure mercury UV lamps (Philips, TUV PL-S 5W) with a dominant wavelength of 254 nm on each side of the filter. First, the UV lamps were turned on and, then, MEK at concentration of 800 ppb was automatically injected using a syringe pump (KD Scientific, Model KDS-210, USA) into the compressed air (RH = 0%). A mass flow controller (MFC; OMEGA, FMA5542A) adjusted the airflow rate at 20 L/min (1.2 m^3/hr) while the relative humidity was kept at 50±1%. To find MEK breakthrough point, a PID detector (ppb3000 RAE, USA) was used to measure MEK concentrations at the reactor downstream. The experiment was continued until the PCO reaction reached the steady-state condition.

6.1.3.4. Steady-state PCO experiment

The steady-state reaction test was conducted using TiO$_2$/SFF filter in both bench-scale and pilot-scale reactors. The PCO experiment in the pilot-scale reactor was carried out by Lee et al. [214] and the data provided from them for the model validation in this study. A layer of PCO filter and a UV lamp were used in the bench-scale experiment, while in the pilot-scale (Fig.6.1), two layers of the filter and two UV lamps (between two layers) were used. The steady-state experiments in the bench-scale were carried out in two steps — lamps turned off (preliminary dark adsorption step) and then turned on (photocatalytic reaction step). For each concentration (from 100 to 1000 ppb), experiments were continued until filters were completely saturated with MEK, and then by turning on the UV lamps, the PCO reaction was initiated. In the pilot-scale reactor, Lee et al.[214] turned on the UV lamp after 10 min injection and started taking samples 5 min after that. The upstream and downstream samples were taken at the same time. PCO experiment in bench and pilot reactors was carried out at temperatures of 20±0.5 °C and 21±1 °C, respectively.

6.1.3.5. Residence time distribution (RTD) experiment

RTD test was performed to characterize the airflow pattern in the PCO reactor by injecting MEK tracers into the inlet airflow. The RTD experiment with MEK in the bench-scale reactor for velocities ranging from 0.015 to 0.1 m/s (equivalent to 110< Re$_D$ <1000) is presented in chapter 4 [183]. This study also reports the RTD test in the pilot-scale reactor to determine the axial dispersion coefficient for velocities between 0.35 to 0.85 m/s (6900< Re$_D$ <17200). In this regard, MEK tracer was injected instantly into the inflow air stream and, then, the outlet concentration was measured, in time for various airflow rates, using a PID detector.

6.2. Results and discussion

6.2.1. Model Validation

6.2.1.1. Model parameters determination

Two models were used to simulate the PCO reactor; the dispersion model (Eq. (3.1) to Eq.(3.5)) and the ideal plug flow model (no dispersion [215]). The kinetic parameters of MEK using **M-3** L-H reaction rate (Eq.(3.15)) for ideal plug flow and dispersion models were evaluated in the bench-scale reactor (see section 5.2.3).

(a)

(b)
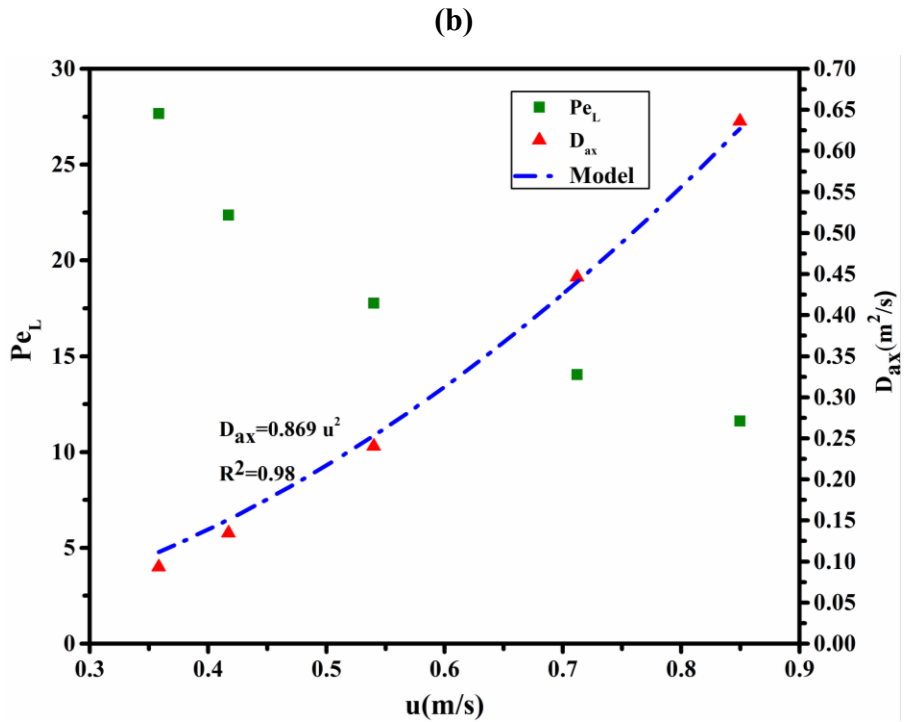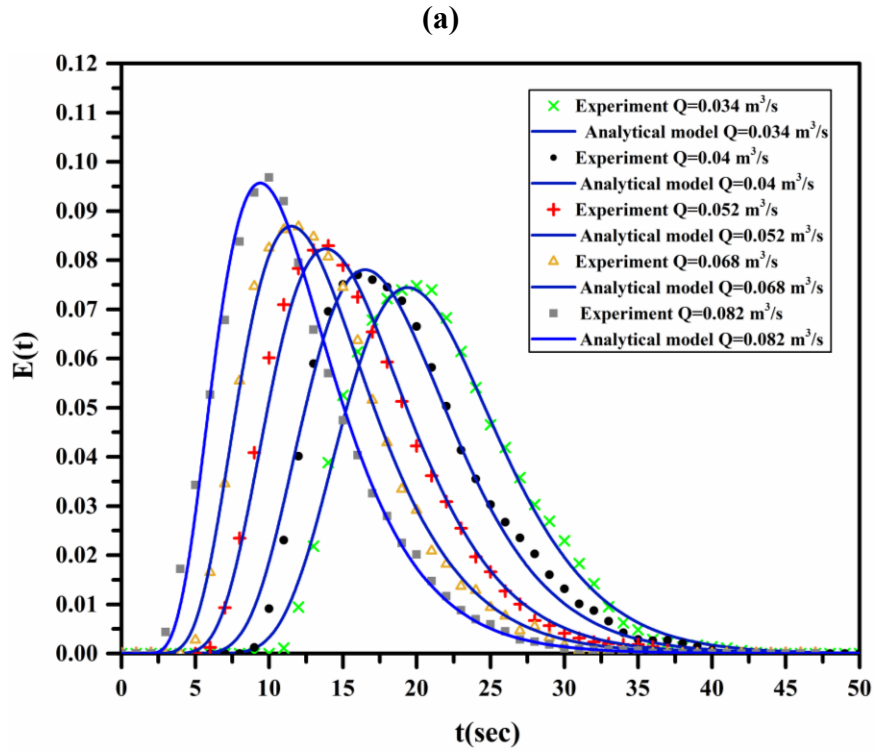
Fig. 6.2. (a) the residence time distribution E(t) of MEK at various flow rates, (b) the dependence of the Peclet number and axial dispersion values on the superficial velocity

Fig. 6.2-a demonstrates the RTD analysis of MEK for the pilot-scale reactor for the flow rates ranging from 0.034 to 0.082 m^3/s. The higher airflow rate, the higher the peak value and the shorter the time after which the peak was observed. The Peclet values and axial dispersion coefficients were plotted versus air velocities in Fig. 6.2-b. The low values of Pe_L number (less than 100 [186]) indicate that the PCO reactor deviates from an ideal plug-flow reactor even at higher airflow rates. A quadratic function, Eq. (6.6), was considered to correlate the axial dispersion coefficient with the superficial velocity:

$$D_{ax} = 0.869 \, u^2 \qquad 6900 < Re_D < 17200 \qquad (6.6)$$

6.2.1.2. Inter-model comparison

The simulation result of the proposed model was compared with the prediction made by two existing models. Model I [145, 150] rests upon an ideal plug flow model in which the model

assumed the presence of a uniform flow without diffusion/dispersion effect. Model II, by Zhong and Haghighat [81], involves the ideal plug flow assumption with the molecular diffusion effect of challenge compound in gas. Table 6.1 summarizes these models and their boundary conditions.

Table 6.1: Models used for inter-model comparison

	Governing equation	Ref.
Model I	$\frac{dC_i}{dt} = -u_b \frac{dC_i}{dx} - k_m a(C_i - C_{is})$ $\frac{dC_{is}}{dt} = k_m a(C_i - C_{is}) - r_i$ I.C: $C_i = C_{si} = 0$ at t=0 B.C: $C_i = C_{i,0}$ at x=0	[145, 150]
Model II	$\frac{dC_i}{dt} = \frac{\varepsilon}{\tau} D_m \frac{d^2 C_i}{dx^2} - u_b \frac{dC_i}{dx} - k_m a(C_i - C_{is})$ $\frac{dC_{is}}{dt} = k_m a(C_i - C_{is}) - r_i$ I.C: $C_i = C_{si} = 0$ at t=0 B.C: $C_i = C_{i,0}$ at x=0 $\frac{dC_i}{dx} = 0$ at x=L_f	[81]
Model III	$\frac{dC_i}{dt} = D_{ax} \frac{d^2 C_i}{dx^2} - u_b \frac{dC_i}{dx} - \frac{(1-\varepsilon)}{\varepsilon} k_m a(C_i - C_{is})$ $\frac{dC_{is}}{dt} = k_m a(C_i - C_{is}) - r_i$ I.C: $C_i = C_{si} = 0$ at t=0 B.C: $u_b C_{i,0} = u_b C_i - D_{ax} \frac{dC_i}{dx}$ at x=0 $\frac{dC_i}{dx} = 0$ at x=L_f	Present study

To compare the simulation results of the developed model (Model III) with the predictions made by model I and II, the experimental data from the time-dependent study in bench-scale was employed. Fig.6.3 compares the simulation result of these three models with experimental data with inlet MEK concentration of 800 ppb (the input parameters are available in Table 6.2). The figure shows that Models I and II have less accuracy than Model III at the steady-state condition. As Model I (ideal plug flow model) developed based on no dispersion/diffusion mass transfer effect, it underestimates the outlet concentration. Model II was simulated by considering the kinetic parameters of the ideal plug flow model as well as the molecular diffusion effect. Diffusion in the reactor causes fresh MEK molecules to mix with converted ones (by-products) and, consequently, the challenge compound concentration decreases (lowers the reaction rate). This resulted in a reduction of PCO conversion (higher outlet concentration) when kinetic parameters of the plug flow model were used.

Model III gives a more accurate fit than the others, especially at the initial stage (before reaching the steady-state condition). The figure shows a higher discrepancy between experimental results and the other two models. At the initial stage, the adsorption process or mass transfer has an

important role in MEK degradation, and Model III, due to more adequate boundary conditions at the inlet and more accurate expression for dispersion term, resulted in a better prediction.

The good agreement between the experimental data and the prediction made by model (III) demonstrates that this model can predict more accurately UV-PCO reactor efficiency trends as a function of time.

Table 6.2: Input parameters for Inter-model Comparision

Parameter	Unit	Value	Model I	Model II	Model III
C_0	ppb	800	✓	✓	✓
t	min	50	✓	✓	✓
L_f	cm	1.2	✓	✓	✓
D_{ax}	m²/s	0.005	-	-	✓
ε	-	0.96	✓	✓	✓
τ	-	3	-	✓	-
μ	μm^{-1}	0.1053	✓	✓	✓
Q	L/min	20	✓	✓	✓
d	μm	10	✓	✓	✓
δ_f	μm	1	✓	✓	✓
D_m	m²/s	9.8×10^{-6}	-	✓	-
ϑ	m²/s	1.8×10^{-5}	✓	✓	✓
k_m	m/s	0.0012	✓	✓	✓
a_s	m²/ m³	109×10^3	✓	✓	✓
I_w	W/m²	65	✓	✓	✓
D_{lamp}	cm	1.4	✓	✓	✓
$X_{distance}$	cm	3	✓	✓	✓
y_{lamp}	cm	2.7	✓	✓	✓
Lp	cm	6.5	✓	✓	✓
I_{ave}	W/m²	90	✓	✓	✓
RH	%	50	✓	✓	✓
k_{disp}	ppm s⁻¹ W⁻¹ m²	14.28×10^3	-	-	✓
$K_{MEK,disp}$	ppm⁻¹	7.5	-	-	✓
$K_{w,disp}$	ppm⁻¹	8.6×10^{-4}	-	-	✓
$K_{byp,disp}$	ppm⁻¹	14	-	-	✓
k_{plug}	ppm s⁻¹ W⁻¹ m²	8.33	✓	✓	-
$K_{MEK,plug}$	ppm⁻¹	7.5	✓	✓	-
$K_{w,plug}$	ppm⁻¹	8.6×10^{-4}	✓	✓	-
$K_{byp,plug}$	ppm⁻¹	13.8	✓	✓	-
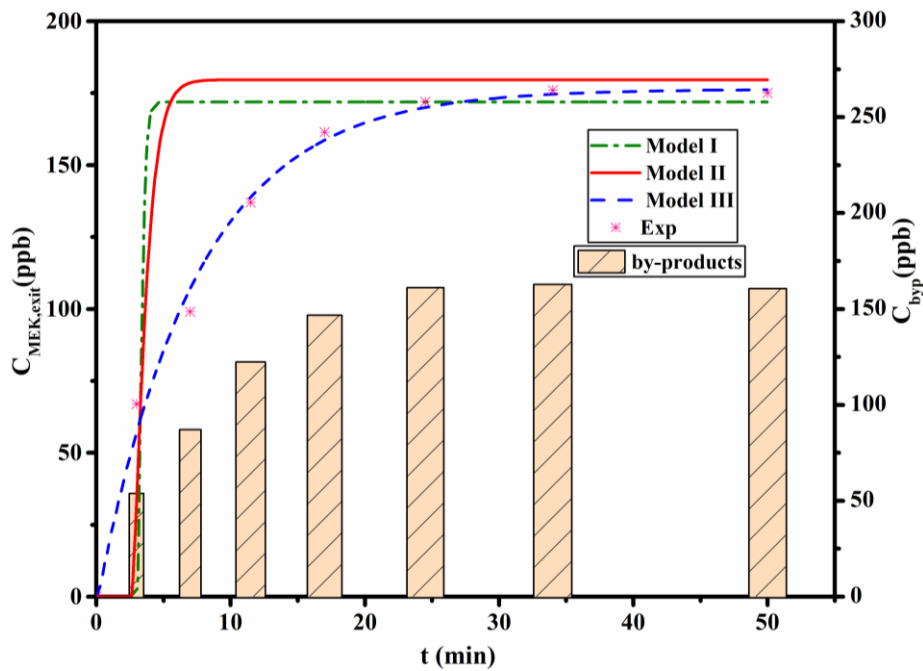
Fig.6.3: Comparison the results of three different model for prediction of MEK outlet concentration at inlet concertation of 800 ppb (u=0.034 m/s, I_{ave}=90 W/m^2).

6.2.1.3. Modeling of bench and pilot-scale reactors at steady-state

Fig.6.4 shows the radiation intensity distribution on the photocatalyst surface for both bench-scale and pilot-scale as predicted by the LSSE model. The figures show that the irradiance distribution in a bench-scale reactor is more uniform than the pilot-scale. The reason is that the UV lamp in the bench scale was placed at a longer distance from the PCO filter. The experimental validation of the LSSE model ($R^2 \geq 0.94$) indicated that the model prediction is close to the experimental data. Fig.6.5 illustrates the dimensionless light absorption rate ($\bar{I} = I/I_{ave}$) within the PCO filter. For the overall effective TiO$_2$ layer thickness of 45 μm (calculated using Eq.(3.11) for one media), the incident light is totally absorbed by TiO$_2$. However, with two PCO filters, half of the filter does not absorb any light intensity (see Fig.6.5), which shows a thicker media has no positive effect on energy absorption. As for the mass of photocatalyst (or thickness of media), Fig.6.6 demonstrates that removal efficiency decreases with decreasing photocatalyst mass and also media is saturated faster.

Fig.6.7 compares the removal efficiency predicted by Model III with the measured catalyst removal efficiency under UV illumination for both bench-scale and pilot-scale. It shows a good agreement between the model prediction and the experimental data for various operating conditions, which is confirmed by Fig.6.8. The linear regression displays the slopes of unity with overall R^2 of 0.98 for experimental measurements versus model predictions.

The result shows that as the inlet concentration, relative humidity, and velocity increase, the removal efficiency decreases in both reactors. Increasing the inlet concentration enhances the number of adsorbed molecules on the catalyst surface and subsequent reaction rate. This causes the number of active sites of catalyst to be reduced, causing MEK molecules to leave the reactor without reaction. Thus, removal efficiency declines. Additionally, introducing excessive humidity also leads to the reduction in catalyst active sites and, consequently, decreases in the reaction rate and removal efficiency. As the velocity increases, the residence time of MEK molecules inside the reactor decreases, which results in a reduction in the adsorption of the pollutant and lower conversion.

In the case of by-products, as challenge compound concentration and residence time increases, by-products generation growths. Nevertheless, with increasing the relative humidity, their generations reduce. This indicates that at higher concentration and lower velocity, by-products have a higher inhibitive effect on the adsorption of challenge compound and, consequently, on the PCO reaction rate.

(a)

(b)
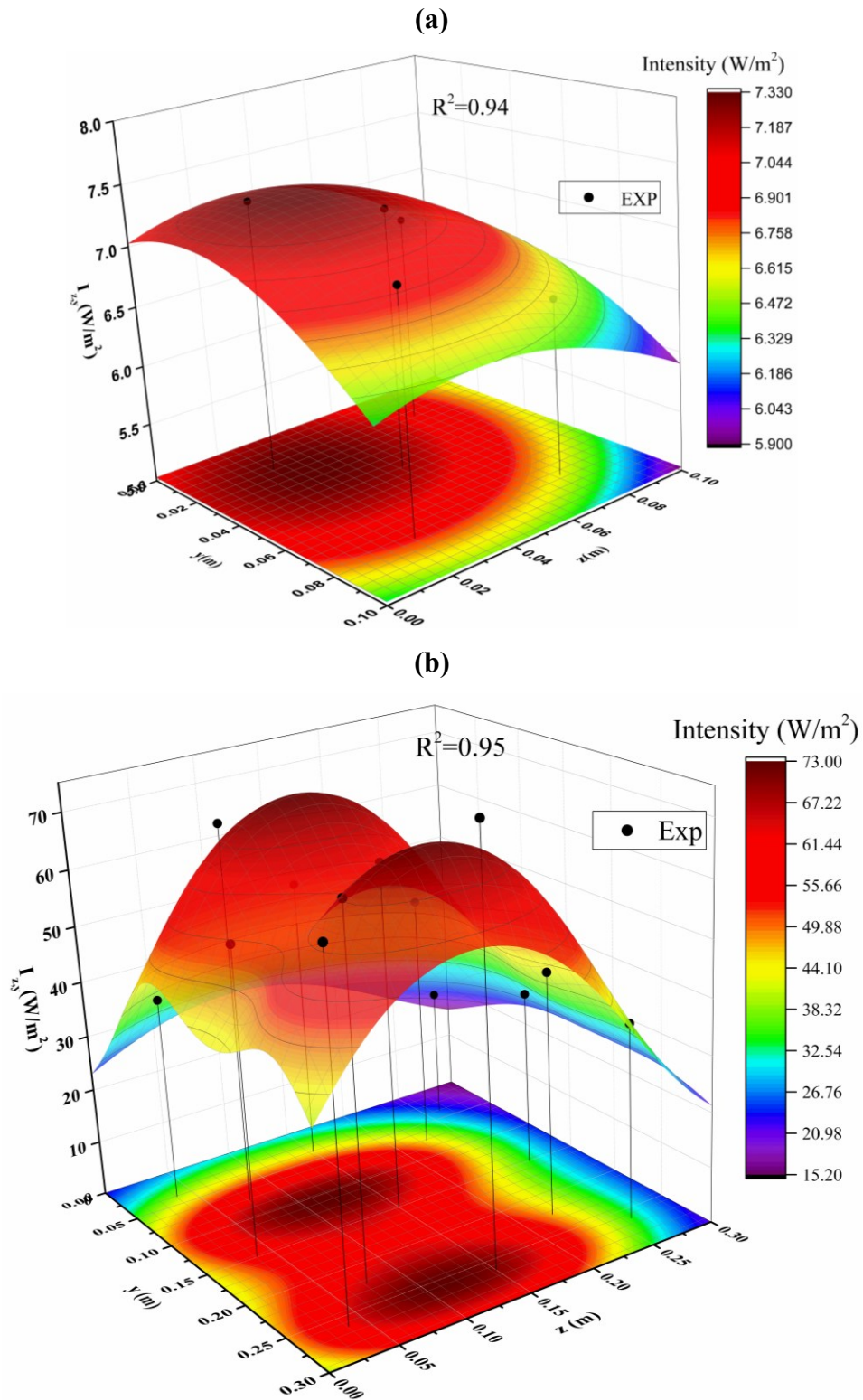
Fig.6.4: Distribution of radiation intensity on the surface of the PCO filter for (a) bench-scale (b) pilot reactor.
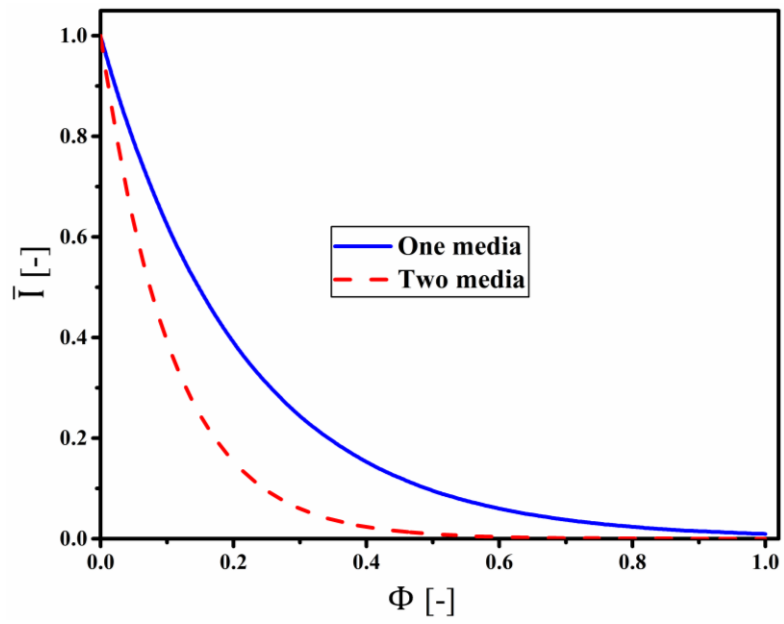
Fig.6.5: Dimensionless light intensity versus overall effective photocatalytic TiO_2 layer thickness.
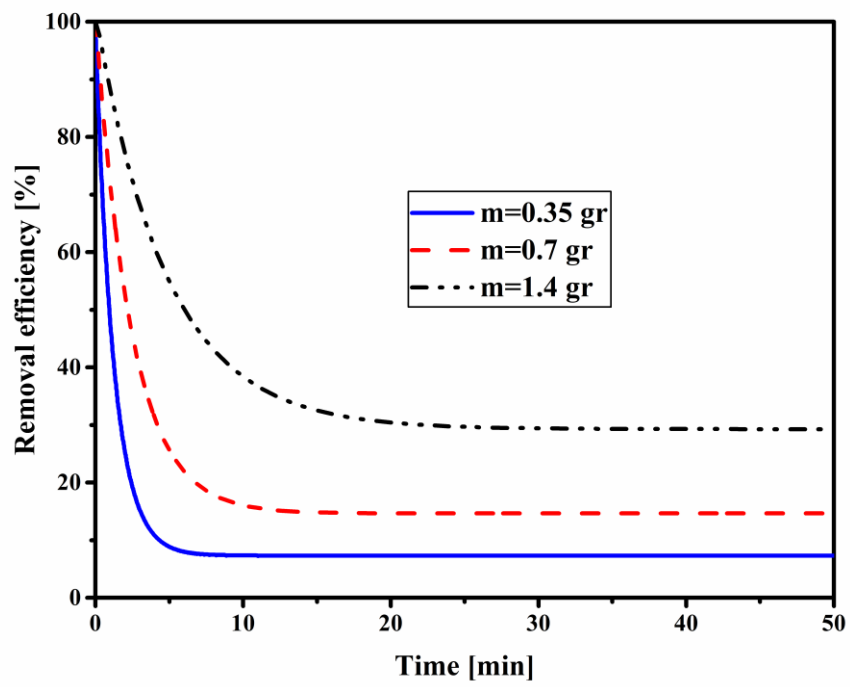
Fig.6.6: Effect of the mass of photocatalyst on removal performance.

(a)

(b)
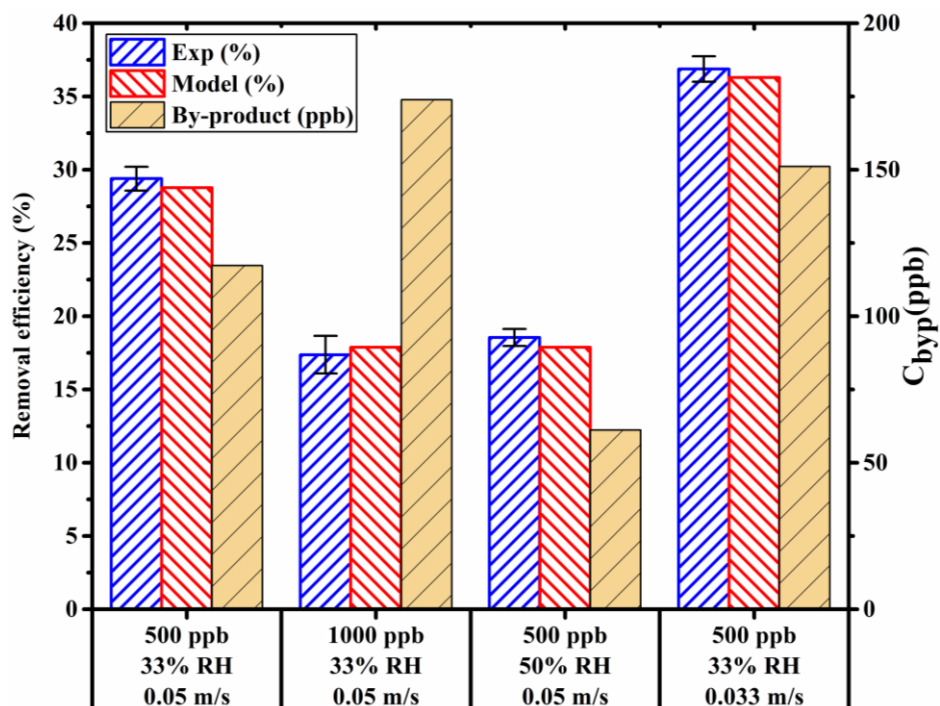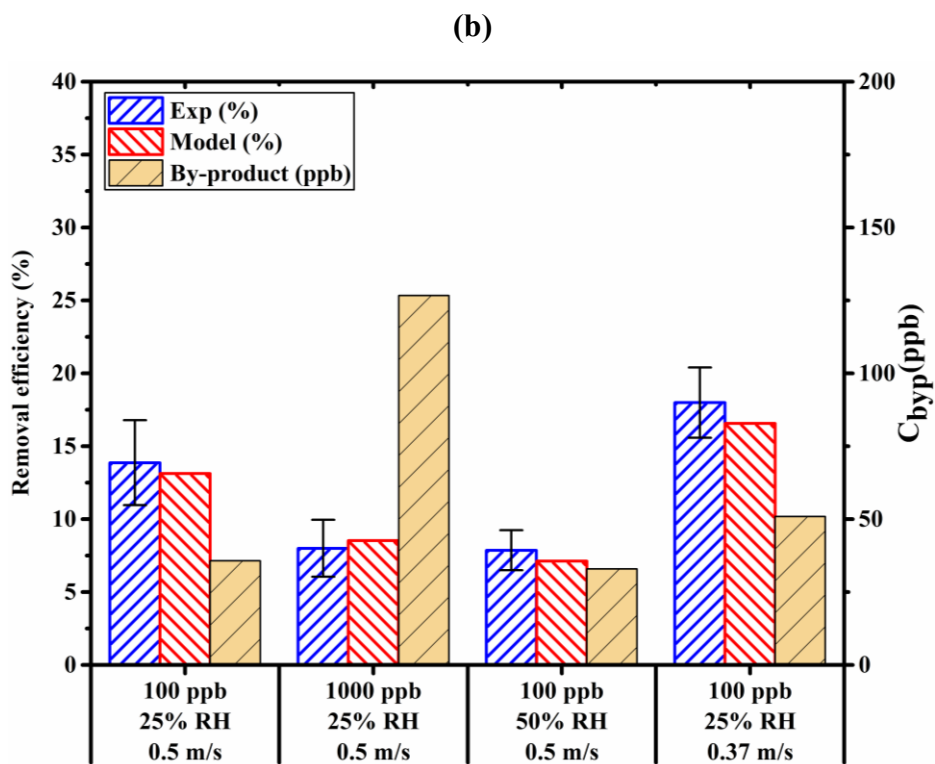
Fig.6.7: Steady-state removal efficiency at different operation conditions in (a) bench-scale (b) pilot reactor (error bars shows the standard deviation of test results)(experimental data was reported in [216]).
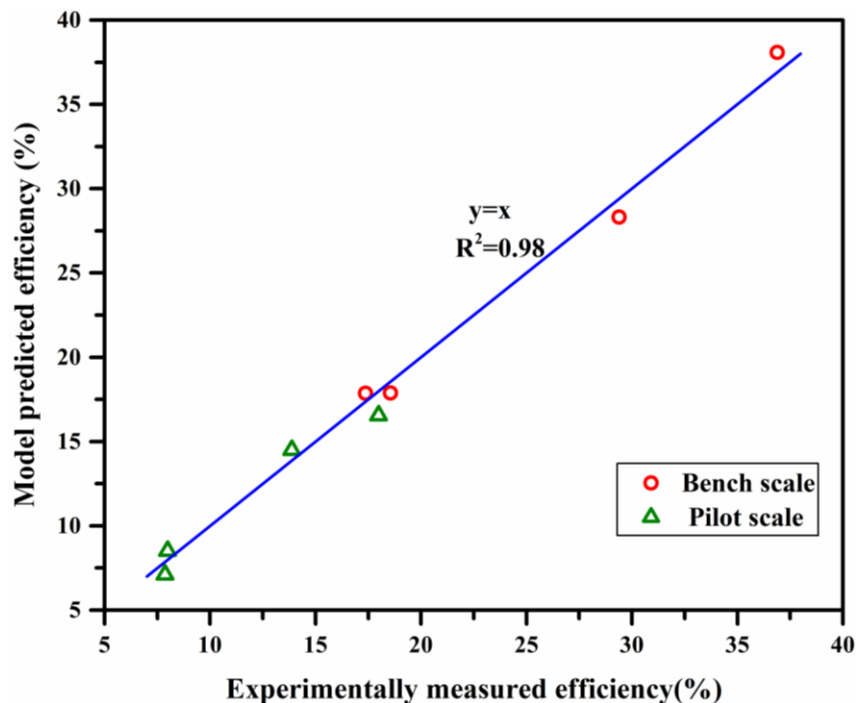
Fig.6.8: Overall model predictions vs. experimental results for bench-scale and pilot reactor

6.2.2. Dimensionless analysis

Fig.6.9 shows the results of dimensionless modeling of the UV-PCO reactor at inlet concentration of 800 ppb in the bench-scale UV-PCO reactor, with two plots: a) removal efficiency versus dimensionless time and b) dimensionless concentration versus length. As Fig.6.9-a shows, at the beginning of the process, removal efficiency (mainly because of adsorption) is at its highest level, due to more available active sites of catalyst for MEK adsorption in the first step and reaction with hydroxyl radical in the second step. While, with time, active sites are occupied by MEK molecules and by-products. Consequently, the removal efficiency by adsorption and PCO reaction decreases after a specific time owing to the reduction in the available catalyst active sites. Finally, an equilibrium state happens between MEK molecule adsorption and surface reaction, resulting in constant conversion (steady-state condition). Increasing Da number improves the removal

efficiency significantly. Enhancing Da means the increase in photocatalytic activity and PCO reaction, which raises the removal performance of the reactor.

(a)

(b)
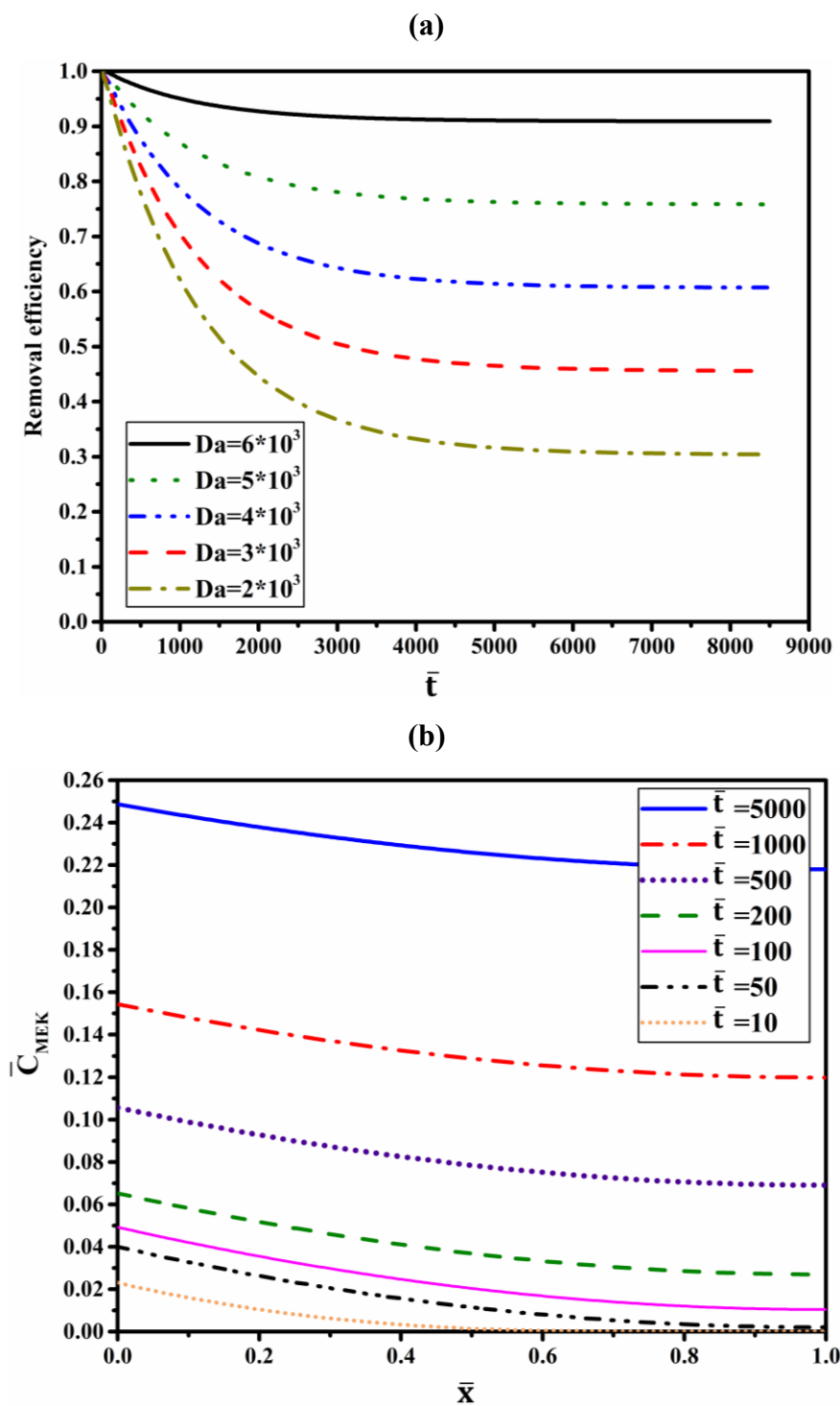
Fig.6.9: a) Removal efficiency of MEK versus dimensionless time at various Da number (Pe=0.16; St=440; α=6; β =12; γ=2.25) and b) Dimensionless concentration versus length (Pe=0.16; St=440; Da=5.13×10^3; α=6; β =12; γ=2.25)

Fig.6.9-b indicates changes in the concentration along the bed at different dimensionless times. It shows the concentration increases as the dimensionless time increases from $\bar{t}$=0 to $\bar{t}$=5000. This occurs due to the reduction of catalyst active sites, which results in a drop in the reaction rate, and causes more MEK molecules leaves the reactor without reaction. Accordingly, the unreacted concentration of MEK in the reactor increases.

6.2.2.1. Sensitivity analysis

Sensitivity analysis provides a systematic framework to study the accuracy and robustness of the developed mathematical models. It can also lead to a systematic search for selecting optimal operating conditions for maximizing reactor productivity. Since Pe and St are the mass transfer indicators in the gas and catalyst phases, respectively, and Da is the removal rate indicator in the

PCO reactor, these three parameters are chosen for the sensitivity analysis. In this section, a sensitivity analysis examines process behavior by varying dimensionless parameters representing operating conditions associated with bench-scale to full-scale set-ups (i.e., flow rate of 0.00017 to 2.36 m^3/s).

6.2.2.1.1. Effect of Peclet number

Fig.6.10-a shows the simulated result of steady-state removal efficiency as a function of the Peclet number (Pe). Theoretically, Pe represents the ratio of advective transport of a molecule to diffusion/dispersion transport. The removal efficiency increases when Pe increases up to 100. Pe increment in this region (Pe=0.1 to 100) indicates dispersion in the reactor decreases and the reactor closes to plug flow reactor. The removal efficiency appears to become independent of Pe as its value increases beyond 100. This shows that in this region PCO reactor operates as a plug flow reactor. At lower Da number, removal efficiency is less sensitive to Pe number since the reactor is strongly reaction rate limited.

Fig.6.10-a also illustrates Pe impact on the removal efficiency at different Damköhler numbers (Da). Increasing Da to 20000 improves the conversion because of the reaction rate limitation. When Pe=0.1, dispersion is at the highest level; removal efficiency stands on the lowest value at constant Da [81]. For Da=20000, where the reaction rate is very high, the removal efficiency is plateaued at the maximum level (=1) for Pe≥100.

6.2.2.1.2. Effect of Stanton number

The Stanton number (St) describes the external mass transfer rate per advection rate. St can play an important role in UV-PCO reactor performance when mass transfer limits the overall rate of reaction. Its effect on the removal efficiency is shown in Fig.6.10-b. Increasing St elevates removal efficiency to an optimum point. In this region, both external mass transfer and reaction rate have a significant effect on VOC degradation since enough active sites are available for adsorbing VOC molecules. Accordingly, all adsorbed reagents can react on the surface quickly, increasing conversion. After the optimum point, removal efficiency stays constant. The process is limited by the reaction rate, which is slow, while the mass transfer is fast and does not impact conversion at any rate; it is therefore not useful to increase its rate. As Da increases, St plays a major role in MEK removal. This can be attributed to more available catalyst active sites, owing to higher photocatalyst activity, and consequently, the growing tendency for adsorbing MEK molecules, in which external mass transfer plays a key role in UV-PCO reactor conversion.

(a)

(b)
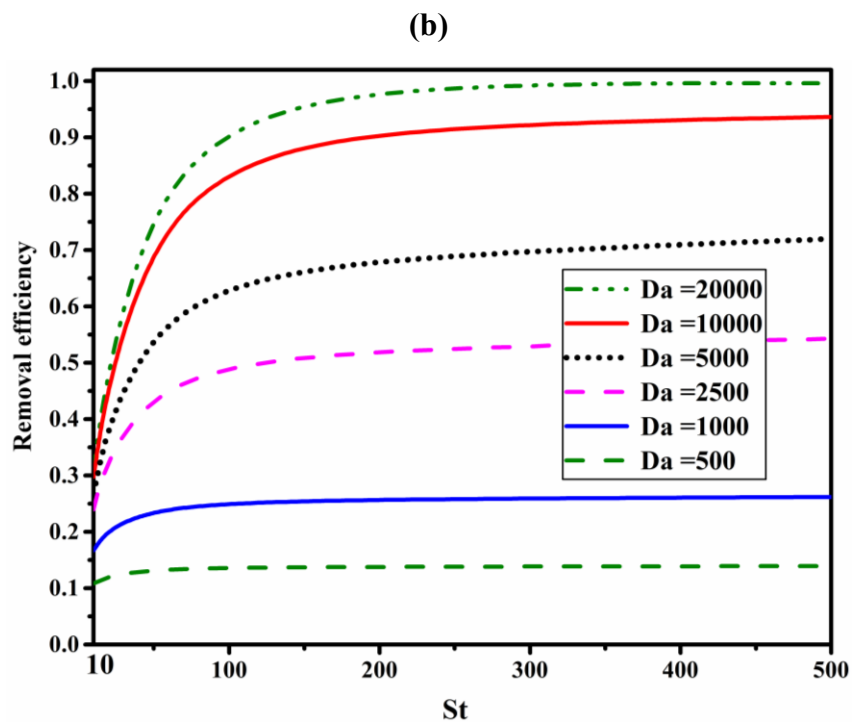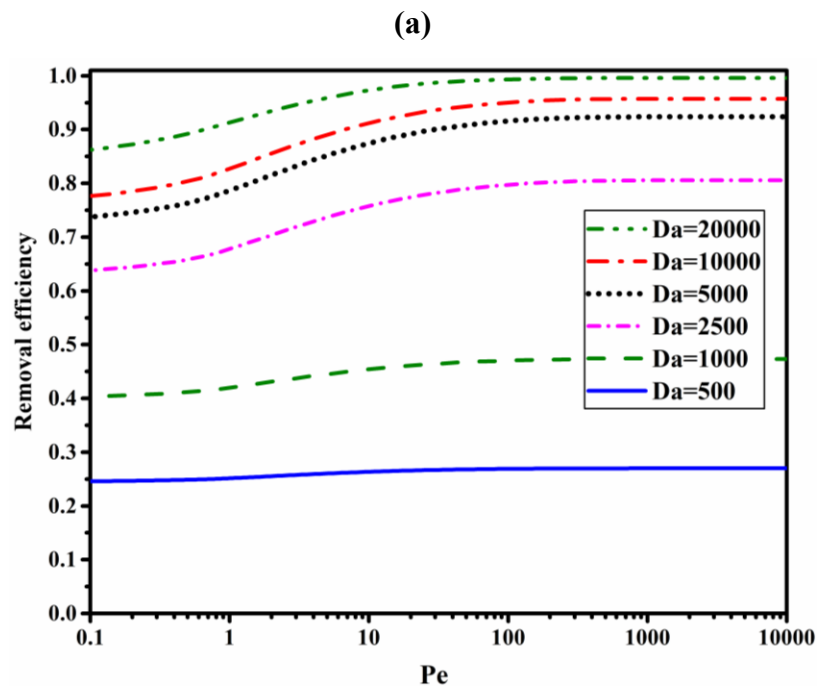
Fig.6.10: Steady-state removal efficiency of MEK versus a) Peclet number (St=440) and b) Stanton number (Pe=10000) at different Damköhler numbers

(a)

(b)
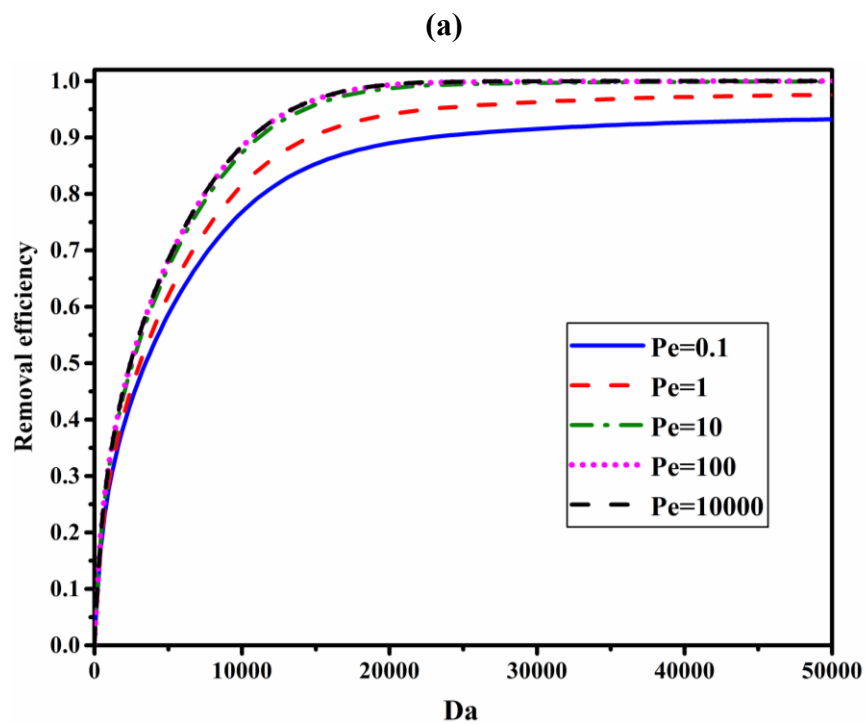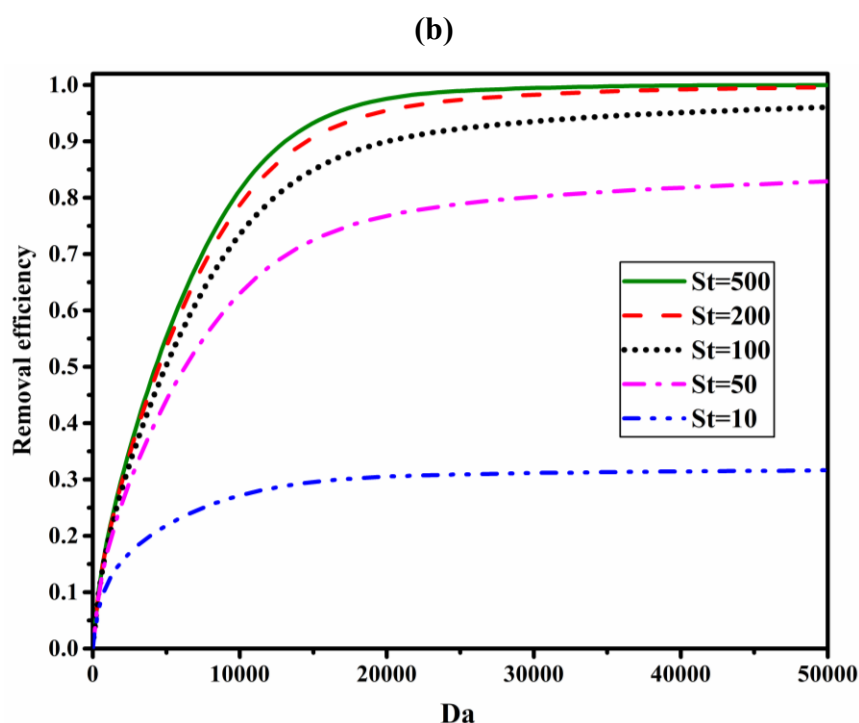
Fig.6.11: Steady-state removal efficiency of MEK versus Damköhler number at different a) Peclet numbers (St=440) and b) Stanton numbers (Pe=10000)

6.2.2.1.3. Effect of Damköhler number

Da represents the ratio of reaction rate to gas advection rate and has a major role in the challenge compound decomposition in the UV-PCO reactor. Fig.6.11-a displays Da impact on MEK removal efficiency at different Pe. This figure demonstrates that increasing Da up to 5000 raises efficiency sharply. For higher than this value, Pe number plays a more significant role such that the maximum MEK degradation (=1) is obtained at higher Pe (≥10) and Da (≥20000). The Da value (Da=5.13×10³) calculated for the experimental condition of bench-scale (see Fig.6.9) indicates that the process is mainly reaction rate limited. To reach a higher conversion rate, both Pe and Da number should be increased. This means, at higher conversions, both reaction rate and advection mass transfer control the process.

Moreover, Fig.6.11-b indicates the significance of mass transfer when Da increases. This means external mass transfer controls the process when St is low. After an optimum value of Da, increasing Da has no more effect on removal efficiency. Therefore, increasing St and Da can lead to maximum removal efficiency. Of note, according to this figure, St in bench-scale is high enough (St=440) to reach maximum efficiency (at higher Da) and the PCO process is not limited by external mass transfer.

To increase the reaction rate and consequently Da number, it can be suggested to improve the surface area, photocatalyst loading and shape of the media. As the surface area is increased, larger number s of active sites and electron-hole pairs on the photocatalyst can be formed. Thus, larger surface area can enhance the photocatalytic activity and PCO reaction. Since the photocatalyst media used in this study is highly porous, another option for improving the PCO efficiency can be increasing the loading of photocatalysts on the fiber media. The shape of the media (plane or pleated) can affect the performance of the PCO reactor[217]. In view of this, pleated media can provide a higher contact time than plane media in the same condition, which can increase the removal performance of PCO.

6.2.3. Practical validation of dimensionless model for scale-up

Overall, the sensitivity analysis using the dimensionless model gave practical advice for scaling up of UV-PCO reactor. The presented analysis using dimensionless parameters in this study covers a wide range of values, which can be used for the design of large-scale PCO reactor (HVAC system) by the information of small-scale reactor. Practical validation of the dimensionless model for the scale-up of this reactor is provided in Fig.6.12. This figure displays the results of the PCO reaction experiment and dimensionless model in bench and pilot-scale at the same operational conditions (u=0.37 m/s, I_{ave} =40 W/m^2, L_f=2 cm, RH=25%, C_{in}=100 ppb). According to sensitivity analysis in the last section, at the same operating conditions, the only affecting dimensionless parameter on the scale-up of UV-PCO reactor is Pe number. By comparing dispersion in bench-scale (see Eq.(4.8)) and pilot-scale (see Eq.(6.6)), Pe number in the pilot-scale is higher than in bench-scale at the same velocity. Fig.6.10-a indicated that removal efficiency at higher Pe should be more than at lower Pe. The result provided in Fig.6.12 also confirmed the bench-scale reactor owing to a lower Pe number has less removal efficiency. However, as it is predicted in Fig.6.10-a, the difference of removal efficiency between bench and pilot scales is less at lower Da numbers (or lower removal efficiencies). In Fig.6.12, both experimental data and model prediction for pilot-scale reactor have around 2% removal efficiency higher than bench scale. This difference becomes more significant as removal efficiency (or Da number) increases. This result verifies that the validated dimensionless model can be used to design and scale up the UV-PCO for the real application. The dimensionless parameters analysis provided in this study can give practical advice, qualitatively and quantitatively, to design the efficient UV-PCO reactor at any scale.
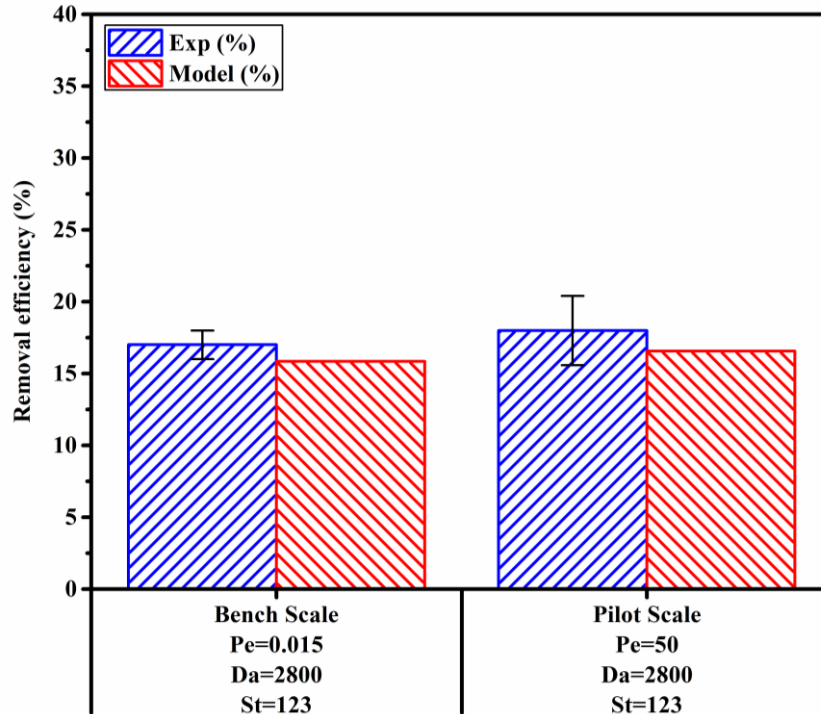
Fig.6.12: Comparison of PCO performance in bench and pilot-scale at the same operational condition using dimensionless model.

7. Reaction pathway and predictive model for generated by-products in PCO reactor

This chapter presents the kinetic modeling of generated by-products for PCO of acetone, MEK and toluene. The primary focus in modeling these compounds in PCO is on the development of an appropriate reaction rate model to describe the generation rate of each by-product in accordance with possible reaction pathways and identified by-products quantitively. In this regard, the methodology described in chapter 3 was applied for each compound using unimolecular L-H base reaction rate expression. Due to the simpler reaction pathway of acetone and MEK, they have fewer unknown reaction parameters. Therefore, these two VOCs were studied separately to find the kinetic parameters and then apply in PCO of toluene that has a more complicated pathway and, subsequently, the greater number of unknown parameters.

7.1. Kinetic modeling and reaction mechanism of generated by-products in a photocatalytic oxidation reactor: A case study of methyl ethyl ketone and acetone

The generation of unwanted by-products during the PCO process is the main concern of this technology. The potential health risk caused by toxic by-products, particularly carcinogenic compounds such as formaldehyde and benzene, impedes the commercial application of PCO-based air cleaners in the indoor environment. Therefore, the PCO air purification system requires more investigation to eradicate the hindrance associated with by-products. Till now, most research works on by-products generation through PCO have been based on experimental observations (qualitative and quantitative measurements). It was also reported that by-product production highly depends on operational conditions, namely photocatalyst properties, challenge compound type and concentration, UV light radiation, reaction residence time, and relative humidity. However, there is no reliable mathematical model that can predict the generation of the by-product under various operating conditions. To be more specific, due to the complicated degradation reaction mechanism of VOCs in the PCO process, the prediction of the kinetic parameters for by-products generation is quite challenging. This work presents the development and validation of a by-product predictive model by considering the mass transfer of pollutants and reaction kinetic expression. Acetone and MEK at ppb levels were chosen as challenge compounds. To include by-products generation in the reaction rate, a possible reaction pathway for each challenge compound was first proposed based on identified by-products (through analytical methods). Then, possible scenarios for reaction rate were considered to find the best kinetic rate describing the experimental result. The unknown kinetic parameters of acetone and MEK, as well as by-products, were estimated by curve fitting at steady state. The model was then validated at different operating conditions, including inlet concentration, relative humidity, irradiation, and air velocity. Further, the model was validated under the transition condition to predict MEK degradation and by-products formations as a function of time. Carbon balance analysis was also performed at different residence times to determine the mineralization efficiency in the PCO system. Finally, a risk assessment was used to analyze the potential adverse health effect of generated by-products under varying operating conditions.

7.1.1. Results and discussion

7.1.1.1. By-products of acetone and MEK

Generated by-products during the photocatalytic reaction of acetone and MEK at steady-state were identified and measured by analytical instruments and were listed in Table 7.1. For acetone, the identified by-products are acetaldehyde, formaldehyde, and acetic acid. For MEK, other by-products, including acetone, propionaldehyde, and ethanol, have been identified additionally. Among these by-products, ethanol and acetic acid peaks were detected by TD-GC-MS, whereas other compounds were measured quantitively by HPLC method. Furthermore, the generation of carbon dioxide through PCO reaction was measured by GC-FID. The carbon atom concentration of quantitively measured compounds for acetone and MEK decompositions in the PCO reactor is presented in Table 7.1. The analysis demonstrated that the mineralization efficiencies for acetone and MEK are 2% and 4.7%, respectively. Consequently, 4.5% acetone and 6.3% of MEK were converted to by-products. According to the carbon balance provided in Table 7.1, 99.63% of carbon in the PCO of acetone and 99.14% of carbon in the PCO of MEK were accounted for, indicating a reasonably accurate quantitative calculation of mass balance.

Table 7.1: By-products generated during the PCO of MEK and acetone and their concentrations detected by analytical methods (at steady-state) with carbon balance analysis (RH=33%, Q=30 L/min)

Compound (i)	Formula	Detected by			Challenge compound and generated by-products concentrations			
					Acetone test		MEK test	
		TD-GC-MS	HPLC	GC-FID	C_i [ppb]	$C_{i,C\text{-}Acetone}$ [ppb]	C_i [ppb]	$C_{i,C\text{-}MEK}$ [ppb]
MEK[a]	C_4H_8O	✓	✓		nd	-	816.3	3265.2
Acetone[a]	C_3H_6O	✓	✓		901.4	2704.2	5.8	17.4
Acetaldehyde	C_2H_4O		✓		35	70	74.6	149.2
Formaldehyde	CH_2O		✓		61.2	61.2	70.5	70.5
Propionaldehyde	C_3H_6O		✓		nd	-	trace	trace
Ethanol	C_2H_6O	✓			nd	-	pd	-
Acetic acid	$C_2H_4O_2$	✓			pd	-	pd	-
Carbon dioxide	CO_2			✓	60	60	175	175

nd: not detected

pd: peak detected

[a] Carbon atom concentration of MEK and acetone in the inlet stream for $C_{feed,MEK}$ =927.3 ppb and $C_{feed,Acetone}$ =968.7 ppb were $C_{C\text{-}MEK,feed}$ =3709.2 ppb and $C_{C\text{-}Acetone,feed}$ =2906.1 ppb, respectively.

7.1.1.2. PCO reaction mechanism of acetone and MEK

Photodegradation reaction pathways for acetone and MEK in the gas phase have been studied [40, 48, 204, 218]. According to previous studies, a possible reaction pathway is proposed for acetone (Fig. 7.1) and MEK (Fig. 7.2). The initiation step of photochemical or photocatalytic degradation of challenge compounds is the formation of hydroxyl radical (•OH). In this step,

valence band electrons are excited to conduction band under UV irradiation and create positive holes, which can further oxidize the adsorbed water molecules to generate hydroxyl radicals. Besides, hydroxyl radicals can be produced through the reaction of superoxide anions (formed by reduction of oxygen molecules in the presence of electrons) and water molecules in the conduction band [165]. The degradation steps of acetone and MEK through PCO are almost similar since they have a similar chemical group (ketone) in the structures. The first step of acetone and MEK photodegradation is metathesis reaction (**H**- abstraction), in which the highly reactive species ($^{\bullet}$OH) react with these molecules to create alkyl radicals. The next step is the decomposition of these radicals into smaller alkyl radicals and organic compounds through $\boldsymbol{\beta}$ session of **C-C** bonds (predominant) as **C-C** binding energy is lower than **C-H** or **C-O** at room temperature. In the case of acetone, the methyl radical ($^{\bullet}CH_3$) can also be combined with alkyl radical to produce MEK [40]. Further, reaction with $^{\bullet}$OH on the catalyst surface can generate alcohols, acids and aldehydes. For example, Bianchi et al. [41] proposed that acetone degradation in PCO can form light aldehydes and acids. In the case of MEK, a larger number of alkyl radicals and, consequently, a greater number of intermediates are generated in $\boldsymbol{\beta}$-session reaction step, such as ethenone, methyl ketene, propionaldehyde, and ethene. TiO_2 surface reaction of $^{\bullet}H_2C\text{-}CH_3$, $^{\bullet}CH_3$, $H_3C^{\bullet}\text{-}C=O$, and $^{\bullet}$OH radicals and the combination of these radicals can lead to the formation of alkanes (such as methane, ethane, propane, and butane), alcohols (such as methanol, and ethanol), acetic acid, acetone, acetaldehyde and formaldehyde [204].

According to identified by-products in this study (shown in Table 7.1), the complete possible reaction pathways for acetone and MEK (provided in Fig. 7.1 and Fig. 7.2) are simplified as Fig. 7.3, in which paths including those by-products have been chosen and others were ignored. The carbon balance analysis in the last section indicated that aldehydes are the major by-products of both challenge compounds. In order to quantitively predict the by-products by the mathematical model, these compounds are considered for kinetic modeling and assumed the major path for PCO degradation towards CO_2 occurs through the solid arrows in Fig. 7.3. It was also assumed that CO_2 is not produced directly from challenge compounds.
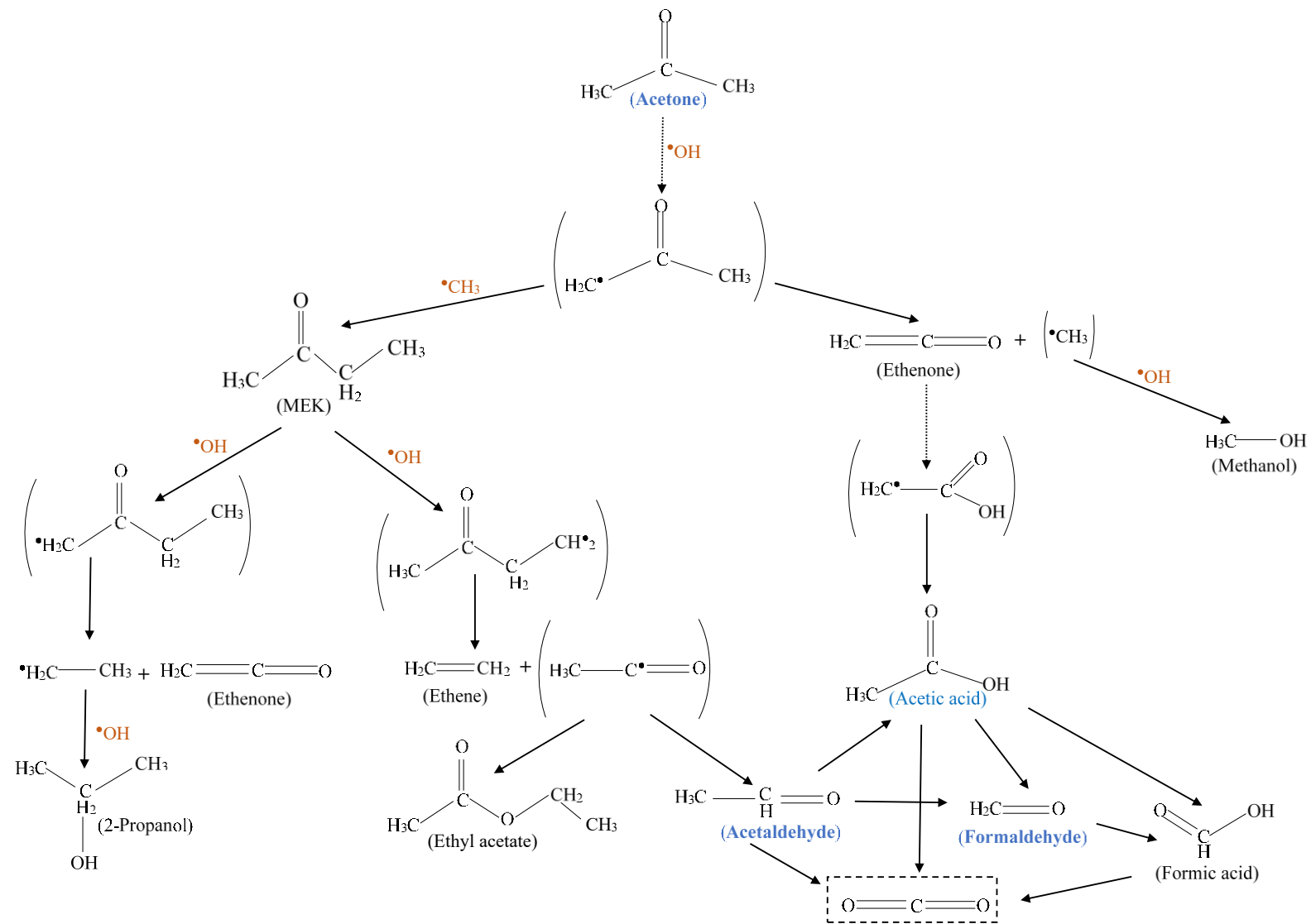
Fig. 7.1: complete possible reaction pathway for acetone degradation in the PCO based on literature [40, 218]
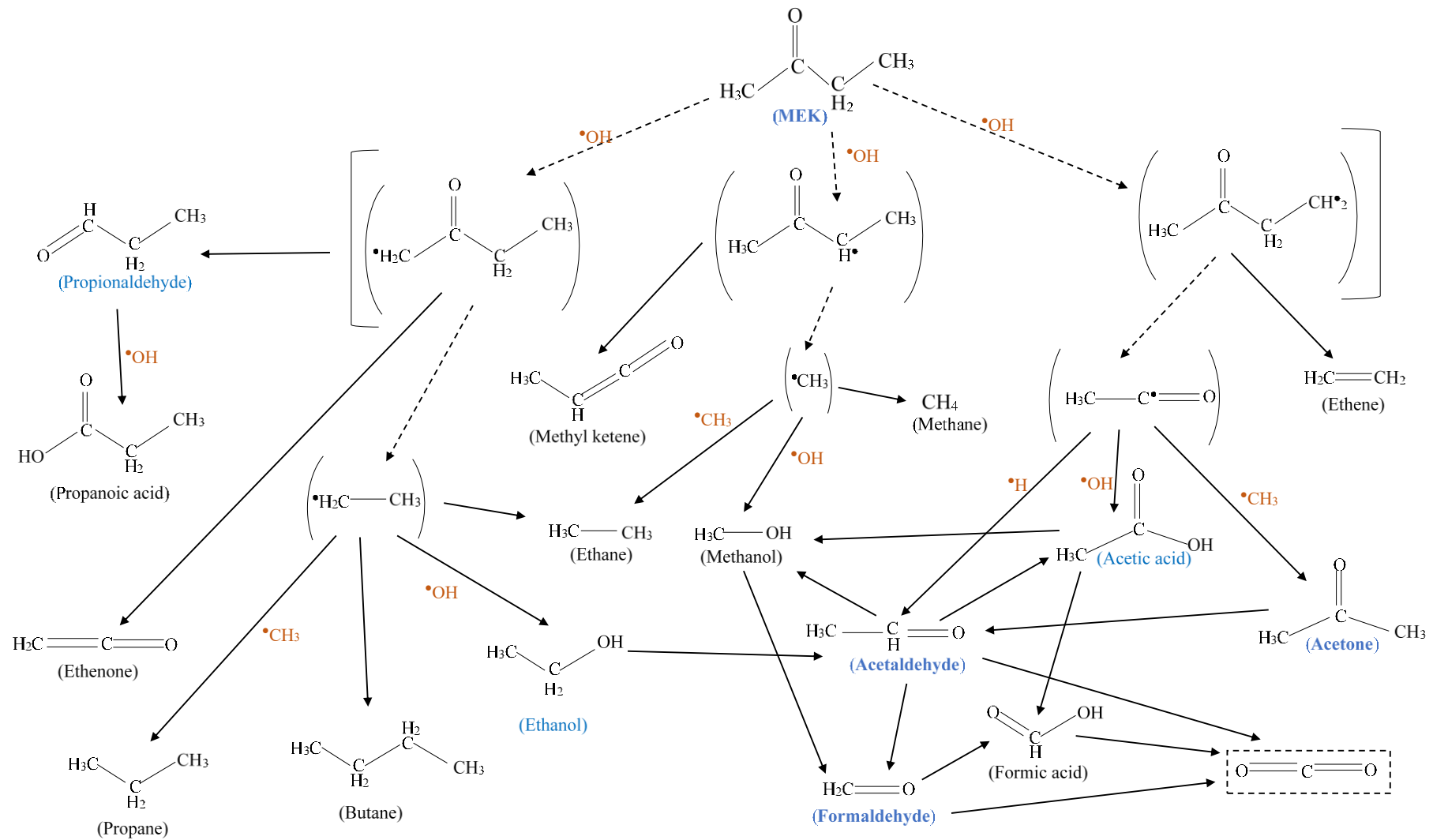
Fig. 7.2: complete possible reaction pathway for MEK degradation in the PCO based on literature [48, 204, 205, 219]
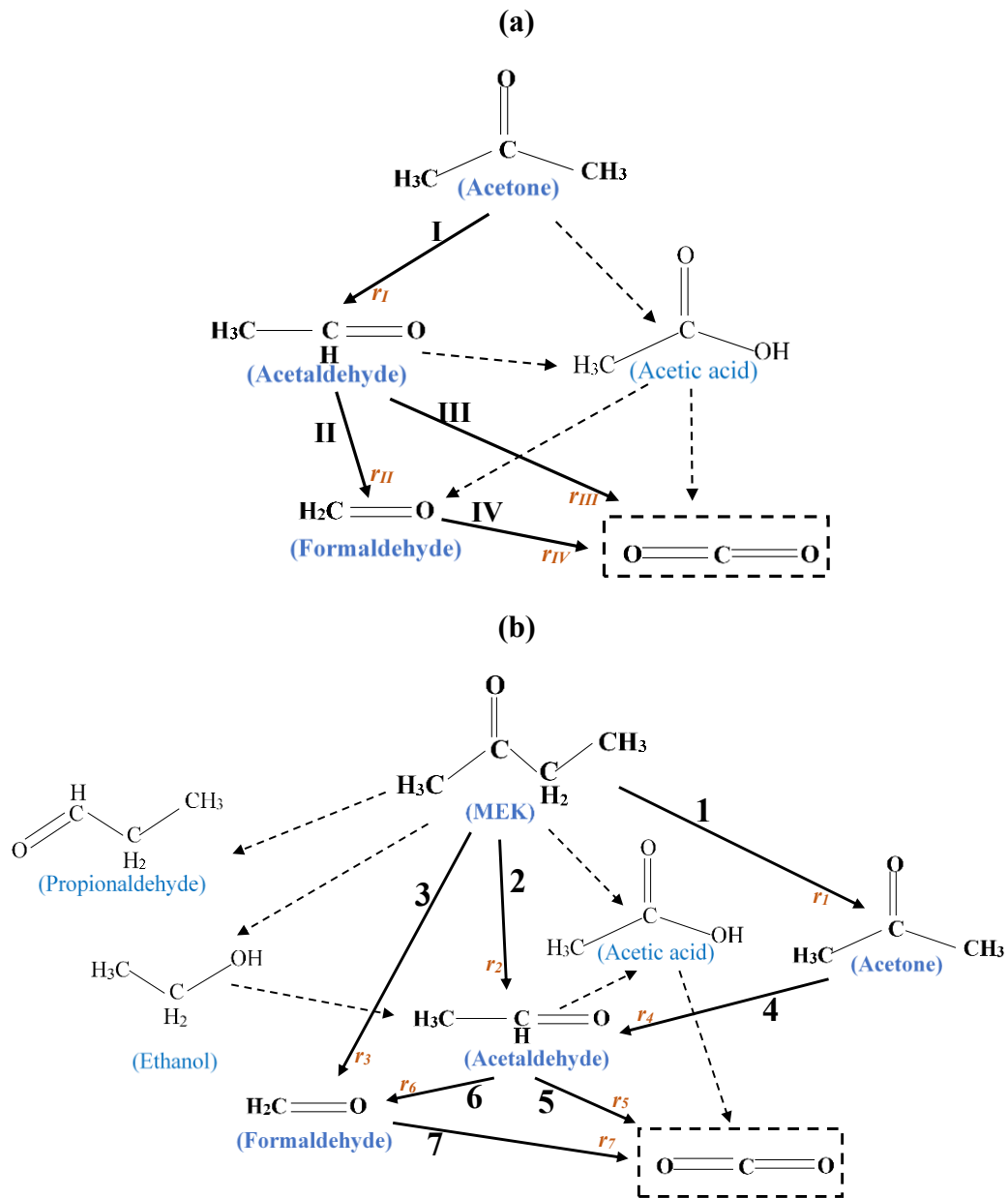
Fig. 7.3: Simplified possible reaction pathway for (a) acetone and (b) MEK

7.1.1.3. Reaction rate model for by-products

Based on the reaction pathway proposed in Fig. 7.3, the reaction rate for generated by-products of acetone and MEK can be defined by using the extended L-H model (Eq. (3.15)). By assuming the first order and elementary reaction for all compounds, the reaction rate for each challenge compound and its by-products are tabulated Table 7.2 and Table 7.3. It was also assumed that the generation rate of other intermediates in the pathway (see Fig. 7.1and Fig. 7.2) is equal to the consumption rate. Two possible scenarios (A-1 and A-2) were considered for the photodegradation reaction of acetone. The first scenario was based on the series reaction pathway ($\xrightarrow{I} \xrightarrow{II} \xrightarrow{IV}$). In the second scenario, path III was also added to the reaction rates. As for MEK, three possible scenarios were considered, in which the impacts of paths 1, 2, and 3 were considered for the reaction rates according to the proposed reaction pathway in Fig. 7.3-b.

Table 7.2: Reaction rate of acetone and by-products in two possible scenarios

Scenario A-1	Scenario A-2
$r_{Ac} = -r_I = -k_I C_{Ac}\alpha$	$r_{Ac} = -r_I = -k_I C_{Ac}\alpha$
$r_{AA} = r_I - r_{II} = (k_I C_{Ac} - k_{II} C_{AA})\alpha$	$r_{AA} = r_I - (r_{II} + r_{III}) = (k_I C_{Ac} - (k_{II} + k_{III})C_{AA})\alpha$
$r_{FA} = r_{II} - r_{IV} = (k_{II} C_{AA} - k_{IV} C_{AF})\alpha$	$r_{FA} = (r_{II}) - r_{IV} = ((k_{II})C_{AA} - k_{IV} C_{AF})\alpha$

Table 7.3: Reaction rate of MEK and by-products in three possible scenarios

Scenario M-1	Scenario M-2	Scenario M-3
$r_{MEK} = -r_1 = -k_1 C_{MEK}\alpha$	$r_{MEK} = -(r_1 + r_2) = -(k_1 + k_2)C_{MEK}\alpha$	$r_{MEK} = -(r_1 + r_2 + r_3) = (k_1 + k_2 + k_3)C_{MEK}\alpha$
$r_{AC} = r_1 - r_4 = (k_1 C_{MEK} - k_4 C_{AC})\alpha$	$r_{AC} = r_1 - r_4 = (k_1 C_{MEK} - k_4 C_{AC})\alpha$	$r_{AC} = r_1 - r_4 = (k_1 C_{MEK} - k_4 C_{AC})\alpha$
$r_{AA} = r_4 - (r_5 + r_6)$	$r_{AA} = (r_2 + r_4) - (r_5 + r_6)$	$r_{AA} = (r_2 + r_4) - (r_5 + r_6)$
$= (k_4 C_{AC} - (k_5 + k_6)C_{AA})\alpha$	$= ((k_2 + k_4)C_{AC} - (k_5 + k_6)C_{AA})\alpha$	$= ((k_2 + k_4)C_{AC} - (k_5 + k_6)C_{AA})\alpha$
$r_{FA} = r_6 - r_7 = (k_6 C_{AC} - k_7 C_{AF})\alpha$	$r_{FA} = r_6 - r_7 = (k_6 C_{AC} - k_7 C_{AF})\alpha$	$r_{FA} = (r_3 + r_6) - (r_7) = ((k_3 + k_6)C_{AC} - k_7 C_{AF})\alpha$

For reaction rates presented in Table 7.2 and Table 7.3, coefficients α and k were defined by:

$$\alpha = \frac{I^{0.5}}{1 + K_A C_A + K_w C_w + \sum_i K_{byp,i} C_{byp,i}} \qquad (7.1)$$

$$k_i = k_{r,i} * K_i \qquad (7.2)$$

The rate constant k_i in Eq.(7.2) stands for the apparent rate coefficient for each compound with the unit of [s^{-1} W$^{-0.5}$ m]. r_{MEK}, r_{AC}, r_{AA}, and r_{FA} represent the reaction rates for methyl ethyl ketone, acetone, acetaldehyde, and formaldehyde, respectively. Considering that the major generated by-products were aldehydes (formaldehyde and acetaldehyde), see Table 7.1, the inhibitive adsorption effects of other by-products were assumed to be negligible.

7.1.1.4. Model fitting and kinetic parameters

The simulation for kinetic modeling of acetone and MEK PCO were conducted under steady-state condition using the dispersion-mass transfer model (Eq.(3.1)-(3.20)) incorporated with reaction rate expressions. In addition, the LSSE and Beer-Lambert models were also employed to simulate the incident radiation, which was validated earlier[220]. Unknown kinetic parameters of the model were also estimated under a kinetics-controlled regime (free of external mass transfer limitations). In the chapter 5, it was shown that external mass transfer resistance in the boundary layer region is negligible compared to the surface reaction because [215]:

$$\frac{-r_A}{k_{m,ext} a_s C_{Ab}} < 0.1 \qquad (7.3)$$

where C_{Ab} is the bulk concentration of challenge compound defined as the average concentration of inlet and outlet.

The adsorption coefficients of MEK and water molecules, as well as by-products (including acetaldehyde and formaldehyde) obtained in the chapter 5 [215], were used for kinetic analysis. The equilibrium adsorption of acetone under various levels of relative humidity is also obtained under dark condition (see Fig. 7.4). Since the adsorption coefficient represents the adsorption affinity between adsorbate and media surface, this coefficient in PCO should be the same under dark condition [208]. The adsorption parameters of the Langmuir isotherm model (Eq.(3.21)) are computed through curve fitting and provided in Table 7.4.
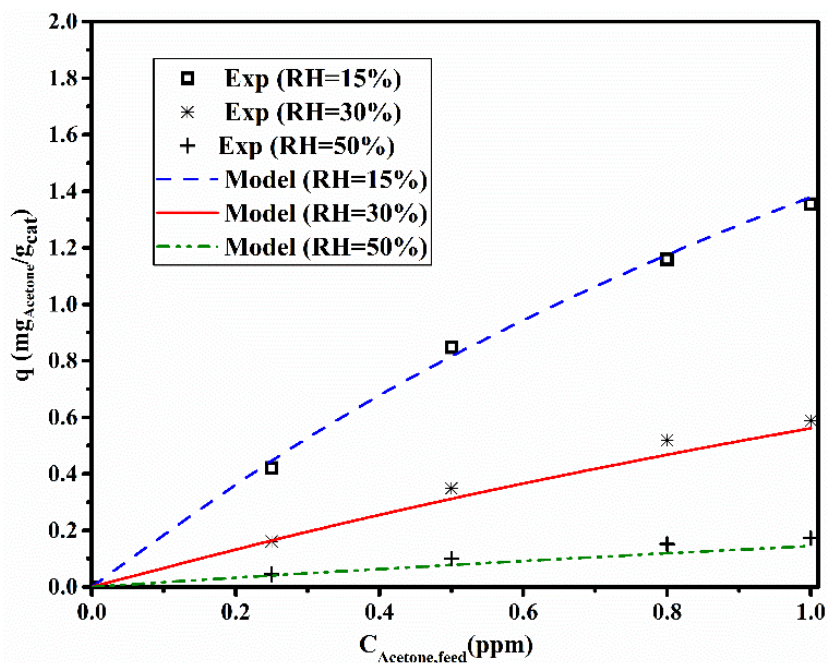
Fig. 7.4. Adsorption of acetone under various relative humilities for TiO_2/SFF filter

Table 7.4: Langmuir parameters for adsorption of acetone on TiO_2/SFF filter.

Parameter	Value	95% CI
q_m (mg$_{AC}$/g$_{cat}$)	-0.0003C$_w$ [ppm]+5.517	-
K_{AC} (ppm^{-1})	2.32	0.081
R^2	0.99	

The kinetic parameters of acetone and its by-products are obtained through adsorption model curve fitting to the experimental results at the steady-state condition. The results of curve fitting with both possible scenarios considered for reaction rates are provided in Table 7.5. The model using both reaction rates A-1 and A-2 provided a high fitting accuracy (R^2>0.99) and the same residual error (S^2_R). However, the acetaldehyde reaction path towards CO_2 is much less than towards formaldehyde, according to kinetic coefficients obtained in scenario A-2. In addition, the confidence interval for unknown kinetic parameters of reaction rate based on scenario A-2 is larger than scenario A-1, indicating kinetic parameters of scenario A-1 provides more reliable values. In the case of kinetic parameters values, the acetaldehyde reaction coefficient is 17 times higher than acetone. Garcia-Hernandez et al.[221] also reported that the reaction coefficient of acetaldehyde in photocatalytic reaction with Degussa P25 photocatalyst is 15 times bigger than that of acetone. This can be attributed to the difference in the chemical structure of acetone and acetaldehyde. With regard to acetaldehyde structure, carbonyl group is placed in terminal carbon, which results in higher reactivity compared to carbonyl group in secondary carbon as for acetone. Besides, from the same chemical group (aldehyde), acetaldehyde, due to higher adsorption affinity towards TiO_2 than formaldehyde, leads to a greater reaction rate coefficient value. For the same compounds in the same chemical class, higher molecular weight and boiling point has greater intermolecular forces, resulting in superior adsorption [68]. Fig. 7.5 also illustrates the curve fitting of acetone and by-products to experimental data using two reaction rate scenarios. This figure shows the generation of formaldehyde is higher than acetaldehyde at the steady-state condition because acetaldehyde kinetic coefficient towards formaldehyde is greater than the degradation coefficient of formaldehyde to CO_2, which causes a larger amount of formaldehyde to remain in the outlet stream. Table 7.6 reports the cross-correlation matrix of the estimated kinetic coefficients in the

PCO of acetone. In the Scenario A-2, low to moderate cross-correlation can be observed among kinetic parameters. Correlation between k_I and other coefficients was close to zero. However, there is a moderate cross-correlation among k_{II}, k_{III}, and k_{IV}. By reducing number of parameters in Scenario A-1, cross-correlation coefficient among the parameters decreased.

Table **7.7** reports the kinetic parameters of MEK and by-products through curve fitting of the mathematical model combined with three possible scenarios for the reaction rate. The results demonstrate that the parameters obtained through scenarios M-2 and M-3 provide better accuracy due to higher R^2 and lower S^2_R. Nevertheless, the range of uncertainty for kinetic parameters is larger in scenario M-3, owing to the presence of more unknown parameters. The kinetic analysis of this table also indicates that the major path for degradation of MEK is through $MEK \xrightarrow{2} Acetaldehyde$ and miner reaction path is through $MEK \xrightarrow{3} Formaldehyde$, which shows k_3 can be negligible in comparison with two others (k_1 and k_2). It is important to note that the reaction coefficients of acetone, acetaldehyde, and formaldehyde obtained in Table 7.5 were used to determine other unknown parameters (k_1, k_2, and k_3) with higher reliability. Since the kinetic parameters are a function of catalyst characteristics at the same temperature, they should be the same value in PCO of both acetone and MEK (because of using the same photocatalyst). Fig. 7.6 displays the experimental data and model curve fitting using scenarios M-1 to M-3 for MEK and its by-products. It can be observed that the model using scenario M-1 failed to predict the by-products generations. The reason is that the acetone degradation rate is much less than expected to generate that high amount of acetaldehyde directly from acetone, which means acetaldehyde is also created through other paths. Instead, the results of modeling using scenarios M-2 and M-3 are very close to experimental data, indicating acetaldehyde is mainly produced through the path $\xrightarrow{2}$. Fig. 7.6 also shows that generated formaldehyde is higher at lower inlet concentrations of MEK, but its amount decreases as the inlet concentration increases. This can be ascribed to more available active sites of photocatalyst at the lower concentration for the reaction of acetaldehyde to formaldehyde, whereas these active sites can be occupied by MEK at higher inlet concentrations, resulting in a higher amount of unreacted acetaldehyde in the outlet of the reactor. Finally, the cross-correlation matrix for the estimated parameters in PCO of MEK is presented in Table 7.8. Both scenarios demonstrated a low cross-correlation between kinetic parameters.

Table 7.5: Kinetic parameters of acetone and its by-products for two possible scenarios (operating conditions are: u=0.05 m/s; RH_{Feed}=33%; I_{ave}=7 W/m^2)

Parameter	Scenario A-1		Scenario A-2	
	Values [s^{-1} $W^{-0.5}$ m]	95% CI	Values [s^{-1} $W^{-0.5}$ m]	95% CI
k_I	43.9×10^3	2.8×10^3	43.9×10^3	2.8×10^3
k_{II}	752.7×10^3	21.5×10^3	746.2×10^3	142×10^3
k_{III}	-	-	6.4×10^3	3.7×10^3
k_{IV}	120.3×10^3	6.5×10^3	116.7×10^3	77×10^3
R^2	0.998		0.998	
$S^2_R \times 10^4$ (ppm^{-2})	9.12		9.12	

Table 7.6: Cross-correlation coefficients for the estimated kinetic parameters in PCO of acetone

	Scenario A-1				Scenario A-2			
	k_I	k_{II}	k_{IV}		k_I	k_{II}	k_{III}	k_{IV}
k_I	1			k_I	1			
k_{II}	-0.13	1		k_{II}	-0.06	1		
k_{IV}	-0.07	0.29	1	k_{III}	0.004	-0.60	1	
				k_{IV}	-0.01	0.53	-0.47	1
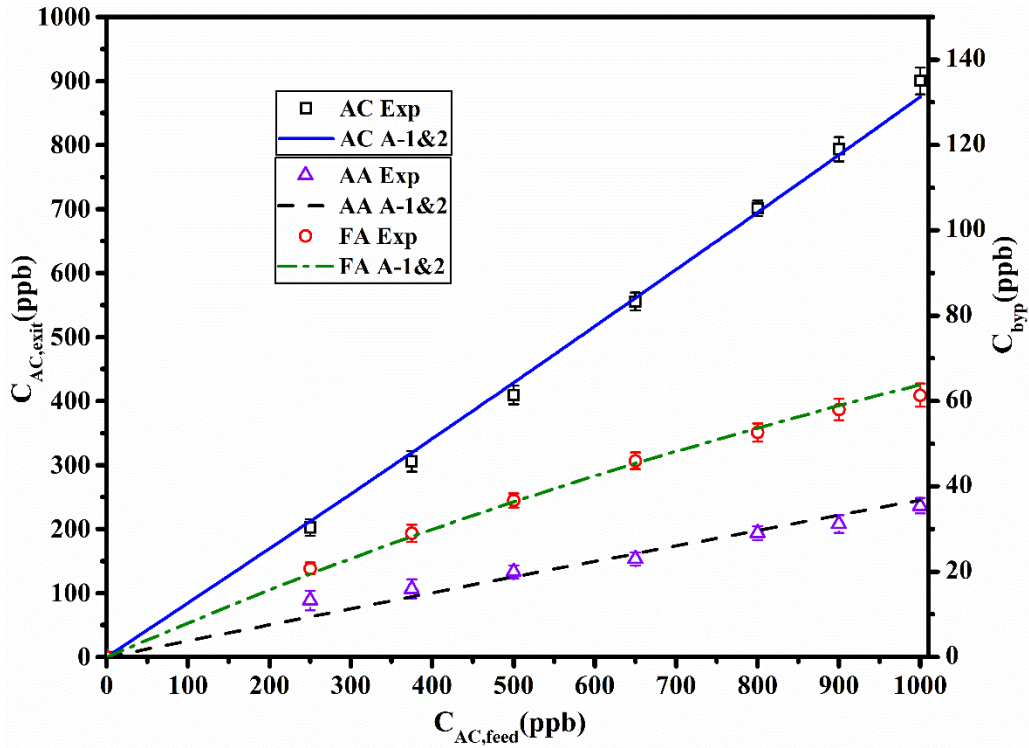
Fig. 7.5. Results of curve fitting for acetone and by-products at u=0.05 m/s; RH_{Feed}=33%; I_{ave}=7 W/m^2.
(AC: acetone, AA: acetaldehyde, FA: formaldehyde)

Table 7.7: Kinetic parameters of MEK and its by-products for three possible scenarios (operating conditions are: u=0.05 m/s; RH_{Feed}=33%; I_{ave}=7 W/m^2)

Parameter	Scenario M-1		Scenario M-2		Scenario M-3	
	Values [s^{-1} W$^{-0.5}$ m]	95% CI	Values [s^{-1} W$^{-0.5}$ m]	95% CI	Values [s^{-1} W$^{-0.5}$ m]	95% CI
k_1	107.1×10^3	30.1×10^3	2×10^3	0.5×10^3	3.4×10^3	0.9×10^3
k_2	-	-	96.1×10^3	4×10^3	95.8×10^3	10.8×10^3
k_3	-	-	-	-	0.01×10^3	0.2×10^3
k_4	k_I	-	k_I	-	k_I	-
k_5	k_{III}	-	k_{III}	-	k_{III}	-
k_6	k_{II}	-	k_{II}	-	k_{II}	-
k_7	k_{IV}	-	k_{IV}	-	k_{IV}	-
R^2	0.978		0.998		0.998	
S^2_R×10^3 (ppm^{-2})	130		3.4		3.5	

Table 7.8: Cross-correlation coefficients for the estimated kinetic parameters in PCO of MEK

	Scenario M-2			Scenario M-3		
	k_1	k_2		k_1	k_2	k_3
k_1	1		k_1	1		
k_2	-0.046	1	k_2	-0.03	1	
			k_3	0.0004	-0.28	1

(a)

(b)
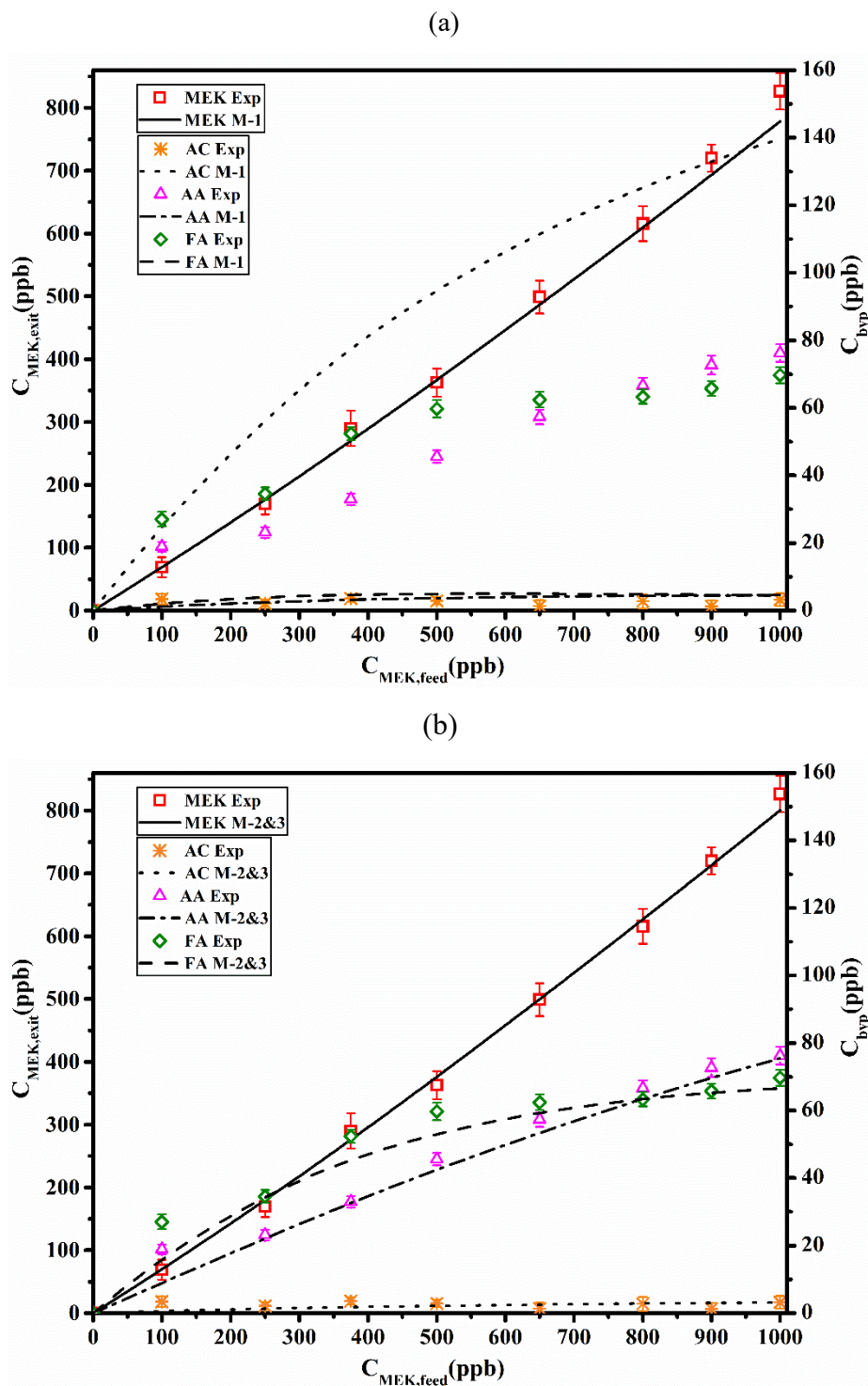
Fig. 7.6. Results of curve fitting for MEK and by-products considering reaction rate scenarios (a) M-1 and (b) M-2&3 (u=0.05 m/s; RH_{Feed}=33%; I_{ave}=7 W/m^2) (AC: acetone, AA: acetaldehyde, FA: formaldehyde)

The result of curve fitting using scenario M-2 was then used to validate the model at different operating conditions. Fig. 7.7-a&b demonstrate the prediction of the model for various inlet concentration of acetone and MEK at RH=50%. At higher relative humidity, a greater amount of water molecule takes part in the competition adsorption and due to its polarity, more active sites

are occupied by water, results in decreasing removal efficiency. Besides, such a decrement in removal efficiency causes less amount of acetaldehyde is decomposed into formaldehyde, leading to the generation of less formaldehyde as compared to that at 33% RH shown in Fig. 7.5 and Fig. 7.6. These figures also show that the by-product generation increases as the inlet concentration of acetone and MEK increases since the reaction rate is enhanced at higher concentration.

The impact of water content on acetone and MEK degradations and by-products generation is observed more clearly in Fig. 7.8-a&b. This figure illustrates the model prediction for various levels of RH at the constant MEK concentration (500 ppb). At lower water vapor concentration, higher amounts of acetone and MEK are adsorbed on the photocatalyst surface and increase the efficiency. Meanwhile, more active sites are available for the decomposition of acetaldehyde into formaldehyde, leading to the generation of a higher amount of formaldehyde in comparison with acetaldehyde at low RH levels. As RH increases at the same inlet concentration, the photochemical reaction rate reduces (and lowers removal efficiency), accordingly the generation of all by-products decreases. Simulation result for MEK (Fig. 7.8-b) states that at the specific point of water vapor concentration (around 12000 ppm or 43% RH), the generation of acetaldehyde and formaldehyde are at the same level, and beyond that value, formaldehyde concentration becomes less than acetaldehyde, owing to hindering effect of water on adsorption of acetaldehyde and consequently less reaction rate of acetaldehyde to formaldehyde. As for acetone (as by-products of MEK in Fig. 7.8-b), its variation is negligible compared to two other by-products because of the low reaction rate of MEK to acetone path according to the kinetic analysis presented in Table **7.7**.

Fig. 7.9 displays the results of modeling and experimental data for various irradiations at the constant concentration (500 ppb). As irradiation increases, photocatalyst activity increases and then degradation efficiency is improved; accordingly, the generation of all by-products increases. Owing to higher photocatalyst activity, the reaction rate of acetaldehyde to formaldehyde grows with the increment in irradiation, results in more generated formaldehyde compared to acetaldehyde.

The effect of air velocity on outlet concentration of acetone and MEK as well as by-products are shown in Fig. 7.10. As air velocity decreases (increases residence time), challenge compounds have more available time for adsorption on the PCO media, which leads to an increase in removal efficiency, consequently, higher concentrations of by-products. Meanwhile, formaldehyde formation rate also becomes more than acetaldehyde with reducing air velocity because of the elevation of acetaldehyde reaction rate to formaldehyde at higher residence time. The results of simulation using mass transfer mathematical model combined with M-3 rate expression provided acceptable accuracy to experimental data for all various operating conditions (Fig. 7.7 to Fig. 7.10).

Fig. 7.11-a&b show the contribution of each compound category in the carbon mass balance for different residence times at concentration of 1 ppm. These figures show that the higher residence time leads to the generation of more carbon dioxide, consequently, greater mineralization efficiency. In addition, increment in residence time intensifies the formation of by-products and reduces the unreacted MEK at the outlet stream. In spite of higher mineralization efficiency at longer residence time, the generation of by-products is greater. It indicates that

unreacted challenge compound takes part more in degradation reaction than by-products at longer residence time, owing to higher concentration and greater adsorption of the challenge compound. Accordingly, it can be concluded that the complete mineralization towards carbon dioxide is obtained at a very high removal efficiency, in which unreacted challenge molecules are decomposed mostly. The mass of undetected intermediates/by-products is negligible compared to identified chemical compounds through analytical methods, which indicates the high potential of the proposed model for real application.

(a)
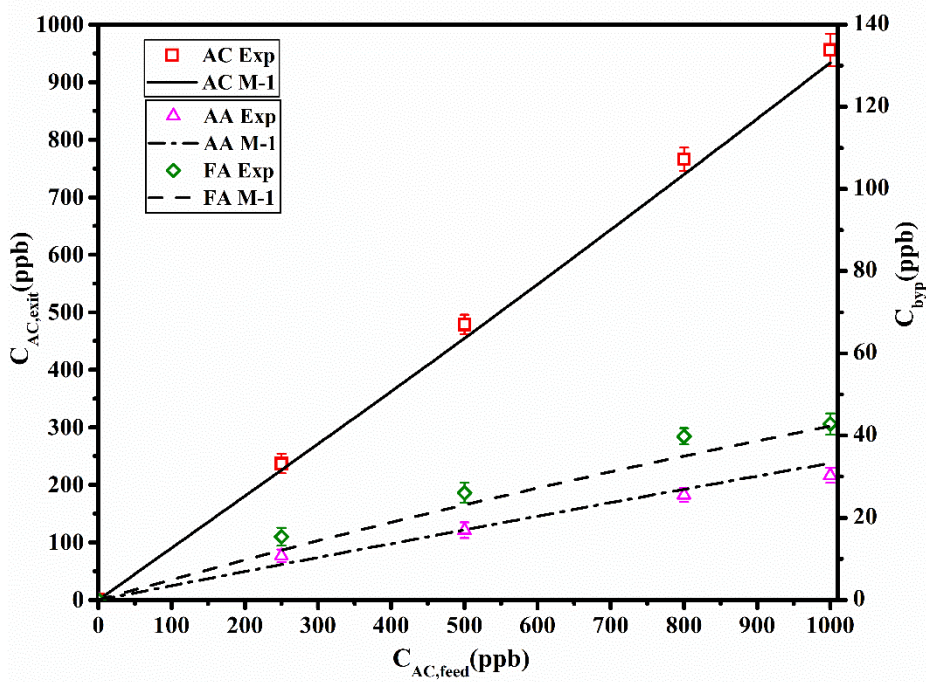
(b)
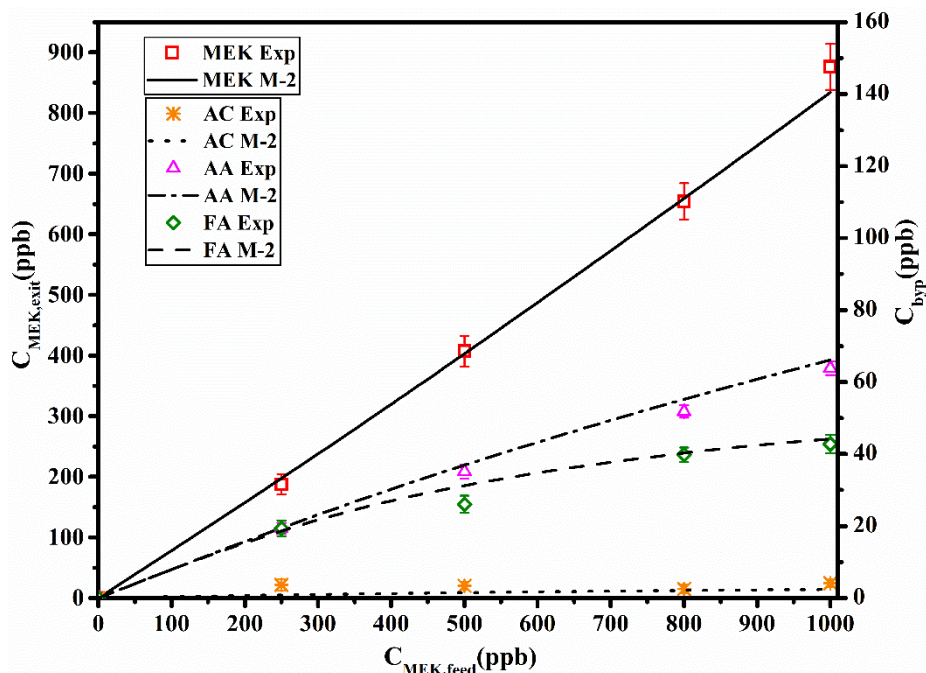
Fig. 7.7. Effect of inlet concentration on the PCO degradation at steady state condition for (a) Acetone and (b) MEK (u=0.05 m/s; RH_{Feed}=50%; I_{ave}=7 W/m^2) (AC: acetone, AA: acetaldehyde, FA: formaldehyde)

(a)
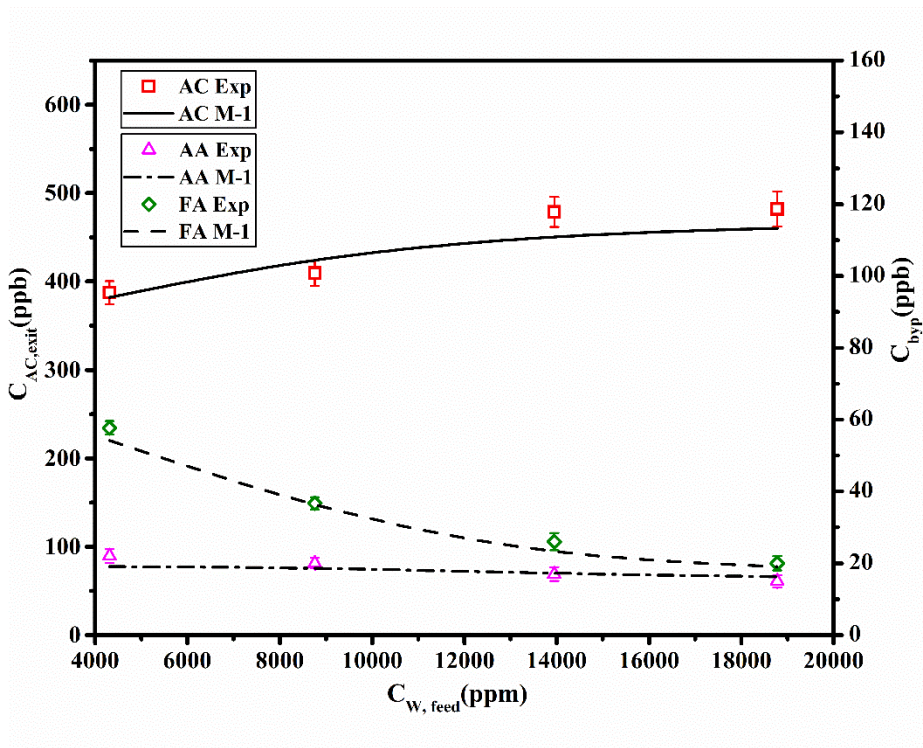
(b)
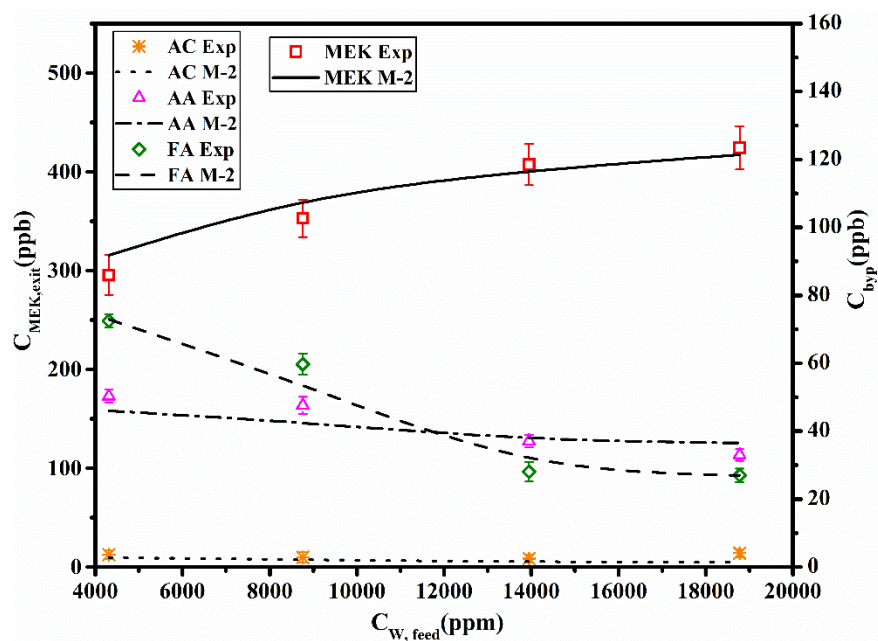
Fig. 7.8. Effect of relative humidity [RH$_{Feed}$] on the PCO degradation at steady state condition for (a) Acetone and (b) MEK (C$_{feed}$=500 ppb; u=0.05 m/s; I$_{ave}$=7 W/m^2)

(AC: acetone, AA: acetaldehyde, FA: formaldehyde)

(a)

(b)
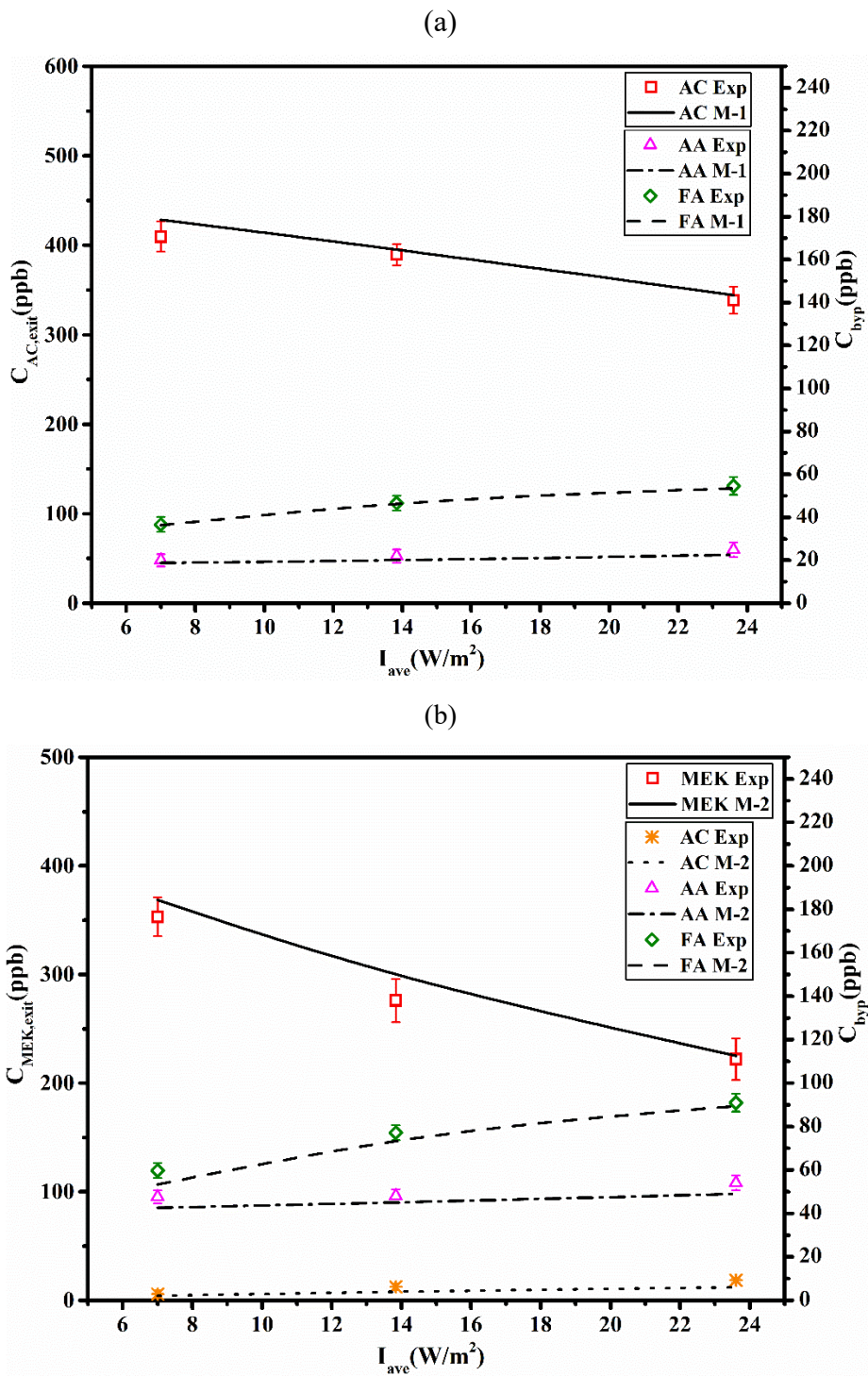
Fig. 7.9. Effect of irradiation [I] on the PCO degradation at steady state condition for (a) Acetone and (b) MEK (C_{feed}=500 ppb; RH_{Feed}=33%; u=0.05 m/s)

(a)

(b)
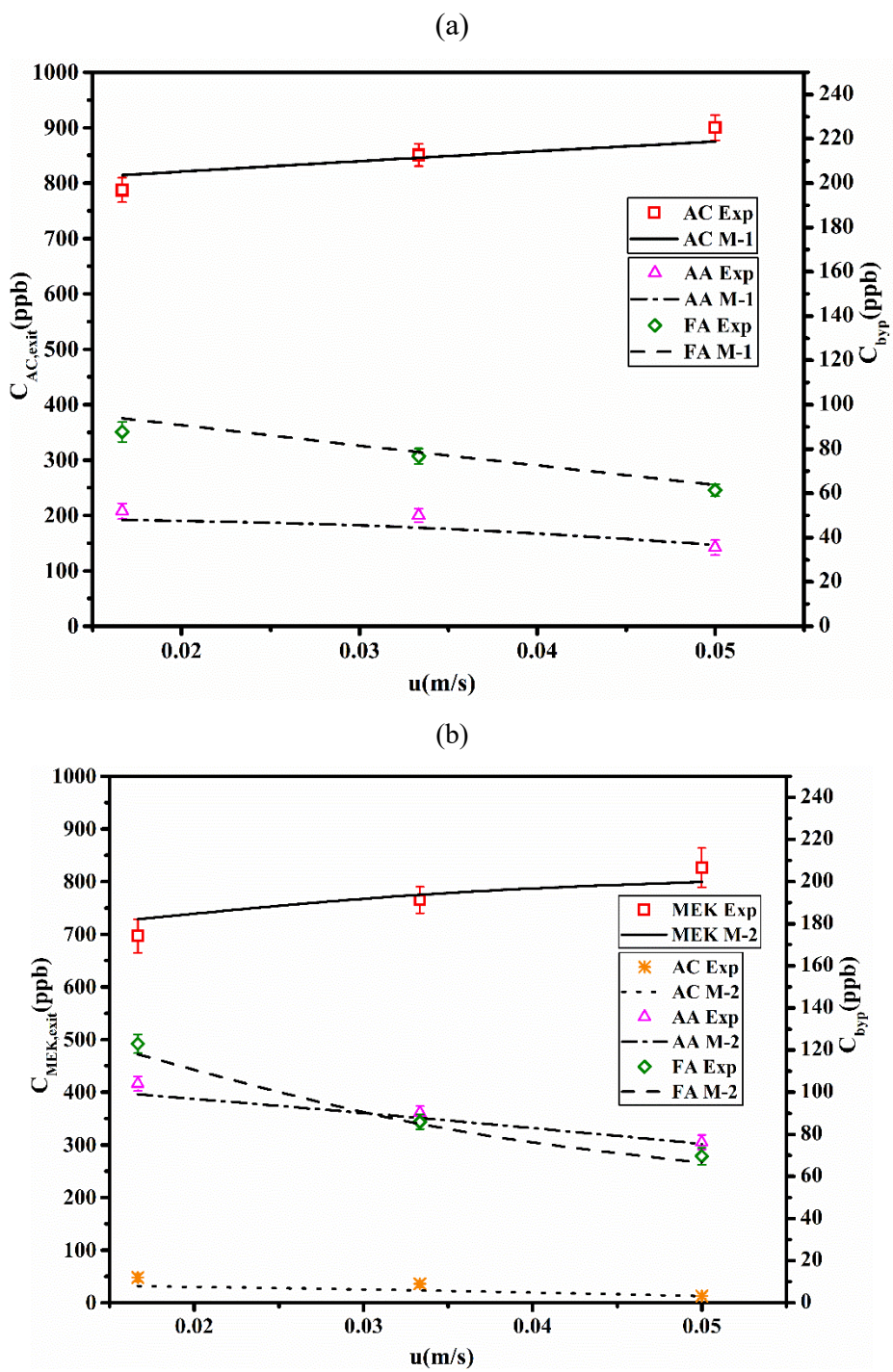
Fig. 7.10. Effect of velocity [u] on the PCO degradation at steady state condition for (a) Acetone and (b) MEK (Cfeed=1000 ppb; RHFeed=33%; Iave=7 W/m2)

(AC: acetone, AA: acetaldehyde, FA: formaldehyde)

(a)

(b)
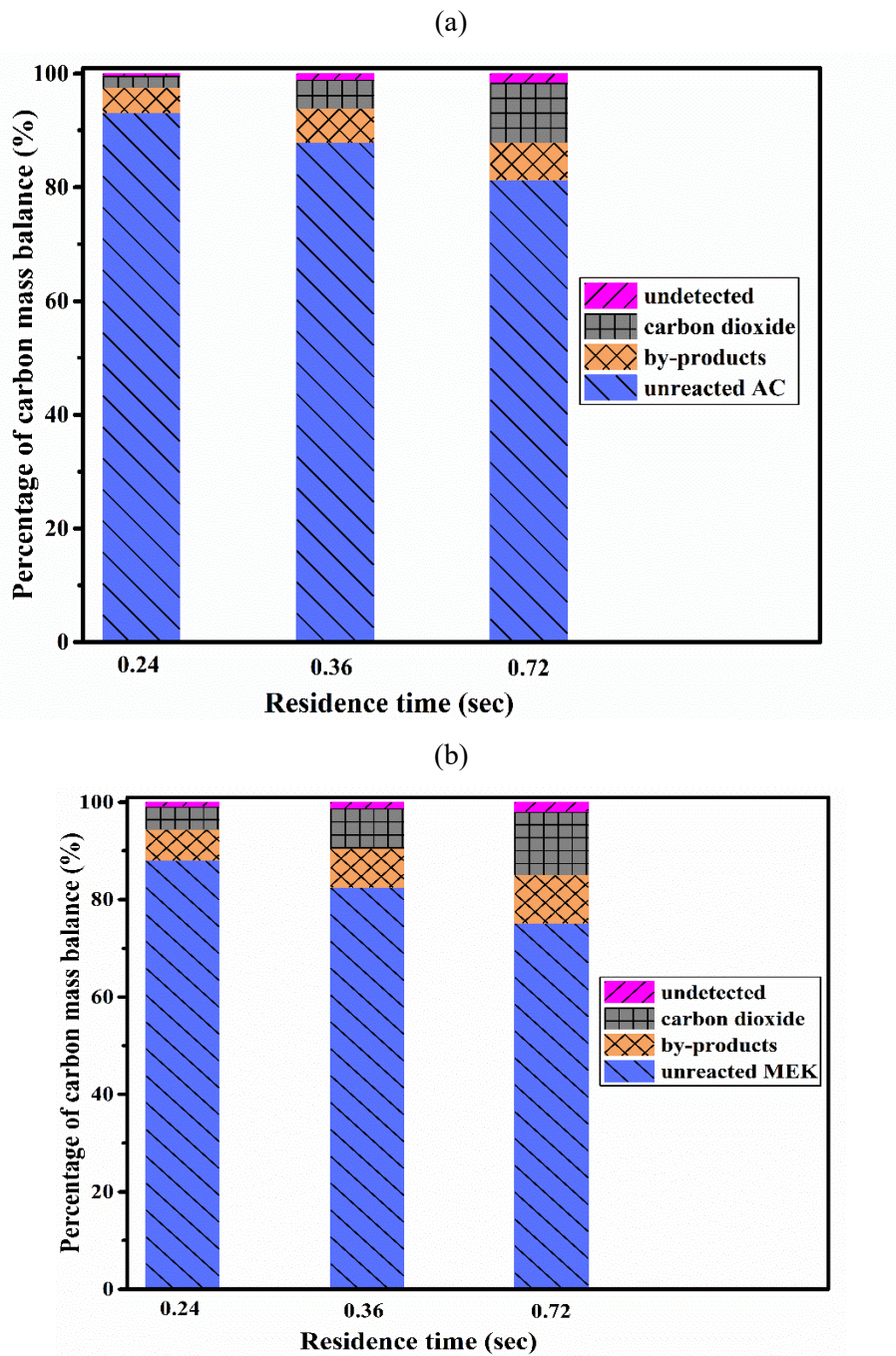
Fig. 7.11. Carbon mass balance of the photocatalytic oxidation of (a) Acetone and (b) MEK for various residence time at steady state condition (C_{feed}=1000 ppb; RH_{Feed}=33; I_{ave}=7 W/m^2)
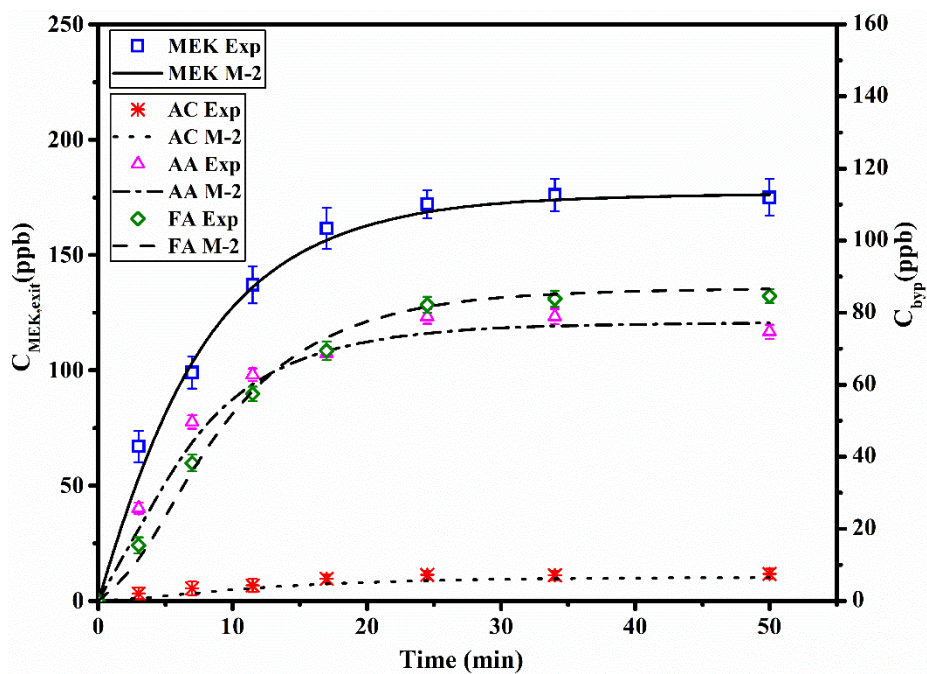
Fig. 7.12. Modeling result for prediction of outlet concentration of MEK and by-products during the time at $C_{MEK,feed}$=800 ppb; RH_{Feed}=50%; I_{ave}=90 W/m^2; u=0.034 m/s (AC: acetone, AA: acetaldehyde, FA: formaldehyde)

111

The validation of the model was also carried out in the transient condition. Fig. 7.12 presents the experimental and simulation results for the prediction of MEK and by-products outlet concentrations as a function of time (for 50 min). The result shows that MEK and by-products concentrations in the reactor outlet reached steady-state after around 30 min. The region before steady-state includes both adsorption and PCO reaction processes, in which outlet concentration grows with the passage of time. In this region, the adsorption process is the rate-limiting step as photocatalyst is fresh and highly active for PCO reaction (high removal efficiency). However, as time passes, more active sites are occupied by MEK and by-products, which results in greater number of the unreacted challenge compounds and, consequently, decrease in removal efficiency. Besides, at the beginning of PCO process, owing to fewer challenge compounds available on the surface, the reaction rate is less and, accordingly, there is lower by-products generation. The figure displays that the generation of acetaldehyde in the gas phase is more than formaldehyde in the initial stage because of the replacement of the generated acetaldehyde by MEK molecules in the unsteady-state step and desorbed to the gas phase. However, the concentration of the challenge compound on the surface increases after some time, result in higher reaction rate and, thereby, more by-product formation. As time approached the steady-state condition, the formation rate of formaldehyde becomes greater than that of acetaldehyde. At the steady-state, the photocatalyst is saturated based on adsorption affinities of chemical compounds towards the catalyst, and the concentration of each compound became stable on the surface. In this condition, due to the higher degradation rate of acetaldehyde than formaldehyde, the outlet concentration level of formaldehyde is greater than acetaldehyde. In the case of acetone, concentration increase over time till it reaches the steady-state, in which the outlet concentration is constant. The modeling result also demonstrated an acceptable accuracy to predict the performance of PCO reactor at transient state.

Acetone is one of the by-products of MEK. Validation of MEK and its by-products in transient condition shows that it can predict acetone as well. Furthermore, kinetic parameters of by-products in PCO of MEK were obtained from those in PCO of acetone (see Table 7.7). Therefore, modeling of MEK and by-products in the transient study, validate the kinetic parameters calculated in modeling of acetone and its by-products as well.

7.1.1.5. Implications of by-products formation in human health context

Generated by-products of MEK and acetone in the PCO can be harmful to human health. In order to investigate potential implications of by-products on human health, Health Risk Index (HRI) is used. HRI is defined as [51]:

$$HRI = \sum \frac{C_i}{REL_i} \qquad (7.4)$$

where C_i is the concentration of compound i and REL_i is the recommended exposure limit reported by regulatory agencies such as the US National Institute for Occupational Safety Health, Office of Environmental Health Hazards Assessments, US Green Building Council, and Agency for Toxic Substances and Disease Registry [222-225] (Table 7.9). The smaller the HRI value, the less risk to humans. Usually, a risk is considered negligible when the value of HRI is less than 1. Fig. 7.13 displays HRI values of pollutants in the outlet of PCO under various operating conditions.

Owing to the generation of carcinogenic by-products during the PCO and low REL values of these compounds, the HRI in the outlet is always greater than in inlet flow, indicating by-products could be more harmful to human health through PCO reaction. Raising concentration and irradiation increase HRI value while elevating RH and velocity reduce its value. In spite of higher removal efficiency at low velocity, the value of HRI is high. Among the by-products, acetaldehyde and formaldehyde are the most hazardous compounds because of the lowest REL values that highly affect the HRI. However, formaldehyde with REL of 0.016 ppm is the most concerning VOC in the outlet. It can be found out that at lower concentrations (less than 0.25 ppm) and higher RH level (higher than 50 %), the HRI value is close to 1, and the PCO system can be used for MEK and Acetone degradation. However, the variation in operating conditions in order to improve the removal efficiency can hinder the PCO system in real application owing to health risks to humans.

Table 7.9:Health related information for pollutants

VOC	REL (ppm)	REL data source	IARC[c] Carcinogenic classification
MEK	1	ATSDR[a]	-
Acetone	13	ATSDR[a]	-
Propionaldehyde	20	AIHA[b]	-
Acetaldehyde	0.078	OEHHA[c], USGBC[d]	Group 2B, possibly carcinogenic to humans
Formaldehyde	0.016	NIOSH[e], USGBC[d]	Group 1, Carcinogenic to humans
Ethanol	1000	NIOSH[e]	-
Acetic acid	10	NIOSH[e]	-

[a] Agency for Toxic Substances and Disease Registry

[b] American Industrial Hygiene Association

[c] California Office of Environmental Health Hazards Assessments

[d] US Green Building Council, LEED v4.1

[e] US National Institute for Occupational Safety Health

(a)

113

(b)
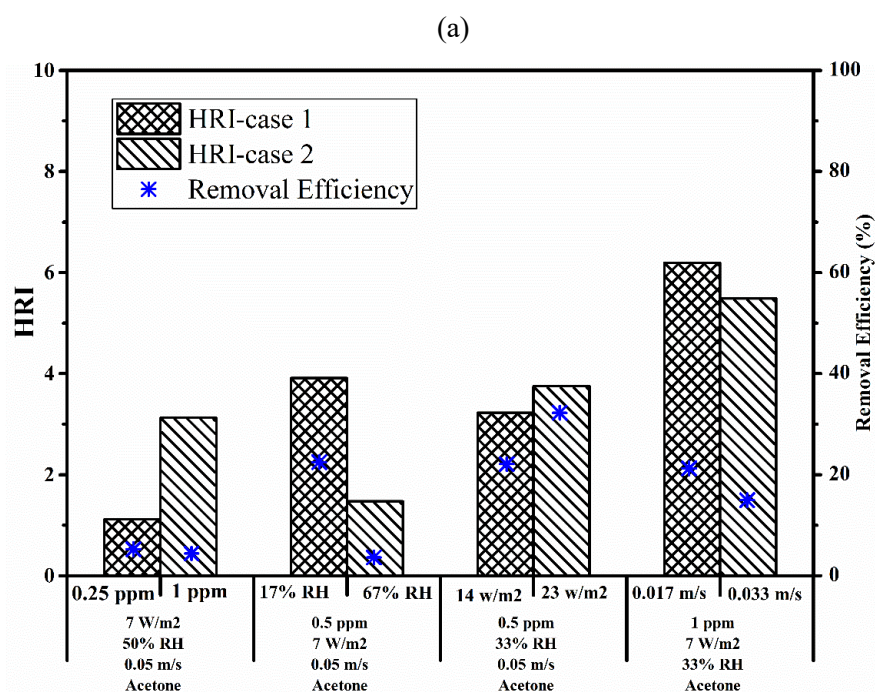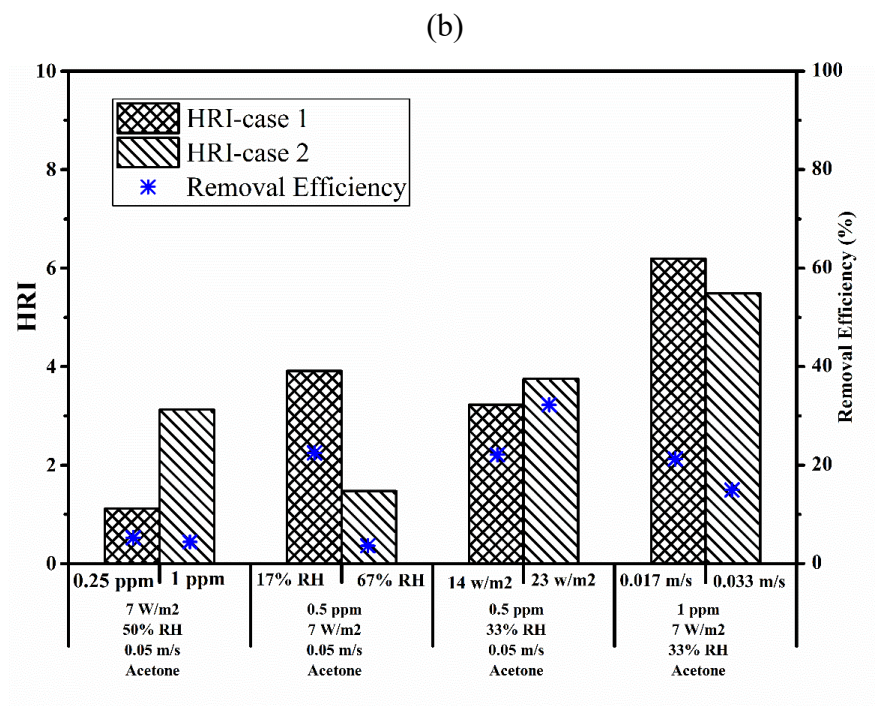
Fig. 7.13. Health related index of pollutant in outlet stream at various operating conditions for (a) Acetone and (b) MEK

114

7.2. Kinetic modeling and reaction mechanism of toluene and by-products in photocatalytic oxidation reactor

Toluene is one of the most predominant indoor environment VOC, which is widely used in paint, building materials and chemical reagents, and its removal can significantly improve indoor air quality; it is associated with short- to long-term health issues, namely eyes and nose irritation, headaches, respiratory illness. Due to the presence of the aromatic ring in the molecule structure of toluene, PCO degradation of toluene results in a complicated path with the formation of various by-products. Many studies have been focused on the identification/quantification of reaction by-products of toluene through PCO. It was reported by some authors that benzaldehyde, benzoic acid, benzyl alcohol, and benzene were the first reaction intermediates/by-products of toluene degradation in PCO. These preliminary intermediates can break down through further oxidation and generate various chemical groups of VOCs, namely, aldehydes, alkanes, acids, and alcohols. The type and quantity of the by-products highly depend on photocatalyst properties and operating conditions. The relationship between generated by-products and operating condition is complicated. This shows the necessity of a deeper understanding of the kinetic reaction of toluene and by-products in PCO. An effective approach to assist in this matter is through the use of mathematical model. The drawback of majority of modeling works on PCO of toluene were neglecting the generation of hazardous by-products, namely aldehydes, due to complicated reaction pathway and formation of various kinds of intermediates/by-products. These by-products can compete with toluene for adsorption on the photocatalyst surface and affect kinetic parameters. For the first time, this work presents the development of by-products predictive model for simulation of generated by-products using a proposed degradation reaction pathway of toluene. To validate the model, toluene was tested in UV-PCO reactor at various operating conditions, such as concentration, relative humidity, irradiance and air velocity. Nonlinear curve fitting analysis was applied to estimate unknown kinetic parameters of the model, including reaction rate coefficients of toluene and by-products. In the end, the impact of toluene and formed by-products on human health were analyzed by the health risk index at different operating conditions.

7.2.1. Results and discussion

7.2.1.1. By-products measurement and carbon balance

Table 7.10 reports the list of generated by-products detected through analytical methods during the PCO of toluene at steady-state condition. The results indicated that major by-products of toluene were from the aldehyde group, in which light aldehydes such as acetaldehyde and formaldehyde have a higher concentration. In addition, other VOCs from aromatic, alcohol and acid groups were detected by TD-GC/MS, namely benzene, ethanol and acetic acid. A small amount of acetone from the ketone group was also detected by both HPLC and TD-GC/MS. The generated carbon dioxide concentration (detected by GC/FID method) was used to evaluate the mineralization efficiency of toluene by Eq. (5.12).

Table 7.10 shows the carbon balance analysis for quantitively measured compounds in PCO of toluene. The major carbon concertation in the outlet flow was related to the unreacted toluene and carbon dioxide, and around 16.6% of toluene mineralized into carbon dioxide. Only 4.5% of toluene was converted to by-products that were measured by analytical methods. However, a very

small portion of converted toluene into by-products (around 0.37%) was not detected. This analysis demonstrates that kinetic modeling based on detected by-products can represent the behavior of PCO for degradation of toluene under TiO_2/SFF photocatalyst.

Table 7.10: Generated by-products in the PCO of toluene detected by analytical methods at steady-state with carbon balance analysis (RH=33%, Q=30 L/min)

Compound (i)	Molecular formula	Analytical method			Concentrations of toluene and generated by-products	
		TD- GC-MS	HPLC	GC-FID	C_i [ppb]	$C_{i,C}$[b] [ppb]
Toluene [a]	C_7H_8	✓			778.96	5452.7
Benzaldehyde	C_7H_6O	✓	✓		10.47	73.3
Butyraldehyde	C_4H_8O	✓	✓		8.95	35.8
Propionaldehyde	C_3H_6O		✓		15.95	47.9
Acetone	C_3H_6O	✓	✓		0.7	2
Acetaldehyde	C_2H_4O	✓	✓		33.2	66.45
Formaldehyde	CH_2O	✓	✓		83.45	83.45
Benzene	C_6H_6	✓			pd	-
Ethanol	C_2H_6O	✓			pd	-
Acetic acid	$C_2H_4O_2$	✓			pd	-
Carbon dioxide	CO_2			✓	1150	1150

pd: peak detected

[a] Carbon atom concentration of toluene in the inlet for $C_{feed,Tol}$ =991 ppb was $C_{C\text{-}Tol,feed}$ =6937 ppb.

[b] $C_{i,C} = C_i * n(C)$

7.2.1.2. Possible reaction pathways

PCO reaction pathways of toluene under UV light were proposed by several authors [41, 51, 226-228]. In this study, a possible reaction pathway has been proposed for toluene degradation in PCO based on the literature in Fig. 7.14. ˙OH radical produced from photo-oxidation degrades adsorbed toluene on the TiO_2 surface. The initial step in the decomposition of toluene is either direct oxidation by the addition of ˙OH radical to the aromatic ring of toluene or the **H**-abstraction from methyl group by ˙OH radical [228]. The latter leads to the formation of benzyl radical and then to the production of benzaldehyde, benzoic acid and benzyl alcohol [45, 49]. These three intermediates were attacked by ˙OH radical addition to the aromatic ring, which resulted in the opening of aromatic ring. The transient state compound generated after ring-opening has several carbonyl bonds and alkenyl bonds, which can be attacked by •OH radical and leads to shorter-carbon-chain, including aldehydes and alcohols. Benzoic acid can also be degraded via a photo-Kolbe reaction (by holes (h^+)) to create benzene [51, 228].

Moreover, direct oxidation of toluene by addition of ˙OH to the aromatic ring results in opening aromatic ring and generation of transition state compound, which can be oxidized further to form acetone and some acids [229, 230]. Acetone and propionaldehyde degradation reaction proceeds by a series of oxidation steps to generate other by-products with smaller molecular mass such as

ethanol, methanol, acetic and formic acids, as well as acetaldehyde and formaldehyde [51, 226]. Additionally, according to the reaction pathway proposed by Mo et al. [51], the generated butyraldehyde is not oxidized further in the PCO of toluene. In this study, it was also assumed that propionaldehyde is mostly produced by oxidation of benzaldehyde and its generation by butyraldehyde is negligible.
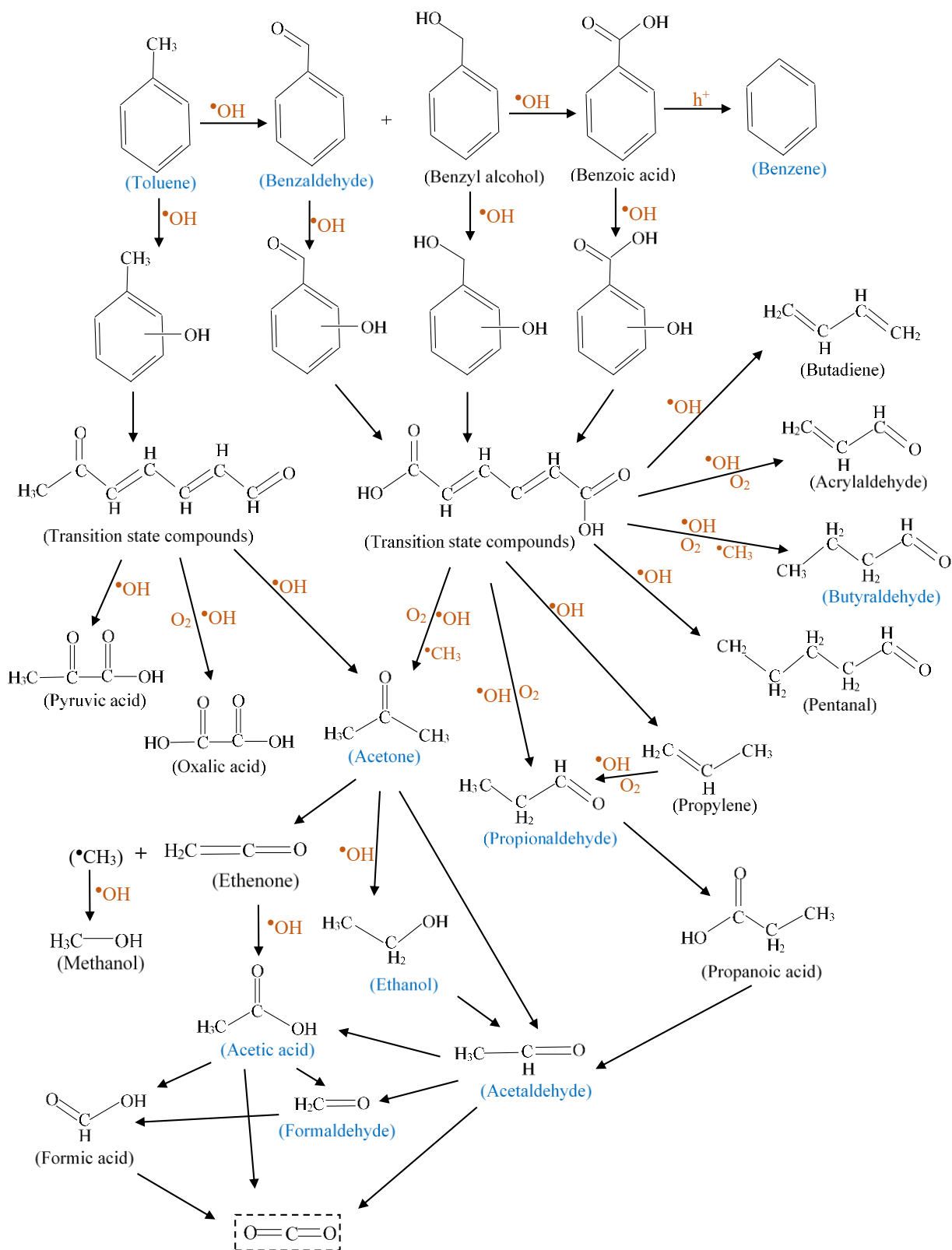
Fig. 7.14: Complete possible reaction pathway for toluene degradation in the PCO based on literature[41, 51, 228, 230].

A simplified reaction pathway (Fig. 7.15) was proposed based on the identified by-products reported in Table 7.10 and in accordance with Fig. 7.14. In Fig. 7.15, the paths including detected by-products in the present study have been selected from the complete possible reaction mechanism (Fig. 7.14). In order to perform modeling of by-products, those compounds that were measured quantitively (see Table 7.10) were considered for the kinetic analysis. Therefore, the

paths with dashed arrows were neglected as carbon balance analysis in the previous section indicated that the mass of by-products not measured quantitively was negligible (around 0.37%).
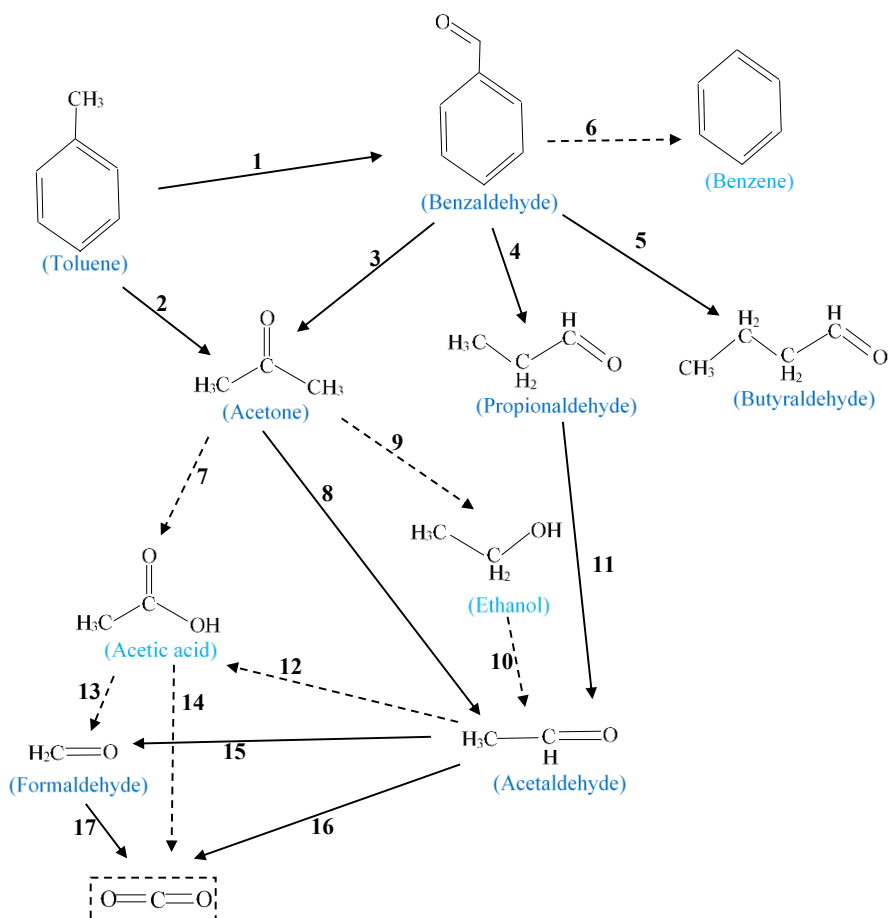
Fig. 7.15. Simplified possible reaction pathway for toluene degradation in PCO (solid arrows are major path, dashed arrows are minor path).

7.2.1.3. PCO reaction rate of by-products

The extended L-H rate expression was employed to describe the PCO reaction rate of toluene and by-products on the basis of possible reaction pathways (Fig. 7.15). The following main assumptions were made to develop the reaction rate model for each compound:

1) First-order and elementary reaction for each VOC,
2) The generation and consumption rates of other intermediates in the pathway are equivalent, and
3) The production of unidentified by-products is negligible.

d'Hennezel et al.[45] found out that the primary pathway in PCO of toluene is the hydrogen abstraction from the methyl group by $^\bullet$OH radical, which leads to the formation of benzyl radical and then benzaldehyde (path 1 in the reaction mechanism). In this regard, two different scenarios were considered for the development of the reaction rate model; 1) the total degradation of toluene is through path 1 (Scenario T-1), and 2) the conversion of toluene is by both paths 1 and 2 (Scenario T-2). In the latter scenario, acetone is generated via toluene and benzaldehyde. Table 7.11 presents reaction rates of toluene and by-products for two scenarios according to the proposed reaction pathways in Fig. 7.15. In this table, the coefficient k_i represents the apparent rate coefficient of each VOC, which is defined by:

$$k_i = k_{r,i} * K_i \qquad (7.5)$$

where $k_{r,i}$ and K_i are the PCO degradation rate coefficient and adsorption equilibrium coefficient, respectively. Due to a large number of unknown parameters in the reaction rate model, the adsorption coefficient of toluene and acetone molecules were obtained separately under dark condition. In addition, as major identified by-products were from the aldehyde group, their adsorption coefficients were lumped into light and heavy aldehydes species to prevent overparameterization problems. Subsequently, by-product adsorption coefficient in Table 7.11 was simplified as:

$$\sum_i K_{byp,i} C_{byp,i} = K_{AC} C_{AC} + \sum_i K_{L-Ald,i} C_{L-Ald,i} + \sum_i K_{H-Ald,i} C_{H-Ald,i} = K_{AC} C_{AC} + $$
$$K_{L-Ald}(C_{AA} + C_{FA}) + K_{H-Ald}(C_{BZ} + C_{BT} + C_{PA}) \tag{7.6}$$

where K_{L-Ald} and K_{H-Ald} represent the adsorption coefficients of light and heavy aldehydes, respectively. It worth mentioning that formaldehyde and acetaldehyde were regarded as light aldehyde and others were considered as heavy aldehyde groups.

Table 7.11: Reaction rates of toluene and by-products for two proposed scenarios (T: toluene, BZ: benzaldehyde, BT: butyraldehyde, PA: propionaldehyde, AC: acetone, AA: acetaldehyde, FA: formaldehyde)

Scenario T-1	Scenario T-2
$r_T = -r_1 = -(k_1)C_T \alpha^*$	$r_T = -r_1 - r_2 = -(k_1 + k_2)C_T \alpha$
$r_{BZ} = r_1 - r_3 - r_4 - r_5 = (k_1 C_T - k_3 C_{BZ} - k_4 C_{BZ} - k_5 C_{BZ})\alpha$	$r_{BZ} = r_1 - r_3 - r_4 - r_5 = (k_1 C_T - k_3 C_{BZ} - k_4 C_{BZ} - k_5 C_{BZ})\alpha$
$r_{BT} = r_5 = (k_5 C_{BZ})\alpha$	$r_{BT} = r_5 = (k_5 C_{BZ})\alpha$
$r_{PA} = r_4 - r_{11} = (k_4 C_{BZ} - k_{11} C_{PA})\alpha$	$r_{PA} = r_4 - r_{11} = (k_4 C_{BZ} - k_{11} C_{PA})\alpha$
$r_{AC} = r_3 - r_8 = (k_3 C_{BZ} - k_8 C_{AC})\alpha$	$r_{AC} = r_2 + r_3 - r_8 = (k_2 C_T + k_3 C_{BZ} - k_8 C_{AC})\alpha$
$r_{AA} = r_8 + r_{11} - r_{15} - r_{16}$ $\qquad = (k_8 C_{AC} + k_{11} C_{PA} - k_{15} C_{AA} - k_{16} C_{AA})\alpha$	$r_{AA} = r_8 + r_{11} - r_{15} - r_{16}$ $\qquad = (k_8 C_{AC} + k_{11} C_{PA} - k_{15} C_{AA} - k_{16} C_{AA})\alpha$
$r_{FA} = r_{15} - r_{17} = (k_{15} C_{AA} - k_{17} C_{FA})\alpha$	$r_{FA} = r_{15} - r_{17} = (k_{15} C_{AA} - k_{17} C_{FA})\alpha$

$$^* \; \alpha = \frac{I^{0.5}}{1 + K_T C_T + K_w C_w + \sum_i K_{byp,i} C_{byp,i}}$$

7.2.1.4. Kinetic parameters and model validation

The adsorption equilibrium constant indicates the affinity between adsorbate and adsorbent. Thus, the adsorption coefficient of VOC on the TiO$_2$/SFF filter surface under UV light is the same as the one under dark condition [208, 215]. The equilibrium adsorption of toluene under dark condition for different relative humidity levels is displayed in Fig. 7.16. The adsorption isotherm of Eq.(3.21) was applied to evaluate the adsorption coefficients of toluene and water molecules. The result of curve fitting to experimental data is demonstrated in Table 7.12.

In order to perform kinetic modeling of toluene and by-products in the PCO reactor, the mass balance equation combined with the validated irradiation field model [215] were applied in accordance with the reaction rate expression developed in Table 7.11. The kinetic parameters of the PCO reaction were estimated under surface reaction limitation as it was found out in previous work that mass transfer resistance in the system is negligible in comparison with photoreaction in the reactor [215].

In order to evaluate the unknown kinetic parameters of the model, the curve fitting analysis was performed in two steps. First, the degradation reaction rate of toluene was employed separately to find the toluene reaction coefficient. Then, it was used in the general reaction rate model of Table

7.11 to estimate kinetic rate coefficients of by-products. In the latter step, only concentrations of by-products were used as the objective function for minimization of the scaled residual and true error between experimental data and model. In this way, the unknown coefficients were estimated with greater accuracy since the concentrations of by-products were much less than toluene. Fig. 7.17 displays the result of curve fitting of the model to experimental data for toluene degradation in PCO. Table 7.13 also reports the values of estimated parameters with high fitting accuracy (R^2=0.99). The adsorption coefficients of acetone and light aldehydes were computed in previous studies [215, 231]. The reaction rate coefficient of toluene and adsorption constants of heavy aldehydes were estimated in the present study and provided in Table 7.13. In the same chemical group (aldehyde), molecules with higher molecular weight and boiling point have greater intermolecular forces, leading to a superior adsorption tendency towards TiO_2 [68]. Table 7.13 shows that the adsorption coefficient of heavy aldehydes is greater than light aldehydes.

The results of kinetic modeling using both reaction rate scenarios (T-1 and T-2) are provided in Table 7.14. Both reaction rate scenarios led to a high coefficient of determination (R^2=0.98) and low residual error (S^2_R). According to the very small value of k_2 compared to k_1, major degradation of toluene occurs through the path $Touene \overset{1}{\rightarrow} Benzaldehyde$ while minor portion of toluene converts to acetone via the path $Touene \overset{2}{\rightarrow} Acetone$. PCO reaction of acetone with the same photocatalyst was studied in previous research work[231], and its kinetic parameters were evaluated. The reaction rate coefficients of k_8, k_{15}, k_{16}, and k_{17} of that study were used for the reaction rate model in this work since the same photocatalyst with similar characteristics was utilized. In this way, other unknown kinetic parameters can be estimated with narrow confidence intervals and higher reliability, as there are many unknown reaction rate coefficients in photodegradation of toluene. The value of kinetic parameters reported in Table 7.14 indicates that heavier aldehydes had a greater reaction rate coefficient due to superior adsorption tendency. In this regard, the rate coefficients followed the order of benzaldehyde > propionaldehyde > acetaldehyde > formaldehyde ($k_3+k_4+k_5>k_{11}>k_{15}+k_{16}>k_{17}$). The high value of k_4 demonstrates that the majority of benzaldehyde was decomposed towards propionaldehyde generation, and less portion of benzaldehyde was converted to acetone.

Fig. 7.18 illustrates the result of the experiment and model of by-products for curve fitting at various concentrations using both scenarios T-1 and T-2. Figure (**a**) shows the results for light aldehyde and figure (**b**) shows the results of heavy aldehyde and acetone. As the inlet concentration of toluene increases, the generation of all by-products increases sharply since higher concentration results in a larger reaction rate and consequently the production of more mass of by-products. In the case of butyraldehyde, the slope of concentration profile reduces as the inlet toluene concentration increases. It can be attributed to the huge reaction rate coefficient of benzaldehyde to propionaldehyde (k_4), which causes more generation of other aldehydes at higher inlet concentrations of toluene. At the low inlet concentration of the challenge compound, more active sites are available for benzaldehyde to convert to butyraldehyde, which results in a relatively greater outlet concentration of butyraldehyde.

Table 7.15 displays the cross-correlation matrix between the estimated kinetic coefficients of by-products for scenarios T-1 and T-2. The cross-correlation coefficients among the parameters in

both scenarios were relatively low and close to zero except correlation between k_1 and k_3 in scenario T-2. By reducing the number of unknown parameters in scenario T-1, the matrix led to a very low and acceptable cross-correlation coefficient among the estimated kinetic coefficients.

Fig. 7.19 to Fig. 7.21 demonstrate the model validation for toluene and by-products at various operating conditions. The effect of relative humidity level on toluene degradation and by-product generation at a fixed concentration is displayed in Fig. 7.19. As the water content in PCO increases, more active sites are occupied by water, due to the hydrophilicity character of TiO_2. It results in a greater inhibitive effect of water on the surface for adsorption of toluene and then, removal efficiency decreases, leading to a higher outlet concentration of toluene. In the case of by-products generation, as the concentration of benzaldehyde in the gas phase increased and the concentration of butyraldehyde and formaldehyde reduced. The generation of other by-products was relatively constant. Owing to lower available active sites for adsorption at higher RH levels, generated benzaldehyde desorbs into the gas phase and its concentration increase gradually. However, butyraldehyde and formaldehyde generations are lower owing to less reaction rate coefficient in comparison with others that have greater rate constants.

Fig. 7.20 display the impact of irradiation on toluene and by-products concertation in the gas phase at concentration of 500 ppb. Raising irradiation in the PCO leads to enhancement of photocatalytic activity and then greater removal efficiency for toluene removal (or lower concentration). Due to the greater PCO reaction rate at higher irradiation, a greater amount of benzaldehyde, propionaldehyde, and acetaldehyde were decomposed to butyraldehyde and formaldehyde. Accordingly, the concentration of two former by-products decreased and that of two latter ones increased. The change in concentration of acetone is much less than other by-products, because of its small value of reaction rate coefficient compared to other by-products.

Fig. 7.21 shows the influence of air velocity on toluene removal efficiency and by-products generation. Reducing the velocity elevates the residence time of VOCs in PCO filter for more reaction on the surface. This results in higher removal efficiency and lower outlet concentration of toluene. Besides, the increase in residence time causes PCO reaction to proceed further through the pathway. Consequently, conversion of benzaldehyde and propionaldehyde to other by-products increased and concentrations of other by-products enhanced. Meanwhile, the concentrations of benzaldehyde and propionaldehyde, due to very high reaction rate coefficients, decreased. In general, all operating conditions had a significant impact on the by-product formation and toluene degradation in PCO and the developed model could predict the concentration of all VOC with acceptable accuracy.

The involvement of toluene and by-products in carbon balance analysis was also examined at various residence times, as shown in Fig. 7.22. The mineralization efficiency, as indicated by CO_2 concentration, is higher at longer residence time. Besides, with raising residence time, by-products generation and undetected by-products increased gradually. However, the mass of unreacted toluene reduced as higher amount of toluene decomposed in PCO. This figure demonstrates that when residence time (lowering air velocity) increased, intermediates/by-products have more time to degrade into carbon dioxide, which results in an increment in toluene removal and carbon dioxide production at the same time. However, owing to the increase in by-product formation, this

result requires to be more investigated in human's health risk aspect before its application in real life. The implications of toluene and by-products in the human health context will be reported in section 7.2.1.5. According to the very small amount of carbon related to unreacted by-products and acceptable accuracy of the developed mathematical model, the proposed model has a high potential to be applied on a larger scale for real application.
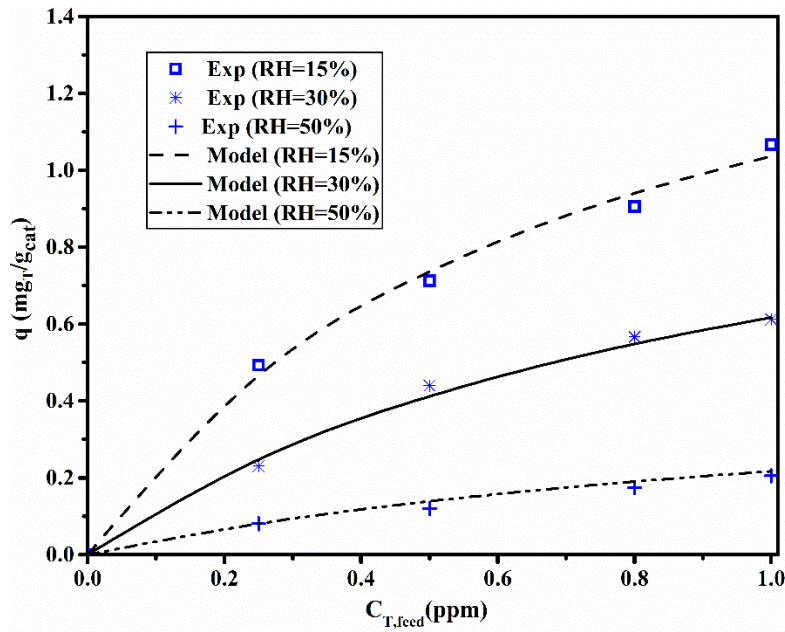
Fig. 7.16. Adsorption of toluene on TiO_2/SFF for different relative humidity levels

Table 7.12: Adsorption parameters of toluene on TiO_2/SFF filter.

Parameter	Value	95% CI
q_m (mg_T/g_{cat})	$-0.0001 C_w$ [ppm]$+2.34$	-
K_T (ppm^{-1})	2.43	0.5
K_w (ppm^{-1})	1.63×10^{-4}	0.7×10^{-4}
R^2	0.99	
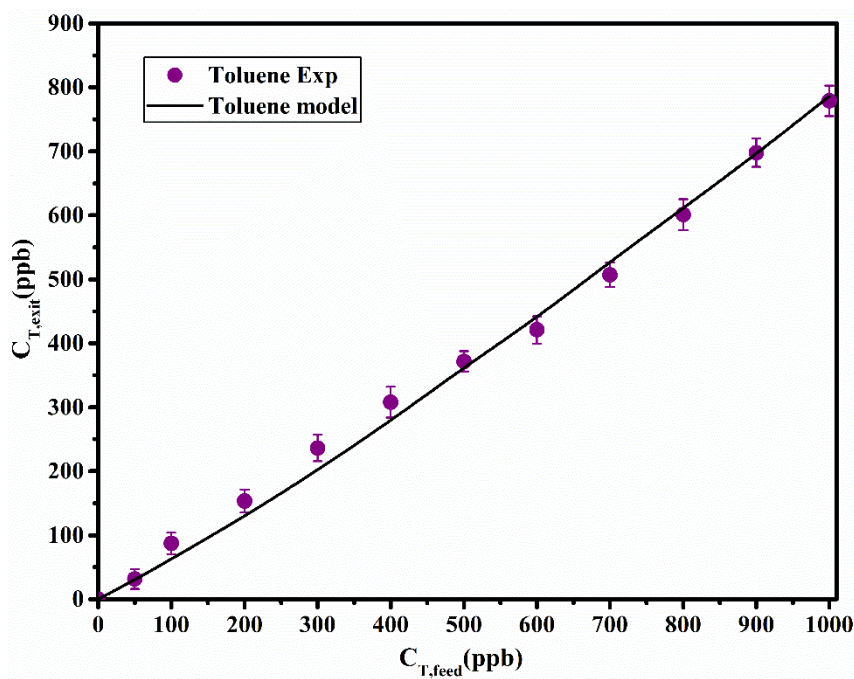
Fig. 7.17. Results of curve fitting for toluene at u=0.05 m/s; RH_{Feed}=33%; I_{ave}=7 W/m^2

Table 7.13: Reaction and adsorption parameters for toluene in PCO.

Parameter	Value	95% CI
k_T (s^{-1} W$^{-0.5}$ m)	46.4×10^3	3.7×10^3
K_T (ppm^{-1})	2.43	-
K_w (ppm^{-1})	1.63×10^{-4}	-
K_{AC} (ppm^{-1})	2.32	-
K_{L-Ald} (ppm^{-1})	14	-
K_{H-Ald} (ppm^{-1})	18.7	7.5
R^2	0.99	
$S^2{}_R \times 10^4$ (ppm^{-2})	42	

(a)

(b)
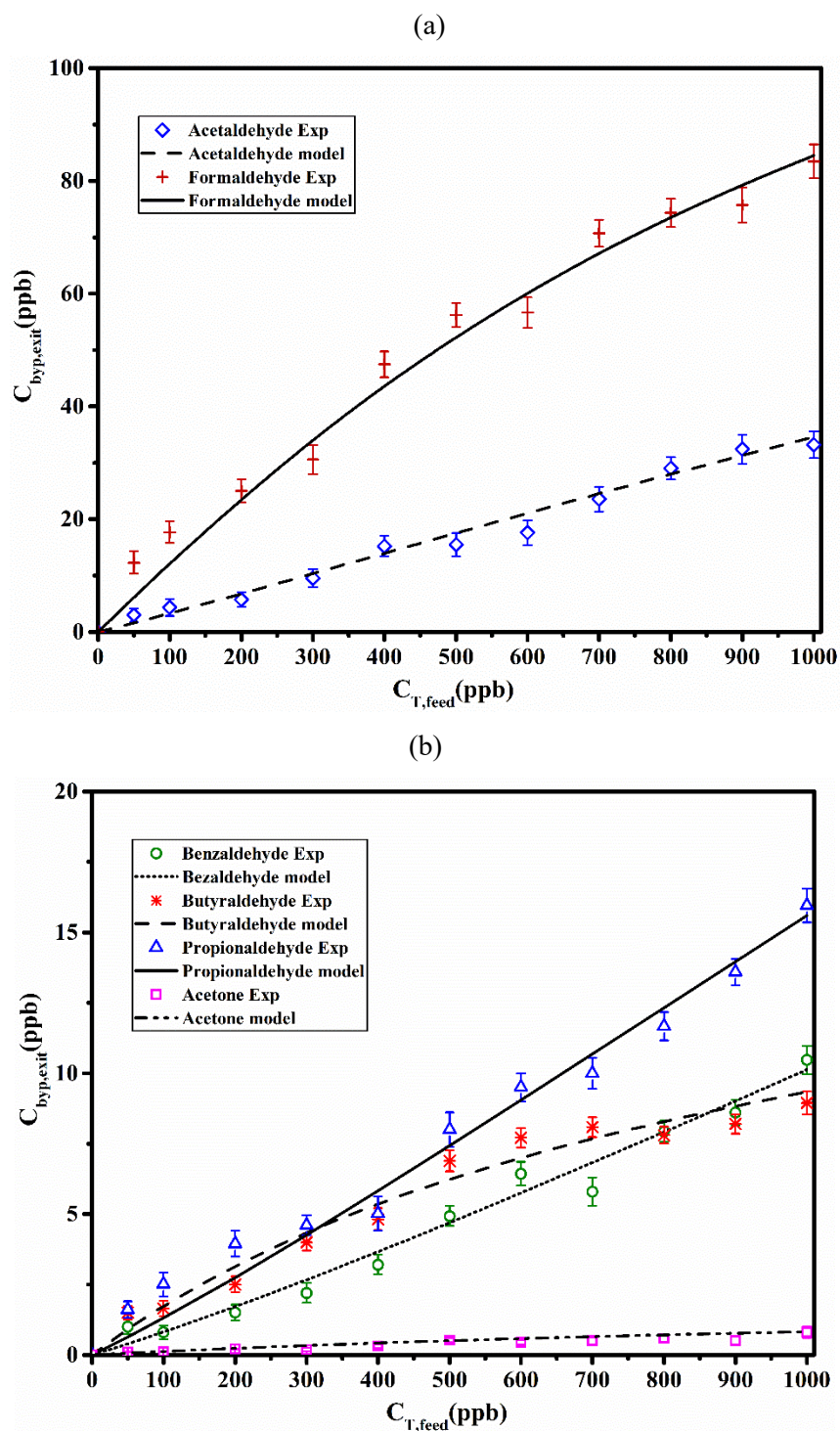
Fig. 7.18. Results of curve fitting for toluene by-products using scenarios T-1 and T-2; a) light aldehydes b) acetone and heavy aldehydes (u=0.05 m/s; RH$_{Feed}$=33%; I$_{ave}$=7 W/m^2)

Table 7.14: Kinetic parameters of toluene and its by-products for two possible scenarios (operating conditions are: u=0.05 m/s; RH_{Feed}=33%; I_{ave}=7 W/m^2)

Parameter	Scenario T-1		Scenario T-2	
	Values [s^{-1} $W^{-0.5}$ m]	95% CI	Values [s^{-1} $W^{-0.5}$ m]	95% CI
k_1	46.4×10^3	-	46.2×10^3	4.6×10^3
k_2	-		0.2×10^3	-
k_3	17.8×10^3	3.5×10^3	9.1×10^3	3.5×10^3
k_4	3352×10^3	613×10^3	3318.5×10^3	606×10^3
k_5	162.8×10^3	42.1×10^3	160.9×10^3	41.8×10^3
k_8	43.9×10^3	-	43.9×10^3	-
k_{11}	1988.1×10^3	234.7×10^3	1987.6×10^3	234.7×10^3
k_{15}	746.2×10^3	-	746.2×10^3	-
k_{16}	6.4×10^3	-	6.4×10^3	-
k_{17}	116.7×10^3	-	116.7×10^3	-
R^2	0.98		0.98	
$S^2_R \times 10^4$ (ppm^{-2})	2.31		2.31	

Table 7.15: Cross-correlation coefficients for the estimated kinetic parameters of by-products in PCO of toluene

	Scenario T-1					Scenario T-2				
	k_3	k_4	k_5	k_{11}		k_1	k_3	k_4	k_5	k_{11}
k_3	1				k_1	1				
k_4	0.21	1			k_3	0.69	1			
k_5	0.09	0.34	1		k_4	-0.04	-0.03	1		
k_{11}	0.08	-0.14	-0.02	1	k_5	-0.04	-0.04	0.26	1	
					k_{11}	-0.02	-0.02	-0.14	-0.01	1

(a)
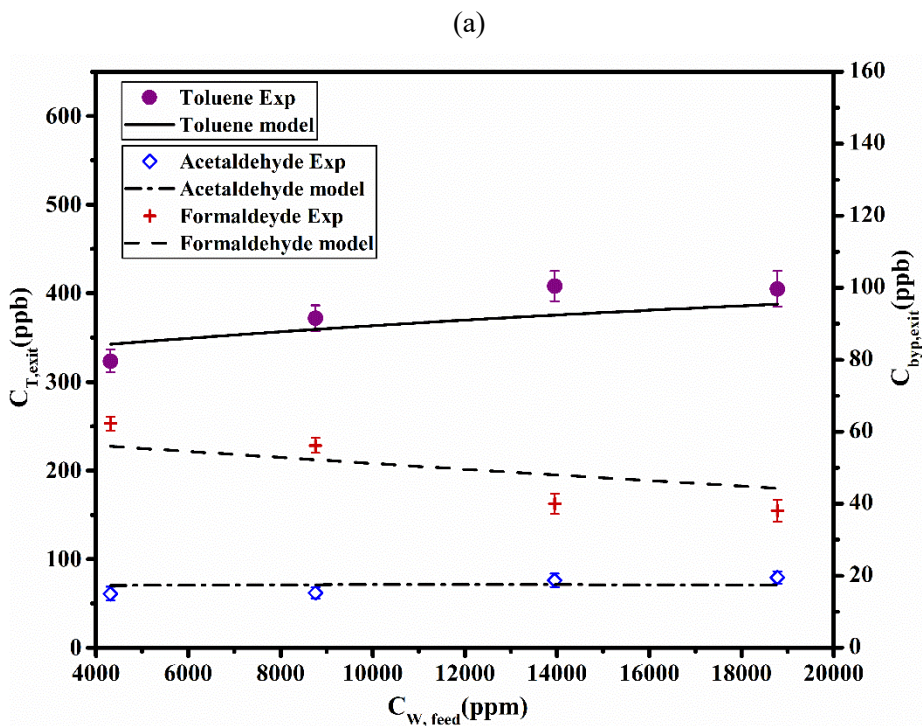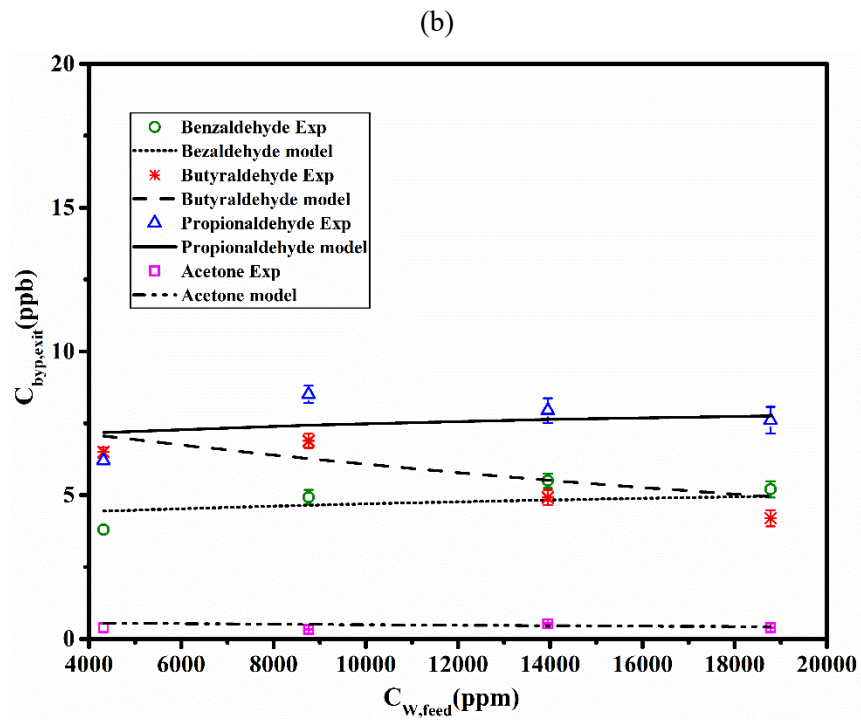
Fig. 7.19. Effect of relative humidity [RH$_{Feed}$] on toluene degradation and by-products generation in PCO; (a) toluene and light aldehydes (b) acetone and heavy aldehydes (C$_{feed}$=500 ppb; u=0.05 m/s; I$_{ave}$=7 W/m^2)

(a)

(b)
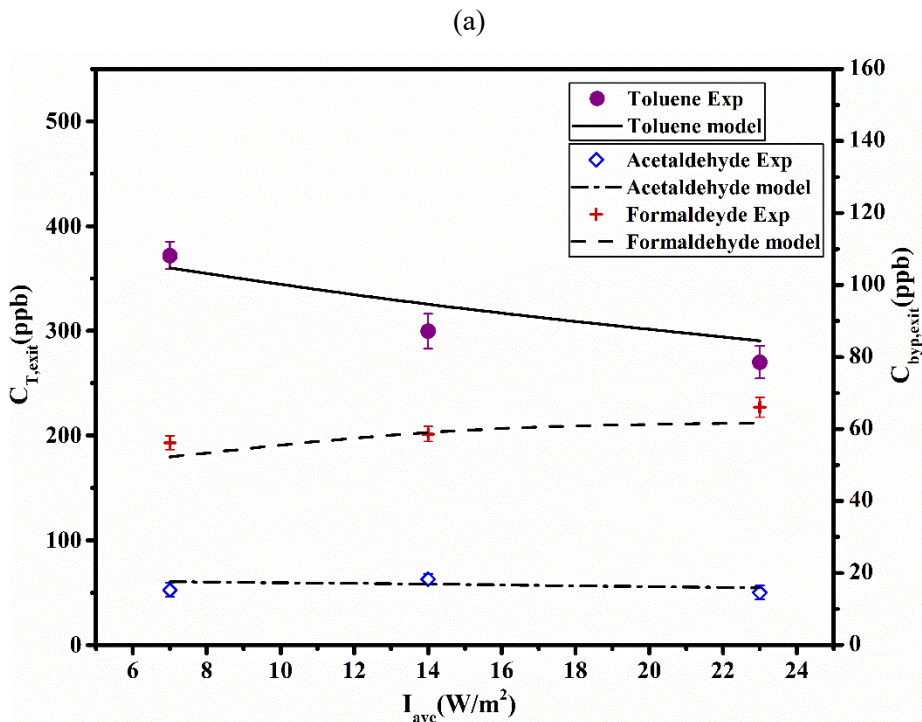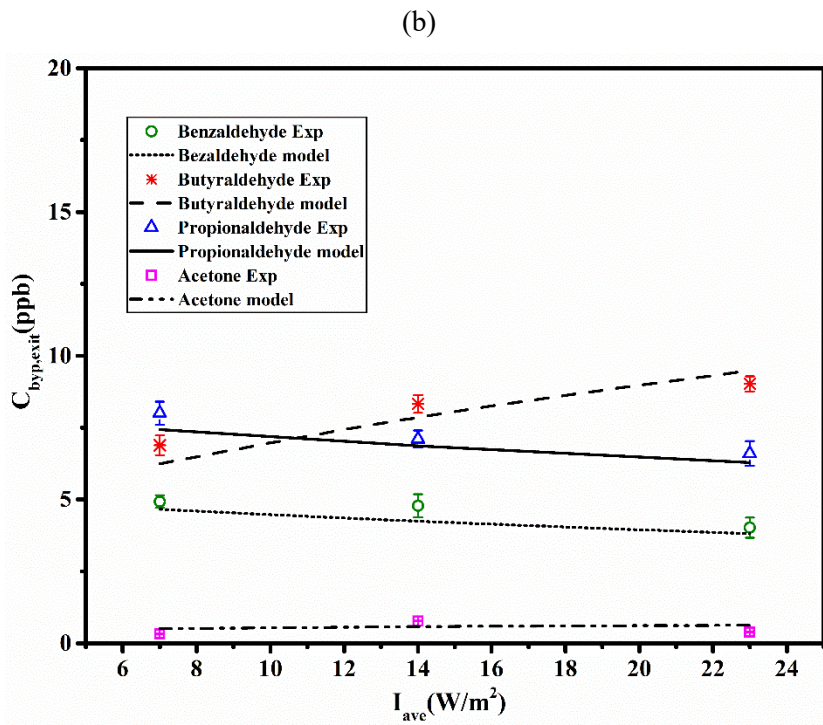
Fig. 7.20. Effect of irradiation [I] on toluene degradation and by-products generation in PCO; (a) toluene and light aldehydes (b) acetone and heavy aldehydes (C_{feed}=500 ppb; RH_{Feed}=33%; u=0.05 m/s)

(a)
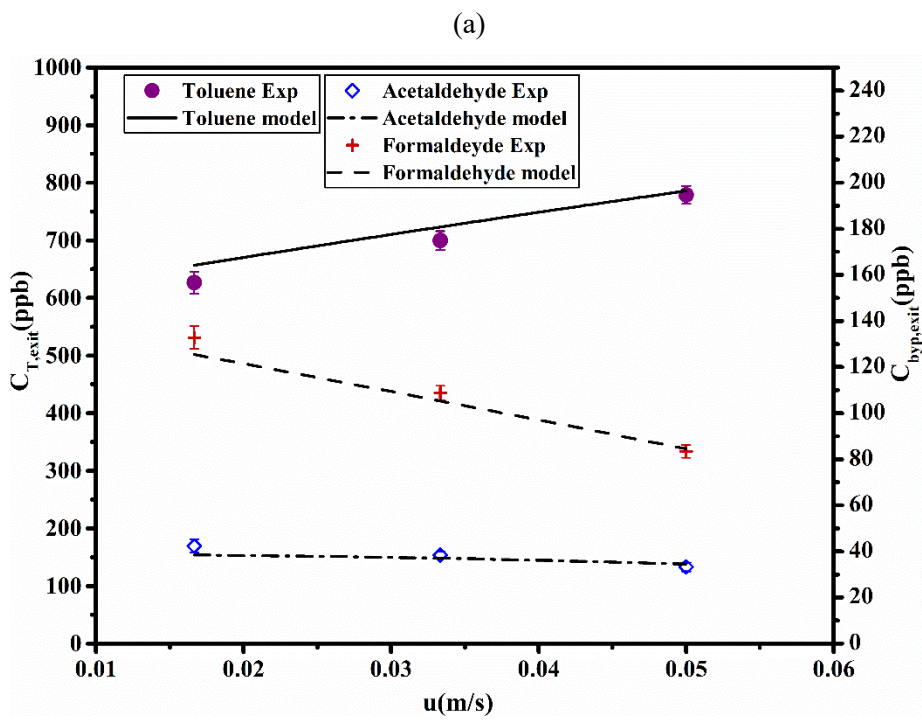
(b)
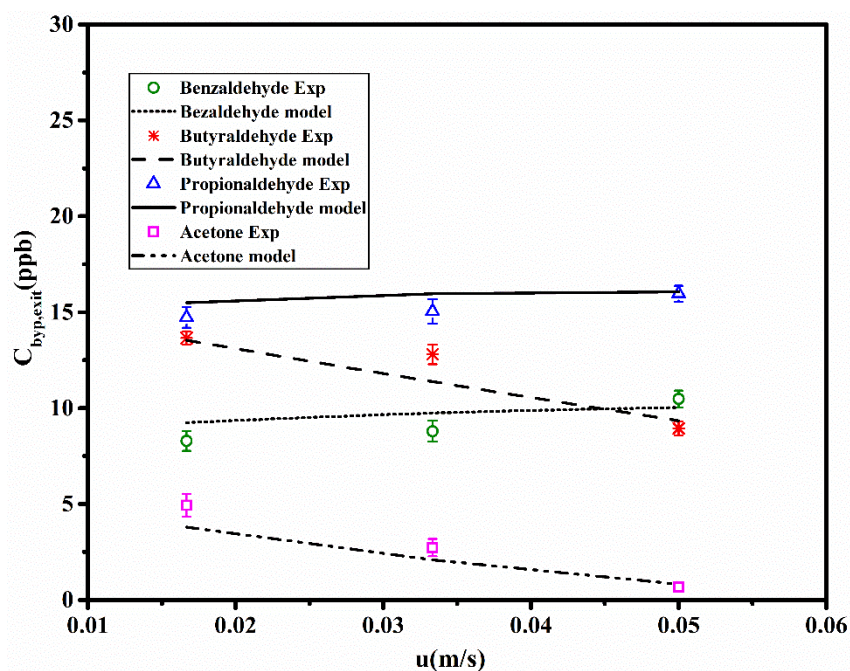
Fig. 7.21. Effect of velocity [u] on toluene degradation and by-products generation in PCO;
(a) toluene and light aldehydes (b) acetone and heavy aldehydes (C_{feed}=1000 ppb;
RH_{Feed}=33%; I_{ave}=7 W/m^2)
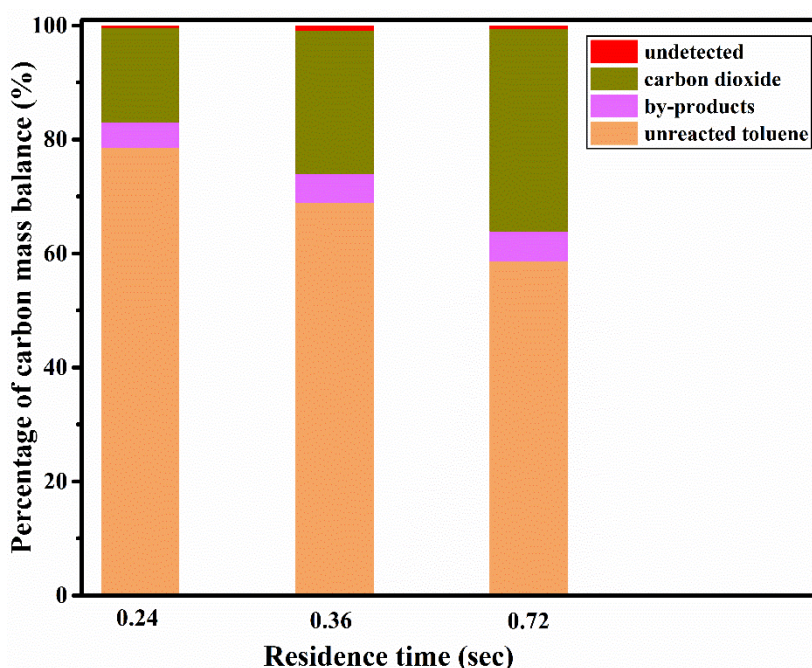
Fig. 7.22. Carbon mass balance of the photocatalytic oxidation of toluene for various residence
time (C_{feed}=1000 ppb; RH_{Feed}=33; I_{ave}=7 W/m^2)

7.2.1.5. Impact of toluene and generated by-products on human health

Due to the potential adverse health effect of toluene and formed by-products on human health, Health Risk Index (HRI) is used to evaluate their negative health effect. REL values of toluene and by-products were reported by some research institutes such as US National Institute for Occupational Safety and Health, California Office of Environmental Health Hazards Assessments, US Green Building Council, LEED v4.1, and etc. (see Table 7.16). Furthermore, some by-products, such as benzene, acetaldehyde and formaldehyde are classified as carcinogens by The International Agency for Research on Cancer (IARC).

127

HRI values of pollutants in the inlet and outlet of PCO reactor were determined under various operating conditions in Fig. 7.23-a. Although PCO removes some toluene in the flow thereby reducing its contribution to the HRI value, formation of by-products actually increased the HRI value in the flow. For instance, reducing velocity (increasing residence time) elevates the HRI dramatically at the concentration of 1 ppm, in spite of higher removal efficiency at low velocity. It was found that formaldehyde was the most contributing VOC to the increased HRI value owing to its low REL (0.016 ppm) and relatively high concentration among measured by-products at downstream of PCO. Fig. 7.23-b illustrated the effect of excluding formaldehyde from generated by-products. In all cases of this figure, the HRI index of downstream became less than upstream, which indicates the potential of using PCO for toluene removal in the indoor environment. This can be achieved by adding an adsorption filter for removing formaldehyde from the outlet of PCO. For instance, ASHRAE standard [232] recommended the permanganate-impregnated alumina media to be used for the removal of formaldehyde.

Table 7.16: Health-related information for toluene and by-products

VOC	REL (ppm)	REL data source	IARC carcinogenic classification
Toluene	0.22	OEHHA[a]	Group 3, not classifiable as to its carcinogenicity to humans
Benzaldehyde	2	AIHA[b]	-
Benzene	0.0017	OEHHA[a]	Group 1, carcinogenic to humans
Butyraldehyde	25	OARS[c]	-
Acetone	13	ATSDR[d]	-
Propionaldehyde	20	AIHA[b]	-
Acetaldehyde	0.078	OEHHA[a], USGBC[e]	Group 2B, possibly carcinogenic to humans
Formaldehyde	0.016	NIOSH[f], USGBC[e]	Group 1, Carcinogenic to humans
Ethanol	1000	NIOSH[f]	-
Acetic acid	10	NIOSH[f]	-

[a] California Office of Environmental Health Hazards Assessments

[b] American Industrial Hygiene Association

[c] The Occupational Alliance for Risk Science

[d] Agency for Toxic Substances and Disease Registry

[e] US Green Building Council, LEED v4.1

[f] US National Institute for Occupational Safety Health
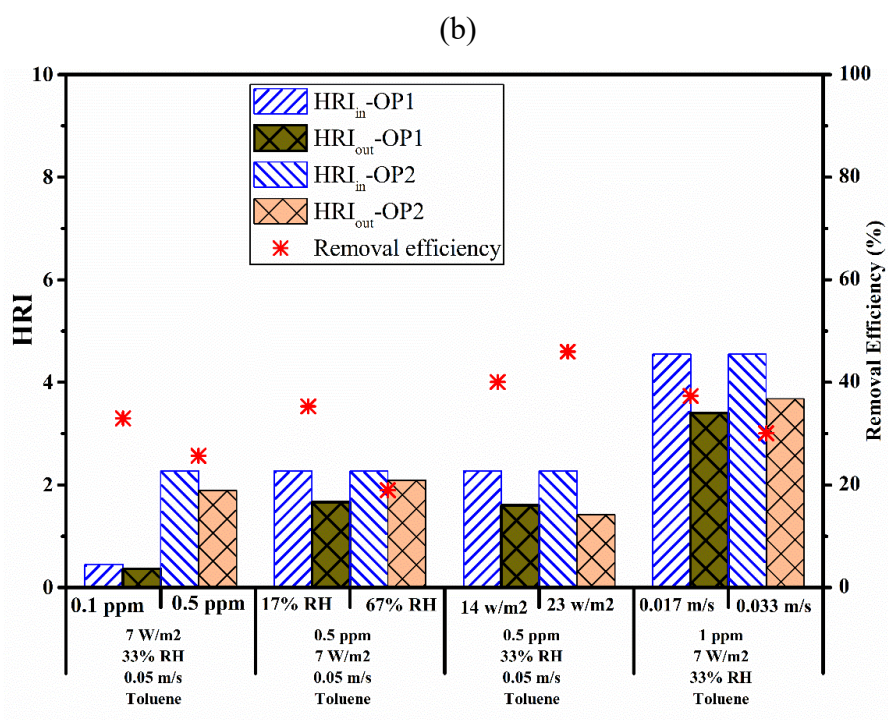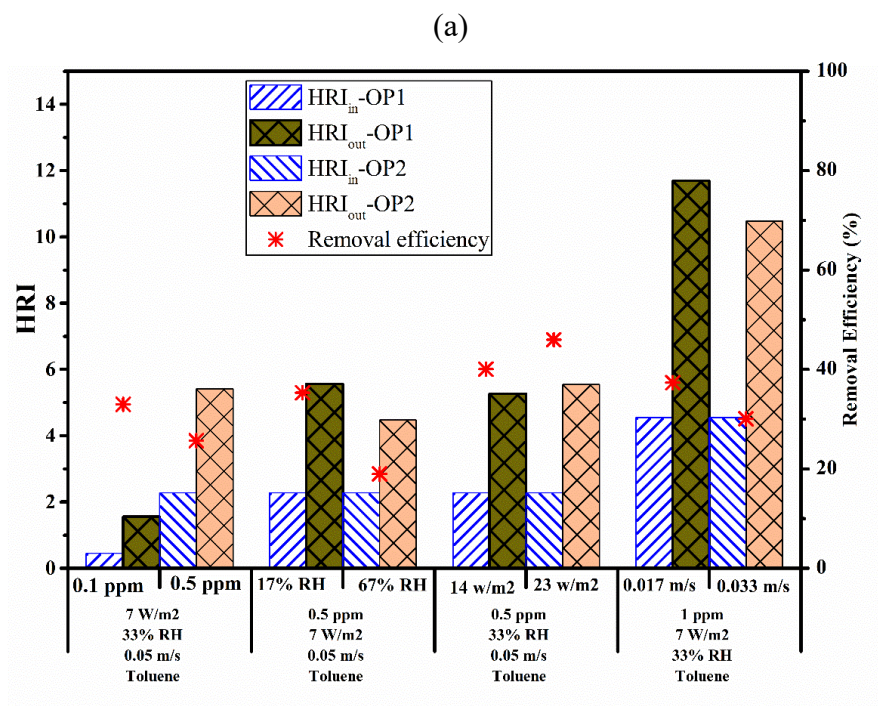
Fig. 7.23. Health related index of toluene and by-products in outlet stream at various operating conditions (OP1 and OP2) by considering (a) formaldehyde and (b) no formaldehyde

8. Conclusions and recommendations

8.1. Summary and conclusion

The increasing concern of health issues from indoor air pollution has significantly attracted worldwide attention for the removal of VOCs. Photocatalytic oxidation (PCO) is an innovative and promising technology for removing VOCs from indoor environment. However, the formation of hazardous by-products hinders the commercialization application of this technology. The main objective of this research was the development of a novel mathematical model to predict VOCs and generated by-products in PCO reactor. In this model, transfer of pollutants by advection and dispersion in bulk phase incorporates with the reaction rate based on the extended Langmuir-Hinshelwood model in catalyst phase. CFD modeling was also used to determine the flow distribution in the reactor at various airflow rates. Moreover, the light intensity distribution on the photocatalyst surface was simulated using the linear source spherical emission model (LSSE). The Beer-Lambert model was applied to describe the diminishment of light intensity in the PCO filter. To validate the model, acetone, MEK, and toluene were tested in UV-PCO reactor with a commercial PCO filter (TiO_2 coated on silica fiber felts) at various operating conditions, such as concentration, relative humidity, irradiance and air velocity. Concentrations of challenge compounds and generated by-products were analyzed by analytical methods (TD-GC-MS and HPLC) and then a reaction pathway was proposed according to the identified by-products. The proposed model was able to predict the degradation of challenge compounds and generation of by-products at various operating conditions with acceptable accuracy. The major results of this research are summarized in the following sections.

Major results of Chapter 4:

- CFD model results for different flow rates showed that the UV lamp had a major impact on the flow distribution at the catalyst surface. It was found that with increasing the inlet flow rate, the velocity distribution (regardless of its magnitude) was almost identical.

- Owing to the high porosity of the filter ($\varepsilon = 0.96$), the RTD in the presence and absence of the filter was almost identical.

- The axial dispersion coefficient increased progressively with the increase of the superficial velocity. Due to a low value of the Peclet number (Pe < 100), indicating the extent of axial dispersion, the flow in the reactor could not be considered as an ideal plug flow reactor as a considerable dispersion took place in the reactor.

- Since the reaction rate was extremely high, the resistance to the PCO reaction is negligible in comparison with the mass transfer resistance, accordingly, the overall rate constant was considered identical to the mass transfer coefficient.

- The comparison of the proposed formula for mass transfer coefficient with other available correlations indicated that all these correlations adopted from the literature overestimated the mass transfer coefficient in cases with low Reynolds numbers 0.01<Re<10.

Major results of Chapter 5:

- The magnitude of light intensity increased, but light uniformity decreased when the distance between the lamp and PCO filter was reduced.

- The results of kinetic study on MEK showed that the dispersion model combined with the unimolecular Langmuir-Hinshelwood model considering the inhibiting effect of water molecules and by-products (model *M-3*) can be chosen as the best model.

- The ideal plug flow model failed to predict the system performance at various light intensities and air velocities.

- The mass transfer effect on the PCO reaction for tested air velocities (0.017–0.05 m/s) is negligible, resulting in PCO reaction being the rate-limiting process.

Major results of Chapter 6:

- Inter-model comparison with two other existing models demonstrated that the proposed model in current study predicts PCO removal performance more accurately than others.

- A good agreement between prediction models and experimental data was obtained when the proposed model was used to simulate the PCO reactor in both bench and pilot-scale under various operating conditions.

- A sensitivity analysis using dimensionless model indicated that Da is the most effective parameter for improving removal efficiency because elevating Da sharply increases efficiency, showing removal efficiency is highly sensitive to this number.

- The UV-PCO process was mainly controlled by the reaction (reaction rate-limited process) at lower removal efficiencies. However, for higher removal efficiencies, both advection transport and photochemical reaction rate have a major impact on removal efficiency.

- Practical validation of the dimensionless model for scale-up using bench-scale and pilot-scale at the same operating conditions showed that the bench-scale reactor, due to lower Pe number (higher dispersion), has lower removal efficiency, which was verified by dimensionless model prediction.

- Dimensionless parameters analysis can give useful advice for the scale-up UV-PCO reactor in the real application, both qualitatively and quantitatively.

Major results of Chapter 7 section 1:

- Acetone, formaldehyde, acetaldehyde, propionaldehyde, and acetic acid were detected by analytical methods (TD-GC-MS and HPLC) as by-products of MEK through PCO. As for acetone, formaldehyde, acetaldehyde, acetic acid, and ethanol were identified as by-products.

- It was showed through carbon balance that the mass of undetected by-products and qualitatively detected by-products are negligible.

- The estimated kinetic parameters for PCO of acetone indicated that the major degradation path occurs through acetone → acetaldehyde → formaldehyde → carbon dioxide. In the case of MEK, it was observed that a minor portion of acetaldehyde is

formed through acetone and the major portion of that is created through other intermediates existed in MEK pathway.

- The mass of by-products generated through PCO is proportional to the inlet concentrations of the challenge compounds and the irradiation. However, it is reduced with increased relative humidity and velocity of the air passing through the catalyst.

- For acetone, the concentration level of formaldehyde is greater than acetaldehyde under all testing conditions of PCO. In the case of MEK, concentration of formaldehyde is less than acetaldehyde at high inlet concentration, RH, and velocity.

- The carbon balance analysis demonstrated that as residence time increases, both by-product generation and mineralization efficiency grow since a greater amount of carbon dioxide is formed in the outlet stream.

- In addition to satisfactory model validation under the steady-state condition, the by-product predictive model also provides acceptable accuracy to simulate the performance of the PCO reactor under transient condition.

- The potential health implications of formed by-products using HRI indicated that higher concentration and irradiation as well as lower relative humidity and velocity in PCO system all contribute to increased HRI values owing to the generation of hazardous formaldehyde and acetaldehyde.

- Safer operating conditions for the application of the PCO system with SFF/TiO_2 photocatalyst could be achieved in an environment with lower VOC levels and using PCO reactor with lower irradiation and residence time.

Major results of Chapter 7 section 2:

- Several by-products, including light and heavy aldehydes, ketone, alcohol and light acids were identified by analytical instruments in PCO of toluene. Light aldehydes (formaldehyde and acetaldehyde) were the major by-products of toluene due to higher concentrations among others.

- The carbon balance analysis at concentration of 1ppm showed 16.6% of toluene mineralized into carbon dioxide and the portion of undetected by-products was 0.37%.

- According to the results of curve fitting using the proposed reaction rate model based on possible reaction pathways, toluene mostly decomposed into benzaldehyde at the initial step.

- Benzaldehyde and propionaldehyde had a greater value of the kinetic coefficient in PCO because of the higher adsorption tendency towards TiO_2. It was also concluded that acetone formation from toluene directly is negligible and is largely generated through benzaldehyde degradation.

- Kinetic analysis of toluene indicated that the rate coefficients followed the order of benzaldehyde > propionaldehyde > acetaldehyde > formaldehyde.

- As inlet concentration of toluene increased, the outlet concentrations of unreacted toluene and all generated by-products increased. Higher inlet concentration resulted in greater reaction rate and then higher concentration of by-products in PCO.

- The concentration of toluene and benzaldehyde in the gas phase increased and that of butyraldehyde and formaldehyde reduced with raising the relative humidity and air velocity.

- The generation of acetone and acetaldehyde decreased at higher velocities while their generation almost kept constant at various ranges of relative humidity.

- At higher irradiation, greater amount of toluene, benzaldehyde, propionaldehyde, and acetaldehyde were converted to butyraldehyde and formaldehyde. Accordingly, the concentration of the three former compounds decreased and that of the two latter ones increased.

- The developed model could predict the concentration of toluene and by-products with acceptable accuracy, indicating its high potential to be applied in a real application.

- The health risk index analysis of toluene and generated by-products demonstrated that the removal of toluene in PCO under various operating conditions resulted in a larger HRI compared to upstream.

- Formaldehyde was the most influential pollutant on HRI due to the very low recommended exposure limit and higher generated concentration, and removing formaldehyde from generated by-products can significantly improve HRI.

8.2. Recommendations for further work

According to the finding in this study and drawbacks of the UV-PCO system for the wide commercialization of this technology, the following possible suggestions are recommended for future work in the modeling aspect.

- There are various ranges of VOCs in indoor environments. They can affect the performance and reaction pathway of challenge compounds. Therefore, it is required to develop a kinetic model for the mixture of VOCs for degradation in the UV-PCO system, in which the effect of all input parameters on the performance should be investigated.

- The effect of photocatalyst deactivation, as well as gradual decrement in irradiation from UV lamp on the developed model, should be considered. This requires long-term experiments with continuous injection of pollutants in UV-PCO.

- The developed model can be extended further for different photocatalysts with various characteristics. Because photocatalyst characteristics highly influence the reaction rate of challenge compound and generated by-products in PCO.

- Due to the generation of hazardous light aldehydes during PCO, using an additional adsorption filter after the PCO system can assist wide applicability of air cleaning system in indoor. Therefore, the development of a model to include the performance of both systems in series is required.

- The model developed in this work was validated in small-scale and pilot-scale PCO reactors. Validation of the model in a full-scale system under a higher Reynolds number (shorter residence time) provides a greater potential for the model to be used in a real application.

- Operating condition highly impacts on the removal performance of challenge compound and the mass of generated by-products. Finding the optimal operating condition for PCO by using the optimization method is suggested to minimize the generation of more toxic by-products at acceptable removal efficiency of challenge compounds.

References

1. Austin, B.S., S.M. Greenfield, B.R. Weir, G.E. Anderson, et al., Modeling the indoor environment. Environmental Science & Technology, 1992. **26**(5): p. 850-858.
2. Yu, B., Z. Hu, M. Liu, H. Yang, et al., Review of research on air-conditioning systems and indoor air quality control for human health. International Journal of Refrigeration, 2009. **32**(1): p. 3-20.
3. IEH (2001) Indoor air quality in the home: Final report on DETR Contract EPG 1/5/12, (Web Report W7) Leicester, UK, Institute for Environmental and Health, http://www.le.ac.uk/ieh/publications/publications.html.
4. Madureira, J., I. Paciência, C. Pereira, J.P. Teixeira, et al., Indoor air quality in Portuguese schools: levels and sources of pollutants. Indoor air, 2016. **26**(4): p. 526-537.
5. Mentese, S., N.A. Mirici, T. Elbir, E. Palaz, et al., A long-term multi-parametric monitoring study: Indoor air quality (IAQ) and the sources of the pollutants, prevalence of sick building syndrome (SBS) symptoms, and respiratory health indicators. Atmospheric Pollution Research, 2020. **11**(12): p. 2270-2281.
6. Salvadó-Estivill, I., D.M. Hargreaves, and G. Li Puma, Evaluation of the intrinsic photocatalytic oxidation kinetics of indoor air pollutants. Environmental Science & Technology, 2007. **41**(6): p. 2028-2035.
7. Bahri, M. and F. Haghighat, Plasma-Based Indoor Air Cleaning Technologies: The State of the Art-Review. CLEAN - Soil, Air, Water, 2014. **42**(12): p. 1667-1680.
8. Singh, J., Impact of indoor air pollution on health, comfort and productivity of the occupants. Aerobiologia, 1996. **12**(1): p. 121-127.
9. Wang, S., H. Ang, and M.O. Tade, Volatile organic compounds in indoor environment and photocatalytic oxidation: state of the art. Environment International, 2007. **33**(5): p. 694-705.
10. Sheng, Y., L. Fang, and J. Nie, Experimental analysis of indoor air quality improvement achieved by using a Clean-Air Heat Pump (CAHP) air-cleaner in a ventilation system. Building and Environment, 2017. **122**: p. 343-353.
11. Yao, M., Q. Zhang, D.W. Hand, D. Perram, et al., Adsorption and regeneration on activated carbon fiber cloth for volatile organic compounds at indoor concentration levels. Journal of the Air & Waste Management Association, 2009. **59**(1): p. 31-36.
12. Haghighat, F., C.-S. Lee, B. Pant, G. Bolourani, et al., Evaluation of various activated carbons for air cleaning – Towards design of immune and sustainable buildings. Atmospheric Environment, 2008. **42**(35): p. 8176-8184.
13. Zhao, J. and X. Yang, Photocatalytic oxidation for indoor air purification: a literature review. Building and Environment, 2003. **38**(5): p. 645-654.
14. Farhanian, D. and F. Haghighat, Photocatalytic oxidation air cleaner: identification and quantification of by-products. Building and Environment, 2014. **72**: p. 34-43.
15. Kim, S.B. and S.C. Hong, Kinetic study for photocatalytic degradation of volatile organic compounds in air using thin film TiO2 photocatalyst. Applied Catalysis B: Environmental, 2002. **35**(4): p. 305-315.
16. Boulamanti, A.K., C.A. Korologos, and C.J. Philippopoulos, The rate of photocatalytic oxidation of aromatic volatile organic compounds in the gas-phase. Atmospheric Environment, 2008. **42**(34): p. 7844-7850.
17. Cassano, A.E. and O.M. Alfano, Reaction engineering of suspended solid heterogeneous photocatalytic reactors. Catalysis Today, 2000. **58**(2): p. 167-197.
18. Zhang, G., Q. Xiong, W. Xu, and S. Guo, Synthesis of bicrystalline TiO2 supported sepiolite fibers and their photocatalytic activity for degradation of gaseous formaldehyde. Applied Clay Science, 2014. **102**: p. 231-237.
19. Yang, L., Z. Liu, J. Shi, H. Hu, et al., Design consideration of photocatalytic oxidation reactors using TiO 2-coated foam nickels for degrading indoor gaseous formaldehyde. Vol. 126. 2007. 359-368.
20. Zhong, L. and F. Haghighat, Photocatalytic air cleaners and materials technologies – Abilities and limitations. Building and Environment, 2015. **91**: p. 191-203.
21. Zhong, L., F. Haghighat, P. Blondeau, and J. Kozinski, Modeling and physical interpretation of photocatalytic oxidation efficiency in indoor air applications. Building and Environment, 2010. **45**(12): p. 2689-2697.
22. Mamaghani, A.H., F. Haghighat, and C.-S. Lee, Photocatalytic oxidation technology for indoor environment air purification: The state-of-the-art. Applied Catalysis B: Environmental, 2017. **203**: p. 247-269.
23. Boyjoo, Y., M. Ang, and V. Pareek, Some aspects of photocatalytic reactor modeling using computational fluid dynamics. Chemical Engineering Science, 2013. **101**: p. 764-784.

24. Yu, J., W. Wang, B. Cheng, and B.-L. Su, Enhancement of Photocatalytic Activity of Mesporous TiO2 Powders by Hydrothermal Surface Fluorination Treatment. The Journal of Physical Chemistry C, 2009. **113**(16): p. 6743-6750.

25. Feng, Y., L. Li, M. Ge, C. Guo, et al., Improved Catalytic Capability of Mesoporous TiO2 Microspheres and Photodecomposition of Toluene. ACS Applied Materials & Interfaces, 2010. **2**(11): p. 3134-3140.

26. Boyjoo, Y., H. Sun, J. Liu, V.K. Pareek, et al., A review on photocatalysis for air treatment: From catalyst development to reactor design. Chemical Engineering Journal, 2017. **310, Part 2**: p. 537-559.

27. Aghighi, A. and F. Haghighat, Using physical–chemical properties of reactants to estimate the performance of photocatalytic oxidation air cleaners. Building and Environment, 2015. **85**: p. 114-122.

28. Tseng, T.K., Y.S. Lin, Y.J. Chen, and H. Chu, A Review of Photocatalysts Prepared by Sol-Gel Method for VOCs Removal. International Journal of Molecular Sciences, 2010. **11**(6): p. 2336.

29. Nakata, K. and A. Fujishima, TiO2 photocatalysis: Design and applications. Journal of Photochemistry and Photobiology C: Photochemistry Reviews, 2012. **13**(3): p. 169-189.

30. Wen, J., X. Li, W. Liu, Y. Fang, et al., Photocatalysis fundamentals and surface modification of TiO2 nanomaterials. Chinese Journal of Catalysis, 2015. **36**(12): p. 2049-2070.

31. Linsebigler, A.L., G. Lu, and J.T. Yates, Photocatalysis on TiO2 Surfaces: Principles, Mechanisms, and Selected Results. Chemical Reviews, 1995. **95**(3): p. 735-758.

32. Fogler, H.S., Elements of chemical reaction engineering. 1999.

33. Nimlos, M.R., E.J. Wolfrum, M.L. Brewer, J.A. Fennell, et al., Gas-phase heterogeneous photocatalytic oxidation of ethanol: pathways and kinetic modeling. Environmental Science & Technology, 1996. **30**(10): p. 3102-3110.

34. Fogler, H., External Diffusion Effects on Heterogeneous Reactions. Elements of Chemical Reaction Engineering, 2006: p. 757-801.

35. Zhong, L., F. Haghighat, and C.-S. Lee, Ultraviolet photocatalytic oxidation for indoor environment applications: Experimental validation of the model. Building and Environment, 2013. **62**: p. 155-166.

36. Chen, D., F. Li, and A.K. Ray, External and internal mass transfer effect on photocatalytic degradation. Catalysis Today, 2001. **66**(2): p. 475-485.

37. Jafarikojour, M., M. Sohrabi, S.J. Royaee, and A. Hassanvand, Evaluation and Optimization of a Novel Immobilized Photoreactor for the Degradation of Gaseous Toluene. CLEAN – Soil, Air, Water, 2015. **43**(5): p. 662-670.

38. Nimlos, M.R., E.J. Wolfrum, M.L. Brewer, J.A. Fennell, et al., Gas-Phase Heterogeneous Photocatalytic Oxidation of Ethanol: Pathways and Kinetic Modeling. Environmental Science & Technology, 1996. **30**(10): p. 3102-3110.

39. Hauchecorne, B., D. Terrens, S. Verbruggen, J.A. Martens, et al., Elucidating the photocatalytic degradation pathway of acetaldehyde: An FTIR in situ study under atmospheric conditions. Applied Catalysis B: Environmental, 2011. **106**(3): p. 630-638.

40. Vincent, G., P.M. Marquaire, and O. Zahraa, Abatement of volatile organic compounds using an annular photocatalytic reactor: Study of gaseous acetone. Journal of Photochemistry and Photobiology A: Chemistry, 2008. **197**(2): p. 177-189.

41. Bianchi, C.L., S. Gatto, C. Pirola, A. Naldoni, et al., Photocatalytic degradation of acetone, acetaldehyde and toluene in gas-phase: Comparison between nano and micro-sized TiO2. Applied Catalysis B: Environmental, 2014. **146**: p. 123-130.

42. Hernández-Alonso, M.D., I. Tejedor-Tejedor, J.M. Coronado, M.A. Anderson, et al., Operando FTIR study of the photocatalytic oxidation of acetone in air over TiO2–ZrO2 thin films. Catalysis Today, 2009. **143**(3): p. 364-373.

43. Tang, F. and X. Yang, A "deactivation" kinetic model for predicting the performance of photocatalytic degradation of indoor toluene, o-xylene, and benzene. Building and Environment, 2012. **56**: p. 329-334.

44. Wang, W. and Y. Ku, Photocatalytic degradation of gaseous benzene in air streams by using an optical fiber photoreactor. Journal of Photochemistry and Photobiology A: Chemistry, 2003. **159**(1): p. 47-59.

45. d'Hennezel, O., P. Pichat, and D.F. Ollis, Benzene and toluene gas-phase photocatalytic degradation over H2O and HCL pretreated TiO2: by-products and mechanisms. Journal of Photochemistry and Photobiology A: Chemistry, 1998. **118**(3): p. 197-204.

46. Farhanian, D., F. Haghighat, C.-S. Lee, and N. Lakdawala, Impact of design parameters on the performance of ultraviolet photocatalytic oxidation air cleaner. Building and Environment, 2013. **66**: p. 148-157.

47. Kirchnerova, J., M.-L.H. Cohen, C. Guy, and D. Klvana, Photocatalytic oxidation of n-butanol under fluorescent visible light lamp over commercial TiO2 (Hombicat UV100 and Degussa P25). Applied Catalysis A: General, 2005. **282**(1-2): p. 321-332.

48. Raillard, C., V. Hequet, P. Le Cloirec, and J. Legrand, Photocatalytic oxidation of methyl ethyl ketone over sol-gel and commercial TiO2 for the improvement of indoor air. Water Science and Technology, 2006. **53**(11): p. 107-115.

49. Guo, T., Z. Bai, C. Wu, and T. Zhu, Influence of relative humidity on the photocatalytic oxidation (PCO) of toluene by TiO2 loaded on activated carbon fibers: PCO rate and intermediates accumulation. Applied Catalysis B: Environmental, 2008. **79**(2): p. 171-178.

50. Sleiman, M., P. Conchon, C. Ferronato, and J.-M. Chovelon, Photocatalytic oxidation of toluene at indoor air levels (ppbv): Towards a better assessment of conversion, reaction intermediates and mineralization. Applied Catalysis B: Environmental, 2009. **86**(3): p. 159-165.

51. Mo, J., Y. Zhang, Q. Xu, Y. Zhu, et al., Determination and risk assessment of by-products resulting from photocatalytic oxidation of toluene. Applied Catalysis B: Environmental, 2009. **89**(3): p. 570-576.

52. Mo, J., Y. Zhang, and Q. Xu, Effect of water vapor on the by-products and decomposition rate of ppb-level toluene by photocatalytic oxidation. Applied Catalysis B: Environmental, 2013. **132-133**: p. 212-218.

53. Vincent, G., P.-M. Marquaire, and O. Zahraa, Photocatalytic degradation of gaseous 1-propanol using an annular reactor: kinetic modelling and pathways. Journal of Hazardous Materials, 2009. **161**(2-3): p. 1173-1181.

54. Kirchnerova, J., M.L. Herrera Cohen, C. Guy, and D. Klvana, Photocatalytic oxidation of n-butanol under fluorescent visible light lamp over commercial TiO2 (Hombicat UV100 and Degussa P25). Applied Catalysis A: General, 2005. **282**(1): p. 321-332.

55. Vincent, G., P.M. Marquaire, and O. Zahraa, Photocatalytic degradation of gaseous 1-propanol using an annular reactor: Kinetic modelling and pathways. Journal of Hazardous Materials, 2009. **161**(2): p. 1173-1181.

56. Van Gerven, T., G. Mul, J. Moulijn, and A. Stankiewicz, A review of intensification of photocatalytic processes. Chemical Engineering and Processing: Process Intensification, 2007. **46**(9): p. 781-789.

57. Khodadadian, F., M.W. De Boer, A. Poursaeidesfahani, J.R. Van Ommen, et al., Design, characterization and model validation of a LED-based photocatalytic reactor for gas phase applications. Chemical Engineering Journal, 2018. **333**: p. 456-466.

58. Sozzi, D.A. and F. Taghipour, UV Reactor Performance Modeling by Eulerian and Lagrangian Methods. Environmental Science & Technology, 2006. **40**(5): p. 1609-1615.

59. Vezzoli, M., T. Farrell, A. Baker, S. Psaltis, et al., Optimal catalyst thickness in titanium dioxide fixed film reactors: Mathematical modelling and experimental validation. Chemical Engineering Journal, 2013. **234**: p. 57-65.

60. Li Puma, G. and A. Brucato, Dimensionless analysis of slurry photocatalytic reactors using two-flux and six-flux radiation absorption–scattering models. Catalysis Today, 2007. **122**(1): p. 78-90.

61. Li Puma, G. and P.L. Yue, Modelling and design of thin-film slurry photocatalytic reactors for water purification. Chemical Engineering Science, 2003. **58**(11): p. 2269-2281.

62. Choi, W., J.Y. Ko, H. Park, and J.S. Chung, Investigation on TiO2-coated optical fibers for gas-phase photocatalytic oxidation of acetone. Applied Catalysis B: Environmental, 2001. **31**(3): p. 209-220.

63. Quici, N., M.L. Vera, H. Choi, G.L. Puma, et al., Effect of key parameters on the photocatalytic oxidation of toluene at low concentrations in air under 254+185nm UV irradiation. Applied Catalysis B: Environmental, 2010. **95**(3): p. 312-319.

64. Mo, J., Y. Zhang, Q. Xu, J.J. Lamson, et al., Photocatalytic purification of volatile organic compounds in indoor air: A literature review. Atmospheric Environment, 2009. **43**(14): p. 2229-2246.

65. Foo, K.Y. and B.H. Hameed, Insights into the modeling of adsorption isotherm systems. Chemical Engineering Journal, 2010. **156**(1): p. 2-10.

66. Goel, C., H. Bhunia, and P.K. Bajpai, Prediction of Binary Gas Adsorption of CO2/N2 and Thermodynamic Studies on Nitrogen Enriched Nanostructured Carbon Adsorbents. Journal of Chemical & Engineering Data, 2017. **62**(1): p. 214-225.

67. Ammendola, P., F. Raganati, and R. Chirone, CO2 adsorption on a fine activated carbon in a sound assisted fluidized bed: Thermodynamics and kinetics. Chemical Engineering Journal, 2017. **322**: p. 302-313.

68. Zhong, L., C.-S. Lee, and F. Haghighat, Adsorption performance of titanium dioxide (TiO2) coated air filters for volatile organic compounds. Journal of Hazardous Materials, 2012. **243**: p. 340-349.

69.   Maudhuit, A., C. Raillard, V. Héquet, L. Le Coq, et al., Adsorption phenomena in photocatalytic reactions: The case of toluene, acetone and heptane. Chemical Engineering Journal, 2011. **170**(2): p. 464-470.

70.   Sleiman, M., P. Conchon, C. Ferronato, and J.-M. Chovelon, Photocatalytic oxidation of toluene at indoor air levels (ppbv): Towards a better assessment of conversion, reaction intermediates and mineralization. Applied Catalysis B: Environmental, 2009. **86**(3–4): p. 159-165.

71.   Tomašić, V., F. Jović, and Z. Gomzi, Photocatalytic oxidation of toluene in the gas phase: Modelling an annular photocatalytic reactor. Catalysis Today, 2008. **137**(2–4): p. 350-356.

72.   Verbruggen, S.W., S. Lenaerts, and S. Denys, Analytic versus CFD approach for kinetic modeling of gas phase photocatalysis. Chemical Engineering Journal, 2015. **262**: p. 1-8.

73.   Kapoor, A., J.A. Ritter, and R.T. Yang, An extended Langmuir model for adsorption of gas mixtures on heterogeneous surfaces. Langmuir, 1990. **6**(3): p. 660-664.

74.   Turchi, C.S., R. Rabago, and A. Jassal, Destruction of volatile organic compound (VOC) emissions by photocatalytic oxidation (PCO): benchscale test results and cost analysis. Inc. Technology Transfer 95082935A-ENG, 1995.

75.   Wang, K.-H., Y.-H. Hsieh, C.-H. Lin, and C.-Y. Chung, The study of the photocatalytic degradation kinetics for dichloroethylene in vapor phase. Chemosphere, 1999. **39**(9): p. 1371-1384.

76.   Ibrahim, H. and H.d. Lasa, Kinetic modeling of the photocatalytic degradation of air-borne pollutants. AIChE Journal, 2004. **50**(5): p. 1017-1027.

77.   Tseng, T.K., Y.S. Lin, Y.J. Chen, and H. Chu, A review of photocatalysts prepared by sol-gel method for VOCs removal. International Journal of Molecular Sciences, 2010. **11**(6): p. 2336-2361.

78.   Pathak, N., O.J. Caleb, M. Geyer, W.B. Herppich, et al., Photocatalytic and photochemical oxidation of ethylene: potential for storage of fresh produce—a review. Food and Bioprocess Technology, 2017. **10**(6): p. 982-1001.

79.   Brame, J., M. Long, Q. Li, and P. Alvarez, Inhibitory effect of natural organic matter or other background constituents on photocatalytic advanced oxidation processes: Mechanistic model development and validation. Water Research, 2015. **84**: p. 362-371.

80.   Lewandowski, M. and D.F. Ollis, Extension of a Two-Site transient kinetic model of TiO2 deactivation during photocatalytic oxidation of aromatics: concentration variations and catalyst regeneration studies. Applied Catalysis B: Environmental, 2003. **45**(3): p. 223-238.

81.   Zhong, L. and F. Haghighat, Modeling and validation of a photocatalytic oxidation reactor for indoor environment applications. Chemical Engineering Science, 2011. **66**(23): p. 5945-5954.

82.   Boulamanti, A.K. and C.J. Philippopoulos, Photocatalytic degradation of C5–C7 alkanes in the gas–phase. Atmospheric Environment, 2009. **43**(20): p. 3168-3174.

83.   Yu, B., W. He, N. Li, F. Zhou, et al., Experiments and kinetics of solar PCO for indoor air purification in PCO/TW system. Building and Environment, 2017. **115**: p. 130-146.

84.   Lopes, F.V.S., R.A.R. Monteiro, A.M.T. Silva, G.V. Silva, et al., Insights into UV-TiO2 photocatalytic degradation of PCE for air decontamination systems. Chemical Engineering Journal, 2012. **204-206**: p. 244-257.

85.   Monteiro, R.A.R., F.V.S. Lopes, A.M.T. Silva, J. Ângelo, et al., Are TiO2-based exterior paints useful catalysts for gas-phase photooxidation processes? A case study on n-decane abatement for air detoxification. Applied Catalysis B: Environmental, 2014. **147**: p. 988-999.

86.   Kamal, M.S., S.A. Razzak, and M.M. Hossain, Catalytic oxidation of volatile organic compounds (VOCs) – A review. Atmospheric Environment, 2016. **140**: p. 117-134.

87.   Assadi, A.A., A. Bouzaza, and D. Wolbert, Photocatalytic oxidation of trimethylamine and isovaleraldehyde in an annular reactor: Influence of the mass transfer and the relative humidity. Journal of Photochemistry and Photobiology A: Chemistry, 2012. **236**: p. 61-69.

88.   Wang, X., X. Tan, and T. Yu, Modeling of Formaldehyde Photocatalytic Degradation in a Honeycomb Monolith Reactor Using Computational Fluid Dynamics. Industrial & Engineering Chemistry Research, 2014. **53**(48): p. 18402-18410.

89.   Chong, S., S. Wang, M. Tadé, H.M. Ang, et al., Simulations of photodegradation of toluene and formaldehyde in a monolith reactor using computational fluid dynamics. AIChE Journal, 2011. **57**(3): p. 724-734.

90.   Wang, K.-H., H.-H. Tsai, and Y.-H. Hsieh, The kinetics of photocatalytic degradation of trichloroethylene in gas phase over TiO2 supported on glass bead. Applied Catalysis B: Environmental, 1998. **17**(4): p. 313-320.

91. Obee, T.N., Photooxidation of Sub-Parts-per-Million Toluene and Formaldehyde Levels on Titania Using a Glass-Plate Reactor. Environmental Science & Technology, 1996. **30**(12): p. 3578-3584.

92. Hossain, M., G.B. Raupp, S.O. Hay, and T.N. Obee, Three-dimensional developing flow model for photocatalytic monolith reactors. AIChE Journal, 1999. **45**(6): p. 1309-1321.

93. Demeestere, K., A. De Visscher, J. Dewulf, M. Van Leeuwen, et al., A new kinetic model for titanium dioxide mediated heterogeneous photocatalytic degradation of trichloroethylene in gas-phase. Applied Catalysis B: Environmental, 2004. **54**(4): p. 261-274.

94. Muñoz-Batista, M.J., A. Kubacka, M.N. Gómez-Cerezo, D. Tudela, et al., Sunlight-driven toluene photo-elimination using CeO2-TiO2 composite systems: A kinetic study. Applied Catalysis B: Environmental, 2013. **140-141**: p. 626-635.

95. Bouzaza, A., C. Vallet, and A. Laplanche, Photocatalytic degradation of some VOCs in the gas phase using an annular flow reactor: Determination of the contribution of mass transfer and chemical reaction steps in the photodegradation process. Journal of Photochemistry and Photobiology A: Chemistry, 2006. **177**(2–3): p. 212-217.

96. Zhou, M., J. Yu, and B. Cheng, Effects of Fe-doping on the photocatalytic activity of mesoporous TiO2 powders prepared by an ultrasonic method. Journal of Hazardous Materials, 2006. **137**(3): p. 1838-1847.

97. Zhong, L., F. Haghighat, C.-S. Lee, and N. Lakdawala, Performance of ultraviolet photocatalytic oxidation for indoor air applications: Systematic experimental evaluation. Journal of Hazardous Materials, 2013. **261**: p. 130-138.

98. Mo, J., Y. Zhang, Q. Xu, and R. Yang, Effect of TiO2/adsorbent hybrid photocatalysts for toluene decomposition in gas phase. Journal of Hazardous Materials, 2009. **168**(1): p. 276-281.

99. Cao, L., F.-J. Spiess, A. Huang, S.L. Suib, et al., Heterogeneous photocatalytic oxidation of 1-butene on SnO2 and TiO2 films. The Journal of Physical Chemistry B, 1999. **103**(15): p. 2912-2917.

100. Lopes, F.V., R.A. Monteiro, A.M. Silva, G.V. Silva, et al., Insights into UV-TiO2 photocatalytic degradation of PCE for air decontamination systems. Chemical Engineering Journal, 2012. **204**: p. 244-257.

101. Einaga, H., T. Ibusuki, and S. Futamura, Photocatalytic Oxidation of Benzene in Air. Journal of Solar Energy Engineering, 2004. **126**(2): p. 789-793.

102. Hajaghazadeh, M., V. Vaiano, D. Sannino, H. Kakooei, et al., Heterogeneous photocatalytic oxidation of methyl ethyl ketone under UV-A light in an LED-fluidized bed reactor. Catalysis Today, 2014. **230**: p. 79-84.

103. Attwood, A.L., J.L. Edwards, C.C. Rowlands, and D.M. Murphy, Identification of a surface alkylperoxy radical in the photocatalytic oxidation of acetone/O2 over TiO2. The Journal of Physical Chemistry A, 2003. **107**(11): p. 1779-1782.

104. Herrmann, J.-M., Heterogeneous photocatalysis: fundamentals and applications to the removal of various types of aqueous pollutants. Catalysis Today, 1999. **53**(1): p. 115-129.

105. Obee, T.N. and R.T. Brown, TiO2 photocatalysis for indoor air applications: effects of humidity and trace contaminant levels on the oxidation rates of formaldehyde, toluene, and 1, 3-butadiene. Environmental Science & Technology, 1995. **29**(5): p. 1223-1231.

106. Ohko, Y., A. Fujishima, and K. Hashimoto, Kinetic Analysis of the Photocatalytic Degradation of Gas-Phase 2-Propanol under Mass Transport-Limited Conditions with a TiO2 Film Photocatalyst. The Journal of Physical Chemistry B, 1998. **102**(10): p. 1724-1729.

107. Moazzem Hossain, M. and G.B. Raupp, Radiation field modeling in a photocatalytic monolith reactor. Chemical Engineering Science, 1998. **53**(22): p. 3771-3780.

108. Changrani, R. and G.B. Raupp, Monte Carlo simulation of the radiation field in a reticulated foam photocatalytic reactor. AIChE Journal, 1999. **45**(5): p. 1085-1094.

109. Raupp, G.B., A. Alexiadis, M.M. Hossain, and R. Changrani, First-principles modeling, scaling laws and design of structured photocatalytic oxidation reactors for air purification. Catalysis Today, 2001. **69**(1): p. 41-49.

110. Alexiadis, A., 2-D radiation field in photocatalytic channels of square, rectangular, equilateral triangular and isosceles triangular sections. Chemical Engineering Science, 2006. **61**(2): p. 516-525.

111. Yu, H., K. Zhang, and C. Rossi, Theoretical study on photocatalytic oxidation of VOCs using nano-TiO2 photocatalyst. Journal of Photochemistry and Photobiology A: Chemistry, 2007. **188**(1): p. 65-73.

112. Chang, H.T., N.-M. Wu, and F. Zhu, A kinetic model for photocatalytic degradation of organic contaminants in a thin-film TiO2 catalyst. Water Research, 2000. **34**(2): p. 407-416.

113. Boyjoo, Y., M. Ang, and V. Pareek, Lamp emission and quartz sleeve modelling in slurry photocatalytic reactors. Chemical Engineering Science, 2014. **111**: p. 34-40.

114. Twesme, T.M., D.T. Tompkins, M.A. Anderson, and T.W. Root, Photocatalytic oxidation of low molecular weight alkanes: Observations with ZrO2–TiO2 supported thin films. Applied Catalysis B: Environmental, 2006. **64**(3): p. 153-160.

115. Tsaiand, C.-W., C.-T. Chang, C.-S. Chiou, J.-L. Shie, et al., Study on the indoor volatile organic compound treatment and performance assessment with TiO2/MCM-41 and TiO2/Quartz photoreactor under ultraviolet irradiation. Journal of the Air & Waste Management Association, 2008. **58**(10): p. 1266-1273.

116. Nguyen-Phan, T.-D., M.B. Song, and E.W. Shin, Removal efficiency of gaseous benzene using lanthanide-doped mesoporous titania. Journal of Hazardous Materials, 2009. **167**(1): p. 75-81.

117. Fox, M.A. and M.T. Dulay, Heterogeneous photocatalysis. Chemical Reviews, 1993. **93**(1): p. 341-357.

118. Twesme, T.M., D.T. Tompkins, M.A. Anderson, and T.W. Root, Photocatalytic oxidation of low molecular weight alkanes: observations with ZrO2–TiO2 supported thin films. Applied Catalysis B: Environmental, 2006. **64**(3-4): p. 153-160.

119. Tseng, T.K., Y.S. Lin, Y.J. Chen, and H. Chu, A review of photocatalysts prepared by sol-gel method for VOCs removal. Int J Mol Sci, 2010. **11**(6): p. 2336-61.

120. Pichat, P. and J. Herrmann, Adsorption–desorption, related mobility and reactivity in photocatalysis. Photocatalysis: Fundamentals and Applications, 1989: p. 217-250.

121. Doucet, N., F. Bocquillon, O. Zahraa, and M. Bouchy, Kinetics of photocatalytic VOCs abatement in a standardized reactor. Chemosphere, 2006. **65**(7): p. 1188-1196.

122. Lin, Y.-T., C.-H. Weng, and F.-Y. Chen, Key operating parameters affecting photocatalytic activity of visible-light-induced C-doped TiO2 catalyst for ethylene oxidation. Chemical Engineering Journal, 2014. **248**: p. 175-183.

123. Obee, T.N. and S.O. Hay, Effects of Moisture and Temperature on the Photooxidation of Ethylene on Titania. Environmental Science & Technology, 1997. **31**(7): p. 2034-2038.

124. Fu, X., L.A. Clark, W.A. Zeltner, and M.A. Anderson, Effects of reaction temperature and water vapor content on the heterogeneous photocatalytic oxidation of ethylene. Journal of Photochemistry and Photobiology A: Chemistry, 1996. **97**(3): p. 181-186.

125. Takeda, N., T. Torimoto, S. Sampath, S. Kuwabata, et al., Effect of inert supports for titanium dioxide loading on enhancement of photodecomposition rate of gaseous propionaldehyde. The Journal of Physical Chemistry, 1995. **99**(24): p. 9986-9991.

126. Rincón, A. and C. Pulgarin, Photocatalytical inactivation of E. coli: effect of (continuous–intermittent) light intensity and of (suspended–fixed) TiO2 concentration. Applied Catalysis B: Environmental, 2003. **44**(3): p. 263-284.

127. Cassano, A.E. and O.M. Alfano, Reaction engineering of suspended solid heterogeneous photocatalytic reactors. Catalysis Today, 2000. **58**(2-3): p. 167-197.

128. Romero, R.L., O.M. Alfano, and A.E. Cassano, Cylindrical photocatalytic reactors. Radiation absorption and scattering effects produced by suspended fine particles in an annular space. Industrial & Engineering Chemistry Research, 1997. **36**(8): p. 3094-3109.

129. Alonso-Tellez, A., R. Masson, D. Robert, N. Keller, et al., Comparison of Hombikat UV100 and P25 TiO2 performance in gas-phase photocatalytic oxidation reactions. Journal of Photochemistry and Photobiology A: Chemistry, 2012. **250**: p. 58-65.

130. Zalazar, C.S., C.A. Martin, and A.E. Cassano, Photocatalytic intrinsic reaction kinetics. II: Effects of oxygen concentration on the kinetics of the photocatalytic degradation of dichloroacetic acid. Chemical Engineering Science, 2005. **60**(15): p. 4311-4322.

131. Amrhein, K. and D. Stephan. Photocatalytic Building Materials and Methods of Measurement. in Ultra-High Performance Concrete and Nanotechnology in Construction. Proceedings of Hipermat 2012. 3rd International Symposium on UHPC and Nanotechnology for High Performance Construction Materials. 2012. kassel university press GmbH.

132. Chen, D., F. Li, and A.K. Ray, External and internal mass transfer effect on photocatalytic degradation. 2001.

133. Yang, L., Z. Liu, J. Shi, H. Hu, et al., Design consideration of photocatalytic oxidation reactors using TiO2-coated foam nickels for degrading indoor gaseous formaldehyde. Catalysis Today, 2007. **126**(3): p. 359-368.

134. Dijkstra, M.F.J., H.J. Panneman, J.G.M. Winkelman, J.J. Kelly, et al., Modeling the photocatalytic degradation of formic acid in a reactor with immobilized catalyst. Chemical Engineering Science, 2002. **57**(22): p. 4895-4907.

135. Sherwood, T.K., R.L. Pigford, and C.R. Wilke, Mass transfer. 1975: McGraw-Hill.

136. Themelis, N.J., Transport and chemical rate phenomena. 1995: Gordon and Breach Publishers.

137. Vezzoli, M., W.N. Martens, and J.M. Bell, Investigation of phenol degradation: True reaction kinetics on fixed film titanium dioxide photocatalyst. Applied Catalysis A: General, 2011. **404**(1): p. 155-163.

138. Yang, L., Z. Liu, J. Shi, H. Hu, et al., Design consideration of photocatalytic oxidation reactors using TiO2-coated foam nickels for degrading indoor gaseous formaldehyde. Catalysis Today, 2007. **126**(3-4): p. 359-368.

139. Dijkstra, M., H. Panneman, J. Winkelman, J. Kelly, et al., Modeling the photocatalytic degradation of formic acid in a reactor with immobilized catalyst. Chemical Engineering Science, 2002. **57**(22-23): p. 4895-4907.

140. Passalía, C., O.M. Alfano, and R.J. Brandi, Modeling and Experimental Verification of a Corrugated Plate Photocatalytic Reactor Using Computational Fluid Dynamics. Industrial & Engineering Chemistry Research, 2011. **50**(15): p. 9077-9086.

141. Passalía, C., M.E. Martínez Retamar, O.M. Alfano, and R.J. Brandi, Photocatalytic degradation of formaldehyde in gas phase on TiO2 films: a kinetic study. International Journal of Chemical Reactor Engineering, 2010. **8**(1).

142. Mahmoudkhani, F., M. Rezaei, V. Asili, M. Atyabi, et al., Benzene degradation in waste gas by photolysis and photolysis-ozonation: experiments and modeling. Frontiers of Environmental Science & Engineering, 2016. **10**(6): p. 10.

143. Assadi, A.A., B. Abdelkrim, and W. Dominique, Kinetic Modeling of VOC Photocatalytic Degradation Using a Process at Different Reactor Configurations and Scales. International Journal of Chemical Reactor Engineering, 2016. **14**(1): p. 395-405.

144. Adjimi, S., J.-C. Roux, N. Sergent, F. Delpech, et al., Photocatalytic oxidation of ethanol using paper-based nano-TiO2 immobilized on porous silica: A modelling study. Chemical Engineering Journal, 2014. **251**: p. 381-391.

145. Tomašić, V., F. Jović, and Z. Gomzi, Photocatalytic oxidation of toluene in the gas phase: Modelling an annular photocatalytic reactor. Catalysis Today, 2008. **137**(2): p. 350-356.

146. Jarandehei, A. and A.D. Visscher, Three-dimensional CFD model for a flat plate photocatalytic reactor: Degradation of TCE in a serpentine flow field. AIChE Journal, 2009. **55**(2): p. 312-320.

147. Wang, Z., J. Liu, Y. Dai, W. Dong, et al., CFD modeling of a UV-LED photocatalytic odor abatement process in a continuous reactor. Journal of Hazardous Materials, 2012. **215–216**: p. 25-31.

148. Zhang, Y., R. Yang, and R. Zhao, A model for analyzing the performance of photocatalytic air cleaner in removing volatile organic compounds. Atmospheric Environment, 2003. **37**(24): p. 3395-3399.

149. Boulinguiez, B., A. Bouzaza, S. Merabet, and D. Wolbert, Photocatalytic degradation of ammonia and butyric acid in plug-flow reactor: Degradation kinetic modeling with contribution of mass transfer. Journal of Photochemistry and Photobiology A: Chemistry, 2008. **200**(2): p. 254-261.

150. Biard, P.-F., A. Bouzaza, and D. Wolbert, Photocatalytic Degradation of Two Volatile Fatty Acids in an Annular Plug-Flow Reactor; Kinetic Modeling and Contribution of Mass Transfer Rate. Environmental Science & Technology, 2007. **41**(8): p. 2908-2914.

151. Marečić, M., F. Jović, V. Kosar, and V. Tomašić, Modelling of an annular photocatalytic reactor. Reaction Kinetics, Mechanisms and Catalysis, 2011. **103**(1): p. 19-29.

152. Jafarikojour, M., M. Sohrabi, S.J. Royaee, and A. Hassanvand, Evaluation and optimization of a novel immobilized photoreactor for the degradation of gaseous toluene. CLEAN–Soil, Air, Water, 2015. **43**(5): p. 662-670.

153. Monteiro, R.A.R., A.M.T. Silva, J.R.M. Ângelo, G.V. Silva, et al., Photocatalytic oxidation of gaseous perchloroethylene over TiO2 based paint. Journal of Photochemistry and Photobiology A: Chemistry, 2015. **311**: p. 41-52.

154. Bouazza, N., M.A. Lillo-Ródenas, and A. Linares-Solano, Photocatalytic activity of TiO2-based materials for the oxidation of propene and benzene at low concentration in presence of humidity. Applied Catalysis B: Environmental, 2008. **84**(3): p. 691-698.

155. Yang, L., Z. Liu, J. Shi, Y. Zhang, et al., Degradation of indoor gaseous formaldehyde by hybrid VUV and TiO2/UV processes. Separation and Purification Technology, 2007. **54**(2): p. 204-211.

156. Maira, A., K.L. Yeung, C. Lee, P.L. Yue, et al., Size effects in gas-phase photo-oxidation of trichloroethylene using nanometer-sized TiO2 catalysts. Journal of Catalysis, 2000. **192**(1): p. 185-196.

157. Arconada, N., A. Durán, S. Suárez, R. Portela, et al., Synthesis and photocatalytic properties of dense and porous TiO2-anatase thin films prepared by sol–gel. Applied Catalysis B: Environmental, 2009. **86**(1): p. 1-7.

158. Huang, Y., W. Ho, S. Lee, L. Zhang, et al., Effect of Carbon Doping on the Mesoporous Structure of Nanocrystalline Titanium Dioxide and Its Solar-Light-Driven Photocatalytic Degradation of NOx. Langmuir, 2008. **24**(7): p. 3510-3516.

159. Zhou, S. and A.K. Ray, Kinetic studies for photocatalytic degradation of Eosin B on a thin film of titanium dioxide. Industrial & Engineering Chemistry Research, 2003. **42**(24): p. 6020-6033.

160. Sillanpää, M., M.C. Ncibi, and A. Matilainen, Advanced oxidation processes for the removal of natural organic matter from drinking water sources: a comprehensive review. Journal of Environmental Management, 2018. **208**: p. 56-76.

161. Danckwerts, P.V., Continuous flow systems. Distribution of residence times. Chemical Engineering Science, 1995. **50**(24): p. 3857-3866.

162. Fogler, H.S., Essentials of Chemical Reaction Engineering. 5th ed. 2010: The Prentice Hall International Series in the Physical and Chemical Engineering Sciences.

163. Salvadó-Estivill, I., A. Brucato, and G. Li Puma, Two-dimensional modeling of a flat-plate photocatalytic reactor for oxidation of indoor air pollutants. Industrial & Engineering Chemistry Research, 2007. **46**(23): p. 7489-7496.

164. Boyjoo, Y., M. Ang, and V. Pareek, CFD simulation of a pilot scale slurry photocatalytic reactor and design of multiple-lamp reactors. Chemical Engineering Science, 2014. **111**: p. 266-277.

165. Malayeri, M., F. Haghighat, and C.-S. Lee, Modeling of volatile organic compounds degradation by photocatalytic oxidation reactor in indoor air: A review. Building and Environment, 2019.

166. Alberici, R.M. and W.F. Jardim, Photocatalytic destruction of VOCs in the gas-phase using titanium dioxide. Applied Catalysis B: Environmental, 1997. **14**(1-2): p. 55-68.

167. Puma, G.L., I. Salvadó-Estivill, T.N. Obee, and S.O. Hay, Kinetics rate model of the photocatalytic oxidation of trichloroethylene in air over TiO2 thin films. Separation and Purification Technology, 2009. **67**(2): p. 226-232.

168. Assadi, A.A., J. Palau, A. Bouzaza, and D. Wolbert, Modeling of a continuous photocatalytic reactor for isovaleraldehyde oxidation: Effect of different operating parameters and chemical degradation pathway. Chemical Engineering Research and Design, 2013. **91**(7): p. 1307-1316.

169. Lopes, F.V., S.M. Miranda, R.A. Monteiro, S.D. Martins, et al., Perchloroethylene gas-phase degradation over titania-coated transparent monoliths. Applied Catalysis B: Environmental, 2013. **140**: p. 444-456.

170. Zhong, L., J.J. Brancho, S. Batterman, B.M. Bartlett, et al., Experimental and modeling study of visible light responsive photocatalytic oxidation (PCO) materials for toluene degradation. Applied catalysis. B, Environmental, 2017. **216**: p. 122-132.

171. Rothenberger, G., J. Moser, M. Graetzel, N. Serpone, et al., Charge carrier trapping and recombination dynamics in small semiconductor particles. Journal of the American Chemical Society, 1985. **107**(26): p. 8054-8059.

172. Bahnemann, D.W., M. Hilgendorff, and R. Memming, Charge Carrier Dynamics at TiO2 Particles: Reactivity of Free and Trapped Holes. The Journal of Physical Chemistry B, 1997. **101**(21): p. 4265-4275.

173. Zhong, L., C.-S. Lee, F. Haghighat, S. Batterman, et al., Photocatalytic cleaning performance of air filters for a binary mixture. Optimization, 2015. **1097**: p. 10002829.

174. Asnin, L., K. Kaczmarski, and G. Guiochon, Empirical development of a binary adsorption isotherm based on the single-component isotherms in the framework of a two-site model. Journal of Chromatography A, 2007. **1138**(1): p. 158-168.

175. Sheng, Y., Y. Zhang, and G. Zhang, Simulation and energy saving analysis of high temperature heat pump coupling to desiccant wheel air conditioning system. Energy, 2015. **83**: p. 583-596.

176. Kierzenka, J. and L.F. Shampine, A BVP solver that controls residual and error. JNAIAM J. Numer. Anal. Ind. Appl. Math, 2008. **3**(1-2): p. 27-41.

177. Gavin, H., The Levenberg-Marquardt method for nonlinear least squares curve-fitting problems. Department of Civil and Environmental Engineering, Duke University, 2011. **28**: p. 1-5.

178. Agency, U.E.P., Compendium Method TO–11A: Determination of formaldehyde in ambient air using adsorbent cartridge followed by high performance liquid chromatography (HPLC). 1999, US Environmental Protection Agency Cincinnati, OH.

179. Jaw, S.Y. and C.J. Chen, Present status of second-order closure turbulence models. I: overview. Journal of Engineering Mechanics, 1998. **124**(5): p. 485-501.

180. Sozzi, D.A. and F. Taghipour, Computational and experimental study of annular photo-reactor hydrodynamics. International Journal of Heat and Fluid Flow, 2006. **27**(6): p. 1043-1053.

181. Sadrehaghighi, I., Turbulence modeling-a review. CFD Open Series, 2019: p. 1-49.
182. Wilcox, D.C., Formulation of the kw turbulence model revisited. AIAA journal, 2008. **46**(11): p. 2823-2838.
183. Malayeri, M., C.-S. Lee, F. Haghighat, and L. Klimes, Modeling of gas-phase heterogeneous photocatalytic oxidation reactor in the presence of mass transfer limitation and axial dispersion. Chemical Engineering Journal, 2020. **386**: p. 124013.
184. Gualtieri, C. and I. Napoli Federico, Numerical Simulation of RTD in Contact Tanks with Comsol Multiphysics 3.2 b. Available as of April, 2015. **19**.
185. Müller, A., J. Petschick, and R. Lange, Model-based investigation of a Pellet String Reactor. Procedia Engineering, 2012. **42**: p. 1189-1201.
186. Levenspiel, O., Chemical reaction engineering. 3rd ed. 1999: Wiley.
187. Charles, G., T. Roques-Carmes, N. Becheikh, L. Falk, et al., Determination of kinetic constants of a photocatalytic reaction in micro-channel reactors in the presence of mass-transfer limitation and axial dispersion. Journal of Photochemistry and Photobiology A: Chemistry, 2011. **223**(2-3): p. 202-211.
188. Sans, V., N. Karbass, M.I. Burguete, E. García-Verdugo, et al., Residence time distribution, a simple tool to understand the behaviour of polymeric mini-flow reactors. RSC Advances, 2012. **2**(23): p. 8721-8728.
189. Saber, M., C. Pham-Huu, and D. Edouard, Axial dispersion based on the residence time distribution curves in a millireactor filled with β-SiC foam catalyst. Industrial & Engineering Chemistry Research, 2012. **51**(46): p. 15011-15017.
190. Aris, R., On the dispersion of a solute in a fluid flowing through a tube. Proceedings of the Royal Society of London. Series A. Mathematical and Physical Sciences, 1956. **235**(1200): p. 67-77.
191. Taylor, G.I., Dispersion of soluble matter in solvent flowing slowly through a tube. Proceedings of the Royal Society of London. Series A. Mathematical and Physical Sciences, 1953. **219**(1137): p. 186-203.
192. Smith, J.M., Chemical engineering kinetics. 2nd ed. 1981: McGraw-Hill.
193. Reichelt, E., M.P. Heddrich, M. Jahn, and A. Michaelis, Fiber based structured materials for catalytic applications. Applied Catalysis A: General, 2014. **476**: p. 78-90.
194. Votruba, J., O. Mikuš, K. Nguen, V. Hlaváček, et al., Heat and mass transfer in honeycomb catalysts—II. Chemical Engineering Science, 1975. **30**(2): p. 201-206.
195. Groppi, G., E. Tronconi, G. Bozzano, and M. Dente, Experimental and theoretical study of gas/solid mass transfer in metallic filters as supports for micro-structured catalysts. Chemical Engineering Science, 2010. **65**(1): p. 392-397.
196. Satterfield, C.N. and D.H. Cortez, Mass Transfer Characteristics of Woven-Wire Screen Catalysts. Industrial & Engineering Chemistry Fundamentals, 1970. **9**(4): p. 613-620.
197. Ahlström-Silversand, A.F. and C.U.I. Odenbrand, Modelling catalytic combustion of carbon monoxide and hydrocarbons over catalytically active wire meshes. Chemical Engineering Journal, 1999. **73**(3): p. 205-216.
198. Nicolella, C. and M. Rovatti, Mathematical modeling of monolith reactors for photocatalytic oxidation of air contaminants. Chemical Engineering Journal, 1998. **69**(2): p. 119-126.
199. Einaga, H., J. Tokura, Y. Teraoka, and K. Ito, Kinetic analysis of TiO2-catalyzed heterogeneous photocatalytic oxidation of ethylene using computational fluid dynamics. Chemical Engineering Journal, 2015. **263**: p. 325-335.
200. Raillard, C., V. Héquet, P. Le Cloirec, and J. Legrand, Kinetic study of ketones photocatalytic oxidation in gas phase using TiO2-containing paper: effect of water vapor. Journal of Photochemistry and Photobiology A: Chemistry, 2004. **163**(3): p. 425-431.
201. Lucio-Ortiz, C.J., J.R. De la Rosa, A. Hernández-Ramírez, E.M. López-Cuellar, et al., La-, Mn- and Fe-doped zirconia catalysts by sol–gel synthesis: TEM characterization, mass-transfer evaluation and kinetic determination in the catalytic combustion of trichloroethylene. Colloids and Surfaces A: Physicochemical and Engineering Aspects, 2010. **371**(1): p. 81-90.
202. Martínez Vargas, D.X., J. Rivera De la Rosa, C.J. Lucio-Ortiz, A. Hernández-Ramirez, et al., Photocatalytic degradation of trichloroethylene in a continuous annular reactor using Cu-doped TiO2 catalysts by sol–gel synthesis. Applied Catalysis B: Environmental, 2015. **179**: p. 249-261.
203. Mamaghani, A.H., F. Haghighat, and C.-S. Lee, Photocatalytic oxidation of MEK over hierarchical TiO2 catalysts: Effect of photocatalyst features and operating conditions. Applied Catalysis B: Environmental, 2019. **251**: p. 1-16.
204. Vincent, G., A. Queffeulou, P.M. Marquaire, and O. Zahraa, Remediation of olfactory pollution by photocatalytic degradation process: Study of methyl ethyl ketone (MEK). Journal of Photochemistry and Photobiology A: Chemistry, 2007. **191**(1): p. 42-50.

205. Jiang, Z., C. He, N.F. Dummer, J. Shi, et al., Insight into the efficient oxidation of methyl-ethyl-ketone over hierarchically micro-mesostructured Pt/K-(Al)SiO2 nanorod catalysts: Structure-activity relationships and mechanism. Applied Catalysis B: Environmental, 2018. **226**: p. 220-233.

206. Pichat, P., Some views about indoor air photocatalytic treatment using TiO2: Conceptualization of humidity effects, active oxygen species, problem of C1–C3 carbonyl pollutants. Applied Catalysis B: Environmental, 2010. **99**(3): p. 428-434.

207. Kibanova, D., M. Sleiman, J. Cervini-Silva, and H. Destaillats, Adsorption and photocatalytic oxidation of formaldehyde on a clay-TiO2 composite. Journal of Hazardous Materials, 2012. **211**: p. 233-239.

208. Bouzaza, A. and A. Laplanche, Photocatalytic degradation of toluene in the gas phase: comparative study of some TiO2 supports. Journal of Photochemistry and Photobiology A: Chemistry, 2002. **150**(1-3): p. 207-212.

209. Lin, Y.-H., C.-H. Weng, J.-H. Tzeng, and Y.-T. Lin, Adsorption and photocatalytic kinetics of visible-light response N-doped TiO2 nanocatalyst for indoor acetaldehyde removal under dark and light conditions. International Journal of Photoenergy, 2016. **2016**.

210. Hoffmann, M.R., S.T. Martin, W. Choi, and D.W. Bahnemann, Environmental applications of semiconductor photocatalysis. Chemical Reviews, 1995. **95**(1): p. 69-96.

211. Xu, Y. and C.H. Langford, Variation of Langmuir adsorption constant determined for TiO2-photocatalyzed degradation of acetophenone under different light intensity. Journal of Photochemistry and Photobiology A: Chemistry, 2000. **133**(1-2): p. 67-71.

212. Arconada, N., Y. Castro, A. Durán, and V. Héquet, Photocatalytic oxidation of methyl ethyl ketones over sol–gel mesoporous and meso-structured TiO2 films obtained by EISA method. Applied Catalysis B: Environmental, 2011. **107**(1): p. 52-58.

213. Raillard, C., V. Héquet, P.L. Cloirec, and J. Legrand, TiO2 coating types influencing the role of water vapor on the photocatalytic oxidation of methyl ethyl ketone in the gas phase. Applied Catalysis B: Environmental, 2005. **59**(3): p. 213-220.

214. Lee, C.-S., Z. Shayegan, F. Haghighat, L. Zhong, et al., Experimental evaluation of in-duct electronic air cleaning technologies for the removal of ketones. Building and Environment, 2021. **196**: p. 107782.

215. Malayeri, M., F. Haghighat, and C.-S. Lee, Kinetic modeling of the photocatalytic degradation of methyl ethyl ketone in air for a continuous-flow reactor. Chemical Engineering Journal, 2021. **404**: p. 126602.

216. Lee, C.-S., F. Haghighat, A.H. Mamaghani, Z. Shayegan, et al., Removal of toxic vapors by oxidation - Development of laboratory test procedures for in-duct air-cleaning systems,. 2020, Report No.R-1080, Institut de recherche Robert-Sauvé en santé et en sécurité du travail (IRSST).

217. Whyte, H.E., A. Subrenat, C. Raillard, and V. Héquet, Understanding the influence of media geometry on the degradation of acrylonitrile: Experimental and CFD analysis. Chemical Engineering Science, 2019. **209**: p. 115217.

218. Bianchi, C., S. Gatto, C. Pirola, A. Naldoni, et al., Photocatalytic degradation of acetone, acetaldehyde and toluene in gas-phase: comparison between nano and micro-sized TiO2. Applied Catalysis B: Environmental, 2014. **146**: p. 123-130.

219. He, C., J. Cheng, X. Zhang, M. Douthwaite, et al., Recent Advances in the Catalytic Oxidation of Volatile Organic Compounds: A Review Based on Pollutant Sorts and Sources. Chemical Reviews, 2019. **119**(7): p. 4471-4568.

220. Malayeri, M., C.-S. Lee, and F. Haghighat, Modeling of Photocatalytic Oxidation Reactor for Methyl Ethyl Ketone Removal from Indoor Environment: Systematic Model Development and Validation. Chemical Engineering Journal, 2020: p. 128265.

221. Garcia-Hernandez, J.M., B. Serrano-Rosales, and H. de Lasa, Energy Efficiencies in a Photo-CREC-Air Reactor: Conversion of Model Organic Pollutants in Air. Industrial & Engineering Chemistry Research, 2012. **51**(16): p. 5715-5727.

222. S. NIOSH, National Institute for Occupational Safety and Health (NIOSH), (2019) http://www.cdc.gov/niosh/.

223. Hickox, W.H. and J.E. Denton, The Determination of Acute Reference Exposure Levels for Airborne Toxicants. 1999.

224. Gentry, P.R., T. Covington, H. Clewell, and M. Anderson, Application of a physiologically based pharmacokinetic model for reference dose and reference concentration estimation for acetone. Journal of Toxicology and Environmental Health Part A, 2003. **66**(23): p. 2209-2225.

225. USGBC, L., LEED v4.1 for Building Design and Construction. US Green Building Council, Washington DC, 2020.

226. Bo, L., S. Xie, H. Meng, J. Liu, et al., Photocatalytic Oxidation of Gaseous Toluene by Visible-Light-Driven CoCuMnO x: Performance and Mechanism. Catalysis Letters, 2017. **147**(7): p. 1623-1630.

227. Chu, H., Y. Lin, and C. Lin. Characterization, degradation, and reaction pathways of indoor toluene over visible-light-driven S, Zn Co-doped TiO2. in IOP Conference Series: Earth and Environmental Science. 2017. IOP Publishing.

228. Sleiman, M., P. Conchon, C. Ferronato, and J.-M. Chovelon, Photocatalytic oxidation of toluene at indoor air levels (ppbv): Towards a better assessment of conversion, reaction intermediates and mineralization. Applied Catalysis B: Environmental, 2009. **86**(3-4): p. 159-165.

229. Frankcombe, T.J. and S.C. Smith, OH-initiated oxidation of toluene. 2. Master equation simulation of toluene oxide isomerization. The Journal of Physical Chemistry A, 2007. **111**(19): p. 3691-3696.

230. Zhao, W., J. Dai, F. Liu, J. Bao, et al., Photocatalytic oxidation of indoor toluene: Process risk analysis and influence of relative humidity, photocatalysts, and VUV irradiation. Science of The Total Environment, 2012. **438**: p. 201-209.

231. Malayeri, M., C.-S. Lee, J. Niu, J. Zhu, et al., Kinetic and reaction mechanism of generated by-products in a photocatalytic oxidation reactor: Model development and validation. Journal of Hazardous Materials, 2021: p. 126411.

232. ASHRAE, Control of Gaseous Indoor Air Contaminants. American Society of Heating, Refrigerating and Air-Conditioning Engineers, 2015.